

# A GRANULAR MODEL OF SOLIDIFICATION AS APPLIED TO HOT TEARING

THÈSE N° 3795 (2007)

PRÉSENTÉE LE 27 AVRIL 2007

À LA FACULTÉ DES SCIENCES ET TECHNIQUES DE L'INGÉNIEUR

Laboratoire de simulation des matériaux

PROGRAMME DOCTORAL EN SCIENCE ET GÉNIE DES MATÉRIAUX

ÉCOLE POLYTECHNIQUE FÉDÉRALE DE LAUSANNE

POUR L'OBTENTION DU GRADE DE DOCTEUR ÈS SCIENCES

PAR

**Stéphane VERNÈDE**

Diplôme d'Ingénieur des Arts et Manufactures, Ecole Centrale de Paris, France  
et de nationalité française

acceptée sur proposition du jury:

Prof. H. J. Mathieu, président du jury

Prof. M. Rappaz, directeur de thèse

Dr Ph. Jarry, rapporteur

Prof. L. Laloui, rapporteur

Prof. M. Suéry, rapporteur



ÉCOLE POLYTECHNIQUE  
FÉDÉRALE DE LAUSANNE

Suisse  
2007



# Abstract

Hot cracking is a spontaneous failure of an alloy during solidification. It is a severe problem for casting industry as it reduces the productivity of cast houses and limits the range of alloys compositions that can be industrially produced.

Hot tears occurs at the end of solidification, when solid grains are separated by thin liquid films. At this stage of solidification, fluid flow between the grains is difficult and the solid network is not continuous enough to transmit stresses. The material is extremely brittle. Moreover, the deformation induced by the thermal shrinkage of the material tends to localize in hot spots, *i.e.*, in zones which solidify at last. These zones become in tension and the concomitant effect of the tensile stress with the intrinsic brittleness of the material result in a hot crack. Even though the general mechanisms of hot tearing are understood, the importance of each physical parameter remains ill defined.

The present work is mainly focused on the derivation of a granular model of mushy zone (the zone where solid and liquid coexist) for aluminium alloys, *i.e.*, a model which explicitly considers the behaviour of each grain while being sufficiently simple to allow the computation of large mushy zones. First, a solidification model based on the Voronoi diagram of a random set of nuclei is derived. This model computes the solidification in each polyhedron considering back-diffusion and coalescence. Second, a pressure drop calculation is performed in the network of connected liquid channels assuming the centre of solid grains to be fixed. This model considers a Poiseuille flow in each channel, Kirchhoff's conservation of flow at nodal points and flow Losses compensating solidification (KPL model). Finally, the displacement of the solid grain centres is considered and the mechanical behaviour of the mushy zone is computed assuming perfectly rigid solid grains.

This model shows the progressive formation of grain clusters and the localization of fluid flow at high solid fraction. Therefore, it allows to define transitions in the behaviour of the mushy zone. These transitions are essential for hot cracking models, but should be introduced as parameters in continuum approaches. Finally, the mechanical model shows a strong localization of deformation in liquid channels normal to the stress direction. Such channels create ideal sites for the nucleation and the propagation of hot cracks.

**Keywords :**

Hot cracking, Permeability, Solidification, Percolation, Granular model





# Résumé

La fissuration à chaud est une rupture spontanée d'un alliage métallique lors de sa solidification. C'est un problème grave pour l'industrie car il réduit la productivité des fonderies et limite la gamme de composition des alliages qui peuvent être produits industriellement.

La fissuration à chaud se produit à la fin de la solidification lorsque les grains de solides sont séparés par de fins films de liquide. A ce point, l'écoulement du liquide est difficile et le réseau de solide n'est pas suffisamment continu pour transmettre des contraintes. Le matériau est extrêmement fragile. De plus, les déformations induites par le retrait thermique tendent à se localiser dans des points chauds, *i.e.*, les zones se solidifiant en dernier. Ces zones sont donc soumises à de fortes contraintes en tension qui, étant donnée la fragilité intrinsèque du matériau, engendrent une fissuration à chaud. Bien que le mécanisme général de la fissuration à chaud soit bien compris, le rôle respectif de chaque phénomène physique reste mal défini.

Ce travail de thèse s'est principalement concentré sur le développement d'un modèle granulaire de la zone pâteuse (la zone où le liquide et le solide coexistent), *i.e.*, un modèle qui prend en compte le comportement de chaque grain tout en restant suffisamment simple pour permettre le calcul de grandes zones pâteuses. Tout d'abord, nous dérivons un modèle de solidification basé sur le diagramme de Voronoï d'un ensemble de germes répartis aléatoirement. Ce modèle calcule la solidification dans chaque polygone en considérant la rétro-diffusion ainsi que la coalescence des grains. Ensuite, un calcul de la chute de pression dans le réseau des canaux de liquide est effectué en considérant que les centres des grains de solide sont fixes. Ce modèle considère un écoulement de Poiseuille dans chaque canal, la loi de Kirchhoff pour la conservation des flux à chaque noeud du réseau et des Pertes de flux induites par le retrait de solidification (modèle KPP). Finalement, nous considérons le déplacement des grains de solide tout en supposant que ces grains restent parfaitement rigides.

Ce modèle montre la formation progressive d'amas de grains et la localisation du flux de liquide à forte fraction de solide. Ces phénomènes permettent de définir des transitions dans le comportement de la zone pâteuse. Ces transitions sont essentielles pour les modèles de fissuration à chaud mais sont introduites en tant que paramètres dans les approches continues. De plus, le modèle mécanique montre une forte localisation de la déformation dans des canaux de liquide orientés perpendiculairement à la direction des contraintes. De tels canaux créent des sites idéaux pour la germination et la propagation des fissures à chaud.

## Mots clés :

Fissuration à chaud, Perméabilité, Solidification, Percolation, Modèle granulaire



# Remerciements

Au cours de ce travail, j'ai eu la chance de bénéficier des conseils de mes deux tuteurs, Michel Rappaz, professeur au Laboratoire de Simulation des Matériaux et Philippe Jarry, ingénieur au Centre de Recherche de Voreppe (CRV) Alcan. J'ai souvent été frappé par la fertilité des rencontres entre leurs deux points de vue.

J'aimerais remercier Michel Rappaz de m'avoir accueilli dans son laboratoire et de m'avoir proposé un sujet qui m'a tant passionné. Je voudrais aussi le remercier de m'avoir fait bénéficier de sa grande intuition scientifique et de son esprit d'analyse clair et précis. L'ambiance sympathique et cordiale qui règne dans le laboratoire est aussi un reflet de ses grandes qualités humaines.

Je tiens aussi à remercier Philippe Jarry de m'avoir fait bénéficier de sa profonde compréhension de la solidification et de m'avoir fait entrevoir une partie de son immense culture.

Cette thèse a été financée par le CRV Alcan, l'Association Nationale de la Recherche Technique (ANRT) France et l'Ecole Polytechnique Fédérale de Lausanne. Je tiens à remercier ces institutions de leur soutien et de leur confiance.

Je remercie Michel Suéry de ses conseils, de l'intérêt qu'il a porté à ce travail tout au long de sa réalisation et d'avoir accepté de participer au jury de ce travail. Je voudrais aussi remercier Hans Jörg Mathieu d'avoir présidé le jury de cette thèse et Lyesse Laloui d'avoir accepté d'être rapporteur interne.

L'approche développée dans cette thèse a débuté par le travail de diplôme de Vincent Mathier. Je voudrais le remercier des conseils précieux qu'il m'a donné tout au long de ce travail.

Benoît Commet m'a encadré lors de mon stage au CRV. Il m'a introduit au domaine de la solidification et de la fissuration à chaud avec poésie et passion. Je voudrais l'en remercier.

Je tiens aussi à remercier Jon Dantzig qui a été comme un troisième tuteur lors de cette thèse. Il m'a énormément aidé pour la mise au point des différents modèles.

J'ai pu profiter des conseils et de l'aide de nombreuses autres personnes. Je voudrais les en remercier chaleureusement : Olivier Ludwig pour la rhéologie de la zone pâteuse, Andrew Hoadley pour la perméabilité des milieux poreux, Alain Jacot pour les simulations de Pseudo Front Tracking, Christophe Martin pour la Méthode des Eléments Distincts, Gael Couturier pour les problèmes de porosité, Laurent Ponson pour les propriétés d'échelle des fractures, Jean-Luc Desbiolles pour la programmation, Jean-Marie Drezet pour les problèmes de mécanique, Jean-Daniel Wagnière pour la réalisation des traces laser.

Je voudrais aussi remercier Lucien Germond et Tanya Meredith qui ont apporté des résultats à cette thèse grâce à leur projet de semestre au laboratoire.

Tout au long de ces années j'ai partagé mon bureau avec Simona Moldovan, je voudrais la remercier de son amitié, de sa sympathie et de l'apport régulier en vitamine que m'ont apporté les pommes qu'elle m'a gentiment données. Plus récemment, nous avons eu la chance de partager notre bureau avec Martin Rhème.

Je voudrais aussi remercier l'incroyable équipe avec qui j'ai passé tant de bons moments et qui a toujours été là lorsque j'en avais besoin, Frédéric Gonzales, Amin Rostamian, la famille Lapin, Janine Conde, Evelyn Hollenstein, Milan Felberbaum, Mario Salgado, Frédéric Kohler, Christoph Niederberger, Alvaro Artieda, Denis Favez, Audrey Chaumartin, Aurèle Mariaux, Emmanuelle Courjault, Christine Leroy, Jonathan Friedli, Jonas Vannod.

J'aimerais remercier les deux secrétaires successives du laboratoire, Arlette Blatti et Anne Roy, pour leur aide au quotidien.

C'est aussi l'occasion pour moi d'adresser ma reconnaissance à deux enseignants qui ont marqué mes études. Victor Zyma, professeur au Laboratoire d'Elaboration des Matériaux de l'Ecole Centrale Paris, m'a sensibilisé à l'observation attentive de la nature. Mr Chardon, professeur en classe préparatoire au lycée Blaise Pascal, m'a enseigné la physique avec une vision claire et profonde.

Je voudrais remercier mes parents et mon frère de leur amour et de leur soutien tout au long de ces années. J'aimerais aussi remercier toute ma famille et en particulier ma grand-mère maternelle, Jacqueline Fabre, qui m'a communiqué l'amour de la science, et ma grand-mère paternelle, Denise Vernède, qui m'a appris à regarder le côté joyeux de la vie.

Enfin, je voudrais exprimer mon amour à ma femme, 卓娅, sa présence rend les moments heureux plus savoureux et me donne plus de force pour les moments difficiles.

# Contents

<b>1</b>	<b>Introduction</b>	<b>1</b>
1.1	Aluminium . . . . .	1
1.1.1	Aluminium history . . . . .	1
1.1.2	Aluminium alloys . . . . .	2
1.1.3	Aluminium production . . . . .	3
1.2	Direct chill casting . . . . .	3
1.2.1	The process . . . . .	4
1.2.2	Casting defects . . . . .	4
1.3	Hot tearing . . . . .	6
1.4	Hot tearing in DC casting . . . . .	6
1.4.1	Other processes . . . . .	6
1.5	The overall picture of hot cracking: goal of this thesis . . . . .	8
1.5.1	A multi-scale problem . . . . .	8
1.5.2	Approach developed in the present thesis . . . . .	9
1.5.3	Outline . . . . .	9
<b>I</b>	<b>The roots</b>	<b>11</b>
<b>2</b>	<b>Experimental investigation of hot cracking</b>	<b>13</b>
2.1	Parameters sensitivity . . . . .	13
2.1.1	Process parameters . . . . .	13
2.1.2	Alloy parameters . . . . .	14
2.2	Observation of hot cracking . . . . .	16
2.2.1	Local observation . . . . .	16
2.2.2	Macroscopic observations . . . . .	18
2.3	Mushy zone rheology . . . . .	20
2.3.1	Pure phases rheology . . . . .	20
2.3.2	Shear tests . . . . .	21
2.3.3	Compression tests . . . . .	24
2.3.4	Traction tests . . . . .	25
2.3.5	Effect of surface tension . . . . .	29
2.3.6	Summary . . . . .	31
<b>3</b>	<b>Models for hot cracking</b>	<b>33</b>
3.1	Hot cracking criteria . . . . .	33
3.1.1	Criteria based on the solidification interval . . . . .	33
3.1.2	Criteria based on feeding ability . . . . .	33

3.1.3	Criteria based on liquid films strength . . . . .	35
3.1.4	Criteria based on accumulated strain . . . . .	36
3.1.5	Comparison between the criteria . . . . .	37
3.2	Continuum modelling of mushy zone . . . . .	38
3.2.1	Balance equations . . . . .	39
3.2.2	Simplification of the balance equations . . . . .	41
3.2.3	Constitutive equation for the permeability . . . . .	43
3.2.4	Constitutive equations for the effective stress . . . . .	44
3.2.5	Applications of two phase models . . . . .	47
<b>4</b>	<b>Scale invariance</b>	<b>49</b>
4.1	Percolation theory . . . . .	49
4.1.1	Lattice percolation . . . . .	49
4.1.2	Continuum percolation . . . . .	51
4.1.3	Finite size percolation . . . . .	52
4.2	Scaling properties of cracks . . . . .	53
4.2.1	Self-similarity and self-affinity . . . . .	53
4.2.2	Self-affinity of fracture . . . . .	55
<b>II</b>	<b>The trunk</b>	<b>57</b>
<b>5</b>	<b>Experiment</b>	<b>59</b>
5.1	A mushy zone traction test: the Pechiney's rig test . . . . .	59
5.1.1	Description of the apparatus . . . . .	59
5.1.2	The alloys . . . . .	61
5.1.3	Observation of the fracture profiles . . . . .	61
5.2	Laser remelting experiments . . . . .	62
5.2.1	Description of the apparatus . . . . .	62
5.2.2	The alloys . . . . .	63
5.2.3	Observations . . . . .	63
5.2.4	Estimation of grain misorientation . . . . .	63
<b>6</b>	<b>A solidification model for globular microstructures</b>	<b>65</b>
6.1	A model based on Voronoi diagrams . . . . .	65
6.1.1	Derivation of the model . . . . .	65
6.1.2	A model for coalescence . . . . .	67
6.2	A model for grain corners . . . . .	68
6.2.1	Derivation of the model . . . . .	68
6.2.2	Validity and limits of the model . . . . .	71
<b>7</b>	<b>Mushy zone mechanics</b>	<b>77</b>
7.1	A model for feeding: the KPL model . . . . .	77
7.1.1	Derivation of the model . . . . .	77
7.1.2	Numerical integration . . . . .	79
7.2	Grain movement . . . . .	81
7.2.1	Hypothesis and notations . . . . .	81
7.2.2	Dimensional analysis and simplification of the equations . . . . .	82

7.2.3	Integration of the constitutive equation . . . . .	84
7.2.4	Implementation of volumetric shrinkage . . . . .	87
7.3	First analysis of the equations . . . . .	90
7.3.1	Comparison with continuum equations . . . . .	90
7.3.2	Dimensionless matrix . . . . .	92
7.3.3	Linearity of the equations . . . . .	95
7.3.4	Detection of contacts . . . . .	95
<b>III</b>	<b>The leaves</b>	<b>97</b>
<b>8</b>	<b>Experimental results</b>	<b>99</b>
8.1	Traction test . . . . .	99
8.1.1	Mechanical measurements . . . . .	99
8.1.2	Observations of fracture profiles . . . . .	102
8.1.3	Scaling analysis of fracture surfaces . . . . .	106
8.1.4	Summary . . . . .	111
8.2	Laser remelting experiments . . . . .	111
8.2.1	Crack statistics . . . . .	111
8.2.2	Grain orientation relations . . . . .	112
<b>9</b>	<b>Transitions of the mushy zone</b>	<b>115</b>
9.1	Grain structure evolution . . . . .	115
9.1.1	Formation of grain clusters . . . . .	115
9.1.2	Localization of feeding . . . . .	117
9.1.3	Percolation of solid grains . . . . .	122
9.2	Morphological maps for the mushy zone . . . . .	123
9.2.1	Definition of the transition points . . . . .	123
9.2.2	Parameters sensitivity . . . . .	125
<b>10</b>	<b>Mushy zone mechanics</b>	<b>127</b>
10.1	Tractions tests . . . . .	127
10.1.1	Redistribution of fluid . . . . .	127
10.1.2	Transition in the feeding mechanism . . . . .	130
10.2	Toward a criterion for hot tearing . . . . .	135
10.2.1	A simple model for hot tear nucleation . . . . .	135
<b>11</b>	<b>Conclusion</b>	<b>139</b>
<b>A</b>	<b>List of symbols</b>	<b>141</b>
<b>B</b>	<b>Solute balance at a grain corner</b>	<b>145</b>
<b>C</b>	<b>Detailed integration of the constitutive equations</b>	<b>147</b>
C.1	Stress tensor . . . . .	147
C.2	Mass balance . . . . .	148
	<b>References</b>	<b>151</b>

<b>Curriculum Vitae</b>	<b>161</b>
-------------------------	------------

<b>List of publications</b>	<b>163</b>
-----------------------------	------------



# Chapter 1

## Introduction

### 1.1 Aluminium

#### 1.1.1 Aluminium history

Aluminium represents 8% of the Earth crust mass, that is the third most abounding element after oxygen (47%) and silicon (28%). It is found in nature in various oxidized form, *e.g.*, aluminium silicates which are the basic constituent of clay. The industrial production of aluminium starts from bauxite, the main constituent being aluminium hydroxides  $\text{Al}(\text{OH})_3$ ,  $\text{AlO}(\text{OH})$ .

The name of aluminium comes from alum, which denominates the family of aluminium bi-sulphates, *e.g.*,  $\text{KAl}(\text{SO}_4)_2 \cdot 12(\text{H}_2\text{O})$ . These compounds were used since the very early antiquity for the fixation of colour in dyeing processes and as an astringent in medicine [1]. These properties were already mentioned in ancient Assyrian and Egyptian texts [2]. Today colours produced by petrochemistry are much cheaper than natural colours and alum has lost its strategical position in textile industry. Yet, this product is still used as a flocculation agent in water purification processes.



**Figure 1.1:** Various representations of alum in hieroglyph script [2].

The first reference to a metal “very light, and almost as bright as silver” is found in *Historia Naturalis* of Pliny the Elder: A goldsmith presented to the Emperor Tiberius a plate made of this metal. He told the emperor that he made this metal out of clay and that only he and the gods knew how to do it. Tiberus, as a financial expert, became afraid that the production of this new metal decreased the value of the gold and silver he had accumulated. He therefore ordered the goldsmith to be beheaded [3].

Because of its very high electro-positivity, aluminium is difficult to reduce and the presence of metal in alum remained an open question during all the Middle Age. It is only in 1808 that Sir Humphry Davy identified the existence of this metal. He named it *aluminium* and later *aluminum*. The first synthesis of aluminium was probably done in 1821 by the Danish Oersted via the reaction of aluminium chloride with potassium, but the results of his work were contested. In 1827, based on Oersted works, Friedrich

1xxx :	Almost pure aluminium (at least 99 % of aluminium in mass)
2xxx :	Al-Cu alloys
3xxx :	Al-Mn alloys
4xxx :	Al-Si alloys
5xxx :	Al-Mg alloys
6xxx :	Al-Mg-Si alloys
7xxx :	Al-Zn-Mg alloys
8xxx :	Miscellaneous series that contains in particular the Al-Li alloys

**Table 1.1:** Standard nomenclature of wrought aluminium alloys

Wöhler produced globules of aluminium. In parallel, Pierre Berthier, discovered that the mineral present near the village Les Baux de Provence in the south of France was mainly an aluminium hydroxide. Sainte-Claire Deville improved the reduction process of Wöhler and created in 1858 a process to produce alumina (aluminium oxide  $\text{Al}_2\text{O}_3$ ) out of bauxite. With funding from the emperor Napoleon III he created an aluminium manufacture in Salindres, a village near les Baux de Provence. With this chemical process, the industry of aluminium developed in France, Germany and Great Britain.

In 1886, Paul Héroult (France) and Charles Hall (USA) simultaneously deposited a patent for the reduction of aluminium with an electrolytic process. In this process, alumina is dissolved in a bath of molten cryolite. An electric current is passed through the bath and molten aluminium deposits at the cathode while the consumable graphite anode reacts with dioxygen, thus producing  $\text{CO}_2$ . The two first companies exploiting this technology are funded in 1888, in the USA (The Pittsburgh Reduction Company) and in Switzerland (Société Anonyme pour l'Industrie de l'Aluminium). The last key-stone for the production of aluminium was done by Bayer in 1890 who developed a simple and efficient process for the extraction of alumina out of bauxite. Nowadays, the Bayer process and the Hall-Héroult process are still the base of primary aluminium production.

### 1.1.2 Aluminium alloys

Aluminium has many interesting intrinsic properties. It is a light metal, with a low melting point. It has good thermal and electrical conductivity. Despite its high electropositivity, its oxidation forms an impermeable layer of alumina that protects from further corrosion. Moreover, aluminium exhibits a pleasant surface finish, that can be improved by various surface treatments. As a pure substance, aluminium is an extremely malleable and ductile metal. Addition of alloying elements can considerably increase its strength but necessarily modify the other properties of the metal. Therefore, a large range of aluminium alloys have been developed.

Cast alloys are distinguished from wrought alloys. Cast alloys are directly cast to their definitive form (sand casting, high pressure die casting, investment casting). Wrought alloys are cast into simple shapes and are transformed by subsequent mechanical treatments (rolling, extrusion, forging). Wrought alloys are identified with a four digit number where the first digit indicates the major alloying element (Table 1.1).

The alloys of the series 2xxx, 6xxx, 7xxx are precipitation hardening alloys and thus exhibit high strength. The 2xxx and 7xxx alloys have the best mechanical properties

and are used in applications where high specific properties are required (aeronautics, aerospace, transport, military applications). Yet, the presence of copper in these alloys increases their sensitivity to corrosion. The 6xxx have lower mechanical properties but have very good forming abilities and a good resistance to corrosion. They are thus used for profiled products. They can also be used as electrical conductors.

The other series are hardened by mechanical treatment. The 1xxx alloys are mainly used for their ability to be cold formed. They are widely used for common goods (packaging, cookware, heat exchangers, thin foils). High purity alloys (99.99 %) are used in electronics and optics. The 3xxx series have the same applications as the 1xxx series but with increased mechanical properties. The 5xxx series have relatively good mechanical properties, a good welding ability and a good resistance to corrosion. Therefore, they are used as structural elements. The Al-Si alloys (4xxx) are seldom used as wrought alloys, but are intensively used as cast alloys [4, 5].

### 1.1.3 Aluminium production

Aluminium can thus develop a wide range of properties depending on the alloying elements and treatments (thermal and mechanical). This makes aluminium useful in various applications. They are distributed among (in mass percent of primary aluminium production): 26 % transportation (aircraft, ship, rail road equipment, automotive), 20% packaging (drink can, aluminium foil), 20% construction (bridge infrastructure, window and door frame, heating), 9% electricity (transmission line, transition tower) and 25 % other (furniture, sport equipment, machinery) [6].

World production of primary aluminium has almost tripled in the last 20 years. During the year 2005, more than 30 millions tons of primary aluminium have been produced world wide. This production is distributed among: Africa 5%, North America 17%, Latin America 8%, Asia 10%(without China), West Europe 14 %, East/Central Europe 13 % (including Russia Federation), Oceania 7%, China 24% [6]. Note that today China is largely the world largest producer of aluminium. Its aluminium production has almost doubled in three years. This phenomenon is certainly induced by the fast industrial development of the country and thus its need for raw materials. Moreover China has not signed the Kyoto's agreements and therefore has not limitations for CO<sub>2</sub> emissions.

Production of aluminium is extremely energy consuming, nowadays the electrolysis of one ton of aluminium requires in average 15 MWh, which represents the annual consumption of 4 average Swiss households. Recycling of aluminium scrap requires only 5% of this energy. In 2005, recycled aluminium represents only around 1 % percent of the total production [6]. With the increase of energy cost, recycling will become ever more interesting from an economical point of view. In a way, each piece of aluminium can be viewed as an energy storage.

## 1.2 Direct chill casting

Once aluminium has been separated from oxygen, the most frequent casting process for producing wrought aluminium alloys is direct chill casting (DC casting, Fig. 1.2).

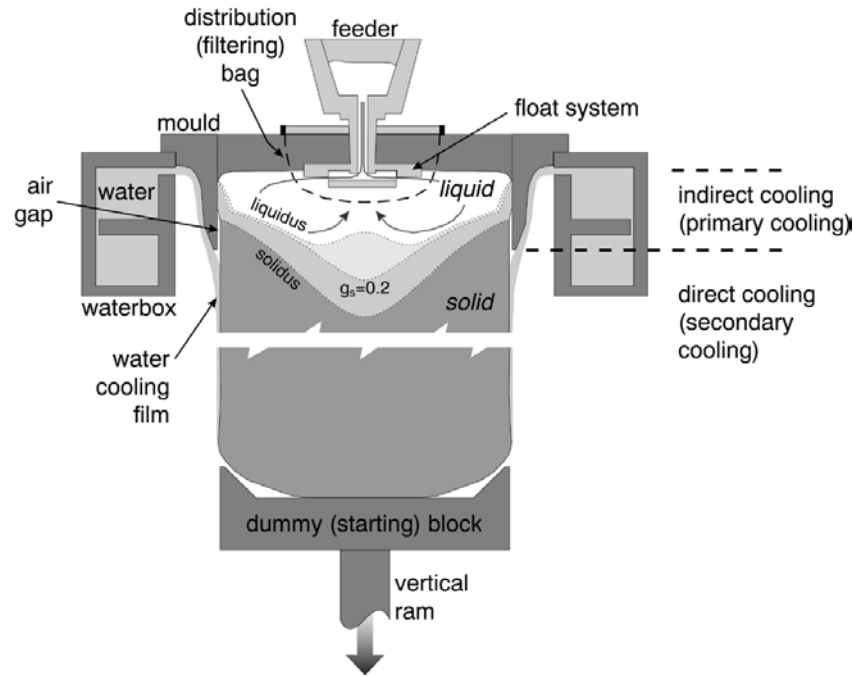


**Figure 1.2:** The DC casting process [7].

### 1.2.1 The process

At the beginning of the process, an open mould is closed by a dummy block. Liquid metal is poured from an oven to the mould via a feeder. A distribution bag ensures an even and smooth flow of the liquid. Once a sufficient solid shell has formed, the dummy block is pulled down. At this stage, the mould is closed by the solidified shell itself. The metal is thus cooled in two steps: First, by contact with the mould (primary cooling) and second by direct contact with the water jet (secondary cooling). While the dummy block is pulled down, the level of liquid metal in the mould is kept constant by a flux of liquid metal. Once the product has reached the maximum length, the process is stopped. This process is used to cast billets of diameters up to almost 1 m and slabs of section up to  $2000 \times 600 \text{ mm}^2$ . The cast products are generally around 10 m long.

This process, inspired from steel continuous casting, was introduced for aluminium alloys in 1936 [8]. It brings many advantages upon the traditional ingot casting. It increases productivity as products are cast in a shape directly suitable for the subsequent mechanical treatment, *e.g.*, slabs can be directly hot rolled after scalping the rolling faces. Moreover, it is possible to cast several products at the same time. It also increases products quality. Surface aspect is enhanced and the very high cooling rate due to the direct contact with water favours a fine grain structure.

### 1.2.2 Casting defects

DC casting is nonetheless a process that should be carefully controlled. Between primary and secondary cooling, the solid shell contracts and loses thermal contact (Fig. 1.2). Therefore the shell tends to partially remelt. Partial remelting (exudation Fig. 1.3 (1)) decreases the surface quality of the final product. Moreover, the start-up phase is a

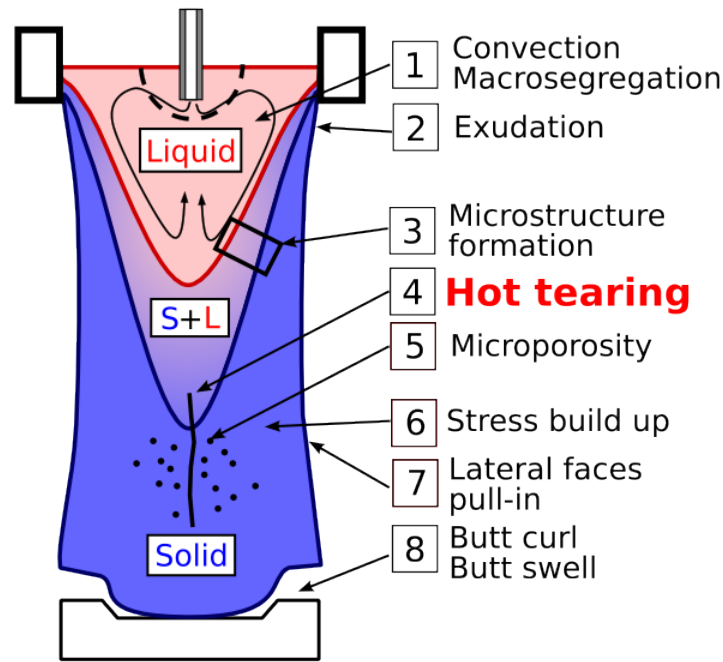


**Figure 1.3:** Phenomena controlling the quality of cast products (adapted from M. Rappaz).

very sensitive phase during which many defects can be produced, or even worse, during which water can flow in between the casting and the bottom block leading to a risk of explosion. In order to control these problems, the DC casting process is nowadays largely automatised [9].

Despite this control many phenomena are still limiting the DC casting process. As temperature decreases, the material naturally shrinks and because of the very steep thermal gradients this shrinkage is very inhomogeneous. This induces natural convection in the liquid phase (besides forced convection), which, associated with microsegregation (composition variation of the alloy at the scale of the microstructure induced by solidification), can result in macrosegregation (composition variation at the scale of the product) (Fig. 1.3 (2)). This is clearly a problem as the final products will get non-homogeneous properties. Similarly, the shrinkage inhomogeneity in the solid phase induces deformation and residual stresses in the cast product (Fig. 1.3 (6)). These stresses are dangerous for subsequent mechanical working (in particular sawing) and have to be released with annealing treatment.

Microstructure forms during solidification, in the zone where both solid and liquid coexist (Fig. 1.3 (3)). An art of metallurgist and casting engineer is to control this microstructure formation. For example, the size of the grains can be decreased by the presence of  $\text{TiB}_2$  (or  $\text{TiC}$ ) particles which act as nucleation centres for the solid phase (inoculation). Furthermore, during solidification two major casting defects can occur. First porosity, *i.e.*, formation of gaseous pockets, and second hot tearing which is the main focus of this work.

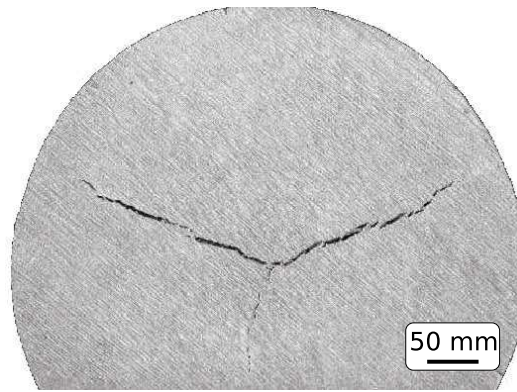


**Figure 1.4:** Hot cracking in a billet (From ALCAN CRV).

### 1.3 Hot tearing

Hot tearing is a spontaneous failure of an alloy during its solidification. It occurs near the end of solidification and leaves an intergranular fracture profile. In the literature this phenomenon can be called hot cracking, hot tearing or hot shortness. We are mainly interested in hot cracks of aluminium alloys but this phenomenon is present in most metallic system, *e.g.*, steels, magnesium alloys, nickel based super alloys, copper alloys.

### 1.4 Hot tearing in DC casting

Hot cracking is a severe defect for casting industry. Indeed, Fig. 1.4 shows an internal hot crack which starts from the centre of the billet and spawns as a three branch star. It is clear that a product with such a crack has to be remelted as scrap.

Precipitation hardening high strength alloys (2xxx, 6xxx, 7xxx series) are particularly sensitive to hot tearing as explained in Sec. 3.1.5. Note that some work hardening alloys, in particular in the 5xxx series, are also sensitive to hot cracking. Many compositions could give very good mechanical properties, but such alloys are so prone to hot tearing that their industrialisation is not possible, *i.e.*, poor castability. Thus, a high strength commercial alloy is an equilibrium between final product properties and castability.

The occurrence of hot cracking presents a random nature. Therefore even under very well controlled casting parameters, the casting of a sensitive commercial alloys can create up to 10% scrap. Moreover small hot cracks can initiate dangerous cold cracks (cracks driven by stress accumulation in the fully solid state).

#### 1.4.1 Other processes

Hot cracking is a problem in welding processes. Not surprisingly, the aluminium alloys sensitive to hot cracking in casting processes tend to crack during welding [4]. Welding these alloys generally requires to add a soft filler material which considerably weakens the welded joint.

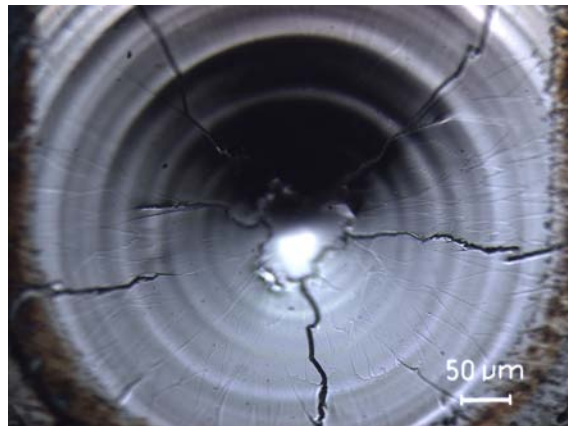


**Figure 1.5:** Hot crack at the final spot of a laser remelting experiment on an Al-Cu alloy. Despite the very different scales, the similarity with hot cracking in a billet is striking [10].



**Figure 1.6:** A raku pottery [12].

Welding experiments are generally difficult to interpret as they generate very complex thermal and mechanical fields. Yet, because welding tests are easy and rapid, they are a convenient way of testing the hot tearing sensitivity of a wide range of alloy compositions.

As the hot cracking phenomenon is common to all metallic systems, we might wonder if non-metallic materials present similar phenomena during their solidification. One poetic example is maybe the raku technique, *i.e.*, a traditional Japanese glazing process.

In this process, the pottery is taken out of the oven when the glazing is liquid, and is quickly put in a combustible substance such as sawdust or straw. The glazing is then reduced by the smoke, which creates a wide range of colours and a metallic aspect. Another consequence is the presence of multiple failures in the glazing, which creates an aesthetic pattern. [11]

Hot cracking occurs in a 3D media, whereas raku cracking occurs in a 2D layer. Moreover, it is an open question to know whether this failure occurs during solidifi-

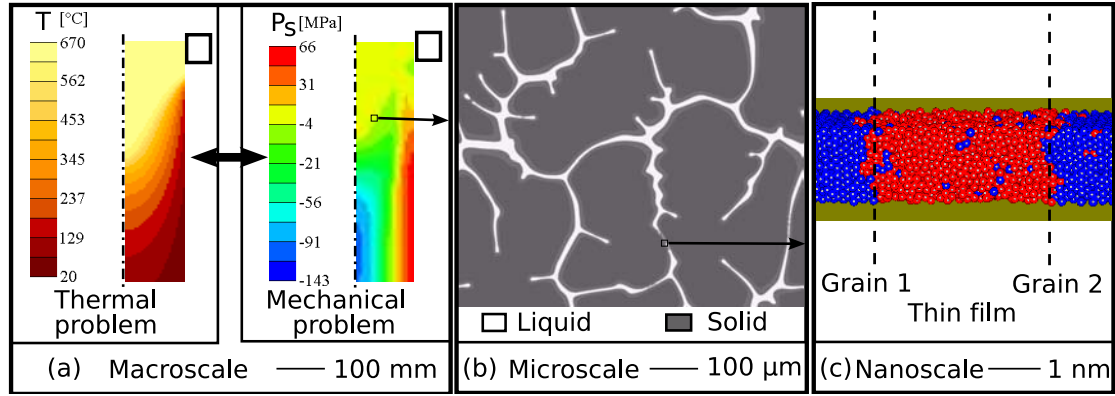


**Figure 1.7:** The various scales relevant for hot cracking formation. (a) Process (Finite Element simulation [14]), (b) Microstructure (Pseudo Front Tracking simulation [15]), (c) Coalescence of grains (Molecular Dynamics simulation [16]).

cation or once the glazing layer has solidified. A detailed observation of such glazing shows that there are two networks of failures (Fig. 1.6), one of big failures and another one of smaller failures. It is possible that the first network is generated during solidification whereas the second occurs afterwards.

## 1.5 The overall picture of hot cracking: goal of this thesis

### 1.5.1 A multi-scale problem

Hot cracking is probably a problem since the very early metallurgy. Yet, in 2006 casting industry still needs research on this topic. This is maybe due to the large range of scales implied in this phenomenon.

Thermal and mechanical fields are generated by the process. Therefore a good description of the material and of the transport phenomena at this scale ( $\sim 1\text{m}$ ) is necessary.

In the mushy zone, *i.e.*, the zone where both solid and liquid coexist, nucleation and growth of primary phase can form a wide variety of microstructures, including columnar dendrites, equiaxed dendrites or globular grains. Moreover, other phases can form, *e.g.*, in eutectic or peritectic solidification [13]. Thus solidification models require a good description of transport phenomena at the scale of the microstructure ( $\sim 10^{-4}\text{m}$ ).

The solidification of the last liquid films between two grains implies the bonding of two crystal lattices. In the present work we call *coalescence* this formation of a grain boundary out of two solid-liquid interfaces. Models for coalescence have to consider interactions at the nanometer scale ( $\sim 10^{-9}\text{m}$ ).

In the present problem these different scales are particularly interdependent. Microstructure formation is highly dependent on macroscopic fields, in particular thermal history. In return, microstructure determines macroscopic transport properties, in particular mechanical properties. For example, microstructure influences the coherency solid fraction, *i.e.*, the point above which significant stresses can be transmitted through the solid network (see Sec. 2.3.6). Similarly, coalescence determines the transition from



a fragile fracture behaviour to a ductile fracture behaviour, and thus have spectacular influence on the macroscopic properties of the material (see Sec. 8.1).

Moreover during solidification a progressive transition from a continuous liquid phase to a continuous solid phase occurs. This transition consist in the progressive coalescence of solid grains and thus the formation of grain clusters. Near the percolation transition, *i.e.*, the formation of the continuous solid phase [17], the size of grains clusters is close to the process size (see Sec. 4.1). The heterogeneity due to microscale becomes macroscopic. This transition occurs near the end of solidification precisely in the region sensitive to hot cracks.

Nowadays the basic phenomena implied in hot cracking are identified (see Chaps. 2 and 3). Yet, their respective importance is still not clearly understood. Indeed, it is difficult to find a point of view which brings together the various scales of hot tearing.

### 1.5.2 Approach developed in the present thesis

We have decided to model each grain while keeping this model simple enough to compute the behaviour of a large mushy zone. This approach is called a *granular model*. Therefore, we will look at the mushy zone at the mesoscale, *i.e.*, in between microscale and macroscale.

The goal of this thesis is thus to provide an insight into the role of microstructure in hot cracking and in particular to study the progressive formation of a continuous solid phase. A good understanding of the phenomena at that scale should allow to provide reliable constitutive equations for continuum approaches such as developed by V. Mathier during his PhD thesis [18, 14] and therefore to bring together the different scales of hot tearing.

### 1.5.3 Outline

This thesis is organized in a classical fashion.

- First part presents the basic knowledge necessary to an original work on hot tearing. This includes a review on the present hot tearing knowledge and the presentation of theoretical tools. This represents the roots of this work.
- Second part, the trunk and the branches, is devoted to the model development and the description of the experimental set up.
- Third part presents the various applications of the model and their consequences. Comparison with experiments and known tendencies will be presented. This represents the leaves of the work and I hope some fruits can be found in it.



# **Part I**

## **The roots**



## Chapter 2

# Experimental investigation of hot cracking

## 2.1 Parameters sensitivity

### 2.1.1 Process parameters

Naturally, the first experiences of hot tearing come from the casting practice. Hot tears occur in hot spots, *i.e.*, zones where the alloy solidifies last. These zones are weak as compared to the fully solidified surrounding metal and thus concentrate deformations.

In billet DC casting process, three types of cracks can be found (see Fig. 2.1) [19]:

- Internal cracks. The solidified shell at the edges of the billet prevent the global contraction. Shrinkage localises at the centre of the billet which becomes in tension and is thus prone to crack.
- Lateral cracks. Around the air gap the solidified shell remelts, creating a local hot spot. Mechanical simulations show that the material is locally in tension due to the intense secondary cooling. These cracks are more frequent in slabs than in billets.
- Butt cracks. These cracks which form during the transient start-up phase are difficult to prevent.

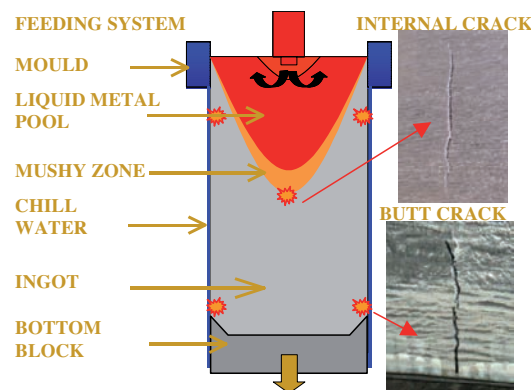


**Figure 2.1:** Hot cracks formation spots in DC casting [19].

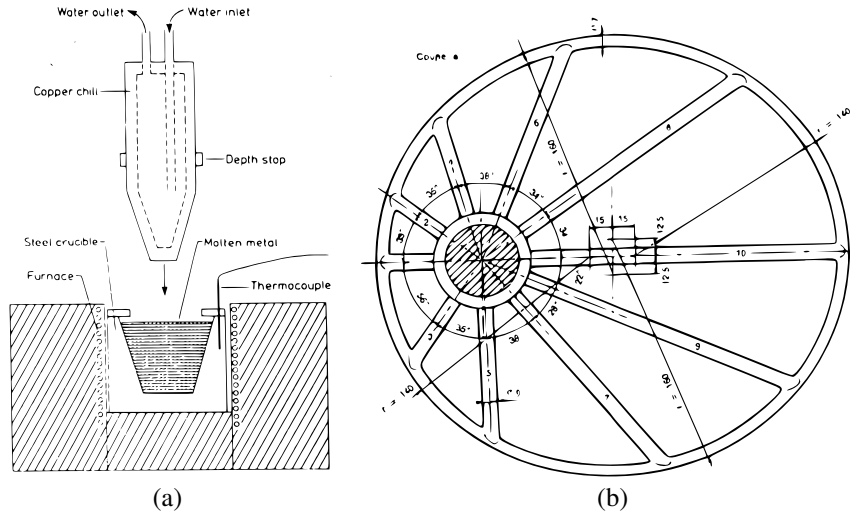


**Figure 2.2:** Hot cracking susceptibility tests. (a) Cold finger [21]. (b) Tatur test-tube [22].

More generally, the start-up phase is decisive for the formation of hot cracks. Internal cracks are generally initiated during this phase. Hot crack formation is very sensitive to start-up acceleration, which should be as low as possible. Yet, a too slow start-up phase can make the whole casting abort [19].

Casting speed is also an important parameter for hot cracking, large casting speed favouring hot cracking. Increasing the casting speed makes the liquid pool deeper and the lateral faces pull-in larger [20]. As another result, it brings more tension in the central zone of the casting.

### 2.1.2 Alloy parameters

Alloy composition is an other parameter that controls hot cracking, even though composition is mainly dictated by the desired final product properties. Figure 2.2 shows two devices to assess hot cracking susceptibility (HCS) of alloys.

In the cold finger experiment [21] (Fig 2.2(a)), a conical copper chill is immersed into liquid metal. Liquid metal solidifies but its contraction is restrained by the chill itself. Deformation localises in a hot spot created by an insulated band along the chill, and thus only one crack forms. The length of this crack characterises the HCS of the alloy.

Another classical approach is to cast constrained bars of different length [22] (Fig 2.2(b)). The longer the bar, the more intense is the shrinkage which localises in the hot spot at the centre of the bar. The longest bar that did not crack characterises the HCS of the alloy.

Another family of hot tearing tests measures an indicator during constrained solidification. Clyne and Davies cast metal in a dog bone shaped mold [23]. The electrical resistance of the sample is measured, which allows to quantify damage (Fig. 2.3(b)).

Instone *et al.* used a load cell to record the load in the bar, the maximum stress recorded appear to be proportional to the alloy HCS [24]. In their apparatus, two bars are cast with the same feeder, one to record temperature evolution, the other to do the mechanical measurements. Moreover, the central feeder is close to the hot spot and can

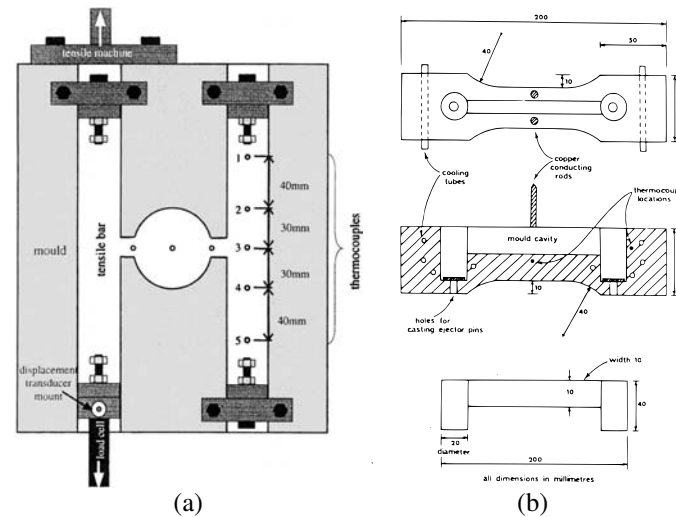


**Figure 2.3:** Constrained solidification tests . (a) Instone *et al.* test [24].(b) Clyne *et al.* test [23].

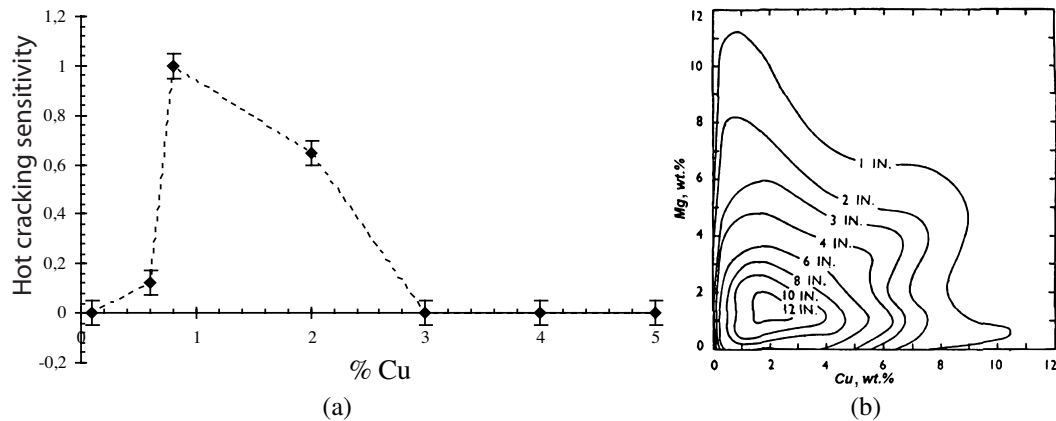


**Figure 2.4:** Hot cracking susceptibility as a function of composition. (a) Al-Cu alloys [25]. (b) Al-Cu-Mg alloys, the length reported correspond to the average length of cracks measured in a constrained solidification test [27].

provide liquid metal as under real DC casting conditions.

### Composition sensitivity

Figure 2.4(a) shows the HCS as a function of composition for Al-Cu alloys as measured by Spittle *et al.* [25]. For pure aluminium, the HCS is very low. It increases sharply for lean alloys, reach a maximum for a composition around 1wt% Cu. The HCS decreases for composition over 3wt% Cu. Because of its shape this curve is called the lambda-curve [26].

If we consider a more complex alloy such as Al-Cu-Mg, the trend of HCS is very similar [27]. In this case the maximum is reached for an Al-2wt%Cu-1.5wt%Mg. At high solute content, the HCS is very low.

This lambda-curve will be explained by the presence of a brittle range in which the mushy zone has very low ductility and permeability (see Sec. 2.3.4). This brittle range

is particularly important for low solute content alloys (see Sec. 3.1.5).

### Grain morphology

The role of the grain size and morphology is well known in casting practice. Fine globular microstructures have the lowest HCS. For equiaxed dendritic grains, this HCS increases with the grain size. Finally, columnar grains are very sensitive to hot cracking, in particular when tensile stresses are normal to their growth direction [28, 29].

### Intermetallic phases

Intermetallic phases might have an important role in hot cracking. Indeed, they can be denser than the liquid and induce an important shrinkage during solidification [30]. This is particularly important for eutectics which can solidify on a limited range of temperature. Intermetallic phases can also have a role on the formation of a continuous solid network and thus on the increase of the mushy zone strength (see Secs. 3.1.5 and 8.1.1).

### Hydrogen

An increased concentration of hydrogen increases porosity [31] and thus increases the number of nucleation sites for hot cracks. Therefore hydrogen is generally assumed to increase the HCS [30]. Yet, inspired by observation on industrial castings, Barnett *et al.* have measured the HCS for various hydrogen concentration in Al-Si alloys. They observed significant reduction of HCS with the increase of hydrogen concentration for an Al-1.6wt%Si alloy. This is maybe because porosity formation accommodate some deformation and thus increases the ductility of the mushy zone.

### Surface tension

Solid liquid surface energy has an important role on the shape of last liquid films [32] and on the coalescence of solid grains [33]. This can have practical applications as only a few ppm of surfactant elements can drastically modify the surface tension. Yet, the study of these effects is only at its beginning (see Sec. 2.3.5).

## 2.2 Observation of hot cracking

### 2.2.1 Local observation

A detailed observation of the fracture profiles already provides a valuable insight in the mechanism of hot tearing. Figure 2.5 shows Scanning Electron Microscope (SEM) micrographies of hot tears fracture surfaces and gives an overview of the various observations reported in the literature [23, 28, 34].

The hot cracking fracture reveals smooth dendrites arms (Fig. 2.5(a))[28, 7]. Fracture is thus inter-granular and the solid does not seem to have encountered appreciable deformation during fracture. Locally, a gap between two grains can be observed [37, 38]. This observation is completed by the fact that the two sides of a hot tear do not



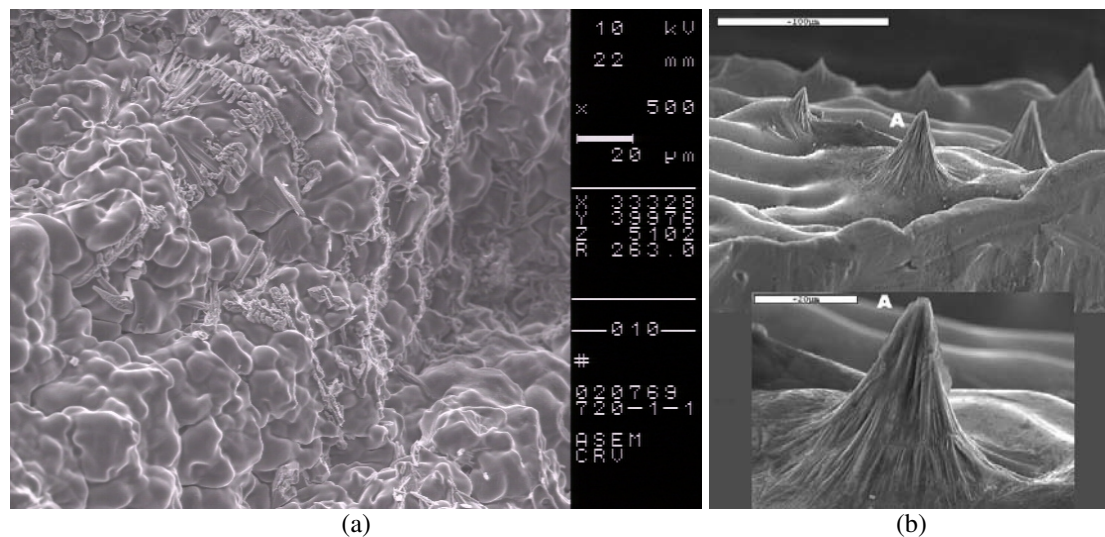


**Figure 2.5:** SEM pictures of hot tears surfaces. (a) Hot crack in a commercial 5182 alloy. The fracture has occurred during a billet casting [28]. (b) Spikes observed on a Al-3wt%Cu fractured during a rig mold test experiment [35, 36].

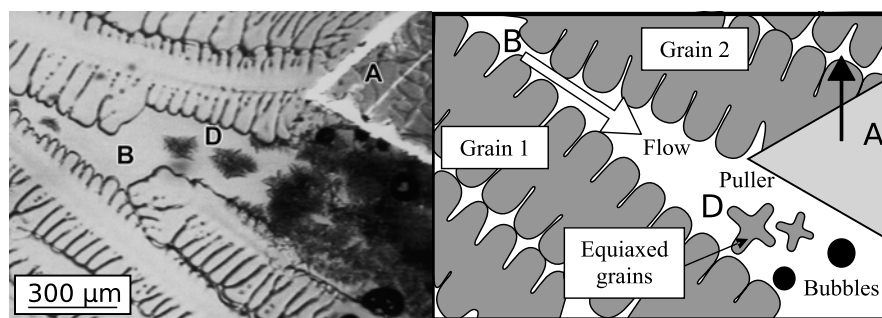


**Figure 2.6:** A healed hot tear [35].

match anymore after the fracture. Thus, fracture induces deformation in the material which is localised between grains.

Secondary phases can be observed on the dendrite surface as in Fig. 2.5(a). In this present case, Al-MnFeMg and Al-MnFeMgSi precipitates have been identified [28].

Another observation characteristic of hot cracking is the presence of spikes on the grains (Fig. 2.5(b)). They have well defined dimensions ( $\sim 20\mu\text{m}$ ) and present a surface rich in solute elements [35, 34].

In situ observations of hot tearing in transparent organic alloys (succinonitrile acetone) have been done by I. Farup *et al.* [35] and Grasso *et al.* [7]. This alloy is very useful as it melts at a low temperature, is transparent, and has solidification characteristics very close to metallic systems. In these experiments, the alloy is directionally solidified under a microscope. A stick is put in the melt and is used to pull apart dendrites at different solid fractions (Figs 2.6-2.8 A). The applied deformation is localized at a grain boundary (Figs 2.6-2.8 B).

When the stick is pulled at low solid fraction (Fig 2.6), the permeability of the mush is relatively high and liquid can flow to fill the gap between the grains. This liquid

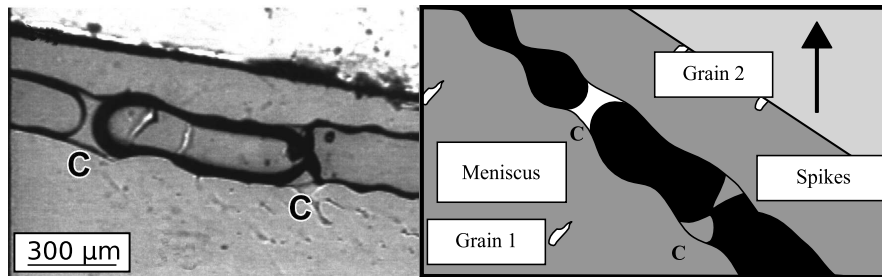


**Figure 2.7:** First mechanism of hot tearing [35].

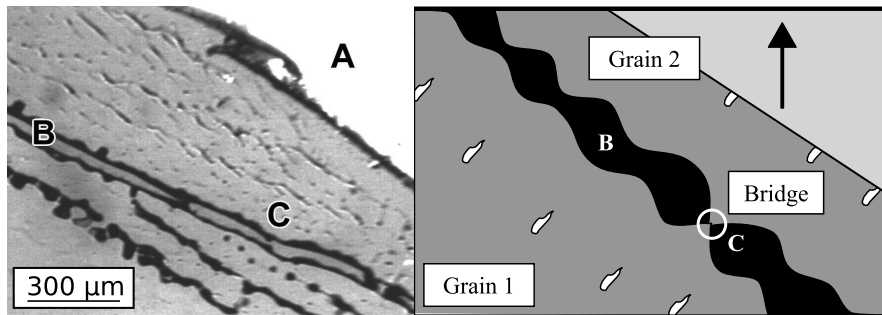


**Figure 2.8:** Second mechanism of hot tearing [35].

flow is lean in solute and equiaxed grains nucleate and quickly grow within the opened channel (Fig 2.6 D). This phenomenon has been called “healed hot tear”.

At a higher solid fraction (Fig. 2.7), the permeability of the mush is too low and liquid cannot flow to compensate deformation. The thin liquid film remaining between the grains breaks down into menisci. These menisci can solidify and their subsequent deformation forms spikes (Fig. 2.7 C).

Thin liquid films can remain at grain boundaries during a significant range of temperatures (see Sec. 2.3.5). In the experiment represented on Fig. 2.8 deformation is localised at such a grain boundary. A hot tear appears as an elongated pore without the formation of a meniscus. Spikes (Fig. 2.8 C) are formed on the tear surface from the rupture of solidified bridges.

These observations give two interpretations of spikes: 1°) spikes result from the solidification and rupture of liquid menisci, 2°) spikes result from the plastic rupture of small solid bridges between grains. The presence of copper rich regions around the spikes indicates that mechanism 1 should be the most frequent [35, 34].

### 2.2.2 Macroscopic observations

A very interesting experiment has been carried out by Commet *et al.* [28]. A billet of 5182 alloy is DC cast with an continuously increasing speed. Once the casting speed has reached a prescribed maximum it is continuously decreased. The speeds at which failure appears (Initiation Speed IS) and disappears (Healing Speed HS) have been measured for various compositions. In most cases,  $IS > HS$  which shows that initiation of hot tears requires more energy than propagation.

Figure 2.9 shows optical observations of the hot crack at various positions in the

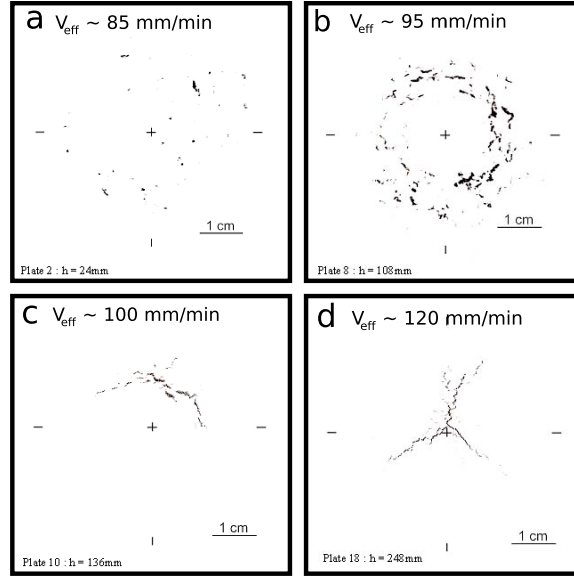


**Figure 2.9:** Optical observation of crack at various height in the billet. The estimated equivalent casting speed  $v_{eff}$  is mentioned [7].

billet, *i.e.*, at various casting speeds. The apparent casting speed at the centre of the billet  $v_{eff}$  has been estimated taking into account the thermal inertia of the system [28, 7]. At very low casting speed, the billet is sound. As the casting speed increases, porosity appears in the billet (Fig 2.9 (a)). This porosity develops and smoothly organises into an annular configuration of microcracks (Fig 2.9 (b)). Then, these microcracks coalesce in a half annular crack (Fig 2.9 (c)) and finally take a three branches star configuration. For even higher casting speed, four branches stars have been reported and in processes with extreme cooling rates, such as laser remelting, five branches stars can be observed (see Fig. 1.5)[10].

The annular shape, the three branches stars or the five branches stars are probably induced by the cylindrical symmetry of the billet and can represent different breakdown nodes of the symmetric tension field [39]. This illustrates the multiscale nature of hot tearing that has been presented in the introduction. We have observed in section 2.2.1 the microscopic mechanism of hot tearing. Here, we observe that hot tearing might reflect the macroscale symmetry of the problem.

Moreover, these observations confirm the very ramified nature of hot cracks. They also point out that hot tears might start with a progressive accumulation of damage in the form of porosity.

The recent work of Phillion *et al.* [40] further illustrates this progressive formation of hot cracks. The authors have done a tensile test on a 5182 commercial alloy remelted up to 0.98 solid fraction. Each sample has been deformed to a given strain and observed with an X-ray micro-tomographic device. Strains are localised in the hot spot at the centre of the sample.

Figure 2.10 shows the microtomography of damage for various strains. The void region appears in black. The as-cast structure presents some voids, *i.e.*, microporosity (Figs 2.10 (a)). The samples accommodate low strains by diameter reduction, but for higher strain damage starts to develop. At 0.02 strain, consequent damages can be observed, the number of pores in the sample is almost the same as in the as-cast sample

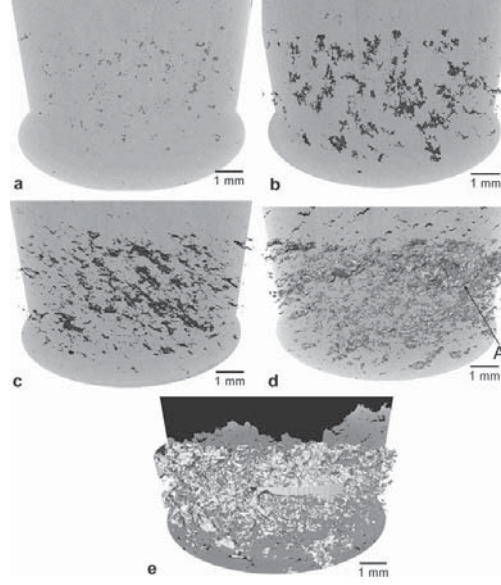


**Figure 2.10:** Micro-tomographic reconstruction of the damage in 5182 commercial alloy specimens strained to values of : (a) as-cast, (b) 0.02, (c) 0.06, (d) 0.16, (e) 0.20 [40].

but the pore size is significantly larger. Thus, damage is created by the growth of as-cast porosity (Figs 2.10 (b)). For larger strain (0.06), this void growth continues but is accompanied by the formation of new voids. At 0.16 strain, large macrocracks/hot tears are present in the sample and at 0.20 strain, the sample is totally cracked (Figs 2.10 (b)). See also Ref. [41] for other in-situ observations of hot cracking propagation.

## 2.3 Mushy zone rheology

### 2.3.1 Pure phases rheology

Liquid metals can be modelled as incompressible Newtonian fluids, *i.e.*, stress and strain are related by the following relationship:

$$\overleftrightarrow{\tau} = 2\mu \overleftrightarrow{\dot{\epsilon}} \quad (2.1)$$

where  $\overleftrightarrow{\tau}$  is the deviatoric part of the stress tensor,  $\mu$  the viscosity of the fluid and  $\overleftrightarrow{\dot{\epsilon}}$  the strain rate tensor. Liquid aluminium alloys have a low viscosity, on the order of  $10^{-3}$  Pas at liquidus temperature [42].

At high temperature, solid metal have a very small elastic regime at low strain and then exhibit a viscoplastic behaviour. If we neglect this elastic regime, stress and strain are related by:

$$\overleftrightarrow{\sigma}_D = K(\sqrt{3}\dot{\epsilon}_{eq})^{m-1} \overleftrightarrow{\dot{\epsilon}} \quad (2.2)$$

where  $K$  is the viscoplastic coefficient,  $m$  the strain rate sensitivity coefficient and  $\dot{\epsilon}_{eq}$  is the equivalent viscoplastic shear rate given by the second invariant of the strain rate tensor. Note that if  $m = 1$ , we get a Newtonian fluid law with  $K = 2\mu$ . For solid aluminium alloys at the solidus temperature,  $m \approx 0.3$  and thus the solid behaves as a

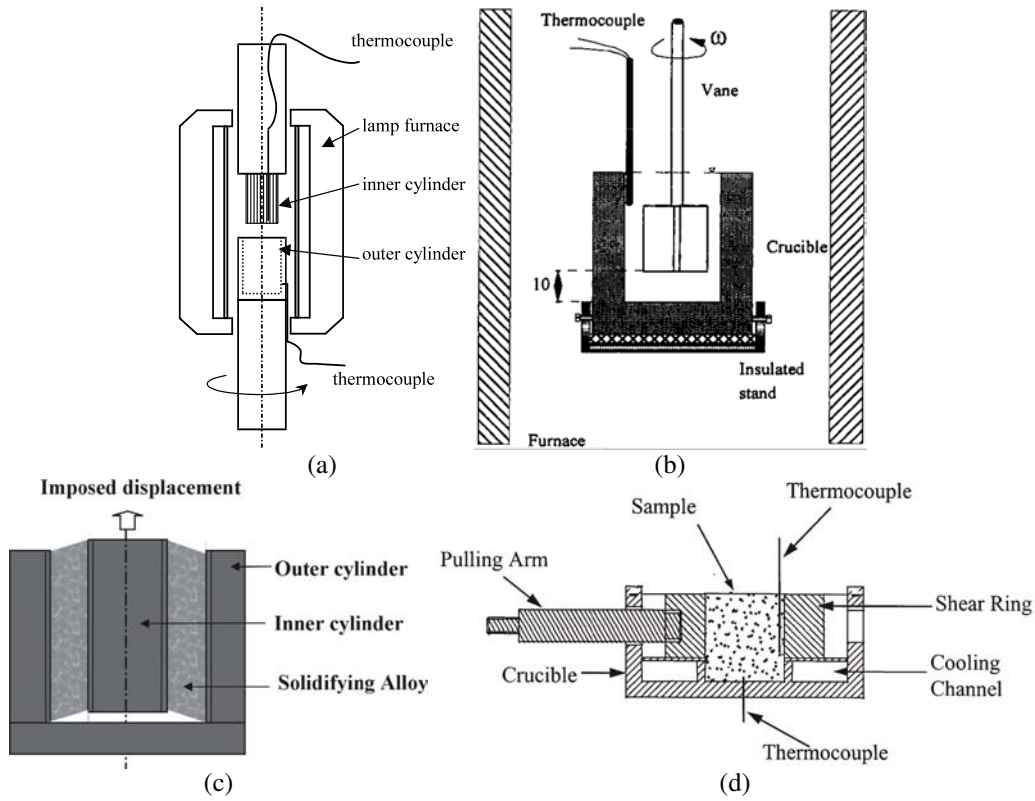


**Figure 2.11:** Various shear tests for mushy aluminium alloys: (a),(b) Couette viscometer [43, 44], (c) translation shear test [45], (d) direct shear cell [46, 47].

non-Newtonian fluid whose equivalent viscosity  $\mu_{eq} = 0.5K(\sqrt{3}\dot{\epsilon}_{eq})^{m-1}$  decreases with shear rate (a shear thinning fluid). At the solidus temperature for an Al-8wt%Cu with a typical strain rate of  $10^{-3}\text{s}^{-1}$ ,  $\mu_{eq} \sim 10^{10}$  Pas [43].

There is therefore more than 12 orders of magnitude between the apparent viscosity of the solid and the viscosity of the liquid at the solidus and liquidus temperature respectively. Solid can thus sustain large stresses with small strain rates, whereas in the fluid small stresses induce large strains. Moreover, in the solid the small elastic regime propagates stresses at the speed of sound in the material, and mechanical equilibrium is quickly reached. In the liquid, shear stresses are transmitted by viscosity and fluid advection, which can induce inertial regimes (high Reynolds numbers) and transient regimes.

Even though we know well the mechanical behaviour of each phase, the behaviour of their mixture is not an easy question as we shall see in the following section. Note also that damage can form in the mush (see section 2.2), thus influencing its apparent mechanical behaviour.

### 2.3.2 Shear tests

Shear tests generate pure shear and thus create a well-defined mechanical state in solid or liquid materials. Therefore, it is natural to also investigate the behaviour of a mushy zone with such tests. Moreover, it is relatively easy to contain liquid metal in these tests, and thus no particular problem arises for in-situ solidification.



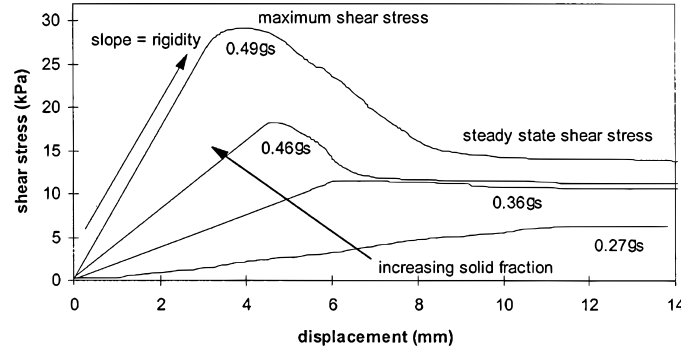


**Figure 2.12:** Stress strain curve for an Al-7wt%Si-1wt%Cu at various solid fractions. The experimental device is represented on Fig. 2.11(d). The sample is sheared with a speed of  $1.7 \text{ mm s}^{-1}$  [46].

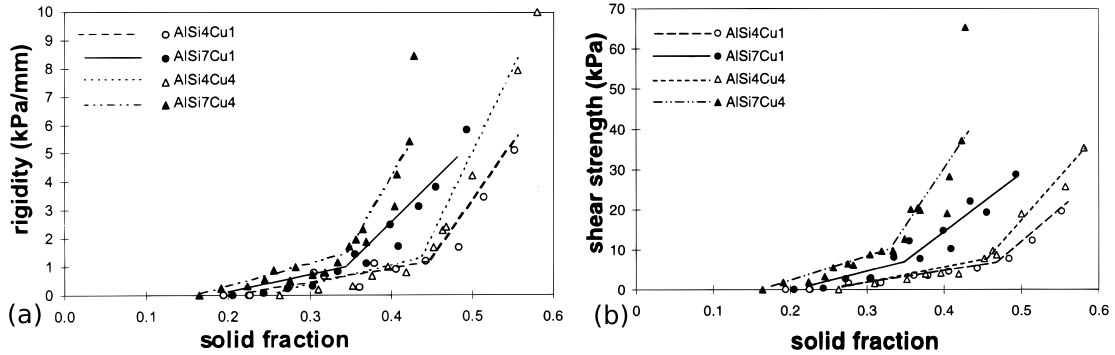


**Figure 2.13:** Evolution of rigidity (a) and strength (b) as a function of solid fraction for various compositions [46].

Figure 2.11 shows some of the experiments developed for the shear behaviour investigation of mushy aluminium alloys. Couette viscometers have been developed by Braccini *et al.* Fig. 2.11(a) [43] or Dahle *et al.* Fig. 2.11(b) [44]. In these experiments, liquid metal is poured in a cylindrical crucible and a central cylinder is introduced in the melt. At a given temperature, a rotation speed is imposed to one of the cylinder (outer for Braccini *et al.*, inner for Dahle *et al.*). The torque exerted on the inner cylinder is recorded. Such a test can be done at fixed temperature (isothermal tests) or upon cooling (non-isothermal). In the test developed by Ludwig *et al.* [45] (Fig. 2.11(c)), liquid metal is also poured between two cylinders but the inner cylinder is pulled in the axial direction, generating a pure linear shear. Another example of linear shear test has been developed by Nabulsi *et al.* [46, 47], inspired by the old work of Metz and Flemings [48] (Fig. 2.11(d)). In their test, a fixed force is imposed to the upper part of the crucible which can slide with respect to the lower part. These two last tests are always isothermal.

Figure 2.12 shows the displacement-stress curves recorded by Sumitomo *et al.* on a Al-7wt%Si-1wt%Cu alloy with the test of Fig. 2.11(d). The stress increases linearly, reaches a maximum and for the relatively high solid fraction decreases to a steady state value. The authors have called rigidity the slope of the linear stress response, and shear strength the maximum stress recorded.

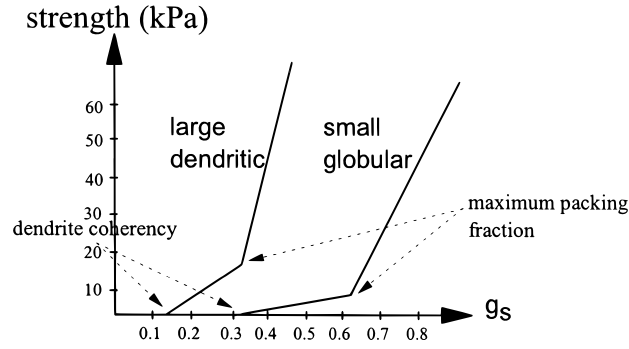


**Figure 2.14:** Schematic evolution of strength with solid fraction for two extreme grain morphology. [46, 49]

These two quantities are reported as a function of the solid fraction in Fig. 2.13 for various Al-Si-Cu alloys. The strength starts to be measurable at a given solid fraction which depends on the alloy composition (around  $g_s = 0.2$ ) and then increases linearly. Above another solid fraction (around  $g_s = 0.4$ ), the strength increases more rapidly. It is interesting to note that the evolutions of strength and rigidity have the same shape and that the solid fractions at which transitions occur are the same for these two quantities.

The first transition occurs when the dendrite arms start to impinge. The solid network is then able to bypass shear stresses. Solid grains are in contact locally but they are still able to rotate and to rearrange. We will call this point *shear coherency* solid fraction ( $g_s^{sc}$ ).

The second transition has been interpreted by Dahle *et al.* [49] as the point where dendrites become interlocked. At this point the solid grains form a dense structure, they can not rearrange to form a more compact structure. Therefore these authors have called this point *maximum packing* solid fraction ( $g_s^{pk}$ ). Above  $g_s^{pk}$ , permeability of the mush starts to be significantly reduced and Sumitomo *et al.* have systematically observed microcracks for samples sheared above  $g_s^{pk}$ , but never for samples sheared below  $g_s^{pk}$  [46].

The influence of the alloy composition on the two transitions,  $g_s^{sc}$  and  $g_s^{pk}$  (Fig. 2.13) is mainly due to the grain morphology. Indeed, the Al-4wt%Si alloys presented a globulo-dendritic morphology whereas the Al-7wt%Si alloys presented a dendritic morphology. For a regular arrangement of spherical grains, maximum packing solid fraction occurs at  $g_s^{pk} = 0.74$  [49]. For a highly inoculated alloys with globular grains  $g_s^{sc} \sim 0.3$  and  $g_s^{pk} \sim 0.6$ . For large dendritic grains  $g_s^{sc} \sim 0.15$  and  $g_s^{pk} \sim 0.35$  (See Fig. 2.14).

Figure 2.15 shows the stress strain curve of a fully solid Al-4.5wt%Cu at 530 °C and of a mushy Al-8wt%Cu with 0.8 solid fraction [43]. These curves have been measured by Braccini *et al.* with the set up of Fig. 2.11(a) and with a strain rate of  $10^{-2} \text{ s}^{-1}$ . These two alloys have been refined and have a fine globulitic microstructure. Because of microsegregation, solid in the mushy Al-8wt%Cu alloy has a composition of approximately 4.5wt% Cu. Therefore these curves allow to directly compare the mechanical behaviour of the mushy zone with the behaviour of the solid phase alone.

The fully solid shows an ideal elastic-viscoplastic behaviour, the viscoplastic plateau is reached after 1 % strain and is nearly horizontal (slight strain softening visible). The stress in the mushy zone increases much more gently and a plateau is reached for 50 %

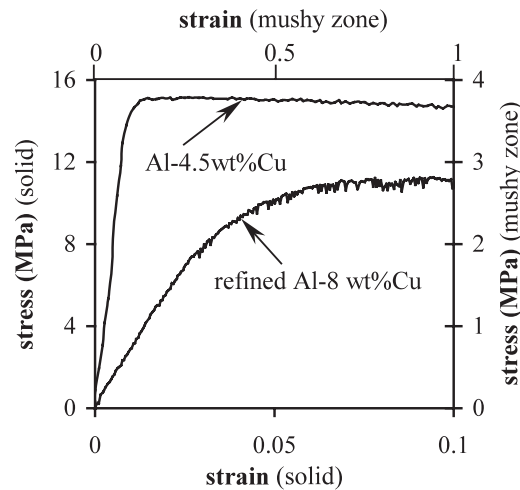


**Figure 2.15:** Comparison between the stress strain curve of a fully solid Al-4.5wt%Cu at 530 °C and a mushy Al-8 wt%Cu with 0.8 solid fraction [43].

strain. As already observed in Fig. 2.12, the stress increases linearly with strain. This linear increase is interpreted as the progressive formation of solid to solid contacts. The stress plateau reached in the mushy zone (3 MPa) is substantially lower than in the fully solid alloy (15 MPa). The author has measured the strain rate sensitivity coefficient of the mush and found it close to the fully solid one. Thus, this plateau is mainly dictated by solid-solid contacts. It is nonetheless interesting to note how the presence of 20 % liquid drastically modifies the behaviour of the material.

If we compare the curves of Figs. 2.12 and 2.15, we observe that their shape is different. This is because the test reported in Fig. 2.15 is performed on a fine globular microstructure. For more dendritic microstructures, the authors report stress-strain curves similar to those of Fig. 2.12. For dendritic grains the peak stress reflects structure breakdown, whereas the plateau stress in globular microstructure reflects equilibrium between formation and destruction of solid-solid contacts [43].

### 2.3.3 Compression tests

Compression tests can be divided into two classes, uniaxial compression and drained compression [50]. In drained compression, the fluid can be expelled from the mushy zone through a filter. In uniaxial compression, the liquid is constrained to stay within the mushy zone. Both tests are useful to characterise the rheological behaviour of the mushy zone [37]. Here, we only report the drained compression test carried out by Ludwig *et al.* [37, 45].

In this test the liquid metal in the container is cooled down to the test temperature of 555 °C. Then, a piston presses the metal with an imposed velocity and liquid metal can flow out of the sample. Different copper contents are used, thus allowing to test different solid fractions (Fig. 2.16(a)). In this test, the stress state in the system is not perfectly known as the radial stresses are not measured. Nonetheless, an analytical solution of this mechanical problem has been derived by Drezet *et al.* [51] using the constitutive law derived by Ludwig *et al.* (see Sec. 3.2.4). This test models the part of a casting that is under compression and from which liquid is squeezed out.



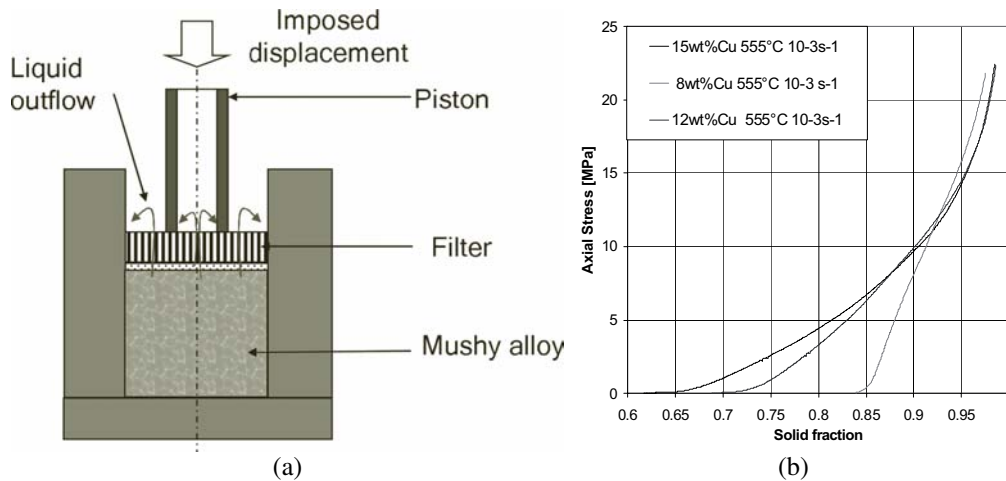


**Figure 2.16:** (a) Drained compression test. (b) compression curve obtained with this test for Al-Cu alloys at 550 °C and a strain rate of  $10^{-3} \text{ s}^{-1}$ .

Figure 2.16(b) shows the compression curve for an Al-15wt%Cu, Al-12wt%Cu and Al-8wt%Cu, which correspond to solid fractions at the beginning of the test of 0.62, 0.72 and 0.84 (compression expels liquid from the solid network and solid fraction increases). It is very interesting to note that the three curves converge for a solid fraction of 0.9. For the Al-8wt%Cu, the compression curve is stiffer above 0.9 solid fraction. This is maybe because grain clusters are already present at the beginning of the compression. Note also that the stresses measured are significantly larger than in shear tests.

### 2.3.4 Traction tests

Hot tearing is a failure under tensile stresses mainly. The understanding of mushy zone tensile behaviour is thus essential. Yet, tensile tests are difficult to carry out because the liquid metal of the mush has to be contained during the load. Several experiments have been designed with different approaches that are illustrated in Fig. 2.17.

Figure 2.17(a) shows the apparatus designed by Spittle *et al.* [52]. It is a commercial tensile machine (Housfield H10K-C), where an electric current coming from a Gleeble machine is passed through the sample. The Gleeble machine uses the electrical resistance of the sample to control temperature. The sample is heated up, remelted to a given solid fraction, and tested. The advantages of this method are that no container is needed for high solid fractions as the sample is never completely melted, and that the temperature field in the sample is well controlled. The disadvantage is that the microstructure evolves and coarsens during remelting and thus is not the same as the solidified one.

In the apparatus used by Suéry's group [45, 53] (Fig. 2.17(b)) the center of the sample is completely melted by induction heating and then cooled down with a constant cooling rate to the desired solid fraction. Traction is performed isothermally. This design allows to test a solidification microstructure with fairly well controlled conditions.

Another approach has been developed by Engler *et al.* [54]. A mold is fixed between the jaws of a tensile machine. Liquid metal is poured in the mold via a gating system. The metal is cooled down by a copper chill on the top of the mold. Once a solidified shell has formed on the top of the mold, the chill is removed and heat is mainly extracted via the jaws of the tensile machine. Once the temperature at the center of the sample

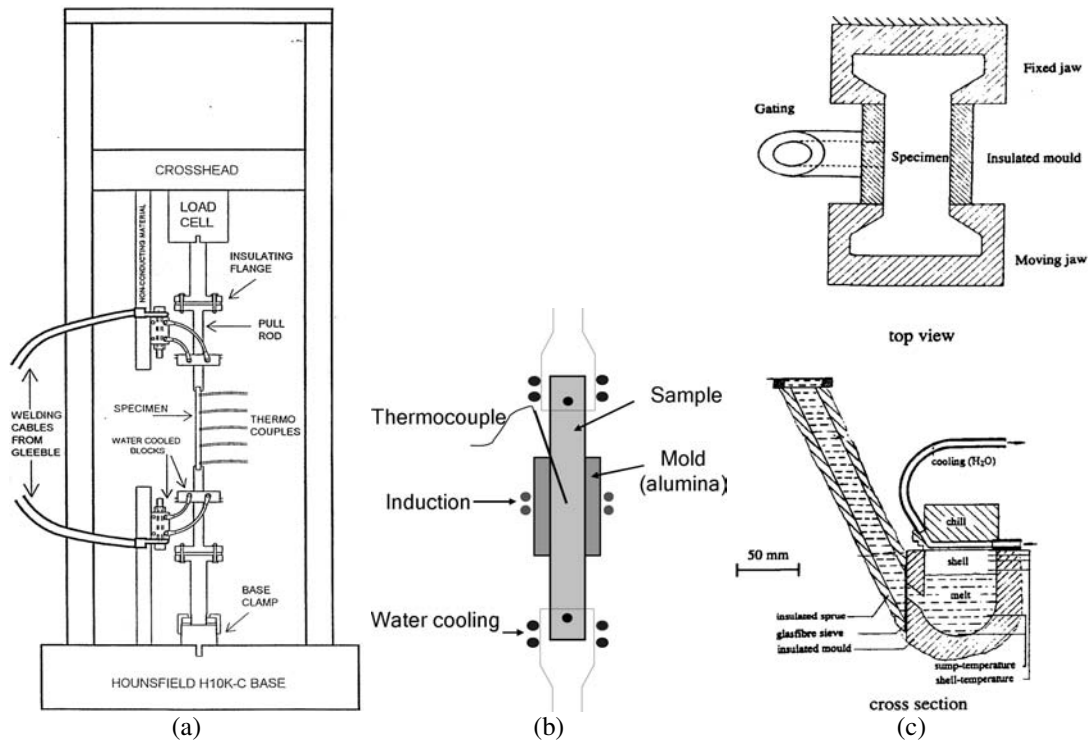


**Figure 2.17:** Three approaches of mushy zone tensile test. (a) partial remelting [52], (b) complete remelting and solidification [53], (c) casting [54].

has reached the desired value, traction starts. This test has the advantage of creating a real as-cast microstructure. The copper chill represents primary DC casting cooling, that is followed by the formation of an air gap. Yet, the thermal field in the sample is complex and the test is necessarily non-isothermal. A similar apparatus (rig test) has been developed in the Centre de Recherche de Voreppe (CRV) of ALCAN France (formerly Pechiney). The present thesis has been started with an intensive measurement campaign on this machine [38]. The details of this experiment are presented in Sec. 5.1.

Figure 2.18(a) shows the maximal tensile stress as a function of solid fraction for Al-2wt%Cu and Al-4wt%Cu both heavily inoculated (fine globular microstructure). This curve has been measured with the apparatus of Fig. 2.17(b) by Ludwig *et al.*. The strain rate is on the order of  $10^{-3}\text{s}^{-1}$ . With this morphology maximal tensile stress can be measured only for solid fraction above  $g_s = 0.65$  [37, 45], this transition is called *nil stress temperature* (NST) [55] or more frequently *traction coherency* ( $g_s^{tc}$ ). Above this solid fraction the maximal tensile stress rises gently until  $g_s = 0.95$  and then increases much more abruptly. This second transition is called *coalescence transition* ( $g_s^{coal}$ ) [37, 45]. It is interesting to note that these two transitions occur at the same solid fractions for the two alloys.

The deformation at fracture as a function of solid fraction is shown on Fig. 2.18(b). In this experiment strains are localised on a zone of about 20 mm, this estimation has been confirmed by numerical simulations [37]. Therefore at  $g_s = 0.76$  the ductility is around 20% and drops to less than 1% at  $g_s = 0.9$ . Above  $g_s = 0.95$  (coalescence transition) ductility increases with solid fraction.

The tendency curve is reported in dotted line on Fig. 2.18(b). This curve has been measured with tensile tests by several authors [56, 22, 54, 57, 38]. It has also been

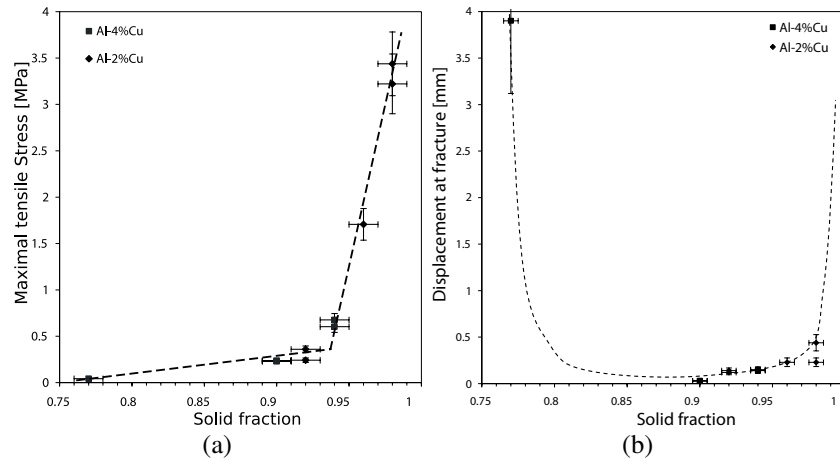


**Figure 2.18:** Traction test on heavily inoculated Al-2wt%Cu and Al-4wt%Cu [45, 37]. (a) Maximum tensile stress as a function of solid fraction. (b) Displacement at fracture as a function of solid fraction.

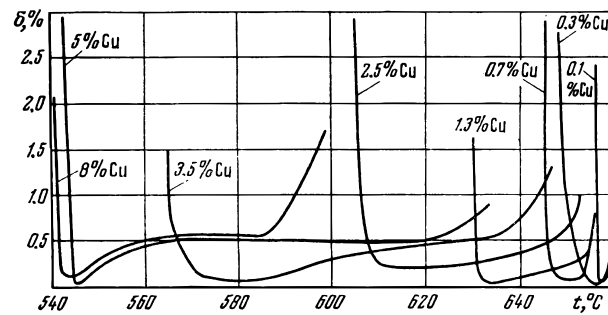


**Figure 2.19:** Strain at fracture,  $\delta$ , as a function of temperature for dendritic Al-Cu alloys [57, 56].

measured by Matsuda *et al.* by in-situ observation of crack opening during welding [58]. Because of its shape this curve is called the U-curve. At low solid fraction the permeability of the mush is high and fluid flow can compensate deformation. At high solid fraction a continuous solid network can sustain stresses and present a viscoplastic flow. In between, both fluid flow is difficult and solid phase is not continuous enough to sustain stresses, the material is extremely brittle. This zone is called the *Brittle Temperature Range (BTR)*. The increase of ductility at  $g_s = 0.95$  is achieved by the progressive formation of solid-solid bridges [37], which justifies the name “coalescence transition”.

A transition from a brittle behaviour to a ductile behaviour is observed very close to  $g_s = 1$  [56, 54, 38]. This transition is represented in the U curve by the very steep increase of ductility near  $g_s = 1$ . This transition is due to the formation of a fully continuous solid network, and therefore will be called *solid percolation transition* ( $g_s^{sp}$ ). The theory of percolation will be presented in Sec. 4.1.

The Russian scientist Novikov has studied extensively the ductility of semi-solid aluminium alloys. His work is published in Russian [57] but some of his results are accessible thanks to the review article of Eskin *et al.* [56]. All his results presented here were measured by the progressive loading of a remelted sample [56]. Figure 2.19

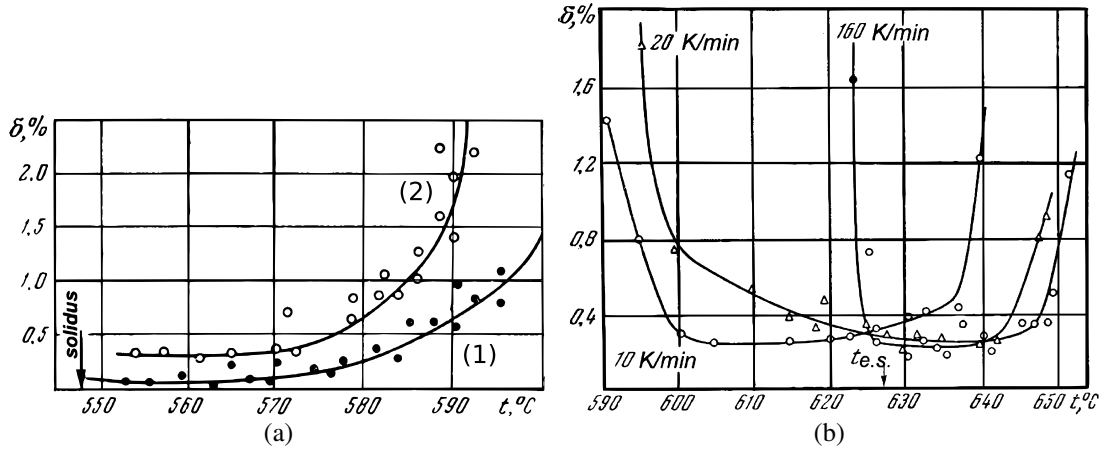


**Figure 2.20:** Strain at fracture  $\delta$  as a function of temperature. (a) Al-4wt%Cu, (1) large grains (880 °C melt overheating), (2) fine grains (750 °C melt overheating). (b) Al-1.5wt%Cu, effect of cooling rate.

shows ductility versus temperature of non-inoculated aluminium copper alloys for various copper contents. The brittle range spans on various temperature ranges due to the variation of the solidification interval of the alloy. In order to have a better interpretation of these measurements, the temperature scale can be converted into a solid fraction scale using the back-diffusion model presented in Sec. 6.1. A characteristic diffusion length of 100  $\mu\text{m}$  was used as we do not have access to the secondary arm spacing in those experiments. It appears that the increase in ductility (coalescence transition) always occurs for  $g_s \sim 0.9$ . The only exception is the Al-8wt%Cu for which eutectic solidification occurs before  $g_s = 0.9$ . This confirms that transition solid fractions do not directly depend on alloy composition [23].

The influence of grain size and grain morphology is illustrated on Fig. 2.20. In Fig. 2.20(a), two Al-4wt%Cu have been cast with different melt over-heatings. It appears that the alloy with the smallest grain size (lowest melt over-heating) has a much higher ductility than the coarse grain alloy. This fact can be explained if we consider that inter-granular sliding is the principal deformation mechanism [56]. If we consider a given deformation  $\delta$  the average displacement between two grains  $\Delta l$  will be on the order of [57, 56]:

$$\Delta l \sim D\delta \quad (2.3)$$

where  $D$  is the average grain size. A larger grain size increases the localisation of deformation at grain boundaries and thus decreases ductility.

Figure 2.20(b) shows the ductility of an Al-1.5wt%Cu for various cooling rates. The solidification conditions have been chosen in such a way that the grain size remains the same in each experiment. The temperature limits of the brittle range clearly depend on the cooling rate. We have estimated that for  $\dot{T} = -160 \text{ Kmin}^{-1}$ ,  $g_s^{coal} \sim 0.9$  whereas for  $\dot{T} = 10 \text{ Kmin}^{-1}$   $g_s^{coal} \sim 0.95$ . For a high cooling rate, a fine dendritic structure is produced which can entrap more liquid. Thus the contact between grains occurs at a relatively low solid fraction. For a coarse structure, liquid remains between the grains and solid contact occurs at high solid fraction. It is interesting to note that the ductility in the brittle range is not affected by the cooling rate, and thus mainly depend on the grain size (Fig. 2.20(a)) and not on their morphology (Fig. 2.20(b)).

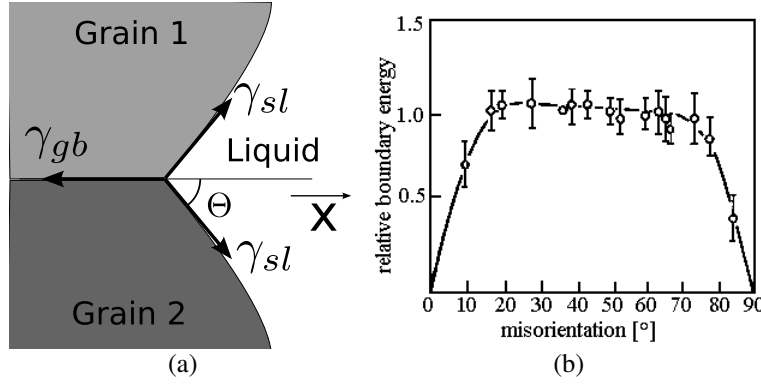


**Figure 2.21:** (a) Equilibrium of forces at a triple junction between two grains and the liquid. (b) Relative grain boundary energy (normalised by the maximum grain boundary energy) as a function of disorientation angle for a pure tilt boundary in aluminium [61] .

The work of Novikov shows that the ductility of low alloyed alloys in the brittle range does not depend on the strain rate. This result will be confirmed by the results presented in Sec. 8.1. For more alloyed alloys, *e.g.*, Al-6.5wt%Cu, Novikov observed that the ductility decreases with the strain rate at low solid fraction ( $g_s < 0.8$ ), but remains unchanged at higher solid fraction (see [56] Fig. 27).

### 2.3.5 Effect of surface tension

Surface energy plays a critical role at the very end of solidification. Figure 2.21 shows a triple junction between two grains and the liquid. Equilibrium of forces at this triple junction imposes (Young-Laplace equation):

$$\gamma_{gb} = 2\gamma_{sl} \cos \Theta \quad (2.4)$$

where  $\gamma_{gb}$  is the grain boundary energy,  $\gamma_{sl}$  is the solid-liquid interfacial energy, and  $\Theta$  is the dihedral angle.

Figure 2.21 shows the evolution of the grain boundary energy as a function of misorientation  $\theta$  for a pure tilt boundary (the rotation axis is parallel to the grain boundary). At low tilt angle, the interface is almost coherent and edge dislocations compensate the misorientation. Surface energy follows the Read and Shockley formula [59]. For  $\theta > 15^\circ$ , the density of dislocations is too large and the interface is highly disordered. The surface energy is maximum and does not depend on the orientation. Note that for specific angles, the grain boundary energy can decrease due to special coincidences of the crystal lattices. The grain boundary energy is difficult to measure, but in Al alloys, a good order of magnitude is  $\gamma_{gb}^{max} \sim 0.3 \text{ Jm}^{-2}$  and  $\gamma_{sl} \sim 0.1 \text{ Jm}^{-2}$  [60].

Figure 2.22 shows the shape of liquid inclusions as a function of liquid fraction and dihedral angle as calculated by Wray [32]. The authors supposed a regular polygonal arrangement of solid grains (tetrakaidecahedron) and a uniform dihedral angle. They further assumed that the shape of liquid inclusions is only dictated by surface tension. In our problem, thin liquid films do not exist long enough to reach such an equilibrium and the liquid inclusion shape is also dictated by solidification. Yet, this diagram shows the tendency induced by surface tension.

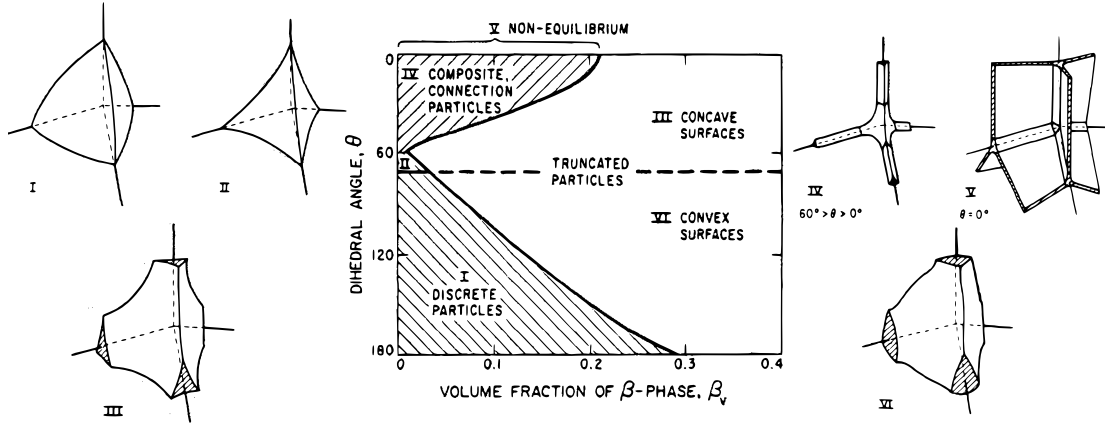


**Figure 2.22:** Shape of liquid inclusions dictated by surface tension as a function of liquid fraction and dihedral angle [32].

For  $\Theta = 0$ , i.e.,  $\gamma_{gb} > 2\gamma_{sl}$  (Fig. 2.22 V), the liquid films wet perfectly the grain boundaries and a thin liquid film is always present everywhere between the grains. For  $0 < \Theta < 60^\circ$ , i.e.,  $\gamma_{sl} < \gamma_{gb} < 2\gamma_{sl}$  (Fig. 2.22 IV, III), the edges between three grains are wetted by the liquid, whereas for  $\Theta > 60^\circ$ , i.e.,  $\gamma_{sl} > \gamma_{gb}$  (Fig. 2.22 I, II, VI) liquid tends to concentrate at grains corners. The transition between interconnected and isolated pockets of liquid is interesting but, as already mentioned, is not necessarily representative of solidification microstructures.

Another important aspect of surface tension has been outlined by Rappaz *et al.* [33]. For  $\Theta > 0$ , i.e.,  $\gamma_{gb} < 2\gamma_{sl}$ , it is thermodynamically interesting to form one grain boundary out of two solid-liquid interfaces. Once the two interfaces impinge, the grain boundary is formed. This case is called attractive interfaces and occurs in particular between two dendrite arms of the same grain ( $\gamma_{gb} = 0$ ). If  $\Theta = 0$ , i.e.,  $\gamma_{gb} > 2\gamma_{sl}$ , not only the grain boundaries are wetted by a thin liquid layer, but the formation of “dry” grain boundaries needs an extra free energy. This extra free energy can be viewed as an undercooling for the solidification of the last liquid films :

$$\Delta T_{coal} = \frac{\gamma_{gb} - 2\gamma_{sl}}{\Delta S_f \delta} \quad (2.5)$$

where  $\Delta S_f$  is the volumetric entropy of fusion and  $\delta$  is the thickness of the diffuse solid-liquid interface. In the case of highly disordered grain boundaries, this undercooling can be on the order of  $40^\circ\text{C}$  [60], which means that thin liquid films can remain well below the solidus line of the alloy.

Fallet *et al.* have investigated the effect of barium on the tensile properties of mushy Al-Cu alloys [62]. Barium has a very low solubility in solid aluminium and thus strongly segregates in the liquid films. Moreover barium has been shown to have a surfactant effect in these alloys [63]. This effect has been confirmed by Chichignoud *et al.* who observed an increase of 40% in specific primary phase/eutectic interface with the addition of 0.03 wt%Ba. Figure 2.23(a) shows the measured eutectic film thickness as a function of the misorientation of its two surrounding grains. The authors did not find any eutectic film for misorientation below  $10^\circ$  without barium, and below  $4^\circ$  with barium. This denotes a reduction of 40% in solid liquid surface energy [62].

Figure 2.23(b) shows the maximum tensile stress as a function of solid fraction for

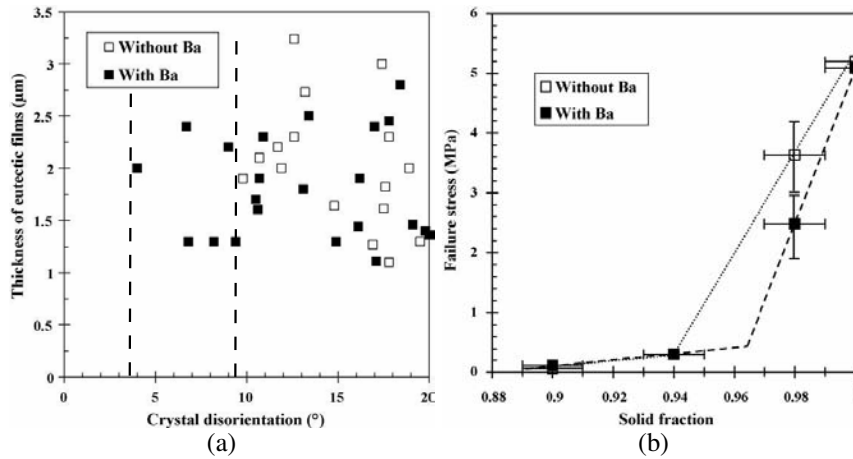


**Figure 2.23:** (a) Thickness of eutectic films as a function of grain boundary misorientation. (b) Maximum tensile stress as a function of solid fraction [62].

an Al-4.3wt%Cu, with and without barium. The presence of barium has no effect at low solid fractions. At high solid fractions ( $g_s = 0.98$ ), when only thin liquid films remain in the alloy, the presence of barium considerably decreases the strength of the alloy. The authors interpreted this as a delay in the coalescence transition induced by barium.

Wang *et al.* used a laser to weld two super alloy single crystals with a controlled tilt angle [64]. At low tilt angle no crack forms, whereas for tilt angles superior than  $12^\circ$  a hot crack was observed under otherwise identical conditions. These experiments clearly outline the role of grain boundary energy on the formation of hot tearing.

Fredriksson and Lehtinen have done in-situ observation of hot cracking in a electron microscope [65]. In the Sn-Al system liquid wets perfectly the grain boundaries and participate to the deformation mechanism. The fracture is extremely brittle. In the Al-Cd system, liquid is present in the form of droplets. These droplets do not participate to the deformation mechanism. Fracture is intergranular but local plastic deformation of the solid is observed.

### 2.3.6 Summary

Several transitions of the mushy zone mechanical behaviour are observed during solidification. These transitions are particularly important for mushy zone models and for hot cracking criteria (see next chapter). It is therefore useful to summarise them briefly.

At very low solid fraction, the melt is a suspension of small solid grains, *i.e.*, a slurry. Both solid and liquid are free to move and the resultant behaviour is very close to a fluid. This feeding mechanism is called mass feeding [23, 30].

At *shear coherency* ( $g_s^{sc}$ ), the dendrites arms touch each other locally, the solid network is able to transmit stresses in shear. Yet, the arrangement is not dense and grains can rearrange by rotating or sliding. Liquid can have a flow relative to dendrite network and thus the feeding mechanism is called interdendritic feeding [23, 30].

At *maximum packing* ( $g_s^{pk}$ ), the solid grains can not rearrange to form a denser structure. Their main displacement mechanism is grain boundaries sliding. The structure is sufficiently interlocked to transmit stresses in tension and thus this point is also called *traction coherency* ( $g_s^{tc}$ ). The liquid is still able to flow though the solid network and

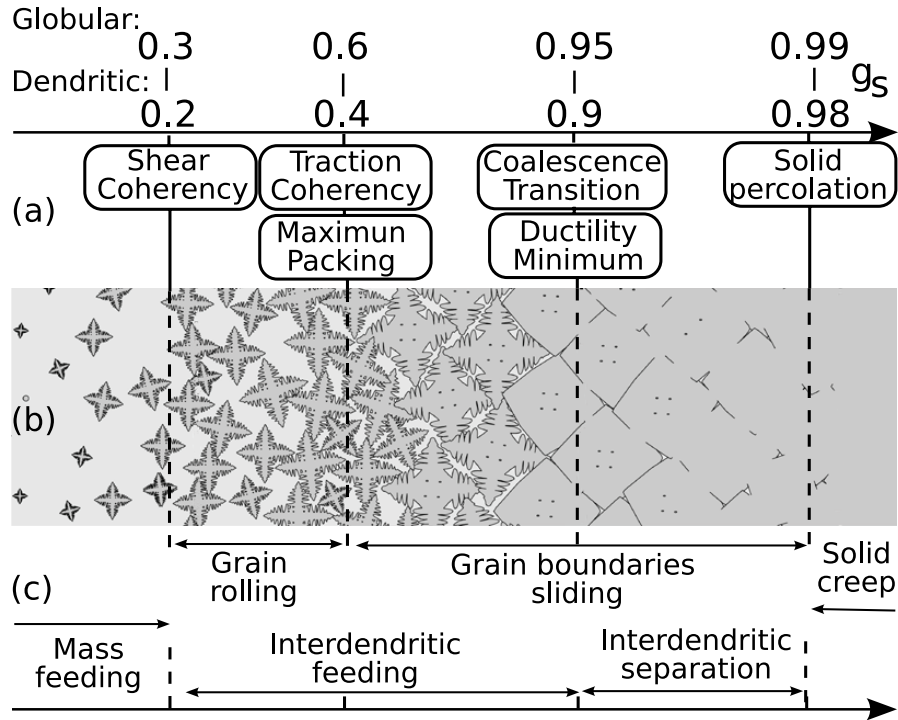


**Figure 2.24:** Evolution of mushy zone during solidification. (a) Transition solid fractions. (b) Schematic representation of the mushy zone (from P.D. Grasso thesis [7]). (c) Dominant deformation mechanism for solid phase and for liquid phase. Solid fraction scales are represented for a dendritic microstructure and for a globulitic microstructure.

keeps an important role in the deformation mechanism.

At *coalescence transition* ( $g_s^{coal}$ ), the solid grains start to coalesce to form clusters. Permeability of the mush is very low and no significant liquid can flow through the mush. The feeding mechanism is thus called interdendritic separation [23, 30]. The mechanical behaviour of the mush reveals the viscoplasticity of the solid maybe through creation / annihilation of intergranular bridges. At this point, ductility is minimum, the material is prone to hot cracking.

At *solid percolation* ( $g_s^{sp}$ ), coalesced solid grains form a continuous network and can fully transmit stresses, fracture becomes ductile.

Note that both coalescence transition and solid percolation might depend on solid-liquid surface energy. A decrease of solid-liquid surface energy should delay these two transitions. In particular, solid percolation can occur below the solidus line.



## Chapter 3

# Models for hot cracking

### 3.1 Hot cracking criteria

#### 3.1.1 Criteria based on the solidification interval

The most simple hot tearing criterion is based on the solidification interval: the hot cracking sensitivity (HCS) index is proportional to the solidification interval of the alloy [30]. At high Fourier numbers (thermodynamic equilibrium), the lever rule applies and the maximum hot cracking sensitivity is found for the maximum solubility of the solid ( $\sim 4.5$  wt% for Al-Cu). Under realistic solidification conditions, however, back-diffusion is partial and eutectic solidification occurs in alloys whose concentration is lower than the maximum solubility of the solid. The maximum HCS is displaced toward lower solute content.

This simple criterion allows having an estimation of the HCS as a function of concentration and predicts a maximum HCS for dilute alloys. Yet, the experimental peak of HCS is much sharper than the tendency predicted with this criterion (see Fig. 3.5(a)).

Borland introduced the various feeding mechanisms in the mushy zone summarised in Sec. 2.3.6 [66]. Based on this work, Clyne and Davis considered that interdendritic separation zone, the region where thin liquid films remain, is vulnerable to hot tearing. They derived an HCS criterion as the ratio of the time spent in the vulnerable zone  $t_v$  to the time spent in the interdendritic feeding zone  $t_r$  (recovery)[23].

$$\text{CSC} = \frac{t_v}{t_r} \quad (3.1)$$

The authors fixed the boundaries of the interdendritic separation as  $0.9 < g_s < 0.99$  and those of the interdendritic feeding as  $0.6 < g_s < 0.9$ . This approach allows to reproduce well the  $\lambda$ -curve but do not take into account process parameters. Furthermore, applied to some processes such as DC casting, this criterion gives the wrong tendency [56].

#### 3.1.2 Criteria based on feeding ability

Feurer introduced a criterion that compares the solidification shrinkage to the feeding ability of the mush derived with Darcy's equation [26]: If the first one exceeds the second one, a tear is susceptible to form. This approach also reproduces the shape of the  $\lambda$ -curve (see Fig. 3.5(a)). This approach is close to Niyama's porosity criterion [67],

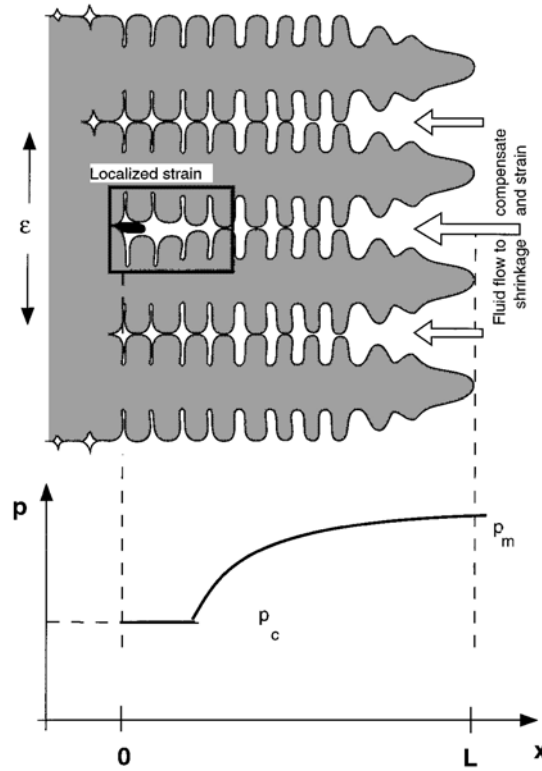


**Figure 3.1:** Pressure drop along the mushy zone induced by solidification shrinkage and deformation [68].

but it only takes into account hydrostatic depression. Yet hot tears are mainly induced by deviatoric stresses, *e.g.*, unidirectional tensile stresses [30].

The first two-phase approach has been introduced by Rappaz *et al.* for a columnar mushy zone (RDG model) see Fig. 3.1 [68]. We present here the main lines of this approach, the equations are not detailed as they are common to all two-phase approaches and are therefore presented in Sec. 3.2.2. A mass balance is done on the mushy zone, assuming that solidification shrinkage and deformation are compensated by fluid flow (Eq. 3.14). Note that the imposed deformation rate  $\dot{\epsilon}$  is only considered in the direction normal to the dendrite trunks. Fluid flow induces a pressure drop (Eq. 3.23). Permeability of the mush is evaluated using the Kozeny-Carman law [69] with the secondary dendrite arm spacing as a characteristic length scale (see Sec. 3.2.3). In summary, two integrations are done from the liquidus to the bottom of the mushy zone. The first is an integration of the mass balance to compute the fluid flow. The second is an integration of the Darcy equation to find the pressure drop. If the pressure becomes lower than a prescribed value (cavitation pressure), a hot tear nucleates. The criterion is expressed as a critical strain rate  $\dot{\epsilon}_c$  above which hot cracks nucleate.

This criterion reproduces well the hot cracking tendency of most alloys. Moreover, it can be implemented in a DC casting code to take into account process parameters [70]. The most susceptible region is the centre of the billet which is in agreement with casting practice.

This criterion has been extended by different authors. Braccini *et al.* have implemented a law for the average mush behaviour around the hot crack and for the propagation of the failure [22, 71]. Their model is derived for both columnar and equiaxed

microstructures. Their criterion allows to define three zones as a function of imposed strain rate: sound casting, porosity (nucleation without propagation) and hot cracking.

Grandfield *et al.* have also extended the RDG model to equiaxed and globular microstructures [72]. They have defined more accurately the cavitation pressure as a function of capillarity forces, and derived a model for surface cracks. In the case of the globular microstructures, the grain size is used as a characteristic length scale in the Kozeny-Carman law. Hot cracking susceptibility is shown to be reduced with globular grains because of the higher mushy zone permeability.

It is important to note that the permeability of the mush becomes nil when  $g_s = 1$  which implies a divergence of pressure in the mush (which tends to  $-\infty$ ). The model needs to stop the integration of Darcy's law before  $g_s = 1$ . Rappaz *et al.* used the value of the solid percolation as the upper bound of the integration. They fixed it to  $g_s^{sp} = 0.98$ . The predictions of the RDG criterion are highly dependent on this integration bound. In particular, it influences the position of the maximum HCS as a function of composition. Grandfield *et al.* computed the pressure drop at the experimentally observed coalescence transition ( $g_s = 0.95$  for globulitic microstructures) and compared it to the measured stress, they found a good agreement [73]. This approach is interesting because the RDG model might be fully valid only up to the coalescence transition (fluid dominated behaviour).

The models of the RDG family derive the HCS as a critical strain rate. Yet, experiments have shown that failure during tensile test is largely independent of strain rate (see Secs. 2.3 and 8.1)[56, 38]. It is one of the major problems of these models. Moreover, the metallostatic pressure at the tips of the dendrites shifts the whole pressure profile in the mush and therefore has an important influence on the predicted HCS. Yet, an important variation of HCS with the metallostatic pressure has never been experimentally observed.

### 3.1.3 Criteria based on liquid films strength

Ohm *et al.* have modelled the fracture stress of hot tearing as the stress required to pull apart a liquid meniscus [74]. They consider perfect wetting of liquid on the solid, and consider that the grains are infinite in the  $y$  direction (see Fig. 3.2(a)). Laplace equation gives:

$$\sigma = \frac{2\gamma_{lg}}{h} \quad (3.2)$$

where  $\gamma_{lg}$  is the liquid-gas surface tension, and  $h$  the width of a liquid film. Note that perfect wetting is relative to the triple junction solid-liquid-gas and not solid-liquid-grain boundary as in Sec. 2.3.5. Note also that in this model, gas cavitation is not considered, some porosity is supposed to be always present. Yet, the range of stresses predicted is in agreement with experimental data [75].

Lahaie and Bouchard have extended this criterion using a regular hexagonal arrangement of grains (Fig. 3.2(b)) [75]. This arrangement can be extended in 3D as polyhedra to form an equiaxed microstructure or as columns to form a columnar microstructure. It is then possible to write a relation between solid fraction, grain radius and liquid film thickness.

$$\frac{h}{a} = \sqrt{3} \left( \frac{1 - g_s^m}{g_s^m} \right) \quad (3.3)$$

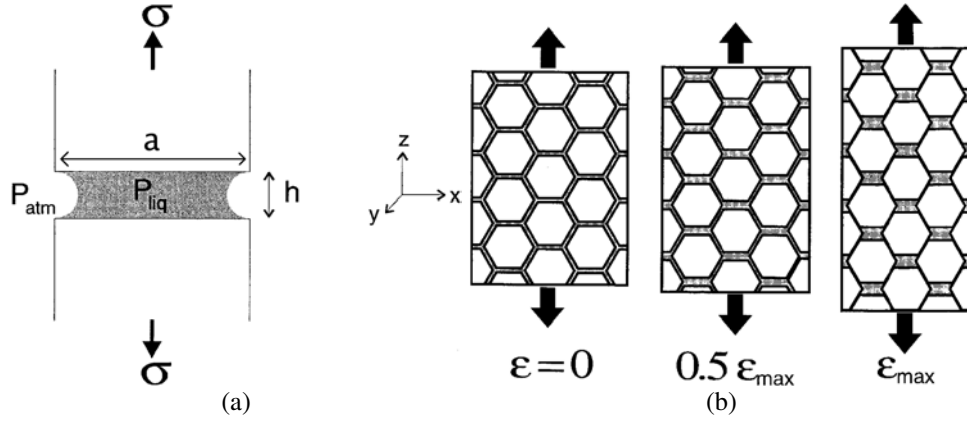


**Figure 3.2:** (a) A liquid meniscus between two grains. (b) Deformation of a regular arrangement of hexagonal grains. [75]

where  $h$  and  $a$  are respectively the thickness and the length of a liquid film (see Fig. 3.2(a)).  $m$  is an exponent which is  $1/3$  for equiaxed grains and  $1/2$  for columnar grains. At low strain, stress is dictated by the viscous flow from the lateral channels to the horizontal channels as derived by Drucker [76]. When the grains start to be interlocked ( $\epsilon \sim \epsilon_{max}$ ), the dilatation of horizontal liquid films is considered. When the computed stress is larger than the stress necessary for the breakdown of a liquid meniscus in a horizontal channel (Eq. 3.2), a hot tear propagates.

Practically, stress remains weak and abruptly raises at  $\epsilon_{max}$  (see 3.2(b)) when solid grains impinge. Thus, the ductility of the mush is mainly dictated by the geometry of the grains and is largely independent of strain rate. This criterion is important because it is the only criterion which outlines the influence of microstructure on ductility. Moreover, its simplicity allows the authors to study its dependence on various parameters.

The shape of the ultimate tensile stress as a function of solid fraction is fairly close to experimental data, but the U-curve of the ductility is not reproduced. In this model, ductility continuously decreases with increasing solid fraction and becomes nil at  $g_s=1$ . This is because the authors consider neither solid grains deformation, nor their progressive coalescence. This last point will be largely developed in the present work. Moreover, this criterion is isothermal and the mush behaviour is only function of the solid fraction. Thus, the HCS as a function of composition has not been derived.

### 3.1.4 Criteria based on accumulated strain

A semi-empirical criterion has been derived by Magnin *et al.* [54]. These authors compute the viscoplastic strain accumulated by the mushy zone from the coherency to the solidus. If the maximum principal strain accumulated in the mushy zone is larger than the experimental ductility, the risk of hot cracks is high (see Fig. 3.3).

This criterion has been implemented in a DC casting simulation code which allows to compute the strain field generated during the process. Figure 3.3 shows the computed strain at the centre of the billet for two casting speeds: at low casting speed, strain remains below the experimental ductility and no crack forms. At higher casting speed, experimental ductility is overpassed and a hot crack forms. Novikov derived a similar criterion [56]. Recently, a similar criterion has been implemented by M'Hamdi *et al.* in

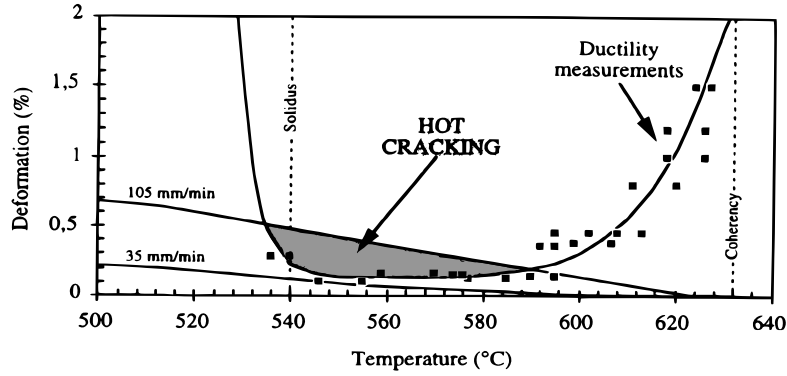


**Figure 3.3:** Computed strain at the centre of the billet for two casting speeds as compared to experimental ductility [54].

a fully-coupled two-phase model of mushy zones (see Sec. 3.2)[77].

Along the same line, Commet and Larouche presented a criterion of cumulated damage (CDI) [19]. Damage is defined as the infinitesimal viscoplastic strain  $d\epsilon(T)$  divided by the experimental ductility  $\epsilon_{rupt}(T)$ . Hot cracking susceptibility is defined as the damage integral from traction coherency to solidus.

$$CDI = \int_{T_{ic}}^{T_{sol}} \frac{d\epsilon(T)}{\epsilon_{rupt}(T)} \quad (3.4)$$

A single master curve relating ductility to solid fraction is used for different compositions. This approach reproduces well the  $\lambda$ -curve.

This criterion is very useful for the casting practice, but does not bring information on the hot tearing mechanisms.

### 3.1.5 Comparison between the criteria

Commet and Larouche have computed three hot cracking criteria for various industrial alloys [19]. It appears that the predictions of the RDG criterion and of the cumulated damage index CDI are fairly similar and in agreement with casting practice. The predictions of Clyne and Davies criterion are less reliable.

It is interesting to note how different approaches on hot tearing can give similar predictions, despite the fact that they are focused on different phenomena (permeability for RDG, ductility for CDI). This becomes clear if we look precisely at the solidification paths. Figure 3.5(b) shows the solid fraction as a function of time for Al-Cu alloys cooled at a constant cooling rate of  $1 \text{ Ks}^{-1}$ . If we consider a given point on the solidification path, its temperature difference with the liquidus point of the alloy reflects its depth in the mushy zone (considering a constant temperature gradient), whereas the distance to the  $g_s = 1$  line reflects the average liquid channels width. All hot cracking criteria that can reproduce the  $\lambda$ -curve correspond to an integration along the mushy zone. The solidification interval criteria do not predict well the HCS because they give the same weight everywhere in the mushy zone. Both RDG and CDI give a more important weight to the high solid fraction zone, because respectively of its low permeability and low ductility. A cut-off is introduced at very high solid fraction by the solid phase

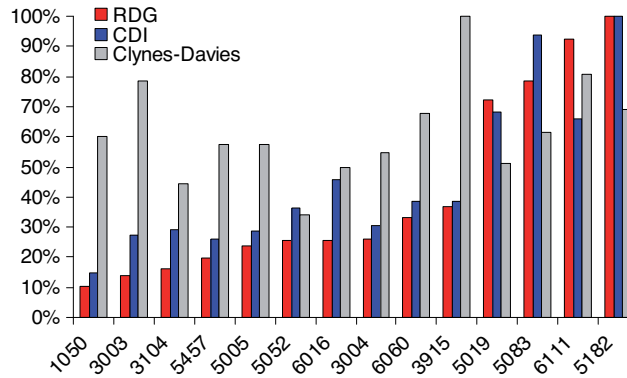


**Figure 3.4:** Hot cracking indexes computed for various industrial alloys [19].

percolation. The solidification path of the alloy at the end of solidification is a key factor for hot tearing.

Therefore, the maximum HCS is found for alloys which present a long solidification path at high solid fraction. They correspond to low alloyed alloys which produce a small amount of eutectic, *e.g.*, Al-1.5wt%Cu on Fig. 3.5(b) .

This also explains why, generally speaking, precipitation hardening alloys have high hot tearing susceptibility. A good precipitation hardening alloy should have a large amount of solute dissolved in the primary phase (to form hardening precipitates) but few intermetallic phases which could embrittle grain boundaries. This is precisely the conditions for high HCS.

The brittle range is clearly identified as the source of hot cracking. Yet the understanding of hot tearing physics remains partial. Each criterion brings a valuable point of view on a hot tearing mechanism, but no criterion is able to explain all the experimental tendencies.

Another important remark is that most criteria highly depend on the transition solid fractions introduced in Sec. 2.3.6, especially traction coherency and solid percolation. A more detailed study of these transitions is therefore important, which is one of the goals of the present study.

## 3.2 Continuum modelling of mushy zone

Both micro and macro scales are relevant during solidification. A way to solve this problem is to consider the two phase mixture as a continuum at the macroscale. Microscopic quantities are averaged over a representative elementary volume (REV) which should be large as compared to the microstructure scale in order to smooth local variations. This representative volume should also be small as compared to the process scale (boundary conditions), in order to have a good resolution of averaged values variations at the macroscale. Thus, this approach requires the existence of an intermediate scale, the mesoscale, which clearly separates the microscale from the macroscale.

We will only briefly present this homogenisation method, a full development can be found in references [78, 79]. The theory of porous media whose formalism is close to the present method is reviewed in reference [80].

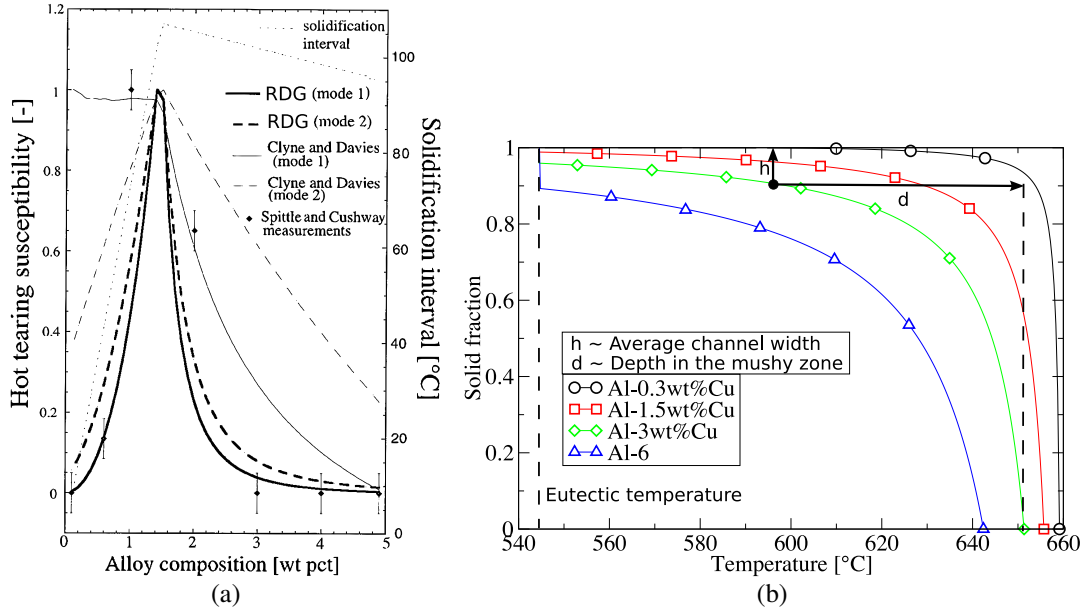


**Figure 3.5:** (a) Comparison between experimental measures and various HCS criteria for Al-Cu alloys (mode 1=constant cooling rate, mode 2=constant enthalpy extraction rate)[68]. (b) Solidification path for various Al-Cu alloys cooled at  $-1 \text{ Ks}^{-1}$ .

### 3.2.1 Balance equations

We note  $\Omega$  the volume of the REV. We note  $\alpha, \beta \dots$  the phases present in the material,  $x$  a space variable at the macroscale, and  $\xi$  a space variable at the microscale. A function  $\chi_\alpha(\xi)$  whose value is one in phase  $\alpha$  and zero elsewhere is introduced. Therefore, any quantity  $A$  of phase  $\alpha$  can be averaged on the REV.

$$\langle A(x)^\alpha \rangle = \frac{1}{\Omega} \int_{\Omega} A(x + \xi) \chi_\alpha(x + \xi) d\xi \quad (3.5)$$

The intrinsic average of  $A$  on phase  $\alpha$  is defined as:

$$A_\alpha = \langle A(x) \rangle^\alpha = \frac{1}{\Omega_\alpha} \int_{\Omega_\alpha} A(x + \xi) \chi_\alpha(x + \xi) d\xi \quad (3.6)$$

where  $\Omega_\alpha$  is the volume of phase  $\alpha$  in the REV. As  $\chi_\alpha$  is nil outside phase  $\alpha$  we have:

$$\langle A(x)^\alpha \rangle = \frac{\Omega_\alpha}{\Omega} \langle A(x) \rangle^\alpha = g_\alpha A_\alpha \quad (3.7)$$

where  $g_\alpha$  is the volumetric fraction of phase  $\alpha$ . For the sake of simplicity, we will use the notation  $\langle A(x) \rangle^\alpha = A_\alpha$  and  $\langle A(x)^\alpha \rangle = g_\alpha A_\alpha$ , but we should keep in mind that they represent averaged values.

With these definitions, we can write balance equations in the mushy zone as derived by Ni and Beckerman [79]. We consider two phases, liquid and solid, noted respectively with the subscript  $l$  and  $s$ , and suppose that no gaseous phase forms. The integration of a mass balance over the solid phase gives:

$$\frac{1}{\Omega} \int_{\Omega} \left( \frac{\partial \rho}{\partial t} + \nabla \cdot (\rho \vec{v}) \right) \chi_s(x + \xi) d\xi = 0 \quad (3.8)$$

where  $\rho$  is the density and  $\vec{v}$  the material velocity. As the volume of integration  $V$  is constant, this expression can be integrated by part to give

$$\frac{\partial}{\partial t} \left( \frac{1}{\Omega} \int_{\Omega} \rho \chi_s(x + \xi) d\xi \right) + \nabla \cdot \left( \frac{1}{\Omega} \int_{\Omega} \rho \vec{v} \chi_s(x + \xi) d\xi \right) = \frac{1}{\Omega} \int_{\Omega} \left( \rho \frac{\partial \chi_s}{\partial t} + \rho \vec{v} \cdot \nabla \chi_s \right) d\xi \quad (3.9)$$

With the notation of Eq. 3.7 this can be written :

$$\frac{\partial(g_s \rho_s)}{\partial t} + \nabla \cdot (\rho_s g_s \vec{v}_s) = \Gamma_s \quad (3.10)$$

where the solid density  $\rho_s$  is considered homogeneous at the scale of the REV and has been taken out of the second integral in Eq. 3.9. The term  $\Gamma_s$  is due to the evolution of the function  $\chi_s$  and can be written as an integral over the solid-liquid interface [78]:

$$\Gamma_s = \frac{1}{\Omega} \int_{\Omega} \left( \rho \frac{\partial \chi_s}{\partial t} + \rho \vec{v} \cdot \nabla \chi_s \right) d\xi = \frac{1}{\Omega} \int_{S_{sl}} \left( \rho_s (\vec{w}_{sl} - \vec{v}_s^*) \cdot \vec{n}_s \right) ds \quad (3.11)$$

where  $S_{sl}$  represents the solid-liquid interface,  $\vec{w}_{sl}$  the local interface velocity,  $\vec{n}_s$  the normal to the interface pointing from the solid to the liquid, and  $\vec{v}_s^*$  is the local speed of the solid at the interface. The term  $(\vec{w}_{sl} - \vec{v}_s^*)$  represents the interface speed in the local frame of the solid, and therefore  $\Gamma_s$  represents the mass transfer due to phase transformation.

Moreover, it is interesting to note that  $\Gamma_s$  can also be written

$$\Gamma_s = \frac{S_{sl}}{\Omega} \frac{1}{S_{sl}} \int_{S_{sl}} \left( \rho_s (\vec{w}_{sl} - \vec{v}_s^*) \cdot \vec{n}_s \right) ds = S_v \rho_s \overline{w_{ns}} \quad (3.12)$$

where  $S_v = S_{sl}/\Omega$  is the interface density and  $\overline{w_{ns}}$  is the average normal velocity of the interface relative to the solid velocity, the overbar denoting an average over the interfacial area. All the transfer phenomena between the two phases can be written as an average flux times the interface density and therefore  $S_v$  is an important parameter in two-phase models [79].

The same procedure can be applied to the liquid phase,

$$\frac{\partial(g_l \rho_l)}{\partial t} + \nabla \cdot (\rho_l g_l \vec{v}_l) = \Gamma_l = -\Gamma_s \quad (3.13)$$

where the mass transfer from liquid to solid due to phase transformation compensates the mass transfer from liquid to solid. Therefore, Eqs. 3.10 and 3.13 give:

$$\boxed{\frac{\partial \rho}{\partial t} + \nabla \cdot (\rho_s g_s \vec{v}_s + \rho_l g_l \vec{v}_l) = 0} \quad (3.14)$$

where  $\rho = g_s \rho_s + g_l \rho_l$  is the average density of the mushy zone. Note that this equation is formally similar to the single phase mass balance.

Similarly, the momentum balance on phase  $k = s, l$  can be written [79]:

$$\frac{\partial}{\partial t} (\rho_k \vec{v}_k) + \nabla \cdot (\rho_k \vec{v}_k \otimes \vec{v}_k) = -\nabla (g_k p_k) + \nabla \cdot (g_k \overleftrightarrow{\tau}_k) + g_k \rho_k \vec{g} + \vec{M}_k \quad (3.15)$$

where  $\otimes$  denotes the tensorial product,  $p_k$  is the average pressure in phase  $k$ ,  $\overleftrightarrow{\tau}_k$  is the deviatoric stress tensor,  $\rho_k \vec{g}$  is the average body force in phase  $k$  due to gravity, and  $\vec{M}_k$



is the interfacial momentum transfer to phase  $k$ . Note that the stress tensor  $\overleftrightarrow{\sigma}$  has been separated into its hydrostatic and deviatoric parts by:

$$\langle \overleftrightarrow{\sigma}^k \rangle = \left\langle \left( -p \overleftrightarrow{I} \right)^k \right\rangle + \langle \overleftrightarrow{\tau}^k \rangle = -g_k p_k \overleftrightarrow{I} + g_k \overleftrightarrow{\tau}_k \quad (3.16)$$

where  $\overleftrightarrow{I}$  is the identity tensor. The interfacial momentum transfer to phase  $k$ ,  $\overrightarrow{M}_k$ , can be separated into two terms, one due to the phase change  $\overrightarrow{M}_k^\Gamma$ , the other due to interfacial stress,  $\overrightarrow{M}_k^\sigma$ . This last term does not exist for the mass balance as there is no mechanism for mass diffusion.

$$\overrightarrow{M}_k^\Gamma = \overrightarrow{v}_{ki} \Gamma_s \quad (3.17)$$

where  $\overrightarrow{v}_{ki}$  is the interfacial average velocity of phase  $k$ .

$$\overrightarrow{M}_k^\sigma = \overline{p}_{ki} \nabla g_k + S_v \overrightarrow{t}_{ki} \quad (3.18)$$

where  $\overline{p}_{ki}$  is the interfacial average of pressure in phase  $k$  and  $\overrightarrow{t}_{ki}$  is the interfacial average of the force on the interface induced by the shear stress in phase  $k$ . Therefore, the first term in Eq. 3.18 represents a buoyant force, whereas the second term is the dissipative drag between the phases. The momentum transfers are related by:

$$\overrightarrow{M}_s + \overrightarrow{M}_l + \overrightarrow{M}_i = \overrightarrow{0} \quad (3.19)$$

where  $M_i$  is the average force created by the surface tension of the interface [79].

This average procedure can be done for any conservative quantity in the system, in particular for energy and solute [78, 79]. In the porous media theory, an entropy inequality is also formulated in order to give restrictions to the constitutive equations [80]. This procedure has been recently developed by Laschet and Benke for a mushy zone [81].

The obtain set of average equations is exact, but it does not provide enough information to solve the problem. Constitutive equations have to be provided to the model, they should represent the various transport phenomena in the system but also the evolution of  $\Gamma_s$  (solidification) and of  $S_v$  [79]. Moreover, the resulting set of equations is strongly coupled and thus is difficult to solve.

### 3.2.2 Simplification of the balance equations

We are specifically interested in hot cracking and therefore we do not necessarily need to model all the phenomena of DC casting. Thus, appropriate approximations can considerably reduce the complexity of the equations. We present here a model first derived by Farup and Mo [82] and whose general form is used in most two-phase models of mushy zone [83, 45, 14].

The first simplification is to decouple the thermal problem from the mechanical problem. The energy balance is written :

$$\left( \rho c_p - \rho_l L \frac{dg_s(T)}{dT} \right) \frac{\partial T}{\partial t} = \nabla \cdot (\lambda \nabla T) \quad (3.20)$$

where  $c_p$  is the heat capacity, supposed the same in the solid and liquid phases,  $L$  is the latent heat of solidification,  $T$  is the temperature, and  $\lambda$  the thermal conductivity of the mixture. The energy dissipated by mechanical work is neglected, which is a good approximation. The function  $g_s(T)$  is a parameter imposed to the model and is computed by an analytical model for solidification, *e.g.*, Clyne-Kurz model [13], or a numerical microsegregation model [84] (see also Sec. 6.1). This hypothesis supposes that the average Fourier number of the solidification is known and that the solidification conditions do not vary much in the casting. Note also that those solidification models are based on a solute balance at the microscale, and thus the transport of solute due to fluid advection is neglected. The advective transport of energy is also neglected. These assumptions are clearly wrong at low solid fraction [85], but as we are mainly interested to the high solid fractions, where the mush permeability is low, these approximations are reasonable.

The thermal calculation can thus be done independently from the mechanics with a standard commercial code. The computed thermal history is then imposed to the mechanical problem.

For the mechanical problem, the inertia terms are neglected in both liquid and solid phases [82]. Moreover the interfacial momentum transfer due to phase change is neglected. The momentum balance is therefore :

$$-\nabla(g_k p_k) + \nabla \cdot (g_k \overleftrightarrow{\tau}_k) + g_k \overrightarrow{b}_k + \overline{p_{ki}} \nabla g_k + S_v \overrightarrow{t_{ki}} = 0 \quad (3.21)$$

where  $k = s, l$ . The average interfacial pressure in both phases  $\overline{p_{ki}}$  is taken equal to the liquid pressure  $p_l$ , which implies that the interfacial tension is neglected. Note that the average pressure in the solid  $p_s$  can be different from  $p_l$  as a coherent solid network can transmit stresses. Finally, the interfacial momentum transfer due to dissipative force  $S_v \overrightarrow{t_{ki}}$  is modelled by Darcy's law and the diffusion of momentum in the liquid phase is neglected in front of this term [82]. Finally the momentum equations are

$$-\nabla(g_s p_s) + \nabla \cdot (g_s \overleftrightarrow{\tau}_s) + g_s \rho_s \overrightarrow{g} + p_l \nabla g_s + \frac{g_l^2 \eta_l}{\kappa(g_l)} (\overrightarrow{v}_l - \overrightarrow{v}_s) = 0 \quad (3.22)$$

in the solid and

$$-g_l \nabla p_l + g_l \rho_l \overrightarrow{g} - \frac{g_l^2 \mu}{\kappa(g_l)} (\overrightarrow{v}_l - \overrightarrow{v}_s) = 0 \quad (3.23)$$

in the liquid.  $\mu$  represents the fluid viscosity and  $\kappa(g_l)$  is the permeability of the mush. Note that the  $g_l^2$  term in Darcy's law is due to the definition of permeability (see Sec. 3.2.3).

Equations 3.22 and 3.23 gives

$$\nabla \cdot (g_s \overleftrightarrow{\tau}_s) + (p_l - p_s) \nabla g_s + g_s \nabla (p_l - p_s) - \nabla p_l + \rho \overrightarrow{g} = 0 \quad (3.24)$$

that is

$$\boxed{\nabla \cdot (\overleftrightarrow{\sigma}_s^e \overrightarrow{v}_s) + \rho \overrightarrow{g} = \nabla p_l} \quad (3.25)$$

where  $\overleftrightarrow{\sigma}_s^e$  is the Terzaghi effective stress classically introduced in soil mechanics [86]. It expresses that the solid skeleton behaviour is essentially sensitive to the difference

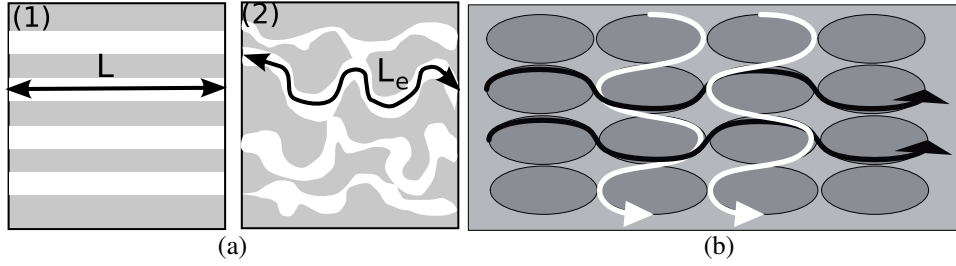


**Figure 3.6:** (a) (1) Kozeny model of a regular arrangement of pipes, (2) tortuous medium. (b) Anisotropy of tortuosity in a medium under compression [88].

of pressure between solid and liquid. Note that  $\overleftrightarrow{\sigma}_s^e$  is implicitly function of the solid velocity.

$$\overleftrightarrow{\sigma}_s^e = g_s \overleftrightarrow{\sigma}_s + g_s p_l \overleftrightarrow{I} = g_s \overleftrightarrow{\tau}_s - g_s (p_s - p_l) \overleftrightarrow{I} \quad (3.26)$$

Equation 3.23 expresses the relative velocity of the liquid as a function of liquid pressure and body forces. Therefore, it can be introduced in the mass balance (Eq. 3.14) to give

$$\nabla \cdot \left( \rho_l \frac{\kappa(g_l)}{\mu} (\nabla p_l - \rho_l \vec{g}) \right) = \frac{\partial \rho}{\partial t} + \nabla \cdot (\rho \vec{v}_s) \quad (3.27)$$

The left hand term describes the pressure drop due to fluid flow, whereas the second hand term represents the pump term due to solid displacement and solidification. Note that in the RDG criterion the pressure drop is calculated by the double integration of this equation along the mushy zone, with a prescribed solid velocity.

Equation 3.25 and 3.27 couple the liquid pressure to the solid velocity. They are sufficient to solve the whole mechanical problem provided constitutive laws for the permeability and the effective stress are given.

### 3.2.3 Constitutive equation for the permeability

The permeability  $\kappa$  is defined from Darcy's law for a fluid flow through a granular packed bed [87]:

$$\frac{\kappa}{\mu} \frac{\Delta P}{L} = \langle v^l \rangle = g_l v_l \quad (3.28)$$

where  $\Delta P$  is the difference of pressure between the ends of the packed bed, and  $L$  is its length. Note that, permeability should be expressed as a tensor in an anisotropic medium.

Kozeny has modelled a packed bed as a regular arrangement of pipes with a Poiseuille flow of the fluid [89]. He showed that

$$\kappa = \frac{g_l^3}{k_0 S_v^2} \quad (3.29)$$

where  $k_0$  is a constant equal to 2 for circular pipes and varies only slightly with the shape of the cross-section [69]. If we consider a real medium, the path of the flow is tortuous. We note  $L_e$  the average length of the fluid effective path. The ratio of  $L_e$  to the length of the media  $L$  is called the tortuosity  $r = L_e/L$  (see Fig. 3.6(a)). Therefore, the

average effective speed of the fluid is  $v_l^e = rv_l$  and the effective gradient of pressure is  $\Delta P/L_e$ . Thus

$$\frac{g_l^3}{k_0 S_v^2 \mu} \frac{L}{L_e} \frac{\Delta P}{L} = g_l r v_l \quad (3.30)$$

and

$$\kappa = \frac{g_l^3}{k_0 r^2 S_v^2} \quad (3.31)$$

Carman has shown that the constant  $k = k_0 r^2$  varies only slightly with the geometry of the packed bed [69]:

$$k = k_0 r^2 \simeq 5 \quad (3.32)$$

The permeability of mushy zones has been measured by Nielsen *et al.* for various types of microstructures (from small globules to large equiaxed dendrites)[90]. The measurements were done just above the eutectic temperature and therefore  $S_v$  can be measured by image analysis after quenching the sample. The authors observed a good agreement with Eqs. 3.31 and 3.32, namely the Kozeny-Carman relationship. Bernard *et al.* have done X-Ray tomography on these samples and reconstructed the permeability tensor by solving the Stokes equation in the measured geometry [91]. The computed permeability is anisotropic but its trace is in good agreement with the experiment of Nielsen *et al.*

The tortuosity is often included in the constant  $k$ , but its identification is useful when the medium is anisotropic. Scholes *et al.* have modelled the evolution of the permeability anisotropy in a porous medium under compression (Fig. 3.6(b)) [88]. They showed that the evolution of the tortuosity anisotropy with compression is independent of the particle shape and can be used to model the evolution of permeability.

Another form of Kozeny-Carman's equation is frequently used by replacing the specific surface  $S_v$  by the specific surface per unit solid  $S_s = 1/g_s S_v$  [68]. Indeed,  $S_s$  can easily be related to the characteristic length scale of the grain  $d$  (average grain size for globulitic grains, secondary arm spacing for dendritic grains)  $S_s \sim 6/d$  [69]. Thus

$$\kappa \simeq \frac{g_l^3 d^2}{180 g_s^2} \quad (3.33)$$

### 3.2.4 Constitutive equations for the effective stress

During DC casting, solid deformations in the mushy zone remain small, on the order of 0.1 to 1% strain [19]. Therefore, the small strain formalism can be used. The deformation tensor is separated into its elastic, plastic and thermal component :

$$\overleftrightarrow{\varepsilon}_s = \overleftrightarrow{\varepsilon}_s^{el} + \overleftrightarrow{\varepsilon}_s^p + \overleftrightarrow{\varepsilon}_s^T \quad (3.34)$$

The elastic strains  $\overleftrightarrow{\varepsilon}_s^{el}$  are related to the effective stress  $\overleftrightarrow{\sigma}_s^e$  by Hooke's law. Note that even though this elastic regime is small, its presence stabilizes the numerical scheme [83]. The thermal strain rate tensor is given by:

$$\overleftrightarrow{\dot{\varepsilon}}_s^T = \frac{1}{3} \beta_{T,s} \frac{\partial T}{\partial t} \overleftrightarrow{I} \quad (3.35)$$

where  $\beta_{T,s}$  is the thermal contraction coefficient of the solid phase.

In hot tearing models, we are specifically interested in the high solid fraction behavior of the mush. Therefore, the constitutive laws for the plastic strain are derived as an extrapolation of the fully solid behavior.

A first phenomenological approach is to multiply the viscoplastic law of the solid by a term which varies with the solid fraction and tends to one at the solidus [92, 93]. Yet, with this approach, the plastic strains are only function of the deviatoric stress and no consolidation due to pressure is predicted.

Nguyen *et al.* have developed a more rigorous approach inspired by soil mechanics. A viscoplastic potential is expressed as a function of the first two invariants of the effective stress (pressure and von Mises stress) and the solid fraction. The viscoplastic strains are expressed by the normality rule (Eq. 3.39)[50]. This approach has been further modified by Martin *et al.* to take into account the asymmetry in the mush behavior between traction and compression [94, 95]. These models have been developed for the modeling of semi solid state forming and are suited for process with high deformation. They fail to describe correctly the mushy zone behavior at small strain, in particular the progressive increase of stress with deformation (see Sec. 2.3)[37].

Therefore, Ludwig *et al.* have developed a model for the viscoplastic behavior of the mush at low strain and high solid fraction, *i.e.*, a model oriented toward hot cracking [37, 45].

These authors model the viscoplastic potential  $\omega$  of the mushy zone as :

$$\omega = \omega(p_s^e, \sigma_s^{eq}, g_s, T, C) \quad (3.36)$$

where  $p_s^e$  is the effective pressure

$$p_s^e = -\frac{1}{3}tr(\overleftrightarrow{\sigma}_s^e) = g_s(p_s - p_l) \quad (3.37)$$

$\sigma_s^{eq}$  is the Von Mises stress

$$\sigma_s^{eq} = \sqrt{\frac{3}{2} \overleftrightarrow{\tau}^e : \overleftrightarrow{\tau}^e} \quad (3.38)$$

where  $\overleftrightarrow{\tau}^e$  is the deviatoric effective stress and  $:$  represents the contracted product.  $C$  is an internal variable representing the coherency of the mush (see below).  $\omega$  represents the power dissipated by the viscoplastic deformation and the strain rate tensor is expressed by the normality rule, which states that the strain rate tensor is normal to the isosurfaces of  $\omega$  [96].

$$\overleftrightarrow{\dot{\epsilon}}_s^p = \frac{\partial \omega}{\partial \overleftrightarrow{\sigma}_s^e} \quad (3.39)$$

The authors start from  $\omega_0$ , the viscoplastic potential of the fully solid material at the solidus temperature(see [37, 45]). The first effect considered is the concentration of stress in the solid due to the presence of liquid inclusions. This effect has been studied by Michel and Suquet [97]. The new potential can be written:

$$\omega^1 = \omega^0 \left( A_2 X^2 + A_3 \right)^{\frac{n+1}{2}} \quad (3.40)$$

where  $1/n$  is the strain rate sensitivity coefficient of the fully solid phase,  $X$  is the stress triaxiality ( $X = p_s^e / \sigma_s^{eq}$ ),  $A_2$  and  $A_3$  are functions of  $g_s$  and  $n$  (see [37, 45]).

Yet, this effect does not represent well the important influence of the liquid phase on the mush behavior (see Sec. 2.3.2 Fig. 2.15). Indeed, the solid phase might not be fully coherent and some deformations can be accommodated by fluid flow. Therefore, these authors introduce an internal variable  $C$  which represents the mush coherency :

$$\omega = \frac{1}{C^n} \omega^1 \quad (3.41)$$

Note that  $C = 1$  corresponds to a fully coherent solid (the effect of liquid inclusions on stress concentration is solely considered) and  $C \rightarrow 0$  corresponds to solid grains fully surrounded by liquid.

The heart of the model is the equation for the evolution of  $C$  :

$$\frac{\partial C}{\partial t} = \alpha(g_s, T) \left( 1 - \frac{C}{C^*(g_s, X)} \right) \dot{\varepsilon}_s^{eq} \quad (3.42)$$

where  $\dot{\varepsilon}_s^{eq}$  is the second invariant of the plastic strain rate tensor and is thus a measure of the plastic deformation rate.  $C^*(g_s, X)$  is the target coherency, *i.e.*, the maximum coherency that can be reached for a given solid fraction and triaxiality.  $\alpha(g_s, T)$  represents the evolution rate of  $C$  with deformation, and appears as the initial slope of the stress-strain curve in pure shear [37] (see Sec. 2.3.2 Fig. 2.12).

The functions  $C^*$  and  $\alpha$  have been identified by mechanical tests with different stress states [37, 45].

$$C^*(g_s, X \leq 2) = 1 - (1 - g_s)^p, \quad C^*(g_s, X > 2) = 1, \quad C^*(g_s \leq g_s^{tc}, X) = 0 \quad (3.43)$$

where  $g_s^{tc}$  is the solid fraction at traction coherency (see Sec. 2.3.6) and the exponent  $p$  is fitted to experiments. The maximum coherency  $C^*$  is nil below  $g_s^{tc}$  (by definition), and increases up to 1 at  $g_s = 1$ . For  $X > 2$  the stress state is highly compressive and tends to create a fully coherent mushy zone.

$$\alpha^*(g_s, X < 0) = \alpha_0 + \alpha_1 \frac{g_s^{1/3}}{1 - g_s^{1/3}} e^{k(g_s - g_s^{coal})}, \quad C^*(g_s, X \geq 0) = \alpha_0 + \alpha_1 \frac{g_s^{1/3}}{1 - g_s^{1/3}} \quad (3.44)$$

where  $g_s^{coal}$  is the coalescence transition solid fraction,  $\alpha_0$ ,  $\alpha_1$  and  $k$  are fitted on experiments. The asymmetry between traction and compression in the mushy zone behavior is represented by the asymmetry of  $\alpha$ . Indeed, for  $X > 0$  (traction)  $\alpha$  increases significantly only above the coalescence transition due to the exponential term. Note that the term  $(g_s^{1/3})/(1 - g_s^{1/3})$  is proportional to the ratio of the liquid channel length to the liquid channel width in a regular hexagonal network (see Sec. 3.1.3).

In this model, a mushy zone without any accumulated strain has a nil coherency at any solid fraction (except for  $g_s = 1$ ). Moreover,  $\alpha$  is always positive and any deformation makes the coherency  $C$  to evolve toward the target coherency  $C^*$ . The mush coherency can nonetheless decrease with deformation, *e.g.*, if solid fraction and thus  $C^*$  locally decreases.

It is important to remark that, once again, the transitions of the mushy zone play a central role in the model. Yet, these transitions appear as parameters. Moreover, they might be implicitly function of the grain morphology or of the dihedral angle at triple junctions.

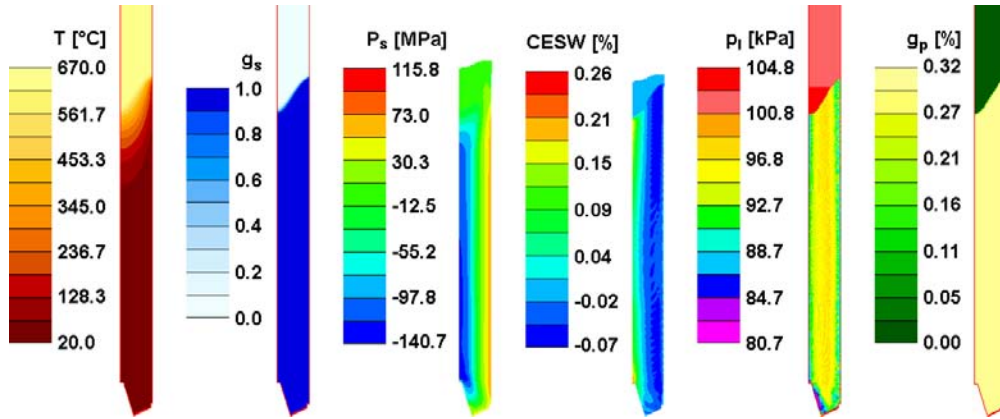


**Figure 3.7:** Simulation of the DC casting process for a billet [18]. The field represented are: thermal calculation, temperature  $T$  and solid fraction  $g_s$ , mechanical calculation, solid pressure  $p_s$  and accumulated volume change due to plastic deformation  $CESW$ , porosity calculation, liquid pressure  $p_l$  and porosity fraction  $g_p$ .

### 3.2.5 Applications of two phase models

The two-phase formalism presented in this section can be implemented in numerical codes for the simulation of solidification processes [82, 83, 51, 14]. This provides an insight in the mechanical fields during solidification, but does not model hot cracking. The computed mechanical and thermal fields can be used to locally evaluate hot cracking criteria, *i.e.*, RDG, CDI [70, 19, 77].

Pequet *et al.* [31] and then Couturier *et al.* [98] have modeled porosity formation with a multi-phase formalism. They computed the pressure drop in the mush (Eq. 3.27) while neglecting solid deformation in a first approximation (Eq. 3.25). The cavitation depression is evaluated taking into account dissolved gases, *e.g.*, hydrogen, and the Young-Laplace term due to pore curvature. Before pore nucleation, this computation is similar to the RDG criterion when  $\vec{v}_s = 0$ .

Mathier *et al.* have recognized that the pressure drop in the liquid ( $\sim$  kPa) is considerably lower than stresses in the solid ( $\sim$  MPa) and therefore decided to neglect the liquid pressure term in Eq. 3.25 [14]. Thus, the system of Eqs. 3.25 and 3.27 is only semi-coupled. The thermal field is first computed (Eq. 3.20) and imposed to the subsequent calculations. Then, the solid velocity is computed (Eq. 3.25) with a solid-state mechanics commercial software. This velocity field is then imposed in the mass balance and the pressure field in the liquid (Eq. 3.27) is solved with the porosity code of Pequet and Couturier (Fig. 3.7). This approach allows to compute the formation of porosity in the mush, which is not possible with other two-phase approaches. Yet, a simple criterion based on the porosity fraction does not model satisfactorily the HCS in all situations [18].

These models are also useful for the interpretation of experimental tests (Fig. 3.8). Indeed, during solidification, samples are necessarily non isothermal and thus non homogenous. Only numerical simulation can precisely deduce the local intrinsic fields from the measured macroscopic quantities. Moreover, calculated fields such as porosity or accumulated volume change allow finer interpretations of the experiments [18].

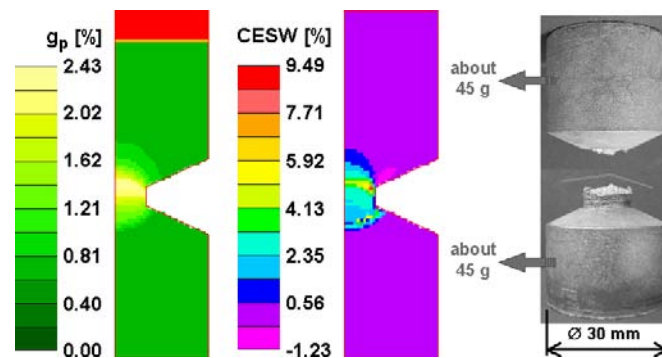


**Figure 3.8:** Simulation of a mushy zone traction test [7, 18].



# Chapter 4

## Scale invariance

In this chapter, we introduce two tools that will be useful for our study and yet do not frequently appear in the hot cracking literature. These tools share a common point, they point out relations between the various scales of a problem.

### 4.1 Percolation theory

The percolation theory studies the progressive formation of a continuous phase and is therefore highly relevant for the study of hot cracking. We present here only a small part of this theory which will be directly useful for the interpretation of our results. More details can be found in references [17, 99].

#### 4.1.1 Lattice percolation

The simplest percolation models start from a regular lattice, *e.g.*, square lattice. Each site can belong to one of two phases, *e.g.*, black or white (see Fig. 4.1). We note  $p$  the probability of a node to belong to the first phase, this probability being the same for each site. Two sites of the same phase which are first neighbors are connected and form a cluster [17].

For a small  $p$  value, we have isolated islands of phase 1 (Fig. 4.1(a)), while with increasing  $p$  larger clusters are formed. For a given probability, phase 1 becomes continuous (Fig. 4.1(c)). This probability is called the percolation threshold  $p_c$ . On a finite size lattice,  $p_c$  may vary with the different possible configurations but on an infinite lattice  $p_c$  is uniquely defined (see Sec. 4.1.2 for the finite size effects). Once  $p$  is larger than  $p_c$ , phase 1 is continuous and thickens with increasing  $p$  (Fig. 4.1(d)).

Table 4.1 shows the percolation thresholds for various regular lattices in 2D and 3D. Site percolation refers to the model described at the previous paragraph whereas bond percolation correspond to a model where the bond between two sites is considered either closed or open. For site percolation, it may appear surprising that  $p_c$  is different from 0.5 as the problem is symmetric by the permutation of phases 1 and 2. Indeed, in 2D there is a range of  $p$  for which neither phases are continuous and therefore  $p_c > 0.5$  (*e.g.*, on Fig. 4.1(b) an continuous path can neither be found on the white phase nor on the black one). In 3D, site percolation threshold is smaller than 0.5 as the two phases can be simultaneously continuous [17].

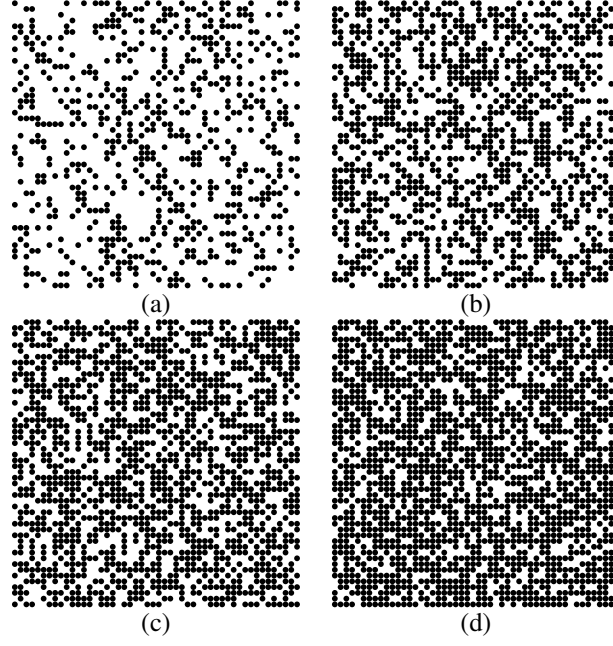


**Figure 4.1:** Percolation simulations for a square lattice of  $50 \times 50$  sites. (a)  $p = 0.3$  (b)  $p = 0.5$  (c)  $p = p_c = 0.593$  (d)  $p = 0.7$  (simulations done during the present work)

We define the gyration radius of a cluster as the the root mean square distance among the sites this cluster. The average gyration cluster  $\xi$  as a function of  $p$  follows a well defined law.

$$\xi \propto |p - p_c|^{-\nu} \quad (4.1)$$

with  $\nu > 0$ . Note that for  $p > p_c$ ,  $\xi$  represents the average gyration radius of clusters that are not connected to the continuous cluster. This quantity is also called the correlation length of the system (see Sec. 4.6). As expected, this law predicts an increase of cluster radius with  $p < p_c$  and its divergence for  $p = p_c$  but the striking fact is that  $\nu$  is independent of the lattice nature. Indeed, it only depends on the dimensionality of the problem and is therefore called a universal exponent [17].

Other quantities such as the average number of sites per cluster  $S$  can be measured. Moreover, if we consider that phase 1 is a conductor whereas phase 2 is an insulator,

lattice	site percolation	bond percolation
Square	0.593	0.5
Hexagonal	0.696	0.653
Triangular	0.5	0.347
Diamond	0.43	0.388
Cubic	0.312	0.249
BCC	0.246	0.180
FCC	0.198	0.119

**Table 4.1:** Percolation threshold for various 2D and 3D lattices considering both site and bond percolation [17].

Associated quantity	exponent	2D	3D
Correlation length	$\nu$	4/3	0.88
Cluster mass	$\gamma$	43/18	1.80
Conductivity	$\mu$	1.30	2.0

**Table 4.2:** A few percolation exponents in 2 and 3D [17]. The fractional numbers give presumed exact values whereas those with decimal numbers are numerical estimates.

the conductivity  $\Sigma$  of the system can also be measured. It is found that these quantities follow a law similar to Eq. 4.1, with the same percolation threshold but with different exponents.

$$S \propto |p - p_c|^{-\gamma} \quad (4.2)$$

$$\Sigma \propto (p - p_c)^\mu \quad p > p_c \quad (4.3)$$

Once again the exponents appear to be only function of the dimensionality of the problem. Table 4.2 shows the value of these three exponents in 2 and 3D. Note that several other exponents can be defined (see [17] for more details)

The rigorous mathematical treatment of percolation is difficult. Indeed, most of the results presented here are extrapolation of numerical results and few of them can be mathematically proven [100]. Yet, it is interesting to note how simple are the laws emerging from the percolation models. Percolation is thus a good illustration of a theoretical advance induced by the study of numerical simulations.

### 4.1.2 Continuum percolation

In the previous section, we have considered percolation on lattices. In order to study a wider range of physical phenomena, the question of percolation in a continuum should be raised.

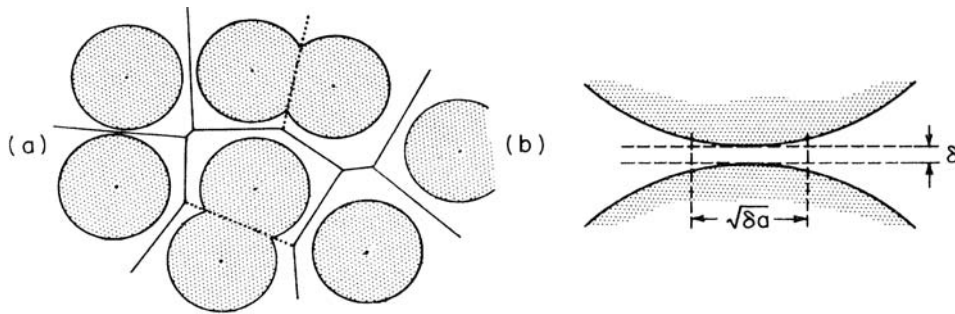


**Figure 4.2:** The swiss cheese model,  $a$  represents the hole radius [101].

An example of a continuum percolation model is the so-called “swiss cheese model” (Fig. 4.2) [101, 102, 103]. Holes of a given radius  $a$  are randomly placed in space. The properties of the remaining space is studied. Kerstein has shown that this problem could be mapped on a lattice percolation problem by using the Voronoi diagram of the holes’ centers set (Fig. 4.2 (a)) [103]. In that sense, this problem is very close to percolation in the Voronoi solidification model developed in the present work (Sec. 6.1).

The same scaling laws as Eqs. 4.1-4.3 are observed in the swiss cheese model and the correlation length exponent  $\nu$  is the same as in lattice problems [101, 103]. Moreover, these laws can be equally expressed as functions of the fraction of open bonds (projected on the Voronoi diagram) or as functions of the solid fraction (non void)  $g_s$  [103], *e.g.*,

$$\xi \propto |g_s - g_{s,c}|^{-\nu} \quad (4.4)$$

where  $g_{s,c}$  is the solid fraction at percolation threshold. These properties are common to all continuum percolation models (provided there is no strong local correlations) [17].

Halperin *et al.* have studied the transport properties of the swiss cheese model [101, 104]. In such a continuum model, the permeability of open channel (carrying flow) diverges when its width  $\delta$  tends to 0 (Fig. 4.2 (b)). Thus, a channel which is open from the point of view of cluster formation, may have a so high permeability that it cannot participate to the transport properties [101, 104]. This is the major difference with a lattice model for which the permeability of an open channel is constant. As a consequence, the exponent for the transport properties are modified by the local laws for the channels permeability.

In 2D, the authors considered that the narrow necks between two holes are equivalent to rectangles of width  $\delta$  and of length  $\sqrt{\delta a}$ , where  $a$  is the holes radius and  $\delta$  the minimum distance between these two holes (Fig. 4.2). Thus, the electrical conductance of a single channel  $\sigma_e$  varies as  $\sigma_e \sim \delta^{1/2}$  whereas the hydrodynamic conductance (Poiseuille flow) varies as  $\sigma_h \sim \delta^{5/2}$  (see Sec. 7.1). In a lattice model, both electric and hydrodynamic conductance have the same percolation exponent  $\mu$ . In the swiss cheese model, the strong divergence of  $\sigma_h$  with  $\delta$  can modify this exponent up to  $\mu_h = \mu + 3/2$  [101, 104]. For the electrical conductance the divergence  $\sigma_e$  is too slow to affect the exponent  $\mu$ . In 3D, the divergence of the local channel permeability is stronger and both exponents are affected [104].

In summary, percolation in continuum follows the same laws as lattice percolation. The exponent related to the geometry of the clusters, *e.g.*, the correlation length exponent  $\nu$ , are unchanged. The exponents relative to transport properties can be modified by the local rules for transport.

### 4.1.3 Finite size percolation

For percolation in a finite size lattice, a general law is also observed. Let us consider a quantity  $X$  that, in a infinite lattice, scales as

$$X \sim |p - p_c|^{-\chi} \quad (4.5)$$

where  $\chi$  is the percolation exponent of  $X$ . On a finite lattice of size  $L$  we have [17]

$$X(L, \xi) = \xi^{\chi/\nu} x_1(L/\xi) \propto \begin{cases} \xi^{\chi/\nu} & L \gg \xi \\ L^{\chi/\nu} & L \ll \xi \end{cases} \quad (4.6)$$

where  $x_1$  is a function with the proper asymptotic behaviour and  $\xi$  is given by Eq. 4.1. Note that for  $L \gg \xi$  we retrieve the law for  $X$  on a infinite lattice (Eq. 4.5).

Therefore, observed at a scale  $L \gg \xi$ , the material appears as a standard material and its intrinsic properties (such as cluster density or electrical conductivity) do not depend on the sample size.

Observed at a scale  $L \ll \xi$ , the same intrinsic properties do vary with the sample size. This property is a characteristic of the self-similar objects (also called fractals see Sec. 4.2.1). Naturally, there is a lower cut-off of this self-similar nature for a sample size  $L$  on the order of a few elementary sites.

Therefore, a representative elementary volume (REV) defined on a percolating system should be larger than  $\xi$ . Yet, at the percolation transition  $\xi$  becomes infinite (process scale), and thus no REV can be defined. This points out one limit of the average models of mushy zones.

On a finite sample of size  $L$ , a percolation threshold  $p_{c,L}$  can be defined as the lowest fraction of occupied sites for which a cluster spans from the left to the right of the sample. Yet, there is no reason for this probability to correspond exactly to the percolation threshold in an infinite lattice  $p_c$ . Moreover, the value of  $p_{c,L}$  may vary with the precise repartition of the occupied sites. We thus consider  $\langle p_{c,L} \rangle$  the averaged value of  $p_{c,L}$  on several random configurations of the occupied sites. From Eq. 4.6 we can deduce [17].

$$\langle p_{c,L} \rangle - p_c \propto L^{-1/\nu} \quad (4.7)$$

*i.e.*, the average percolation threshold tends to the infinite threshold as  $L^{-1/\nu}$ . We also have

$$\sqrt{\langle (p_{c,L} - \langle p_{c,L} \rangle)^2 \rangle} \propto L^{-1/\nu} \quad (4.8)$$

*i.e.*, the standard deviation of the observed thresholds vanishes as  $L^{-1/\nu}$  when  $L$  tends to infinity. These relations are practically used to numerically determine the infinite percolation threshold.

## 4.2 Scaling properties of cracks

Once again the scaling properties of cracks is a broad subject [105]. Here, we only present a few tools that have been used for the analysis of hot tearing fracture surfaces (see Sec. 8.1.3).

### 4.2.1 Self-similarity and self-affinity

The term of *self-similar* structures or fractals describes objects which present the same aspect at different scales. This concept has probably been introduced by the mathematician Cantor at the end of the XIX century [106], the word “fractal” being due to Mandelbrot [107] who pointed out the importance of this concept to describe natural patterns. Mathematical fractals can be obtained by a recursive construction, *e.g.*, the Sierpinski gasket [108](see Fig. 4.3).

The pure scale invariance of mathematical constructions cannot be observed in nature but objects with a statistical scale invariance are frequent. A well-known example is a coast line [109](as a consequence the length of a coast line depends on the observation scale, see below). Another example is clouds which look the same directly observed in the sky or on satellite images of weather forecast programs [99]. Naturally, this self-similarity can only be observed for a given range of scales. For a coast line, the upper cut-off is the size of the island, whereas the lower cut-off should be around the size of the sand stone.

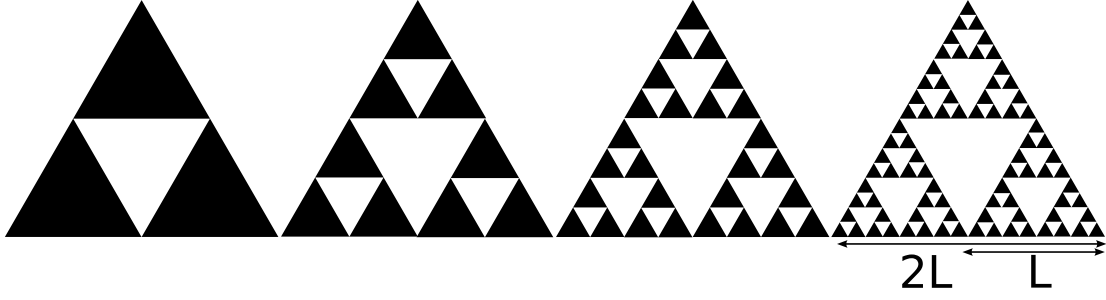


**Figure 4.3:** The Sierpinski gasket is constructed from an elementary equilateral triangle with a triangle hole in it. This pattern is then replicated in each fully solid triangle. This recursive construction repeated to the infinity gives a scale invariant pattern, a fractal [108].

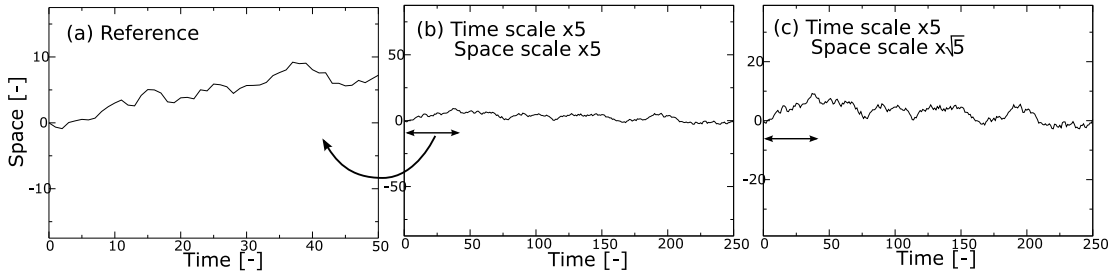


**Figure 4.4:** 1D Brownian motion as observed at different scales. Time and space units are chosen such as the toposythesis  $l$  is one (see text). (b) If both time and space scales are increased by the same factor, the apparent rugosity of the movement decreases. (c) If time scale is increased by a factor  $b$  and space scale by a factor  $\sqrt{b}$ , the statistical properties of the reference scale (a) are preserved. (simulations done during the present work)

If we consider the Sierpinski gasket on Fig. 4.3, we see that if the observation scale  $L$  is doubled, the structure consists in 3 original patterns and therefore the mass (surface)  $m$  of the object is tripled [110]. Thus, the mass of the object varies with the observation scale  $L$  as

$$m \propto L^{d_f} \quad d_f = \frac{\ln 3}{\ln 2} \simeq 1.6 \quad (4.9)$$

For an object with an Euclidian geometry, we have  $m \propto L^d$  where  $d$  is the dimension of the object and therefore  $d_f$  is called the fractal dimension. The form of Eq. 4.9 is also valid for other properties of fractals such as conductivity (with different exponents) [99]. It also recalls the properties of finite size percolation clusters (Eq. 4.6). Indeed, percolation clusters have a self-similar nature for  $a \ll L \ll \xi$  where  $a$  is the size of an elementary site [17].

Another scale property is *self-affinity* [111, 112]. As self-similar structures are (statistically) invariant by a transformation  $(x, y, z) \rightarrow (bx, by, bz)$  where  $x, y, z$  are the three space directions and  $b$  an arbitrary factor, self-affine structures are statistically invariant by an affine transformation [105]

$$(x, y, z) \rightarrow (bx, by, b^H z) \quad (4.10)$$

where  $0 < H < 1$  is called the Hurst exponent of the structure. Let us consider two

points  $r_0 (x_0, y_0)$  and  $r (x, y)$  on the self-affine structure, the height-height correlation function (also called Hurst transformation [112]) is given by

$$\Delta h(\Delta r) = \left\langle (z(r) - z(r_0))^2 \right\rangle^{1/2} \quad \Delta r = ((x - x_0)^2 + (y - y_0)^2)^{1/2} \quad (4.11)$$

where the average  $\langle . \rangle$  is done for all admissible positions of  $r_0$  and  $r$ , *i.e.*, all pairs of points with a distance  $\Delta r$  in the plane  $(x, y)$ . As a consequence of self-affinity, we have [105, 111]

$$\frac{\Delta h}{l} = \left( \frac{\Delta r}{l} \right)^H \quad (4.12)$$

where  $l$  is the toposity of the structure, *i.e.*, the scale at which  $\Delta h = \Delta r = l$ .

A classical example of self-affine structure is a 1D brownian motion expressed as a function of time (Fig. 4.4) [99, 111]. In that case, time plays the role of direction  $x$  and space the role of direction  $z$ . Indeed, the standard deviation of the distance from the starting point scales as  $\Delta h \propto \sqrt{t}$  and thus the Hurst exponent of this structure is  $H = 1/2$  (This property is also denoted in the diffusion Fourier number  $Dt/L^2$ ).

As seen on Fig. 4.4 (a) a self-affine structure observed at a scale close to  $l$  is almost self-similar (with a local fractal dimension  $d_f = 3 - H$  in 3D [105, 111]) but when observed at a scale large as compared with  $l$ , the same structure appears almost Euclidian (Fig. 4.4 (b)) [111].

### 4.2.2 Self-affinity of fracture

Fracture surfaces have a self affine nature, where the direction  $z$  corresponds to the average normal to the fracture surface [105]. Once again, the Hurst exponent of the surface is conjectured to be universal [113], *i.e.*, not to depend on the material or on the fracture speed and mode. This hypothesis has been experimentally verified on very different materials such as glass, concrete, or aluminum and for various fracture speeds [105]. In all situations, the measured Hurst exponent is around  $H \simeq 0.8$  [113].

Yet, the toposity  $l$  may vary greatly from a situation to another. Indeed, toposity is on the order of the typical heterogeneity length in the material (a few nm in glass, a few mm in concrete). This explains why, at our scale, a glass fracture surface appears much smoother than a concrete fracture surface. Moreover, in anisotropic media such as wood, the anisotropy is reflected by an anisotropy of the toposity but not by the Hurst exponent [114].

Another class of materials has been identified which exhibits a Hurst exponent around 0.5. These materials are granular materials with a weak coherency, such as sand stone or sintered glass bead [115]. An explanation for this different behavior may be that in these materials the plastically damaged zone is small as compared with the heterogeneity scale (grain size)[116].

Recently, Ponson *et al.* have analysed fracture surfaces with a 2D height-height correlation function [114]

$$\Delta h(\Delta x, \Delta y) = \left\langle (z(x + \Delta x, y + \Delta y) - z(x, y))^2 \right\rangle^{1/2} \quad (4.13)$$

for several materials (either brittle, ductile or quasi-ductile) and crack velocities. This function has been measured on samples in which the fracture propagation direction was well controlled. If  $x$  is the direction of the crack propagation and  $y$  the direction parallel

to the crack front, the authors measured two different Hurst exponents in these two directions, *i.e.*,

$$\Delta h(\Delta x, 0) \propto \Delta x^\beta \quad (4.14)$$

$$\Delta h(0, \Delta y) \propto \Delta y^\zeta \quad (4.15)$$

with  $\beta \simeq 0.6$  and  $\zeta \simeq 0.75$ . Moreover, the transition between these two behaviours occurs for

$$\Delta y \propto \Delta x^{1/u} \quad u = \frac{\zeta}{\beta} \quad (4.16)$$

See references [114, 117] for more details. This scaling behaviour corresponds to a class of phenomena called the Family-Vicsek scaling [118]. It is observed in several models, in particular the propagation of an elastic line in a random media [111].

The exponent  $\zeta$  describes the geometry of the crack perpendicular to the propagation direction and therefore gives an information on the static geometrical properties of the crack. The exponent  $u$  describes how the influence of a given point propagates with the fracture evolution. Finally, the morphology of the crack in the propagation direction results from the two previous exponents  $\beta = \zeta/u$  [117]. Naturally, if the isotropic height-height correlation function is considered (Eq. 4.11), the exponent  $H$  is retrieved [117].

Therefore, the 2D height-height correlation function (Eq. 4.13) provides an insight in the physics of fracture. Moreover, it can be used to determine the fracture propagation direction on post-mortem fracture surfaces and thus can have significant practical applications [117].



## **Part II**

### **The trunk**



# Chapter 5

## Experiment

### 5.1 A mushy zone traction test: the Pechiney's rig test

The present thesis has been preceded by a Master internship at the Alcan (formerly Pechiney) Voreppe Research Center (CRV) under the supervision of B. Commet. This work was focused on an intensive measurement campaign on a mushy zone traction test, the Pechiney's rig test [38]. This work was held in the frame of an European research program, the VIRCAST (Virtual Cast-house) project.

#### 5.1.1 Description of the apparatus

This machine has been designed by B. Magnin, B. Commet and J.-F. Bonello at Alcan CRV. It is inspired by an apparatus developed at the Aachen foundry institute by Ohm *et al.* [54, 119] (see Sec. 2.3.4).

The machine is based on a commercial Lloyd traction machine with a load cell of 30 kN. The cast-iron jaws of the machine are preheated to 200 °C and cooled down by a water circulation during the test. A consumable refractory mold is placed between the jaws of the machine (Fig. 5.2(a)) and is maintained by a slight compression force (-10N). This gives a dog-bone shape to the whole system. A cast-iron cooler is then placed on the mold to close the system (Fig. 5.2(b)). Tightness is ensured by refractory joints. Four type-K thermocouples (TC 1-4) measure the temperature in the sample (Fig. 5.1): they go 3 mm into the sample in order to limit their perturbation on the mechanics of the system. Two other thermocouples measure temperature in the jaws.

Liquid metal is poured into the feeding system with a dipper (Fig. 5.2(b)). A glass fiber sieve retains the oxide layer (Fig. 5.1). A hole in the feeding system allows to control the metallostatic head in the system, this hole is closed by a cap during mold filling (Fig. 5.2(b)). Liquid metal mainly solidifies on the upper chill and forms a solid shell (phase 1). When a sufficient solid shell has formed (as controlled by the temperature of TC1) the upper cooler is removed and heat is mainly extracted by the machine jaw (phase 2). When the temperature measured by TC 1 has reached a prescribed value, the traction automatically starts at a constant speed (phase 3) (Fig. 5.2(c)).

These three phases are reported on Fig. 5.3. In this picture, mold filling is observed by a sharp increase of temperature, similarly the removal of the chill is visible on both the thermal and mechanical curves (between phase 1 and 2). Note that during phases 1 and 2, the machine controls the force on the sample to -10 N in order to prevent the formation of damage before the traction.

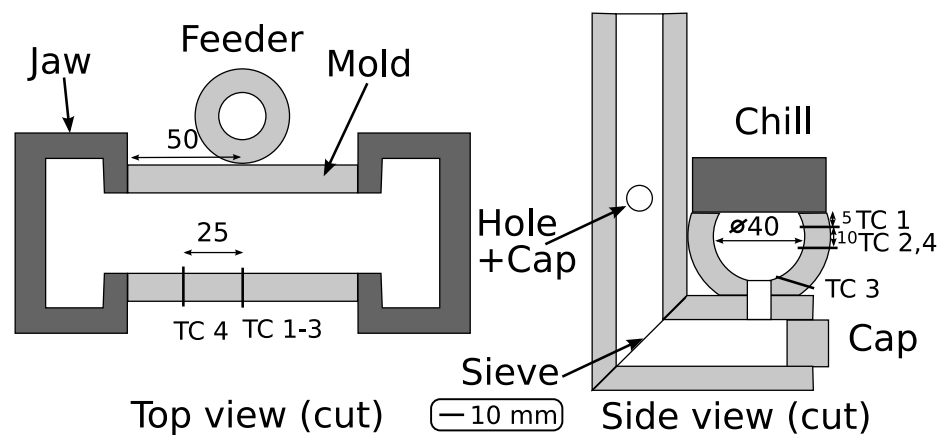


**Figure 5.1:** Schematic diagram of the hot-tearing test apparatus. The position of the 4 thermocouples is indicated by a black line and noted TC.



**Figure 5.2:** Pictures of the apparatus. (a) Mold before the experiment, (b) mold filling (phase 1), (c) traction (phase 3).

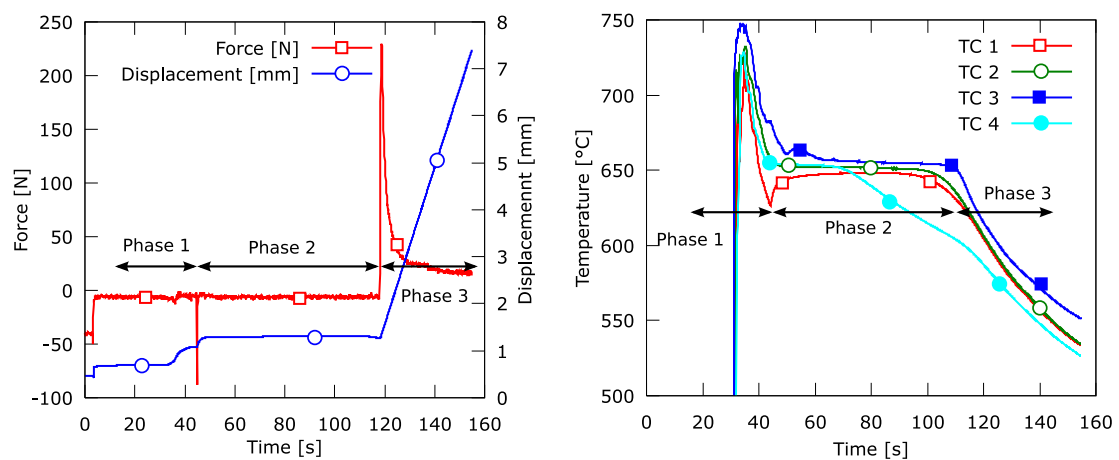


**Figure 5.3:** Thermal and mechanical curves as measured during a typical test.

This protocol has been conceived by Ohm *et al.* in order to reproduce the formation of an air gap after the primary cooling in DC casting [54, 119] (see Sec. 1.2).

The cross section of a test sample is around 10 cm<sup>2</sup>, and this value is used to estimate the stress in the sample. Moreover, the strains are supposed to be localized in the central part of the sample which is the hotter part during the traction. This zone has been first estimated by L. Maenner to be around 4 cm long [120]. These rough estimations have been recently validated by numerical simulations of the apparatus done by V. Mathier [18] and will be used hereafter. Yet, it should be pointed out that, at the end of solidification, deformation tend to localize in a smaller zone. Therefore, this simplified approach tend to slightly underestimate the local strains at high solid fractions [18].

Three imposed traction speeds have been used, 2.5 mm/min, 10 mm/min and 40 mm/min. They respectively correspond to estimated deformation rates of 10<sup>-3</sup>s<sup>-1</sup>, 4 × 10<sup>-3</sup> s<sup>-1</sup> and 1.6 × 10<sup>-2</sup> s<sup>-1</sup> which represents well the range of deformation rates that are encountered in DC casting [19].

Solid fraction is estimated by two methods. First, we use the Prophase software developed at Alcan CRV [121]. This software couples a micro-segregation calculation with thermodynamic data basis and therefore also allows to predict the formation of secondary phases. Second, we use a single pan thermal analysis in which the solid fraction is deduced from the cooling curve of the metal measured in an instrumented crucible (see [38]). This last method is directly done during the experiments and with the same metal.

### 5.1.2 The alloys

Three alloys were used, Al-2wt%Cu, Al-4wt%Cu, and a 5182 commercial alloy (Al-Mg). The Al-Cu alloys were produced from a commercial 1085 alloy (99.88% Al) with the addition of high purity cooper. All three alloys were inoculated by the addition of 2 Kg per ton of a AT5B master alloy (Al-5wt%Ti-1wt%B) and therefore presented a fine grain microstructure.

Al-Cu alloys are well studied alloys and present a pure eutectic diagram in the range of composition considered. Moreover, they are prone to hot cracking in particular at the two compositions considered here (see Sec. 2.1). Therefore, they represent an ideal system for our study. The 5182 alloy is a commercial alloy used for the end of beverage cans. The understanding of hot cracking in this alloy represents a significant industrial issue. In this experiment, as in all this thesis, we only consider a fine globular microstructure (induced by the heavy inoculation). These parameters were fixed in correlation with the work of other participants of the VIRCAST program, in particular the work of Ludwig *et al.* [37, 45].

### 5.1.3 Observation of the fracture profiles

First, the fracture profiles have been simply observed with the naked eye. A longitudinal cut has been done on some samples. This cut is normal to the fracture surface and situated on the vertical symmetry axis on the sample. This cut is polished down with a 1 μm diamond spray, then attacked with a Keller solution and observed with an optical microscope.

Fracture surfaces were directly observed in a scanning electron microscope (SEM) at Alcan CRV. Moreover, 3D reconstructions of the fracture surfaces have been done by

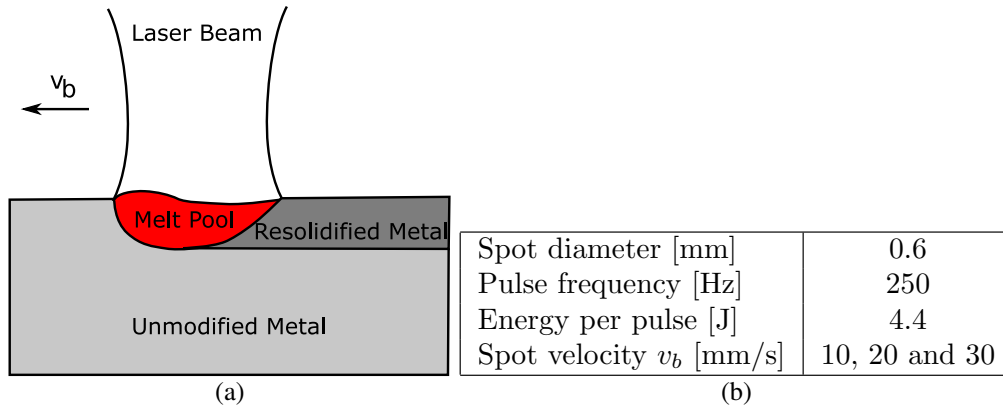


**Figure 5.4:** (a) Schematic of the apparatus [124]. (b) Selected laser parameters [10].

T. Meredith during her student work in the laboratory [122]. In this technique, two SEM pictures of the sample are taken with a tilt angle of respectively  $-3^\circ$  and  $+3^\circ$ . This tilt angle corresponds to the natural tilt angle of human eyes and the superposition of these two images produces a stereographic image of the sample (just as in 3D movies) [122]. Moreover, we used the MeX software [123] which allows to reconstruct the 3D profile from the interpolation of these two images. Pictures were taken with a magnification of 30x (which is the lowest magnification of the SEM) and 50x.

## 5.2 Laser remelting experiments

It is possible to remelt a metal by an intense laser beam. The temperature gradients around the laser spot are very strong and thus solidification conditions are favourable to hot cracks formation. Moreover, such an experiment is quick and requires only small test samples. Therefore, it is a convenient method to assess hot cracking sensitivity. These remelting experiments were done by L. Germond during his student project at the LSMX [10].

### 5.2.1 Description of the apparatus

We have used a Nd:YAG laser whose wavelength is  $1.06 \mu\text{m}$  (near infrared). This laser is pulsed, *i.e.*, the energy is delivered by very brief and intense pulses. The pulses parameters are summarized on Fig. 5.4(b). They have been set up by J.-D. Wagnière in order to produce interesting re-solidification conditions. Indeed, if the energy absorbed by the material is too low no crack forms, but if this energy is too high the matter can be vaporized and form a plasma around the laser spot (Keyhole formation).

In order to have nice planar surfaces, the test samples were polished with a  $1 \mu\text{m}$  diamond spray. During the test, the laser beam had a fixed velocity  $v_b$  relatively to the sample (Fig. 5.4(a)). For each composition, three values of  $v_b$  were used : 10, 20 and 30 mm/s. Note that most of the laser energy is reflected by the sample. Therefore, the normal to the sample surface was tilted by  $8^\circ$  with respect to the beam in order not to redirect the reflected beam in the laser cavity.

### 5.2.2 The alloys

The alloy studied was an Al-4.26wt%Cu produced from a commercial 1085 alloy with the addition of high purity copper. The first two samples were respectively cast directly (non-grain refined) and with the adjunction of 1 kg per ton of an AT5B master alloy (grain refined). Two other samples have been cast in the same conditions but with the adjunction of 300 ppm Barium. These alloys were cast at ALCAN CRV during the Master thesis work of G. Chichignoud at INPG, in order to study the influence of barium, a tensio-active element, on the shape of eutectic films [125, 62] (see Sec. 2.3.5).

### 5.2.3 Observations

First, the samples have been directly observed with an optical microscope. Then, they have been polished with a 1  $\mu\text{m}$  diamond spray, attacked with a Keller solution, and re-polished in order to reveal the cracks. Finally, the polished samples have been observed in a SEM with a secondary electron detector.

Moreover, an Electron Back-Scattered Diffraction (EBSD) have been used to determine the grains' orientations [126]. In order to have a good signal with such a technique, the zone mechanically affected by the mechanical polishing is removed with an electrochemical polishing. This polishing is done with an A2 Struers electrolytic solution under a 30 V tension during 10 s.

### 5.2.4 Estimation of grain misorientation

The EBSD detector can deduce grain orientations from the diffraction pattern of a SEM electron beam. For a cubic lattice, the orientation of a grain is given by the three Euler angles  $(\varphi_1, \phi, \varphi_2)$  which define a rotation  $R$  from the reference frame  $(x_0, y_0, z_0)$  to a frame  $(x_1, y_1, z_1)$  aligned with the directions  $\langle 100 \rangle$  of the grain crystal lattice.

$$\begin{pmatrix} x_1 \\ y_1 \\ z_1 \end{pmatrix} = \begin{pmatrix} \cos \varphi_1 & -\sin \varphi_1 & 0 \\ \sin \varphi_1 & \cos \varphi_1 & 0 \\ 0 & 0 & 1 \end{pmatrix} \begin{pmatrix} 1 & 0 & 0 \\ 0 & \cos \phi & -\sin \phi \\ 0 & \sin \phi & \cos \phi \end{pmatrix} \begin{pmatrix} \cos \varphi_2 & -\sin \varphi_2 & 0 \\ \sin \varphi_2 & \cos \varphi_2 & 0 \\ 0 & 0 & 1 \end{pmatrix} \begin{pmatrix} x_0 \\ y_0 \\ z_0 \end{pmatrix} \quad (5.1)$$

Because of its symmetry the crystal lattice is invariant by a set of permutations  $P_i$ . Therefore, several rotations  $P_i R$  are possible. Note that these transformations can all be expressed as a single rotation with a given axis and a given angle  $\theta(P_i)$ . The Euler angles reported correspond to the rotation  $P_i R$  for which  $\theta(P_i)$  is minimum.

Similarly, if we consider two grains with the orientation given by the rotations  $R_1$  and  $R_2$ , several rotations can transform the frame of grain 1 to the frame of grain 2 :

$$D_{1,2}(P_i) = P_i R_2 R_1^t \quad (5.2)$$

where  $^t$  denotes the transposition. Once again, these transformations can be expressed as a single rotation with an angle  $\theta_{1,2}(P_i)$ . A scalar estimation of the misorientation between the two grains is thus given by the minimum value of  $\theta_{1,2}(P_i)$ .





## Chapter 6

# A solidification model for globular microstructures

In the present work, we aim at describing the mushy zone behavior with a granular model, *i.e.*, taking into account explicitly the behavior of each grain. Yet, this model must be simple at the scale of the grain in order to allow the computation of large mushy zones.

In standard solidification conditions, primary phase solidification forms dendrites (either columnar or equiaxed)[13]. Yet, in many industrial aluminium casting, particles of  $\text{TiB}_2$  or  $\text{TiC}$  are added to serve as heterogeneous nucleation sites and therefore to decrease the grain size (inoculation)[30]. In highly inoculated alloys, the grains do not have enough space to form dendrites and their shape is almost spherical, *i.e.*, globular grains. Inoculation is interesting for casting practice because it gives a more uniform product for further processing and reduces hot cracking sensitivity (see Sec. 2.1).

The shape of globular grains is simple. Moreover, their size is small as compared with the process scale and thus a representative elementary volume (REV) can be defined, which might not be the case for large dendritic grains. Therefore, globular microstructures are particularly well suited for a first granular model.

## 6.1 A model based on Voronoi diagrams

### 6.1.1 Derivation of the model

This two dimensional (2D) solidification model is based on the work of Mathier *et al.* [127, 60]. During the present thesis, the hypotheses of the model were further simplified in order to reduce computation time and thus to allow the computation of large mushy zones. This model has been published in Refs. [128, 129].

The model assumes simultaneous nucleation of grains in a plane with a given density of random sites. This hypothesis will be justified in Sec. 6.2.2. Further assuming that the temperature difference across the average grain size is small with respect to the undercooling (*i.e.*, small thermal gradient), the growth conditions of two neighboring grains are almost identical. Therefore, at the end of solidification each grain will occupy the space which is closer to its nucleus than to any other nuclei [130].

Given a set of points, we can associate to each point the space that is closer to that point than to any other point. This construction creates a tessellation of the space, which

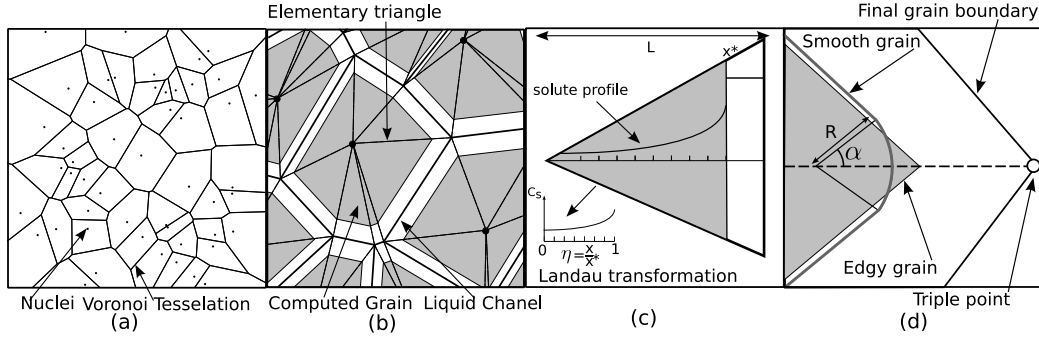


**Figure 6.1:** Various enlargements of the granular model: Voronoi tessellation associated with the nuclei centers (a); shape of the grains during solidification (b); solute balance within one triangle (c); smoothing procedure of the solid-liquid interface near the grain corners (d).

is referred to as the Voronoi tessellation [131]. The final grain structure is thus close to the Voronoi tessellation of the set of nuclei (Fig. 6.1, (a)). In the present work, this tessellation is computed using the free access software *qhull* [132].

In order to further simplify the solidification model, the solute flux between elementary triangles is neglected in a first step. Thus, the smooth interface of each grain during growth can be approximated by a linear segment in each triangle connecting the nucleation center with a Voronoi segment. By construction, these segments are perpendicular to the vectors connecting the nucleation centers and the two triangles issued from the same Voronoi segment are symmetrical, (Fig. 6.1, (b)).

Solidification is therefore reduced to a one-dimensional problem in each triangle, with the assumption of complete mixing of solute in the liquid phase and back-diffusion in the solid. A solute balance integrated over the liquid phase of an elementary triangle gives

$$x^* D_s \frac{\partial c_s^*}{\partial x}(x^*) + v^* x^* (k - 1) c_l + \frac{1}{2} (L^2 - x^{*2}) \frac{\partial c_l}{\partial t} = 0 \quad (6.1)$$

where  $x^*$  and  $v^*$  are the position and speed of the interface, respectively,  $c_s$  and  $c_l$  the solute concentration in the solid and liquid phase,  $c_s^*$  the solute concentration in the solid at the interface,  $k$  the partition coefficient,  $t$  the time,  $D_s$  the diffusion coefficient in the solid,  $L$  the height of the elementary triangle perpendicular to the Voronoi segment and  $x$  the coordinate along this direction (Fig. 6.1, (c)).

For a given temperature, concentrations at the solid-liquid interface are imposed by the phase diagram. Thus, as we assume complete mixing in the liquid, the phase diagram imposes the whole liquid concentration  $c_l$ . We can thus write

$$\frac{\partial c_l}{\partial t} = \frac{\partial c_l}{\partial T} \frac{\partial T}{\partial t} = \frac{\dot{T}}{m} \quad (6.2)$$

where  $m$  is the liquidus slope, and  $\dot{T}$  the local cooling rate. Thus, Eq. 6.1 becomes:

$$x^* D_s \frac{\partial c_s^*}{\partial x}(x^*) + v^* x^* (k - 1) c_l + \frac{1}{2} (L^2 - x^{*2}) \frac{\dot{T}}{m} = 0 \quad (6.3)$$

In the present work, we consider that the cooling rate  $\dot{T}$  is imposed and constant. A constant enthalpy rate condition, which takes into account the latent heat released by

solidification, can also be implemented [84, 60]. This last condition leads to more realistic temperature evolutions but requires to couple Eq. 6.1 with an energy balance. In the present model we look for a very efficient scheme and moreover we are interested in the last stages of solidification during which the cooling rate is in any case almost constant.

The first term in Eq. 6.3 associated with back-diffusion in the solid is computed by solving the cylindrical diffusion equation in the solid phase, which can be viewed as the solute balance between slices of the elementary triangle for constant  $x$ :

$$\frac{\partial c_s}{\partial t} = D_s \left( \frac{\partial^2 c_s}{\partial x^2} + \frac{1}{x} \frac{\partial c_s}{\partial x} \right) \quad (6.4)$$

In order to easily account for solidification, we use a Landau transformation of the solid domain  $[0, x^*(t)]$  into the reference 1D domain  $[0, 1]$ , as introduced by Voller and Sundarraj [133]:

$$c_s(x, t) \rightarrow c_s(\eta, t) \quad \eta = \frac{x}{x^*} \quad (6.5)$$

Eq. 6.4 becomes:

$$\left( \frac{\partial c_s}{\partial t} \right)_\eta = \frac{D_s}{x^{*2}} \frac{\partial^2 c_s}{\partial \eta^2} + \left( \frac{\eta v^*}{x^*} + \frac{D_s}{\eta x^{*2}} \right) \frac{\partial c_s}{\partial \eta} \quad (6.6)$$

where the term  $\eta v^*/x^*$  accounts for the advection of the mesh with the solidification front.

This equation is solved using a finite difference scheme, with a nil flux condition for  $\eta = 0$  and an imposed concentration  $c_s^* = kc_l$  for  $\eta = 1$ . Knowing the flux associated with back-diffusion and the concentration evolution in the liquid, the second term of Eq. 6.3 allows to deduce the velocity of the interface,  $v^*$ , and thus to find the new position  $x^*(t + dt)$ . This back-diffusion model is similar to that of Ohnaka [134].

Note that solidification does not depend on the opening of the elementary triangles but only on its height  $L$ , *i.e.*, on the half-distance between two nucleation centers.

## 6.1.2 A model for coalescence

When two flat interfaces get very close to each other, the coalescence undercooling introduced by Rappaz *et al.* [33] (see Sec. 2.3.5) is considered in the calculations in a way similar to Mathier *et al.* [60]:

$$\Delta T_{coal} = \frac{\gamma_{gb} - 2\gamma_{sl}}{\Delta S_f \delta} \quad \text{if } \gamma_{gb} > 2\gamma_{sl} \quad (6.7)$$

where  $\gamma_{gb}$  is the grain boundary energy,  $\gamma_{sl}$  is the solid-liquid interfacial energy,  $\Delta S_f$  is the volumetric entropy of fusion and  $\delta$  is the thickness of the diffuse solid-liquid interface.

The crystal lattice orientation of a grain  $I$  is chosen at random and is defined by a single angle  $\theta_I$  in 2D. The grain boundary energy is calculated for each boundary  $IJ$  of the Voronoi tessellation, assuming a simplified Read-Shockley distribution (see Sec. 2.3.5 Fig. 2.21(b))[61] in which the initial sinus variation is replaced by a linear variation.

$$\gamma_{gb,IJ} = \frac{|\theta_I - \theta_J|}{20^\circ} \gamma_{gb,max} \quad 0^\circ < |\theta_I - \theta_J| < 20^\circ \quad (6.8)$$

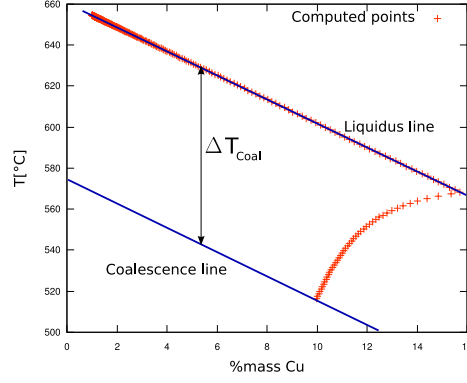


**Figure 6.2:** Evolution of the liquid concentration as a function of temperature in a binary Al-Cu alloy. In the first stage of solidification, liquid concentration is imposed by the phase diagram. When the liquid film thickness is of the order of  $\delta$ , the coalescence effect is felt. Back diffusion progressively reduces the film concentration. Solidification ends when the coalescence line is reached.

$$\gamma_{gb,IJ} = \gamma_{gb,max} \quad 20^\circ < |\theta_I - \theta_J| < 45^\circ \quad (6.9)$$

where  $\gamma_{gb,max}$  is the grain boundary energy of a fully disordered boundary. Note that  $0^\circ < |\theta_I - \theta_J| < 45^\circ$  for a cubic symmetry.

For an alloy Rappaz *et al.* have shown that coalescence occurs when a coalescence line (surface) is reached (see Fig. 6.2) [33]. This coalescence surface or line is parallel to the liquidus but  $\Delta T_{coal}$  below. Due to back-diffusion during the last stage solidification, the concentration of the last liquid film decreases as shown in Fig. 6.2

Coalescence effects are felt when the liquid film thickness is on the order of the diffuse solid-liquid interface thickness ( $\delta \sim 1 - 3$  nm). It is extremely computation intensive to compute the evolution of the interface at the nanometer scale while computing the diffusion equation (Eq. 6.4) at the scale of the microstructure [60]. Moreover, the solute rejected by the solidification of such a thin film is clearly negligible.

Therefore, when the solid-liquid interfaces of two neighbouring grains are closer than  $\delta$ , the exact position of the interface is no longer computed. Back diffusion in the solid fixes the concentration of the thin remaining liquid film and when the liquid composition reaches the coalescence line (for the prescribed temperature), the grain boundary is considered to be dry or solid (see Fig. 6.2).

## 6.2 A model for grain corners

### 6.2.1 Derivation of the model

Although the previous model predicts fairly well the evolutions of the grains, of the solid-liquid interface and of the solid fraction (see section 6.2.2), it leads to polyhedral grains (Fig. 6.1, (d)). This situation is clearly unrealistic as sharp corners are normally remelted by surface tension in non-faceted crystals. Furthermore, no liquid pocket can form at the triple junctions of the grains. As a consequence, this model overestimates the volume fraction of solid at which contact between grains occurs, as compared with experiments [128, 35].

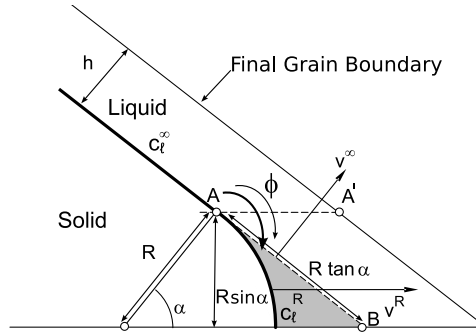


**Figure 6.3:** Schematics of the solute flux model which accounts for the Gibbs-Thomson effect near a grain corner.

In order to remove these limitations, the Gibbs-Thomson effect at grain corners has to be considered. Assuming again that temperature is homogeneous at the scale of a grain, the liquid concentration at an interface with a local radius of curvature  $R$  is given by

$$c_l^R = c_l^\infty + \frac{\Gamma_{sl}}{Rm} \quad (6.10)$$

where  $c_l^\infty$  is the liquid solute concentration for a flat interface and  $\Gamma_{sl}$  is the Gibbs-Thomson coefficient. (Note that, in general, the liquidus slope  $m$  is negative). If solidification were arrested, solute would flow from low curvature areas to high curvature areas, as for coarsening, thus remelting the highly curved zones. Yet, globular grains are not spherical during solidification and another phenomenon should balance the Gibbs-Thomson effect.

Therefore, the idealized situation represented in Fig. 6.3 is considered for smoothing the shape of polyhedral grains based on the Gibbs-Thomson effect. The grain corner is modelled by a curved interface with a constant radius of curvature  $R$ , whereas elsewhere the interface is supposed flat and parallel to the final grain boundary. Moreover, the liquid is divided into two zones, delimited by the dotted line  $AA'$  in Fig. 6.3. This line passes through the point separating the flat and circular portions of the solid-liquid interface (point labelled  $A$  in Fig. 6.3). Close to the corner, the liquid has a concentration equal to  $c_l^R$ , whereas in the second zone, surrounding the planar interface, a homogeneous concentration equal to  $c_l^\infty$  is considered.

The gradient of solute around the corner can be estimated by  $(c_l^R - c_l^\infty)/(R \sin \alpha)$  where  $R \sin \alpha$  is the distance between the tips of the corner and limit of the two zones. Moreover, we consider that the flux of solute is effective over a length of the order of  $R \sin \alpha$ . This leads to an estimation of the overall flux flowing from the zone surrounding the flat interface to the zone surrounding the corner:

$$\Phi \sim D_l(c_l^\infty - c_l^R) = -\frac{D_l \Gamma_{sl}}{mR} > 0 \quad (6.11)$$

We further look for a radius of curvature that is stable with time, *i.e.*,  $\dot{R} = 0$ . This implies that the limit between the curved and planar interfaces stays along the dotted line  $AA'$  in Fig 6.3. Once this constraint is fixed, it can be shown that the rejection of solute associated with a flat interface moving at a velocity  $v^\infty$  is equal to that rejected by the projection of the curved interface moving at a velocity  $v^R$ . Indeed, the projection of

the curved interface is given by  $R \sin \alpha$ , whereas the velocity is given by  $v^R = v^\infty / \cos \alpha$ . So one has:

$$v^\infty R \tan \alpha = R \sin \alpha v^R = R \sin \alpha \frac{v^\infty}{\cos \alpha} \quad (6.12)$$

where  $R \tan \alpha$  is the length of the extended flat interface (dotted line AB in Fig. 6.3). However, the grey surface is an additional volume of liquid, compared to the flat interface, and represents the advantage of the corner for solute diffusion. In other words, the small incoming flux of solute contributes to increasing the concentration of the liquid in the area,  $S$ , of the grey zone. A more rigorous development, based on solute balances, is given in App. B. But in summary, one has:

$$\Phi = \frac{dc_l^R}{dt} S = \frac{dc_l^\infty}{dt} S = \frac{\dot{T}}{m} S = \frac{\dot{T}}{m} \frac{R^2}{2} (\tan \alpha - \alpha) \quad (6.13)$$

Combining Eq. 6.11 and 6.13, one finally gets:

$$R^3 = A_C \frac{2}{\tan \alpha - \alpha} \frac{\Gamma_{sl} D_l}{-\dot{T}} \quad (6.14)$$

where  $A_C$  is a dimensionless constant, arising from the simple description of the solute distribution (see Eq. 6.11). Nonetheless, simply setting its value to 1 produces satisfying results and this value will be used hereafter.

It is interesting to note at this stage that Eq. 6.14 is close to a coarsening law: the radius of curvature of a grain corner is proportional to the third power of a driving force given by  $\frac{\Gamma_{sl} D_l}{\Delta T_o}$ , where  $\Delta T_o$  is the solidification interval of the alloy, and to the third power of the solidification time,  $t_f$ . The geometrical factor in front of this term is such that the radius of curvature becomes infinite when  $\alpha$  is equal to 0 (the grain corner is flat) and nil when  $\alpha$  is equal to  $\pi/2$  (the grain has disappeared).

Using this relationship for the radius of curvature of the grain corners, the shape of the solid-liquid interface can be computed as follows.

- The position of the flat interface or solid fraction is computed for each elementary triangle using the back-diffusion model described in Sec. 6.1
- The radius of curvature at each grain corner is computed using Eq. 6.14. Please note that, for a fixed cooling rate, the radius is constant and can be computed only once before the time stepping procedure.
- The interface in each elementary triangle is approximated by a flat portion and two rounded corners. If the length of the flat interface becomes negative, the interface is approximated by an arc of a circle.
- Rounded interfaces increase the overall volume of liquid by creating liquid pockets at grain corners. The position of the flat interface is then moved slightly forward in order to conserve the solid fraction computed with the flat interface method (see Fig. 6.1 (d)).

## 6.2.2 Validity and limits of the model

The predictions of the present model have been compared with those obtained with a pseudo front tracking method (PFT) [15]. In this technique, the fraction of solid within

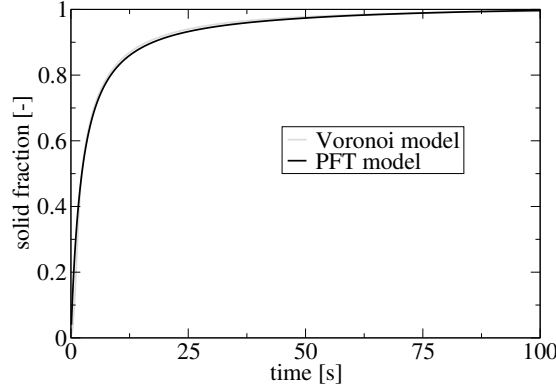


**Figure 6.4:** Solid fraction as a function of time computed with the Voronoi and the PFT methods

each cell of a hexagonal network is computed based on an explicit solute diffusion calculation. A layer of cells always separates the solid and liquid phases and the solute flux balance for such cells is converted into a solid fraction evolution. The position of the interface within these interfacial cells is computed using a piece-wise linear interface calculation (PLIC) algorithm [135]. Once the interface position within each interfacial cell is known, its curvature and the associated Gibbs-Thomson effect are calculated using a distance-field method similar to level-set. This method leads to predictions close to the phase field method as shown in more details in Ref. [15].

The same simulations have been carried out with the PFT and the Voronoi methods. Six nuclei have been randomly placed in a  $4.5 \times 10^{-2} \text{ mm}^2$  domain with periodic boundary conditions. The average grain size  $d_c$  is therefore around  $90 \text{ }\mu\text{m}$ . An Al-1wt%Cu has been considered with a linearised phase diagram ( $m = -6.67 \text{ K/wt\%}$  and  $k = 0.14$ ). The other parameters used in these calculations are:  $D_s = 1.5 \times 10^{-13} \text{ m}^2/\text{s}$ ,  $D_l = 10^{-9} \text{ m}^2/\text{s}$ ,  $\Gamma_{sl} = 5 \times 10^{-7} \text{ Km}$ ,  $\dot{T} = -1 \text{ K/s}$ .

Figure 6.4 shows the evolution of the solid fraction,  $g_s$ , computed with the two methods. Please keep in mind that, in the Voronoi method, the solid fraction calculated with rounded grains is equal to that obtained with polygonal grains. At the very beginning of solidification, grain growth predicted with the PFT method is slightly faster as the Voronoi method assumes complete mixing of solute in the liquid. As soon as a state of complete mixing is reached with the PFT method, the predictions of the two models are in very good agreement, even at high solid fraction. This shows that, despite the fairly strong assumptions of the (flat interface) Voronoi model, solute back-diffusion is well approximated.

In order to compare in more details the shape of the interfaces predicted by the two methods, the normalized specific solid liquid interface,  $S_s^\circ$ , is represented in Fig 6.5 as a function of  $g_s$ . This dimensionless number corresponds to the total length of the solid-liquid interface of the grains divided by the number of grains and by the average final grain size  $d_c$ . This important parameter strongly influences the permeability of the grain assembly via the Carman-Kozeny relationship (see Sec. 3.2.3). In Sec. 9.1 this parameter is used as an indicator of the morphological transitions of the mushy zone [136]. As solid grains grow, the length of the solid liquid interface increases as  $\sqrt{g_s}$  in 2D until impingement/contact of the solid grains makes it go to zero. Thus,  $S_s^\circ$  is maximum when the new contacts between the grains counterbalance the natural

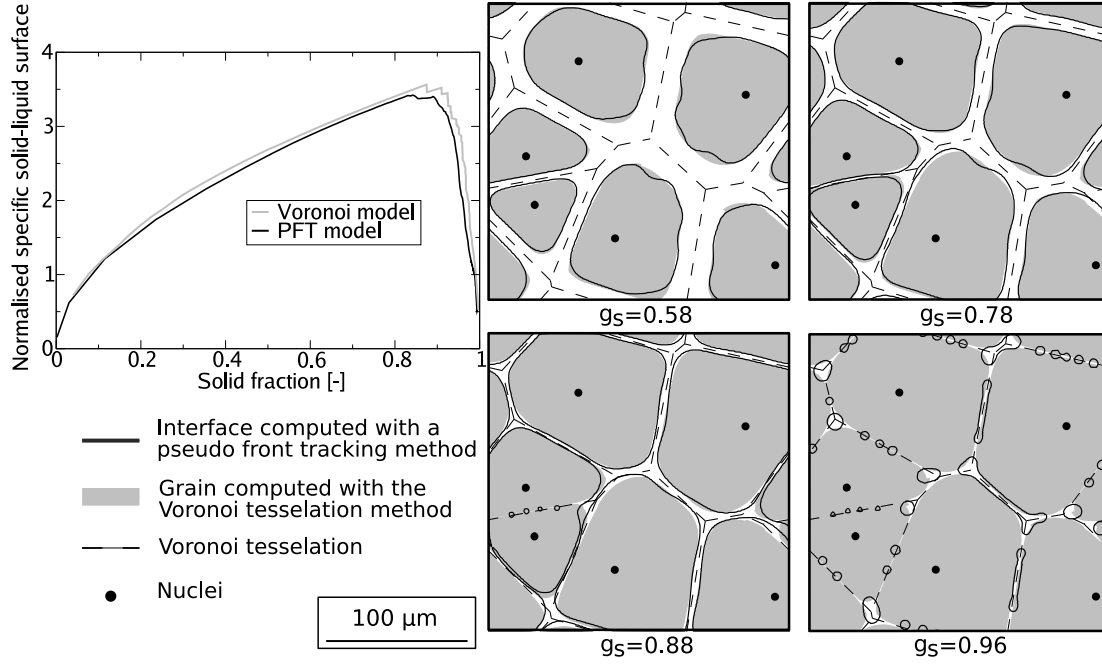


**Figure 6.5:** Comparison of the solid liquid interface shape predicted by the Voronoi and the PFT methods at various solid fractions.

increase of the interface length.

As can be seen on the left of Fig. 6.5, the overall shapes of  $S_s^\circ(g_s)$  are in excellent agreement, but the Voronoi method slightly overestimates this parameter, thus revealing that grains are still slightly less rounded than those calculated with the PFT method. It should be specified that, under these conditions, the grains are clearly globular without significant destabilization of the interface. Formation of dendritic or globular dendritic grains would definitely increase the length of the solid-liquid interface, thus making  $S_{s,PFT}^\circ > S_{s,Vor}^\circ$ .

The grain shapes predicted by the two models at various solid fractions are also represented in Fig. 6.5. For visualization purpose, the grains computed by the Voronoi method are represented in grey, whereas the interfaces predicted by the PFT method are represented with black lines. Again, a fairly good agreement between the two simulations, especially near the grain corners, can be seen. Please note that interfaces predicted with the Voronoi model are not necessarily continuous as solidification is computed separately for each elementary triangle. Yet, these slight discontinuities do not affect much the topology of the liquid channel network, nor the estimation of the channels permeability and mushy zone topology.

The maximum of  $S_s^\circ$  is predicted to occur at  $g_s = 0.86$  by the PFT model, while it is delayed to  $g_s = 0.89$  with the Voronoi model. This difference can be easily understood by looking at the shape of the grains at  $g_s = 0.88$ . With the PFT model, the liquid film in between two close neighboring grains can break down into small droplets by coalescence, whereas with the Voronoi model it remains a film until final impingement. Such a liquid film instability occurs when the grain boundary energy is lower than twice the solid-liquid interfacial energy, *i.e.*, attractive boundaries, and the film thickness is on the order of the thickness of the diffuse solid-liquid interfaces [33]. Here, no grain boundary energy is considered in the PFT and Voronoi calculations, but the instability



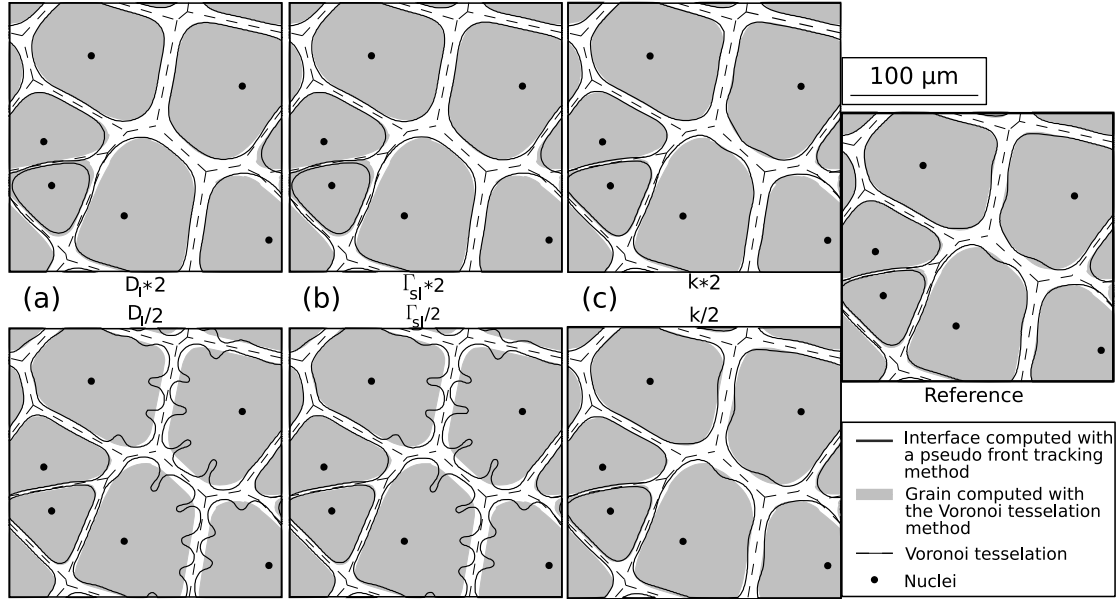


**Figure 6.6:** Comparison of grain shape at  $g_s=0.68$  for various sets of solidification parameters. Starting from the reference simulation (right figure), one parameter is changed at a time:  $D_l$  (a),  $\Gamma_{sl}$  (b) and  $k$  (c) are multiplied (top) or divided (bottom) by 2 with respect to the reference.

occurs too early with the PFT method as it is conditioned by the mesh size rather than the diffuse interface thickness. Note that the quantitative simulation of the coalescence phenomenon remains a challenging topic despite advances done in the thermodynamic framework [33] and in the modelling of triple phase boundaries [137].

Despite the numerical difficulties associated with simulation of the last stage solidification, the radii of curvature at grain corners calculated with Eq. 6.14 are close to those arising from the complex PFT calculation, even for relatively narrow channels. After breakdown of the liquid films, the sizes of the liquid pockets at triple junction points are also in fairly good agreement. Note that the isolated liquid pocket are represented nevertheless with a negative curvature in the Voronoi simulation. It is clear that the rounding procedure does not account for the coalescence phenomenon which transforms globally convex globular grains into convex liquid pockets. This simplified approach nevertheless allows to introduce realistic volumes of liquid at triple junctions, thus decreasing the volume fraction of solid at which the flat portions of the grain interfaces impinge.

Figure 6.6 shows the effect of various parameters on the shape of the solid liquid interfaces. It is convenient to introduce a dimensionless number,  $C$ :

$$C = \frac{1}{d_c} \left( \frac{\Gamma_{sl} D_l}{(-\dot{T})} \right)^{\frac{1}{3}} \quad (6.15)$$

This number is the ratio of a "typical" curvature radius at grains corner, *i.e.*, when  $(\tan \alpha - \alpha)^{-1} = 0.5$ , and the average grain size  $d_c$ . Figures 6.6 a) and b) show that a larger  $C$  number corresponds indeed to a larger radius of curvature at grains corners, regardless whether this is achieved by increasing  $D_l$  or  $\Gamma_{sl}$ . The agreement between the PFT and Voronoi predictions remains when the physical parameters are changed.

Yet, Fig. 6.6 also points out the limits of the present model, in particular at small  $C$  number. Indeed, the PFT predicts a destabilization of the globular grains into dendritic ones when  $C$  decreases. A criterion for the transition from globular to dendritic equiaxed grains has been recently proposed by Diepers *et al.* [138]. These authors found that it occurs when:

$$d_c^{GD} = A_{GD} \left( \frac{L}{k\Delta T_o c_p} \frac{\Gamma_{sl} D_l}{(-\dot{T})} \right)^{\frac{1}{3}} \quad (6.16)$$

where  $c_p$  and  $L$  are the volumetric specific heat and latent of fusion, respectively, and  $A_{GD}$  a dimensionless factor function of the anisotropy of the solid-liquid interfacial energy. Although this criterion has been derived for a sphere and a cooling rate imposed only at the boundaries of the system, it is interesting to note that the same power-law of the ratio  $\frac{D_l \Gamma_{sl}}{\dot{T}}$  is retrieved. The additional term,  $(L/(k\Delta T_o c_p))$ , comes from the solute undercooling ahead of the solidification front and from an overall thermal balance. The destabilisation of the interface occurs at the beginning of solidification when this undercooling is crucial, whereas the selection of the grains corner curvature occurs later in solidification when the solutal profile is flat. A change in the partition factor  $k$ , which does not affect the radius of curvature of the grains calculated with Eq. 6.14, nevertheless slightly influences the destabilization of the grains as predicted by Eq. 6.16 from the factor  $k\Delta T_o$  and as observed with the PFT method (Fig. 6.6 c).

For a high  $C$  number, another limitation of the model is encountered as illustrated by the solidification of the smallest grain in Figs. 6.6 a) b). The Voronoi model does not predict well the solidification of this grain at high  $C$  number. This is because the overall curvature of the grain is not accounted for in the Voronoi method. Yet, the curvature undercooling during growth of globulitic grains remains very small, typically 0.01 K for a spherical grain of 20  $\mu\text{m}$  radius. That of the last liquid droplets is slightly higher considering that the droplets are smaller and have a negative curvature, opposite to that considered here for the last liquid located at triple junctions. But in any case, curvature undercooling, despite its importance for coarsening and for the shape of the dendrite tip, is small in dendritic and globulitic solidification under normal conditions.

In order to use a Voronoi construction, *e.g.*, linear grain boundaries, to predict the final grain structures, two assumptions have been made: first, the temperature is uniform at the scale of the grains, and second, the nuclei all start at the same time. The first hypothesis is usually verified for globulitic structures, *e.g.*, grains of about 100  $\mu\text{m}$  growing in a thermal gradient lower than 1 K/cm. The temperature difference across a reference specimen containing 100 grains is just 1 K in this case. The second hypothesis clearly pertains to alloys which are inoculated. It has been shown in the case of Al-alloys inoculated with  $\text{TiB}_2$  particles that nucleation is athermal [139]. In athermal nucleation, the activation of a nucleant is a function of the undercooling only and not of time. In this case, the range of particle sizes which have been shown to be activated during solidification is typically 2-5  $\mu\text{m}$  in diameter [139]. Therefore, the maximum nucleation undercooling is about 0.2 K for a Gibbs-Thomson coefficient of  $10^{-7}$  Km. This value is small compared to the growth undercooling and thus an instantaneous nucleation assumption appears reasonable.

The most striking feature of the present Voronoi model is its low computation cost. The PFT simulations presented in Fig. 6.5 take around 12 Hours on a 2.8 GHz Pentium 4 personal computer, whereas the Voronoi calculations requires less than 2 s! This represents a gain of more than 4 orders of magnitude. This difference is even more

striking with large mushy zones. The computation of a whole mushy zone solidification that contains 14000 grains (see Sec. 9.1 Fig. 9.1) requires less than 10 seconds on the same computer.



## Chapter 7

### Mushy zone mechanics

Several models have been developed for the simulation of granular materials [140, 141, 142], these models being able to simulate the behavior of a large number of spherical grains, rigid [140, 141] or not [142]. Such methods are generally called Discrete Element Method (DEM). Yet, the interactions between the grains are due to solid-solid contacts and the influence of the surrounding media (air) is neglected. To model hot tearing, we not only need to consider solidification but also need to account for the influence of fluid flow on the mechanical behavior of the mushy zone.

Therefore, in this chapter we progressively build a granular model of mushy zone mechanics. We first suppose that the solid is fixed and derive a simple model for liquid feeding (Sec. 7.1). Then, this approximation is relaxed and grain movement is considered together with thermal shrinkage (Sec. 7.2).

#### 7.1 A model for feeding: the KPL model

In this section we derive a model for mushy zone liquid feeding. In the network of connected liquid films given by the solidification model of Chap. 6, a pressure drop calculation is performed assuming a Poiseuille flow in each channel, Kirchhoff's conservation of flow at nodal points and flow Losses compensating solidification shrinkage (KPL model).

##### 7.1.1 Derivation of the model

Since the densities of the solid  $\rho_s$  and of the liquid  $\rho_l$  are not equal, solidification induces shrinkage. In a first step, it is assumed that the solid remains fixed and that no pore forms. This means that solidification shrinkage should be fully compensated by liquid flow. The speed of the liquid  $\vec{v}_l$  at a solid-liquid interface is given by :

$$v_{l,n} = -\beta v^* \quad (7.1)$$

where  $\beta$  is the solidification shrinkage ( $\beta = \rho_s/\rho_l - 1$ ), and  $v^*$  is the speed of the (flat) solid-liquid interface. The normal  $\vec{n}$  to the interface along which  $\vec{v}_l$  is projected is pointing toward the liquid.

We note  $\Phi_{i \rightarrow j}(x)$  the fluid flow in the channel from vertex  $i$  to  $j$

$$\Phi_{i \rightarrow j}(x) = \int_{-h}^h \vec{v}_l(x, y) \cdot \vec{e}_x dy \quad (7.2)$$

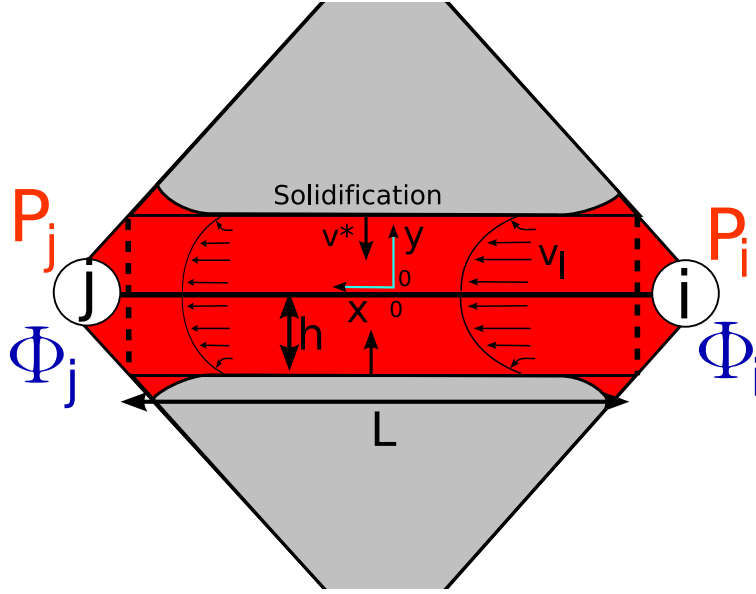


**Figure 7.1:** An elementary liquid channel.

where  $x$  is the coordinate along the channel length and  $y$  is the coordinate along the channel width, the origin of the reference frame being at the center of the channel (see Fig. 7.1).  $\vec{e}_x$  is the elementary vector in the  $x$  direction and  $h$  is the half channel width. For an incompressible flow, the mass balance can be simplified into a volume balance, *i.e.*,

$$\nabla \cdot \vec{v}_l = 0 \quad (7.3)$$

This balance integrated along a slice  $dx$  of the channel gives:

$$\frac{\partial \Phi_{i \rightarrow j}(x)}{\partial x} = -2\beta v^* \quad (7.4)$$

We assume that fluid flow can be modeled by a Poiseuille flow, *i.e.*, a viscous flow (no inertial term) with a no-slip condition at the solid liquid interface. This hypothesis is discussed in Sec. 7.2.2. The fluid velocity is thus linked to the pressure gradient by:

$$\frac{\partial p}{\partial x} = \mu \frac{\partial^2 v_x}{\partial y^2} \quad (7.5)$$

where  $\mu$  is the fluid viscosity and the subscript  $l$  for the fluid velocity is omitted when no confusion is possible. We consider that pressure is homogenous along the width of the channel (Poiseuille flow). The no-slip condition imposes that  $v_x(y = -h) = v_x(y = +h) = 0$ . Thus,

$$v_x = \frac{1}{2\mu} \frac{\partial p}{\partial x} (y^2 - h^2) \quad (7.6)$$

This equation can be integrated along the width of the channel to get the flux of liquid flowing through the channel.

$$\Phi_{i \rightarrow j}(x) = -\frac{2}{3\mu} \frac{\partial p}{\partial x} h^3 \quad (7.7)$$

Equations 7.4 and 7.7 give the master equation:

$$\boxed{\frac{h^3}{3\mu} \frac{\partial^2 p}{\partial x^2} = \beta v^*} \quad (7.8)$$

### 7.1.2 Numerical integration

A simple approach is to integrate Eq. 7.8 along the channel length to get

$$p(x) = \frac{3\mu\beta v^*}{2h^3} \left(x^2 - \left(\frac{L}{2}\right)^2\right) + \frac{P_j - P_i}{L}x + \frac{P_i + P_j}{2} \quad (7.9)$$

where  $L$  is the length of the channel,  $P_i$  and  $P_j$  are the pressures at nodes  $i$  and  $j$  respectively (see Fig. 7.1). Thus,

$$\Phi_{i \rightarrow j}(x) = -2\beta v^* x + \frac{2h^3}{3\mu L} (P_i - P_j) \quad (7.10)$$

We note  $\Phi_i$  the fluid flux entering in the channel at node  $i$ , *i.e.*,

$$\Phi_i = \Phi_{i \rightarrow j} \left(-\frac{L}{2}\right) = \frac{2h^3}{3\mu L} (P_i - P_j) + \beta v^* L \quad (7.11)$$

and

$$\Phi_j = -\Phi_{i \rightarrow j} \left(\frac{L}{2}\right) = \frac{2h^3}{3\mu L} (P_j - P_i) + \beta v^* L \quad (7.12)$$

Therefore, we can write the elementary matrix of the channel, which relates the pressure to the fluid flux at both end of the channel.

$$\boxed{\begin{pmatrix} \Phi_i \\ \Phi_j \end{pmatrix} = \overleftrightarrow{E}_p \begin{pmatrix} P_i \\ P_j \end{pmatrix} - \vec{b}_p} \quad (7.13)$$

with

$$\boxed{\overleftrightarrow{E}_p = \frac{2h^3}{3\mu L} \begin{pmatrix} 1 & -1 \\ -1 & 1 \end{pmatrix}, \quad \vec{b}_p = -\beta v^* L \begin{pmatrix} 1 \\ 1 \end{pmatrix}} \quad (7.14)$$

The matrix  $\overleftrightarrow{E}_p$  represents the hydrodynamic resistance of the channel, whereas the vector  $\vec{b}_p$  represents the flux losses due to solidification shrinkage.

It is interesting to note that this matricial problem can be equally obtain from Eq. 7.8 by a one-dimensional (1-D) Finite Element Method (FEM). We introduce the test function  $\psi_i(x)$  which is 1 at node  $i$ , 0 at node  $j$  and varies linearly along the channel.

$$\psi_i(x) = -\frac{x - \frac{1}{2}L}{L} \quad (7.15)$$

and

$$\psi_j(x) = \frac{x + \frac{1}{2}L}{L} \quad (7.16)$$

The pressure in the channel is approximated by

$$p(x) = P_i \psi_i(x) + P_j \psi_j(x) \quad (7.17)$$

We then use the Galerkin method [143], *i.e.*, we write the weak formulation of Eq. 7.8 for the test function  $\psi_i$ .

$$\int_{-L/2}^{L/2} \frac{2h^3}{3\mu} \frac{\partial^2 p}{\partial x^2} \psi_i(x) dx = \int_{-L/2}^{L/2} 2\beta v^* \psi_i(x) dx \quad (7.18)$$

An integration by part of the right hand side of this equation gives:

$$\left[ \frac{2h^3}{3\mu} \frac{\partial p}{\partial x} \psi_i(x) \right]_{-L/2}^{L/2} - \frac{2h^3}{3\mu} \int_{-L/2}^{L/2} \frac{\partial p}{\partial x} \frac{\partial \psi_i(x)}{\partial x} dx = \int_{-L/2}^{L/2} 2\beta v^* \psi_i(x) dx \quad (7.19)$$

Using the decomposition of Eq. 7.17 we have:

$$\int_{-L/2}^{L/2} \frac{\partial p}{\partial x} \frac{\partial \psi_i(x)}{\partial x} dx = P_i \int_{-L/2}^{L/2} \frac{\partial \psi_i(x)}{\partial x} \frac{\partial \psi_i(x)}{\partial x} dx + P_j \int_{-L/2}^{L/2} \frac{\partial \psi_j(x)}{\partial x} \frac{\partial \psi_i(x)}{\partial x} dx \quad (7.20)$$

Therefore, using Eq. 7.7 for the first term of Eq. 7.19, the integration of the test functions gives:

$$\phi_i - \frac{2h^3}{3\mu L} (P_i - P_j) = \beta v^* L \quad (7.21)$$

Similarly the weak formulation of Eq. 7.8 projected on  $\psi_j$  gives:

$$\phi_j - \frac{2h^3}{3\mu L} (P_j - P_i) = \beta v^* L \quad (7.22)$$

and we retrieve the equations system of Eq. 7.13.

The global problem can be constructed from the elementary problems if we consider the conservation of fluid flow at each node, *i.e.*, Kirchhoff's condition:

$$\forall i \sum_s \phi_i^s = -\phi_i^{ext} \quad (7.23)$$

where the superscript  $s$  denotes a channel linked to node  $i$  and  $\phi_i^{ext}$  represents the fluid flux flowing out node  $i$  due to boundary conditions (non zero only at the domain boundary if a natural condition is applied). The addition of the elementary problems therefore gives:

$$\boxed{\overleftrightarrow{E_p^{tot}} \overrightarrow{P^{tot}} = \overrightarrow{b_p^{tot}}} \quad (7.24)$$

where  $\overrightarrow{P^{tot}}$  is the unknown pressure vector in the whole mushy zone,  $\overleftrightarrow{E_p^{tot}}$  the sum of the elementary matrices, and the component  $i$  of vector  $\overrightarrow{b_p^{tot}}$  is

$$b_p^{tot}(i) = \sum_s -\beta v^{*s} L^s - \phi_i^{ext} \quad (7.25)$$

where the superscript  $s$  denotes the quantities in channel  $s$ . Note that the term  $b_p^{tot}(i)$  corresponds to the fluid losses associated either to solidification shrinkage or boundary conditions.

The problem of Eq. 7.24 can be solved by standard linear algebra method, *e.g.*, Gauss pivot.

As the relation between pressure drop and fluid flow is locally linear, the network of liquid channels is equivalent to an electrical resistance network. However, this network has flow losses corresponding to the shrinkage term, *i.e.*, the resistances are not well insulated from the board on which they are fixed.



## 7.2 Grain movement

### 7.2.1 Hypothesis and notations

In this section, solid grains movement is considered. For the sake of simplicity, we only consider translations and solid contraction of the grains. Indeed, the detection of contacts between polygonal grains is difficult if rotations are considered [140]. This hypothesis is strong but experimental study shows that at high solid fraction the main deformation mechanism is grain boundary sliding (see Sec. 2.3)[56].

Moreover, we suppose that the solid phase is perfectly rigid and therefore that all the deformation is concentrated in the liquid films. This hypothesis should be correct before the ductility minimum, on the descending branch of the ductility curve (see Sec. 2.3). Yet, after the coalescence transition, the mush deformation is dominated by solid plasticity, and thus the present assumption is not valid anymore. Nonetheless, it should be pointed out that natural hot cracking surfaces do not exhibit significant plastic deformation of the solid phase.

In summary, in the present section the hypotheses of the model are:

- The solid grains are perfectly rigid
- The solid grains do not rotate, *i.e.*, the interfaces of a liquid channel remain parallel
- The liquid is a Newtonian fluid
- No gaseous phase forms

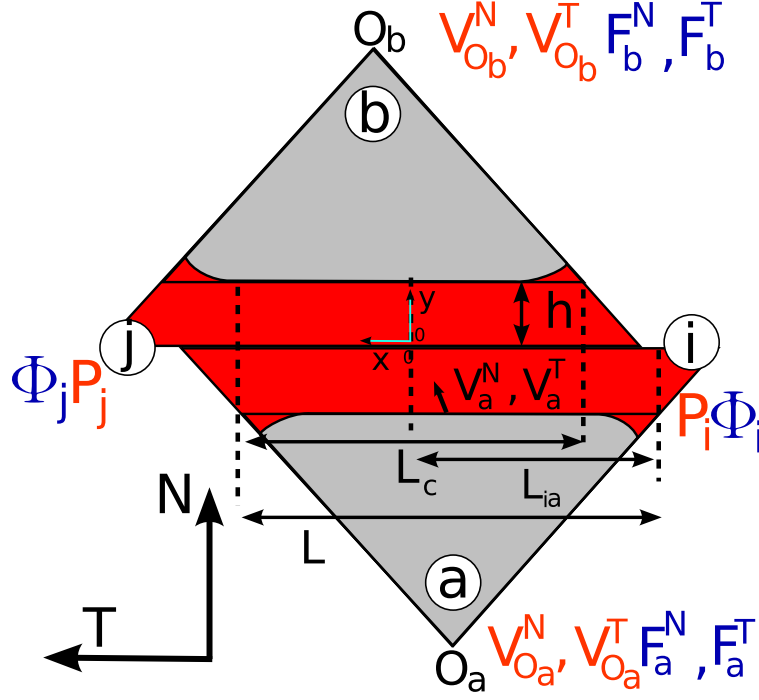
Under these assumptions, the behaviour of the whole mush is dictated by fluid displacement and therefore the model is based on the constitutive equations of an elementary liquid channel.

Figure 7.2 shows the various notations for an elementary liquid channel, as two grains can have a translation displacement with respect to each other, a mismatch between the extremities of the channel can exist. We note  $L$  the length of the solid-liquid interface for one grain,  $L_c$  the length of the channel for which the two grains effectively face each other and  $L_{ia}$  the length of the solid liquid interface from the centre of the channel to the extremity of grain  $a$  near the vertex  $j$ . Note that  $L_{ja} + L_{ia} = L$ .  $h$  is still the half width of the channel. Note also that even though the channel can be curved at its extremities, we model it with straight lines for the determination of the pressure field.

We note  $O_a$  the centre of grain  $a$ , and  $\vec{V}_{O_a}$  its speed (see Fig. 7.2). This last term is the main difference with Sec. 7.1, it adds to the solidification shrinkage to impose the fluid velocity at a solid-liquid interface. The average speed of the liquid at the interface with grain  $a$  is noted  $\vec{v}_l(y = h) = \vec{V}_a$ .

$$\vec{V}_a = \begin{pmatrix} V_{O_a}^T \\ V_{O_a}^N - \beta v^* \end{pmatrix} \quad (7.26)$$

where the normal elementary vector  $\vec{N}$  is directed from grain  $a$  to  $b$ , and the tangential vector  $\vec{T}$  is directed from vertex  $i$  to vertex  $j$  (see Fig. 7.2). Note that vector  $\vec{N}$  is different from vector  $\vec{n}$  which points from solid to liquid, indeed it is important to



**Figure 7.2:** An element of the mechanical model for rigid grains

project the grains velocities on the same vector in order to construct the elementary matrix (see below). Therefore, the liquid speed at grain  $b$  solid-liquid interface can be written:

$$\vec{V}_b = \begin{pmatrix} V_{O_b}^T \\ V_{O_b}^N + \beta v^* \end{pmatrix} \quad (7.27)$$

At the two extremities of the channel, the pressure  $p$  is imposed by the pressure of the integration node and is noted  $P_i$  at point  $i$ .

### 7.2.2 Dimensional analysis and simplification of the equations

In the KPL model, we have supposed that fluid flow can be modeled by a Poiseuille flow. Yet, this hypothesis (together with other implicit hypotheses, see below) can be clearly justified by a dimensional analysis.

Liquid metals can be considered as incompressible Newtonian fluids, therefore :

$$\rho_l \frac{dv_x}{dt} = -\frac{\partial p}{\partial x} + \mu \left( \frac{\partial^2 v_x}{\partial x^2} + \frac{\partial^2 v_x}{\partial y^2} \right) \quad (7.28)$$

We put this equation in dimensionless form using the following normalisation :

$$x^\circ = \frac{x}{L_c}, \quad y^\circ = \frac{y}{2h}, \quad v_x^\circ = \frac{v_x - V_a^T}{V^T}, \quad v_y^\circ = \frac{v_y - V_a^N}{V^N}, \quad t^\circ = \frac{tV^T}{L_c}, \quad P^\circ = \frac{P - P_i}{\Delta P_x} \quad (7.29)$$

where  $V^T = (V_b^T - V_a^T)$ ,  $V^N = (V_b^N - V_a^N)$  and  $\Delta P_x = (P_j - P_i)$ . We get the normalized equation

$$\frac{4h^2 \rho_l V^T}{\mu L_c} \frac{dv_x^\circ}{dt^\circ} = -\frac{4h^2 \Delta P_x}{\mu V^T L_c} \frac{\partial P^\circ}{\partial x^\circ} + \frac{4h^2}{L_c^2} \frac{\partial^2 v_x^\circ}{\partial x^{\circ 2}} + \frac{\partial^2 v_x^\circ}{\partial y^{\circ 2}} \quad (7.30)$$

This form is important as it shows the importance of each term in the equation.

The factor  $\frac{2h}{L_c}$  appears in several terms, it can be expressed as a function of the solid fraction  $g_s$ ,

$$\frac{2h}{L_c} = 2 \frac{H_{tot}}{L_{tot}} \left( \frac{1 - g_s^{1/2}}{g_s^{1/2}} \right) \quad (7.31)$$

where  $H_{tot}$  is the height of the elementary triangle, and  $L_{tot}$  the length of its base. Thus, for a regular hexagonal network of solid grains, we have

$$\frac{2h}{L_c} = \sqrt{3} \left( \frac{1 - g_s^{1/2}}{g_s^{1/2}} \right) \quad (7.32)$$

which is precisely the term introduced by Lahaie and Bouchard in their criterion (Sec. 3.1.3) [75]. We are interested in solid fractions  $g_s > 0.8$  and for  $g_s = 0.8$ ,  $(g_s^{-\frac{1}{2}} - 1) \sim (1 - g_s)/2 \sim 0.1$ .

We consider the typical values of the physical parameters in an inoculated Al-Cu alloy  $\rho_l \sim 2440 \text{ Kg m}^{-3}$ ,  $\mu \sim 1.5 \times 10^{-3} \text{ Pas}$ ,  $L_c \sim 10^{-4} \text{ m}$  [42]. Moreover, in a DC casting the typical strain rate is of the order of  $\dot{\epsilon} \sim 10^{-3} \text{ s}^{-1}$  [19] and thus  $V^T \sim L_c \dot{\epsilon} \sim 10^{-7} \text{ ms}^{-1}$ . Thus

$$\frac{4h^2 \rho_l V^T}{\mu L_c} \sim 10^{-6} \quad (7.33)$$

and the inertia term of Eq. 7.30 are definitely negligible. Similarly

$$\frac{4h^2}{L_c^2} \sim 10^{-2} \quad (7.34)$$

and we can reasonably neglect the term in  $\frac{\partial^2 v_x}{\partial x^2}$ . Thus, we get a simplified equation

$$\frac{\partial^2 v_x^\circ}{\partial y^{\circ 2}} = \frac{4h^2 \Delta P_x}{\mu V^T L_c} \frac{\partial P^\circ}{\partial x^\circ} \quad (7.35)$$

The same procedure on the equation for the y component of the fluid velocity gives

$$\frac{\partial^2 v_y^\circ}{\partial y^{\circ 2}} = \frac{2h \Delta P_y}{\mu V^N} \frac{\partial P^\circ}{\partial y^\circ} \quad (7.36)$$

We get an estimation of the pressure variation in the channel

$$\Delta P_x \sim \frac{\mu V^T L_c}{4h^2}, \quad \Delta P_y \sim \frac{\mu V^N}{2h} \quad (7.37)$$

and thus

$$\frac{\Delta P_y}{\Delta P_x} \sim \frac{2h}{L_c} \quad (7.38)$$

Thus, at first approximation, we can neglect the variation of pressure along the y axis with respect to the variation of pressure along the x axis. Therefore, even though fluid flow exists in the y direction due to solidification shrinkage or grain displacement, the Poiseuille equation gives a good approximation of the flow.

In the derivation of the model, we only consider the dissipation along the channels and neglect the dissipation at triple junctions. Indeed, the dissipation along the channels

is mainly due to viscosity (regular head losses), while the dissipation at triple junctions is due to the brutal direction change of the flow (singular head losses) and therefore is proportional to the kinetic energy of the flow [144]. Equation 7.33 shows that the ratio between kinetic energy and viscous dissipation (Reynolds number) is of the order of  $10^{-5}$  and therefore it is reasonable to neglect the dissipation at triple junctions.

When the channel width becomes of the order of a few nanometers, the Newtonian behavior of the liquid is to be questioned. Yet, Israelachvili has measured the apparent viscosity of Newtonian fluids in very thin films. He measured a good agreement between the apparent viscosity and the bulk viscosity for films larger than 5 nm [145, 146]. Another effect observed in thin films is a slipping at solid liquid interface which may be due to the formation of a nanometric air gap [147, 146]. This slipping occurs when the shear stress overpasses a critical value and might be an interesting phenomenon in hot tearing.

In the present model, we do not model the mechanical behavior of channels smaller than  $\delta$ , the coalescence interaction distance (Sec. 6.1.2) and consider that below this value such very thin channels are mechanically strong. This cut-off also allows to eliminate very large coefficients in the problem matrix and thus to ensure a better conditioning of the problem. For channels larger than  $\delta$ , we consider a pure Newtonian behavior of the fluid.

### 7.2.3 Integration of the constitutive equation

The constitutive equation integration is similar to the KPL model, the only difference being the boundary conditions at solid-liquid interfaces. We start from Eq. 7.35 in dimensional form

$$\frac{\partial p}{\partial x} = \mu \frac{\partial^2 v_x}{\partial y^2} \quad (7.39)$$

and the mass balance equation integrated as before over the width of the channel

$$\frac{\partial \Phi_{i \rightarrow j}}{\partial x} = -V^N \quad (7.40)$$

where  $\Phi_{i \rightarrow j}$  is the flux from vertex  $i$  to  $j$  at a given  $x$  and

$$\boxed{V^N = V_b^N - V_a^N} \quad (7.41)$$

represents the pump term in the channel. These equations can be integrated to give the speed of the fluid and its pressure

$$p(x) = \frac{3\mu V^N}{4h^3} \left( x^2 - \left( \frac{L_c}{2} \right)^2 \right) + \frac{P_j - P_i}{L_c} x + \frac{P_i + P_j}{2} \quad (7.42)$$

$$v_x(x, y) = \left( \frac{3V^N}{4h^3} x + \frac{P_j - P_i}{2\mu L_c} \right) (y^2 - h^2) + \frac{V_b^T - V_a^T}{2h} y + \frac{V_b^T + V_a^T}{2} \quad (7.43)$$

Equation 7.43 can then be integrated to give the liquid flux

$$\Phi_{i \rightarrow j}(x) = -V^N x + \frac{2h^3}{3\mu L_c} (P_i - P_j) + 2h \frac{V_b^T + V_a^T}{2} \quad (7.44)$$

The stress tensor in the liquid can be deduced from the pressure and velocity fields (see App. C) :

$$\overleftrightarrow{\sigma}(x, y) = \begin{pmatrix} -P & (\frac{3\mu V^N}{2h^3}x + \frac{P_j - P_i}{L_c})y + \mu \frac{V_b^T - V_a^T}{2h} \\ '' & -P \end{pmatrix} \quad (7.45)$$

and the force density on grain  $b$  can be written :

$$\vec{t}_b(x) = \overleftrightarrow{\sigma}(x, y = h) \vec{N} = \begin{pmatrix} (\frac{3\mu V^N}{2h^3}x + \frac{P_j - P_i}{L_c})h + \mu \frac{V_b^T - V_a^T}{2h} \\ -p(x) \end{pmatrix} \quad (7.46)$$

Equation 7.45 gives the stress tensor in the part of the channel where the two grains match. In the part where they do not match, we simply consider that we have a homogeneous pressure equal to the pressure of the integration point ( $P_i$  or  $P_j$ , see Fig. 7.2). Thus, we can integrate the force exerted by a grain on the liquid

$$\vec{F}_a = \begin{pmatrix} (P_j - P_i)h - \mu \frac{L_c}{2h} (V_b^T - V_a^T) \\ -\mu \left(\frac{L_c}{2h}\right)^3 V^N + P_i L_{ia} + P_j L_{ja} \end{pmatrix} \quad (7.47)$$

and

$$\vec{F}_b = \begin{pmatrix} (P_j - P_i)h + \mu \frac{L_c}{2h} (V_b^T - V_a^T) \\ \mu \left(\frac{L_c}{2h}\right)^3 V^N - P_i L_{ib} - P_j L_{jb} \end{pmatrix} \quad (7.48)$$

Similarly we can integrate the volume balance for an incompressible fluid flow (see App. C)

$$\nabla \cdot \vec{v}_l = 0 \quad (7.49)$$

This integration is made on the liquid channel with the fluid velocity imposed at the solid-liquid interface,  $(\vec{V}_a, \vec{V}_b)$ , and a pressure imposed at each vertex ( $P_i, P_j$ ). We get

$$\Phi_i = \frac{2h^3}{3\mu L_c} (P_i - P_j) + 2h \frac{V_b^T + V_a^T}{2} + L_{ib} V_b^N - L_{ia} V_a^N \quad (7.50)$$

and

$$\Phi_j = \frac{2h^3}{3\mu L_c} (P_j - P_i) - 2h \frac{V_b^T + V_a^T}{2} + L_{jb} V_b^N - L_{ja} V_a^N \quad (7.51)$$

where  $\Phi_i$  denotes the flux flowing from vertex  $i$  to the liquid channel.

Finally these equations can be written in a matrix, which will be the elementary matrix of our problem.

$$\begin{pmatrix} \Phi_i \\ \Phi_j \\ F_a^N \\ F_b^N \\ F_a^T \\ F_b^T \end{pmatrix} = \begin{pmatrix} +C_1 & -C_1 & -L_{ia} & +L_{ib} & +h & +h \\ -C_1 & +C_1 & -L_{ja} & +L_{jb} & -h & -h \\ +L_{ia} & +L_{ja} & +C_2 & -C_2 & 0 & 0 \\ -L_{ib} & -L_{jb} & -C_2 & +C_2 & 0 & 0 \\ -h & +h & 0 & 0 & +C_3 & -C_3 \\ -h & +h & 0 & 0 & -C_3 & +C_3 \end{pmatrix} \begin{pmatrix} P_i \\ P_j \\ V_a^N \\ V_b^N \\ V_a^T \\ V_b^T \end{pmatrix} \quad (7.52)$$

with

$$C_1 = \frac{2h^3}{3\mu L_c} \quad C_2 = \mu \left(\frac{L_c}{2h}\right)^3 \quad C_3 = \mu \frac{L_c}{2h} \quad (7.53)$$

We will note  $\vec{U}$  the unknown vector

$$\vec{U} = \begin{pmatrix} P_i \\ P_j \\ V_a^N \\ V_b^N \\ V_a^T \\ V_b^T \end{pmatrix} \quad (7.54)$$

Note that this elementary matrix  $\overleftrightarrow{E}$  can be expressed as the sum of a symmetric matrix  $\overleftrightarrow{S}$  and a antisymmetric matrix  $\overleftrightarrow{A}$ . With

$$\overleftrightarrow{S} = \begin{pmatrix} +C_1 & -C_1 & 0 & 0 & 0 & 0 \\ -C_1 & +C_1 & 0 & 0 & 0 & 0 \\ 0 & 0 & +C_2 & -C_2 & 0 & 0 \\ 0 & 0 & -C_2 & +C_2 & 0 & 0 \\ 0 & 0 & 0 & 0 & +C_3 & -C_3 \\ 0 & 0 & 0 & 0 & -C_3 & +C_3 \end{pmatrix} \quad (7.55)$$

and

$$\overleftrightarrow{A} = \begin{pmatrix} 0 & 0 & -L_{ia} & +L_{ib} & +h & +h \\ 0 & 0 & -L_{ja} & +L_{jb} & -h & -h \\ +L_{ia} & +L_{ja} & 0 & 0 & 0 & 0 \\ -L_{ib} & -L_{jb} & 0 & 0 & 0 & 0 \\ -h & +h & 0 & 0 & 0 & 0 \\ -h & +h & 0 & 0 & 0 & 0 \end{pmatrix} \quad (7.56)$$

Matrix  $\overleftrightarrow{S}$  corresponds to the decoupled part of the various phenomena whereas  $\overleftrightarrow{A}$  corresponds to the coupling between grain displacement and liquid pressure. Apparently, there are deep physical reasons for this decomposition, which are related to the different behaviours between vectorial and scalar quantities with respect to time reversal [148, 149]. It is interesting to note that we have found these relations by mere integration. Note that the matrix  $\overleftrightarrow{A}$  can be made symmetric by a modification of the orientations conventions. However, such a convention would lead to negative terms on the diagonal of the matrix. The matrix would loose its physical signification.

Indeed, it is interesting to note that the power dissipation is

$$\dot{W} = \vec{V}_b \cdot \vec{F}_b + \vec{V}_a \cdot \vec{F}_a + P_i \Phi_i + P_j \Phi_j \quad (7.57)$$

that is

$$\dot{W} = \frac{2h^3}{3\mu L_c} (P_i - P_j)^2 + \mu \left( \frac{L_c}{2h} \right)^3 (V_b^N - V_a^N)^2 + \mu \frac{L_c}{2h} (V_b^T - V_a^T)^2 \quad (7.58)$$

and

$$\dot{W} = \vec{U}^t \overleftrightarrow{E} \vec{U} \geq 0 \quad (7.59)$$

where the operator  $^t$  denotes the transposition of a vector. Thus, our elementary matrix is definitely positive and represents a quadratic form related to dissipation in the channel. Moreover if we decompose the elementary matrix  $\overleftrightarrow{E} = \overleftrightarrow{S} + \overleftrightarrow{A}$ , we have

$$\dot{W} = \vec{U}^t (\overleftrightarrow{S} + \overleftrightarrow{A}) \vec{U} = \vec{U}^t \overleftrightarrow{S} \vec{U} \quad (7.60)$$

and thus

$$\vec{U}' \overleftrightarrow{A} \vec{U} = 0 \quad (7.61)$$

For any set of unknowns,  $\overleftrightarrow{S}$ , the symmetric part of the matrix  $\overleftrightarrow{E}$  corresponds to the power dissipation, whereas  $\overleftrightarrow{A}$  is a coupling term that does not dissipate energy.

### 7.2.4 Implementation of volumetric shrinkage

We consider a shrinkage rate  $\alpha_s$  in the solid,  $\alpha_l$  in the liquid. And we note it  $\alpha$  when the considerations apply to both cases. We have in 2D :

$$\alpha = \frac{1}{S} \frac{\partial S}{\partial t} \quad (7.62)$$

where  $S$  is the surface of the domain considered. Yet, there can be different reasons for shrinkage, such as thermal shrinkage or solutal shrinkage. Thus

$$\alpha = \frac{1}{S} \left( \frac{\partial S}{\partial T} \frac{\partial T}{\partial t} + \frac{\partial S}{\partial c} \frac{\partial c}{\partial t} \right) \quad (7.63)$$

where  $c$  is the solute concentration and  $T$  the temperature.

$$\alpha = \beta_T \frac{\partial T}{\partial t} + \beta_c \frac{\partial c}{\partial t} \quad (7.64)$$

where  $\beta_T$  and  $\beta_c$  are the respective coefficients for thermal shrinkage and solutal shrinkage.  $\alpha$  can be related to the density variation.

$$\alpha = -\frac{1}{\rho} \frac{\partial \rho}{\partial t} \quad (7.65)$$

Thus, if we neglect the local variation of density in the flux term we have

$$\nabla \vec{v} = \alpha \quad (7.66)$$

where  $\vec{v}$  represents the velocity field in the material.

In the solid phase, we consider that  $\alpha_s$  is homogeneous and isotropic at the scale of a grain. Thus, the difference of speed between two points  $O$  and  $M$  of a given grain is in 2D:

$$\vec{v}_M - \vec{v}_O = \overrightarrow{OM} \frac{\alpha_s}{2} \quad (7.67)$$

Mathematically speaking this transformation is an homotetie of factor  $1 + \frac{\alpha_s}{2}$ .

Thus, the evolution of a grain is given by the translation of a given point  $O$  and by an homotetie of centre  $O$  and of factor  $1 + \frac{\alpha}{2}$ . Note that any point can be chosen as the centre of the homotetie, as two homoteties with the same factor but with a different centre are equivalent modulo a translation.

We note  $C_b$  the point at the centre of the channel on grain  $b$  see Fig. 7.3, and we consider a point  $M_b$  on the solid-liquid interface of grain  $b$ . The liquid velocity at this point of the interface is :

$$\vec{v}_l(M_b) = \vec{v}_{O_b} + \frac{\alpha_s}{2} \overrightarrow{O_b C_b} - \beta v^* \vec{N} + \frac{\alpha_s}{2} \overrightarrow{C_b M_b} \quad (7.68)$$

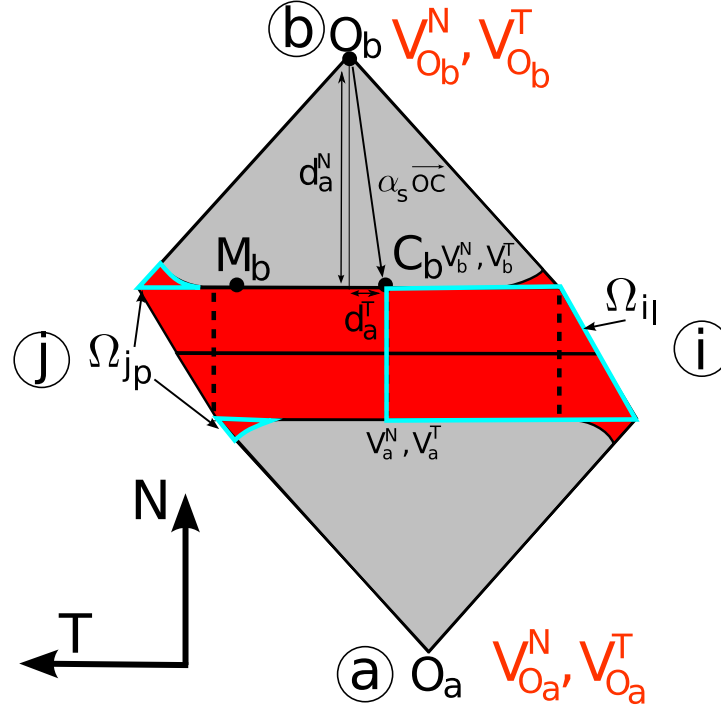


**Figure 7.3:** Notations for the implementation of volumetric shrinkage.

We note  $\vec{V}_b$  the terms that do not depend on the position in the channel.

$$\vec{V}_b = \vec{V}_{O_b} + \frac{\alpha_s}{2} \overrightarrow{O_b C_b} - \beta v^* \vec{N} \quad (7.69)$$

Thus

$$\vec{v}_l(M_b) = \vec{V}_b + \frac{\alpha_s}{2} \overrightarrow{C_b M_b} = \vec{V}_b + \frac{\alpha_s}{2} x \vec{T} \quad (7.70)$$

Similar expressions are obtained for  $\vec{v}_l(M_a)$  on the other interface. The constitutive equation of the flow is unchanged (Eq. 7.39)

$$\frac{\partial p}{\partial x} = \mu \frac{\partial^2 v_x}{\partial y^2} \quad (7.71)$$

This equation should be integrated with the boundary conditions of Eq. 7.70, *i.e.*,

$$v_x = \frac{1}{2\mu} \frac{\partial p}{\partial x} (y^2 - h^2) + \frac{V_b^T - V_a^T}{2h} y + \frac{V_b^T + V_a^T}{2} + \frac{\alpha_s}{2} x \quad (7.72)$$

Similarly, we have in the fluid

$$\nabla \vec{v} = \alpha_l \quad (7.73)$$

and therefore

$$\frac{\partial \Phi_{i \rightarrow j}(x)}{\partial x} - 2h\alpha_l + V_b^N - V_a^N = 0 \quad (7.74)$$

Finally, the pressure in the channel can be integrated from Eqs. 7.72 and Eq. 7.74.

$$p(x) = \frac{3\mu}{4h^3} (V_b^N - V_a^N - 2h\alpha_l + h\alpha_s) (x^2 - (\frac{L_c}{2})^2) + \frac{P_j - P_i}{L_c} x + \frac{P_i + P_j}{2} \quad (7.75)$$



Note that one term is added to the expression of the pressure due to shrinkage. This term also appears in the expression of the force on the grains.

$$\vec{F}_a = \begin{pmatrix} (P_j - P_i)h - \mu \frac{L_c}{2h} (V_b^T - V_a^T) \\ -\mu \left(\frac{L_c}{2h}\right)^3 (V_b^N - V_a^N - 2h\alpha_l + h\alpha_s) + P_i L_{ia} + P_j L_{ja} \end{pmatrix} \quad (7.76)$$

and

$$\vec{F}_b = \begin{pmatrix} (P_j - P_i)h + \mu \frac{L_c}{2h} (V_b^T - V_a^T) \\ \mu \left(\frac{L_c}{2h}\right)^3 (V_b^N - V_a^N - 2h\alpha_l + h\alpha_s) - P_i L_{ib} - P_j L_{jb} \end{pmatrix} \quad (7.77)$$

To understand the physical meaning of this term, one should keep in mind that the shrinkage of the solid grains in the normal direction is included in the velocity of the fluid at the interface  $(V_a^N, V_b^N)$ . Therefore, the term added by shrinkage in the expression of the force corresponds to the effect of shrinkage for fixed solid-liquid interfaces in the normal direction.

Thus if  $\alpha_s < 0$  and  $\alpha_l = 0$ , the solid contracts in the tangential direction. There is a relative outward flow of liquid, which induces a pressure increase at the centre of the channel. If  $\alpha_s = 2\alpha_l$ , the solid contracts twice as fast as the liquid in the tangential direction, but as the liquid also contracts in the normal direction there is no relative flow of matter.

Similarly, the fluid fluxes become :

$$\Phi_i = \frac{2h^3}{3\mu L_c} (P_i - P_j) + 2h \frac{V_b^T + V_a^T}{2} + L_{ib} V_b^N - L_{ia} V_a^N + (\alpha_s - \alpha_l) \Omega_{i_p} - \alpha_l \Omega_{i_l} \quad (7.78)$$

and

$$\Phi_j = \frac{2h^3}{3\mu L_c} (P_j - P_i) - 2h \frac{V_b^T + V_a^T}{2} + L_{jb} V_b^N - L_{ja} V_a^N + (\alpha_s - \alpha_l) \Omega_{j_p} - \alpha_l \Omega_{j_l} \quad (7.79)$$

where  $\Omega_{j_l}$  is the volume of fluid in the linear channel attributed to vertex  $j$  and  $\Omega_{j_p}$  is the volume of liquid attributed to vertex  $j$  entrapped in the polygonal envelope of the grains (see Fig. 7.3). This last term shows that if the liquid contracts more rapidly than the solid, liquid will be sucked in the envelope of the grains.

The modified equations can be introduced to form the new matricial problem,

$$\begin{pmatrix} \Phi_i \\ \Phi_j \\ F_a^N \\ F_b^N \\ F_a^T \\ F_b^T \end{pmatrix} = \overleftrightarrow{E} \begin{pmatrix} P_i \\ P_j \\ V_{O_a}^N + \frac{1}{2} \alpha_s d_a^N - \beta v^* \\ V_{O_b}^N - \frac{1}{2} \alpha_s d_b^N + \beta v^* \\ V_{O_a}^T + \frac{1}{2} \alpha_s d_a^T \\ V_{O_b}^T + \frac{1}{2} \alpha_s d_b^T \end{pmatrix} = \begin{pmatrix} (\alpha_l - \alpha_s) \Omega_{i_p} + \alpha_l \Omega'_{i_l} \\ (\alpha_l - \alpha_s) \Omega_{j_p} + \alpha_l \Omega'_{j_l} \\ C_2(-2h\alpha_l + h\alpha_s) \\ -C_2(-2h\alpha_l + h\alpha_s) \\ 0 \\ 0 \end{pmatrix} \quad (7.80)$$

where

$$d_a^N = \overrightarrow{O_a C_a} \cdot \vec{N} > 0, \quad d_a^T = \overrightarrow{O_a C_a} \cdot \vec{T}, \quad d_b^N = -\overrightarrow{O_b C_b} \cdot \vec{N} > 0, \quad d_b^T = \overrightarrow{O_b C_b} \cdot \vec{T} \quad (7.81)$$

and  $\overleftrightarrow{E}$  is the elementary matrix (Eq. 7.52). Note that the term  $d_a^N$  represents the distance between the interface and the centre of the cluster in the normal direction. Therefore, this term will become more and more important with the increase of the average cluster size.

We keep as unknowns the speed of the grains centre and put all the terms induced by shrinkage in the second member.

$$\begin{pmatrix} \Phi_i \\ \Phi_j \\ F_a^N \\ F_b^N \\ F_a^T \\ F_b^T \end{pmatrix} = \overleftrightarrow{E} \begin{pmatrix} P_i \\ P_j \\ V_{O_a}^N \\ V_{O_b}^N \\ V_{O_a}^T \\ V_{O_b}^T \end{pmatrix} = \overrightarrow{b} \quad (7.82)$$

with

$$\overrightarrow{b} = \begin{pmatrix} (\alpha_l - \alpha_s)\Omega_{i_p} + \alpha_l\Omega_{i_l} + L_{ia}(\frac{1}{2}\alpha_s d_a^N - \beta v^*) + L_{ib}(\frac{1}{2}\alpha_s d_b^N - \beta v^*) - h\alpha_s \frac{d_a^T + d_b^T}{2} \\ (\alpha_l - \alpha_s)\Omega_{j_p} + \alpha_l\Omega_{j_l} + L_{ja}(\frac{1}{2}\alpha_s d_a^N - \beta v^*) + L_{jb}(\frac{1}{2}\alpha_s d_b^N - \beta v^*) + h\alpha_s \frac{d_a^T + d_b^T}{2} \\ C_2(-2h\alpha_l + h\alpha_s - \frac{1}{2}\alpha_s(d_b^N + d_a^N) + 2\beta v^*) \\ -C_2(-2h\alpha_l + h\alpha_s - \frac{1}{2}\alpha_s(d_b^N + d_a^N) + 2\beta v^*) \\ C_3(\frac{1}{2}\alpha_s(d_b^T - d_a^T)) \\ -C_3(\frac{1}{2}\alpha_s(d_b^T - d_a^T)) \end{pmatrix} \quad (7.83)$$

## 7.3 First analysis of the equations

### 7.3.1 Comparison with continuum equations

Classically, the mass balance in 2 phases approaches is written (Sec. 3.2.2 , Eq. 3.27):

$$\nabla \cdot \left( \rho_l \frac{\kappa}{\mu} (\nabla p_l - \rho_l \vec{g}) \right) = \frac{\partial \rho}{\partial t} + \nabla \cdot (\rho \vec{v}_s) \quad (7.84)$$

where  $\kappa$  is the permeability of the mush,  $\mu$  the fluid viscosity. Yet, this equation cannot be directly compared to the present model. We have to get back to the initial form of the equations (Sec. 3.2.1 Eqs. 3.10 and 3.13).

$$\frac{\partial(g_s \rho_s)}{\partial t} + \nabla \cdot (\rho_s g_s \vec{v}_s) = \frac{1}{\Omega} \int_{S_{s/l}} \left( \rho_s (\vec{w}_{s/l} - \vec{v}_s^*) \cdot \vec{n} \right) ds \quad (7.85)$$

$$\frac{\partial(g_l \rho_l)}{\partial t} + \nabla \cdot (\rho_l g_l \vec{v}_l) = -\frac{1}{\Omega} \int_{S_{s/l}} \left( \rho_l (\vec{w}_{s/l} - \vec{v}_l^*) \cdot \vec{n} \right) ds \quad (7.86)$$

where  $\Omega$  is the REV volume,  $S_{s/l}$  is the solid-liquid interface,  $\vec{w}_{s/l}$  is the interface velocity,  $\vec{n}$  the normal to the interface pointing from the solid to the liquid,  $\vec{v}_s^*$  and  $\vec{v}_l^*$  are the material speeds at the interface of the solid and the liquid, respectively. We divide each equation by its respective density and get:

$$\frac{g_s}{\rho_s} \frac{\partial \rho_s}{\partial t} + \frac{\partial g_s}{\partial t} + \frac{g_s \vec{v}_s}{\rho_s} \cdot \nabla \rho_s + \nabla \cdot (g_s \vec{v}_s) = \frac{1}{\Omega} \int_{S_{s/l}} \left( (\vec{w}_{s/l} - \vec{v}_s^*) \cdot \vec{n} \right) ds \quad (7.87)$$

The addition of this equation expressed for the solid and the liquid gives:

$$-\alpha_s g_s - \alpha_l g_l + \frac{g_s \vec{v}_s}{\rho_s} \cdot \nabla \rho_s + \frac{g_l \vec{v}_l}{\rho_l} \cdot \nabla \rho_l + \nabla \cdot (g_s \vec{v}_s + g_l \vec{v}_l) = \frac{1}{\Omega} \int_{S_{s/l}} \left( (\vec{v}_l^* - \vec{v}_s^*) \cdot \vec{n} \right) ds \quad (7.88)$$

where the shrinkage coefficients  $\alpha_s, \alpha_l$  have been introduced. The right hand term of this equation can be evaluated by a local mass balance around the interface [78].

$$\rho_l(\vec{v}_l^* - \vec{w}_{s/l}) \cdot \vec{n} = \rho_s(\vec{v}_s^* - \vec{w}_{s/l}) \cdot \vec{n} \quad (7.89)$$

We introduce  $v^*$ , the normal velocity of the interface in the solid reference frame

$$\vec{w}_{s/l} \cdot \vec{n} = \vec{v}_s^* \cdot \vec{n} + v^* \quad (7.90)$$

and get

$$(\vec{v}_s^* - \vec{v}_l^*) \cdot \vec{n} = \beta v^* \quad (7.91)$$

and thus Eq. 7.88 gives

$$-\alpha_s g_s - \alpha_l g_l + \frac{g_s}{\rho_s} \vec{v}_s \cdot \nabla \rho_s + \frac{g_l}{\rho_l} \vec{v}_l \cdot \nabla \rho_l + \nabla \cdot (g_s \vec{v}_s + g_l \vec{v}_l) + \frac{1}{\Omega} \int_{S_{s/l}} \beta v^* ds = 0 \quad (7.92)$$

This equation represents a volume balance in a Eulerian frame and states that the internal volume change (terms multiplied by  $\alpha$  or  $\beta$ ) is balanced by a volumetric flow of matter. This is as general as Eq. 7.84 and Eq. 7.92 could be equally implemented in two-phase approaches.

In the present approach we introduce Darcy's law to express the relative fluid velocity (Sec. 3.2.2, Eq. 3.23), neglecting the variation of density at the scale of the REV ( $\nabla \rho$  terms) as well as gravity. Thus,

$$-\alpha_s g_s - \alpha_l g_l + \nabla \cdot \vec{v}_s - \nabla \cdot \left( \frac{\kappa}{\mu} (\nabla p_l) \right) + \frac{1}{\Omega} \int_{S_{s/l}} \beta v^* ds = 0 \quad (7.93)$$

This equation can be directly related to the present model:

$$\sum \frac{2h^3}{3\mu L_c} (P_i - P_j) \sim - \int_{\partial\Omega} \left( \frac{\kappa}{\mu} \nabla p_l \right) \cdot \vec{n}_\Omega d(\partial\Omega) \quad (7.94)$$

$$\sum \left( 2h \frac{V_{O_b}^T + V_{O_a}^T}{2} + L_{ib} V_{O_b}^N - L_{ia} V_{O_a}^N \right) \sim \int_{\partial\Omega} \vec{v}_s \cdot \vec{n}_\Omega d(\partial\Omega) \quad (7.95)$$

$$\sum (L_{ib} \beta v^* + L_{ia} \beta v^*) \sim \int_{S_{s/l}} \beta v^* ds \quad (7.96)$$

$$\sum -\alpha_l \Omega_{i_l} \sim \int_{\Omega} -\alpha_l g_l d\Omega \quad (7.97)$$

$$\sum -\frac{1}{2} \alpha_s (L_{ia} d_a^N + L_{ib} d_b^N) \sim \int_{\Omega} -\alpha_s g_s d\Omega \quad (7.98)$$

where the sum is done on all the channels around vertex  $i$ .  $\vec{n}_\Omega$  represents the normal to the REV and  $\partial\Omega$  is its contour. For the last equation, the term  $d_a^N$  is positive and represents the distance from the interface to the cluster centre in the normal direction. As cluster size increases, this term will increase showing the localization of shrinkage at the cluster boundaries. This feature is not present in the continuum form of the equation.

The relationship with the continuum equation for mechanical equilibrium is more straightforward (Sec. 3.2.2, Eq. 3.25), we have

$$\boxed{\nabla \cdot \left( \overleftrightarrow{\sigma}_s^e(\vec{v}_s) \right) = \nabla p_l} \quad (7.99)$$

where  $\overleftrightarrow{\sigma}_s^e$  is the Terzaghi effective stress in the solid. Thus

$$\sum \left( \begin{array}{c} -(P_j - P_i)h \\ -P_i L_{ia} - P_j L_{ja} \end{array} \right) \sim - \int_{\Omega} \nabla p_l d\Omega \quad (7.100)$$

$$\sum \left( \begin{array}{c} \mu \frac{L_c}{2h} (V_b^T - V_a^T) \\ \mu \left( \frac{L_c}{2h} \right)^3 (V_b^N - V_a^N - 2h\alpha_l + h\alpha_s) \end{array} \right) \sim \int_{\partial\Omega} \overleftrightarrow{\sigma}_s^e \vec{n} dS \quad (7.101)$$

where the sum is done on all the channels surrounding one cluster.

### 7.3.2 Dimensionless matrix

It is important to get a dimensionless matrix of the problem not only for a good convergence of the computation but also to get an insight of the physics involved. Here we only write roughly the equations, with the implicit meaning that all the terms with the same dimension are normalised by the same factor.

We introduce a characteristic length scale  $L_{ref}$  of the order of the grain size and a time scale  $t_{ref}$  which is not known yet (it will be imposed by the boundary conditions, see below). Thus, we can do the following normalisation.

$$P \rightarrow \frac{\mu}{t_{ref}} P' \quad V \rightarrow \frac{L_{ref}}{t_{ref}} V' \quad (7.102)$$

We get an equation for the flux

$$\frac{t_{ref}}{L_{ref}^2} \Phi \sim \frac{1}{12} \frac{(2h)^3}{L_c L_{ref}^2} P' + \frac{L}{L_{ref}} V' \quad (7.103)$$

Yet, this equation cannot be considered as a proper normalised form because the term  $\frac{(2h)^3}{L_c L_{ref}^2}$  has a value which varies greatly with solid fraction. A similar term has already been introduced in Eq. 7.30.

We introduce a dimensionless number

$$Norm = \frac{2h_{ref}}{L_{ref}} \quad (7.104)$$

If we consider an hexagonal solid grain, we get, once again, the term introduced by Lahaie and Bouchard [75].

$$Norm = \sqrt{3} \frac{1 - g_s^{1/2}}{g_s^{1/2}} = \sqrt{3} (g_s^{-1/2} - 1) \sim \frac{\sqrt{3}}{2} (1 - g_s) \quad g_s \rightarrow 1 \quad (7.105)$$

This factor decreases with solid fraction and has a value around  $10^{-1}$  for  $g_s = 0.8$ . This term outlines the change of deformation mechanism as solidification proceeds. We see

that it naturally appears in our problem with a power 3. Introducing this term in the equation we get:

$$\frac{t_{ref}}{L_{ref}^2 Norm^3} \Phi = \frac{2}{3} \frac{h^3}{L_c L_{ref}^2} \frac{1}{Norm^3} P' + \frac{L}{L_{ref}} \frac{1}{Norm^3} V' \quad (7.106)$$

We choose

$$P^\circ = P' = \frac{t_{ref}}{\mu} P \quad V^\circ = \frac{1}{Norm^3} V' = \frac{t_{ref}}{L_{ref} Norm^3} V \quad \Phi^\circ = \frac{t_{ref}}{L_{ref}^2 Norm^3} \Phi \quad (7.107)$$

and get a properly normalised equation, *i.e.*, all the coefficients are on the order of 1 :

$$\Phi^\circ = \frac{1}{12} \frac{2h^3}{L_c L_{ref}^2} \frac{1}{Norm^3} P^\circ + \frac{L}{L_{ref}} V^\circ \quad (7.108)$$

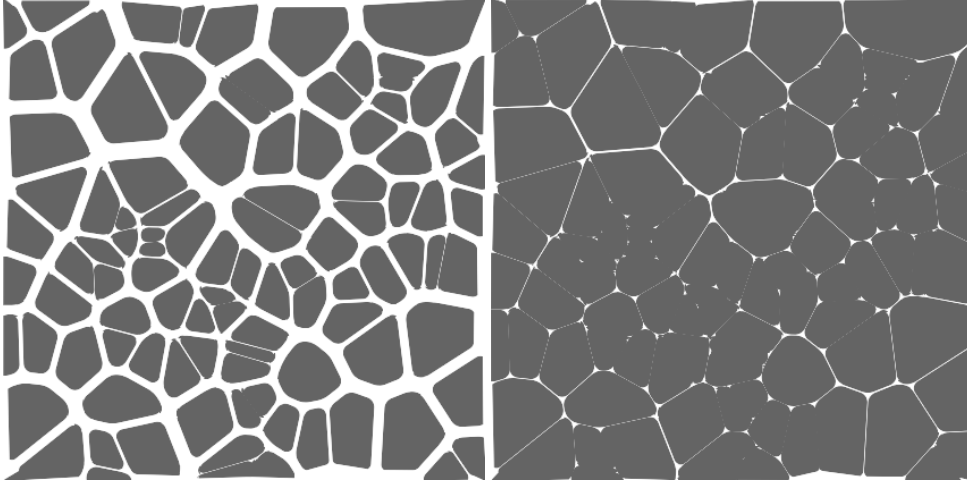


**Figure 7.4:** Grains structure for two different solid fractions. As the solid fraction increases, the displacement of grains and fluid becomes more and more difficult. This fact is simply represented by the  $Norm^3$  term

If we look at the equation for the force balance we get :

$$F^\circ = \frac{L}{L_{ref}} P^\circ + \left( \frac{L}{2h} \right)^3 Norm^3 V^\circ \quad (7.109)$$

with

$$F^\circ = \frac{t_{ref}}{\mu L_{ref}} F \quad (7.110)$$

finally we can write the dimensional matrix as

$$\begin{pmatrix} P^\circ \\ V^\circ \end{pmatrix} = \begin{pmatrix} \frac{t_{ref}}{\mu} & 0 \\ 0 & \frac{t_{ref}}{L_{ref} Norm^3} \end{pmatrix} \begin{pmatrix} P \\ V \end{pmatrix} \quad (7.111)$$

and

$$\begin{pmatrix} \Phi^\circ \\ F^\circ \end{pmatrix} = \begin{pmatrix} \frac{t_{ref}}{L_{ref}^2 Norm^3} & 0 \\ 0 & \frac{t_{ref}}{\mu L_{ref}} \end{pmatrix} \begin{pmatrix} \Phi \\ F \end{pmatrix} \quad (7.112)$$

Here we can see that for a given constrain on the material, the characteristic fluid flux and solid speed scale as  $Norm^3 \sim \left(g_s^{-\frac{1}{2}} - 1\right)^3$  which is already a valuable insight in the mechanics of the problem. Note also that from the numerical point of view, it is much better to solve a properly dimensionless matrix as it ensures a better conditioning of the problem.

### Work done by the second member

If we write the dimensional form of the equations as

$$\begin{pmatrix} \Phi \\ F \end{pmatrix} = \begin{pmatrix} D_1 & L_1 \\ -{}^tL_1 & D_2 \end{pmatrix} \begin{pmatrix} P \\ V \end{pmatrix} = \begin{pmatrix} b_\Phi \\ b_F \end{pmatrix} \quad (7.113)$$

where  $b_\Phi$  and  $b_F$  are the second members for the fluxes and the forces, respectively.

The dimensionless form of the equation is

$$\begin{pmatrix} \Phi^\circ \\ F^\circ \end{pmatrix} = \begin{pmatrix} \frac{\mu}{L_{ref}^2 Norm^3} D_1 & \frac{1}{L_{ref}} L_1 \\ -\frac{1}{L_{ref}} {}^tL_1 & \frac{Norm^3}{\mu} D_2 \end{pmatrix} \begin{pmatrix} P^\circ \\ V^\circ \end{pmatrix} = \begin{pmatrix} \frac{t_{ref}}{L_{ref}^2 Norm^3} b_\Phi \\ \frac{t_{ref}}{\mu L_{ref}} b_F \end{pmatrix} \quad (7.114)$$

It is interesting to note that the time scale does not appear in the normalised matrix but appears in the normalisation of the second member.

If the time scale is imposed by a condition on the flux we have

$$\frac{t_{ref}}{L_{ref}^2 Norm^3} b_\Phi \sim 1 \quad (7.115)$$

thus

$$t_{ref} \sim \frac{L_{ref}^2 Norm^3}{b_\Phi} \quad (7.116)$$

On the other hand, an imposed condition on the force gives

$$\frac{t_{ref}}{\mu L_{ref}} b_F \sim 1 \quad (7.117)$$

thus

$$t_{ref} \sim \frac{\mu L_{ref}}{b_F} \quad (7.118)$$

Some interesting remarks come out if we compute the power dissipation

$$\dot{W} = \begin{pmatrix} P \\ V \end{pmatrix} \cdot \begin{pmatrix} \Phi \\ F \end{pmatrix} = \frac{\mu L_{ref}^2 Norm^3}{t_{ref}^2} \begin{pmatrix} P^\circ \\ V^\circ \end{pmatrix} \cdot \begin{pmatrix} \Phi^\circ \\ F^\circ \end{pmatrix} \quad (7.119)$$

First, the power dissipation coming from the displacement of the grains is on the same order as the dissipation coming from the fluid flow whatever the solid fraction is. Second, introducing a value for  $t_{ref}$  we get :

$$\dot{W} \sim \frac{\mu b_\Phi^2}{L_{ref}^2 Norm^3} \quad (7.120)$$

for a condition of imposed flux and

$$\dot{W} \sim \frac{Norm^3 b_F^2}{\mu} \quad (7.121)$$

for a condition of imposed force.

Therefore, the power dissipation increases as  $g_s$  increases for a condition of imposed flux (same for an imposed velocity), whereas, for an imposed force, the power dissipation decreases as the solid fraction increases. This becomes of particular importance when shrinkage is considered.

### 7.3.3 Linearity of the equations

We can raise a very simple but important remark : all the equations of the problem are linear. Thus, if we consider two sets of second members, the solution for the addition of the second members will be the sum of the solutions for each isolated second member, *i.e.*,

$$\begin{pmatrix} P^1 \\ V^1 \end{pmatrix} = E^{-1} \begin{pmatrix} b_\Phi^1 \\ b_F^1 \end{pmatrix}, \quad \begin{pmatrix} P^2 \\ V^2 \end{pmatrix} = E^{-1} \begin{pmatrix} b_\Phi^2 \\ b_F^2 \end{pmatrix} \Rightarrow \begin{pmatrix} P^1 + P^2 \\ V^1 + V^2 \end{pmatrix} = E^{-1} \begin{pmatrix} b_\Phi^1 + b_\Phi^2 \\ b_F^1 + b_F^2 \end{pmatrix} \quad (7.122)$$

As a consequence, it is possible to isolate the role of each mechanical stress on the material. In particular we can apply to a sample an external deformation rate in one direction, then a deformation rate in the other direction, and compute the rigidity tensor that relates the average deformation rate tensor to the average stress tensor. This feature is particularly important for an up-scaling procedure.

### 7.3.4 Detection of contacts

In the previous derivation of the model, we did not specify a criterion for the detection of the contacts between grains. However, the mechanical resistance of a channel tends to infinity when the channel width tends to 0 (with the power -3). This phenomenon is sufficient to prevent the interpenetration of the grains, providing the time step is sufficiently small. In extremely constrained situations, a dynamic refining procedure of the time step is implemented in the code to prevent grain interpenetration.

However, in the derivation of the model, we have supposed that the first neighbours of the grains remain always the same. For important deformations, this might no longer be the case. Such problems arise earlier for short channels as represented on Fig. 7.5. On this figure, the smooth contour of the grains is represented together with the idealized linear interfaces.

After some deformation, it is possible that the two edges of a channel do not match anymore (Fig. 7.5(b)). In this situation the resistance of the channel is modelled by a small but finite value. Such a situation does not affect much the global response of the simulation as it generally occurs on a short channel whose role is negligible.

A more problematic situation arises when the two not matching edges tend to interpenetrate (Fig. 7.5(c)). In that case, the apparent width of the channel tends to become negative and the problem matrix loses its physical meaning. Another problem is the interpenetration of two grains that were not first neighbours at the beginning of the computation. Indeed, the program cannot detect such a contact as it does not model the

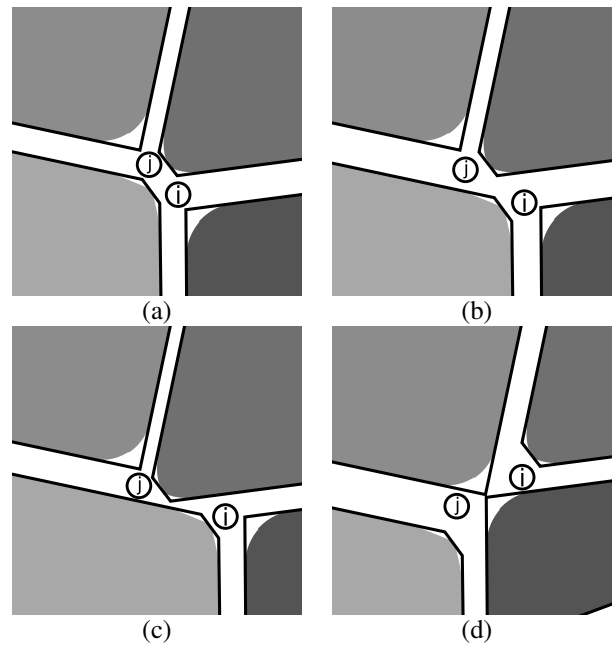


**Figure 7.5:** Various problematic configurations of the channels. (a) Reference. (b) Channel mismatch. (c) Channel interpenetration. (d) Change of neighbourhood.

interaction between these two grains. A similar situation occurs when modelling grain growth by a vertex technique [150].

Such problems can be solved by a real time update of the first neighbours as implemented in DEM methods [140]. Yet, with such a method, the channels between the grains would not be necessarily linear anymore. An important work would be necessary for the modelling of the channels and the detection of contacts.

However, for solid fraction larger than 0.9, the size of liquid channels is very small as compared to the solid grain size. Deformation in the mush is limited and problematic situations almost never arise. Therefore, the present model is suitable for the study of hot cracking but its extension to lower solid fractions would require a significant work.



## **Part III**

### **The leaves**



# Chapter 8

## Experimental results

### 8.1 Traction test

We describe here the results produced with the mushy zone traction test at Alcan CRV (rig test) described in Sec. 5.1.

#### 8.1.1 Mechanical measurements

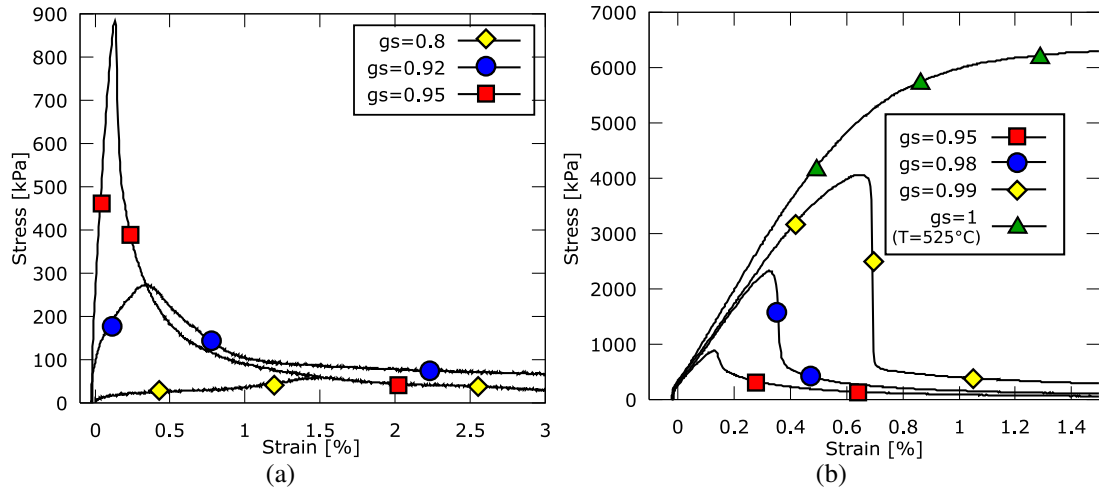
Figure 8.1 shows the evolution of the stress-strain curves for an Al-2wt%Cu (noted AU2) with a deformation rate of  $4 \times 10^{-3} \text{ s}^{-1}$ . The ductility minimum (DM) is observed for  $T = 594^\circ\text{C}$ , *i.e.*, an estimated solid fraction of  $g_s^{coal} = 0.95$ . Note that this value is similar to the value reported by Ludwig *et al.* on the same heavily inoculated alloy [45]. Note also that stress and strain have been estimated from recorded force and displacement as presented in Sec. 5.1.1.

In Fig. 8.1(a) the stress-strain curves are represented for solid fractions below the DM and therefore correspond to the descending branch of the ductility curve (U-curve, see Sec. 2.3.4), *i.e.*, increasing  $g_s$  decreases the ductility. Both stress increase and fracture are smooth. With increasing solid fraction, fracture occurs at a higher stress and a lower deformation. At the DM, stress increases linearly with strain but fracture remains relatively smooth.

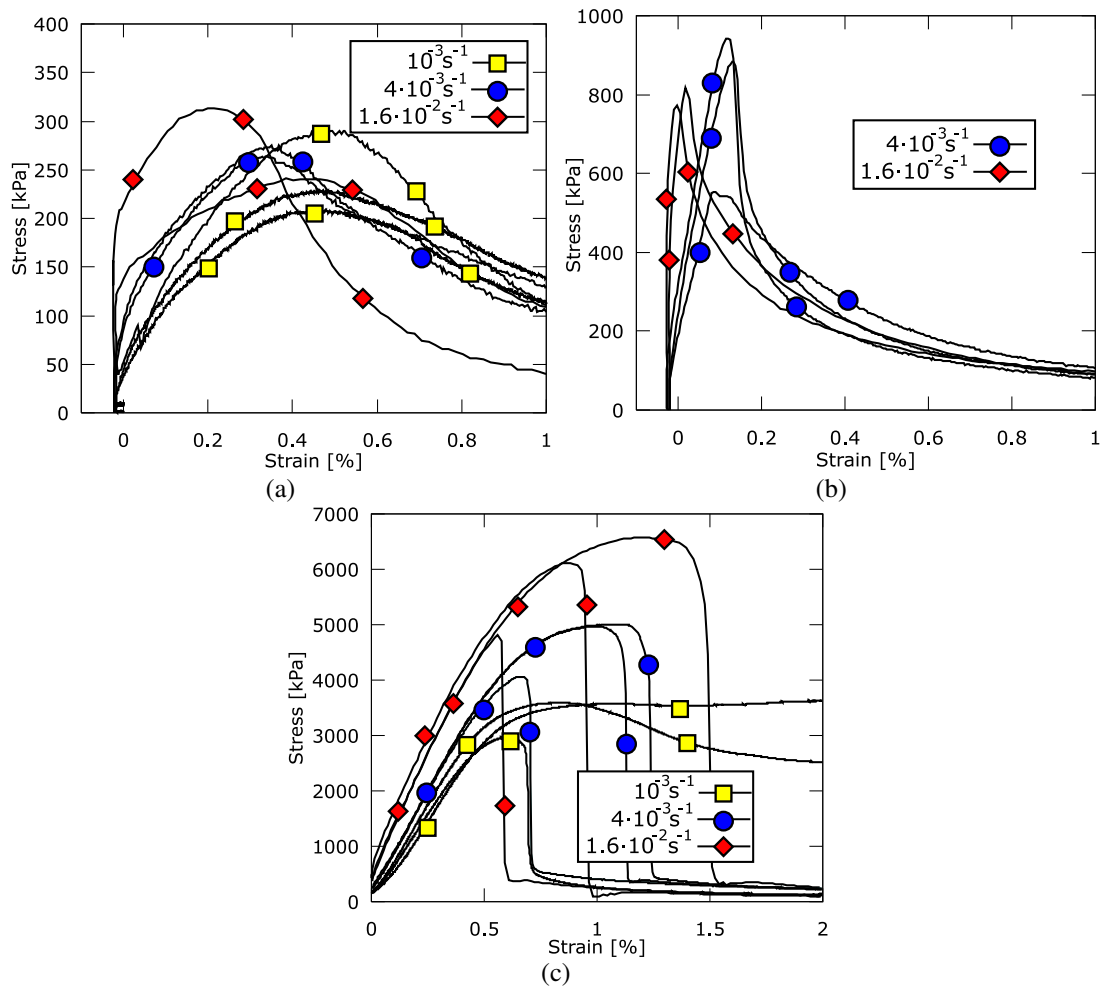
Above the DM, the stress increases linearly with strain at low deformation and fracture is then very abrupt (Fig. 8.1(b)). The initial slope of the stress response increases with solid fraction. These curves can be compared to the fully solid response (Fig. 8.1(b)  $T = 525^\circ\text{C}$ ). The behaviour at low strain is in the continuity of the mushy zone behaviour but no fragile rupture is observed, a viscoplastic plateau is reached and fracture occurs after a very important plastic deformation (not shown on the graph).

Figure 8.2 shows stress-strain curves as recorded for different tests at the same temperature, which allows to appreciate the dispersion of the results and the effect of strain rate. Below the DM (Fig. 8.2(a)), the dispersion of the measured behaviour is relatively important. At low strain rate, the stress response is smoother than that measured at high deformation rate. This effect might be linked to the compliance of the machine. Otherwise, no clear effect of the strain rate can be observed.

At the DM (Fig. 8.2(b)), the initial slope of the stress response increases with the strain rate. There is an appreciable dispersion of strain at fracture and the influence of strain rate on this quantity is not clear.



**Figure 8.1:** Evolution of stress-strain curves with solid fraction for an AU2 alloy with an imposed deformation rate of  $4 \times 10^{-3} \text{ s}^{-1}$ . (a) Descending branch of the U-curve. (b) Ascending branch of the U-curve.



**Figure 8.2:** Stress-strain curves as measured for different tests on a AU2 alloy. (a)  $T = 615^\circ\text{C}$   $g_s = 0.92$ . (b)  $T = 594^\circ\text{C}$   $g_s = 0.95$ . (c)  $T = 540^\circ\text{C}$  (below eutectic temperature)

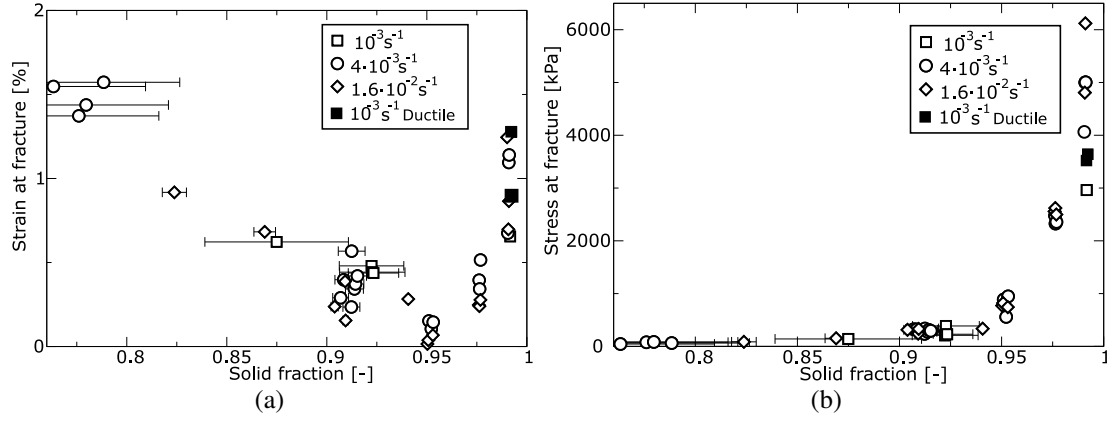


**Figure 8.3:** Fractures properties of AU2 alloy in the mushy zone. (a) Ductility. (b) Stress at fracture. The error bars represent the evolution of solid fraction during the test.

Above the DM (Fig. 8.2(c)), the rheology of the material is well defined and is similar to a viscoplastic behaviour. The initial slope of the stress response increases with strain rate. A viscoplastic plateau can be reached and its height also increases with strain rate. Fracture is very abrupt and occurs randomly on the common rheological behaviour. Note that, despite the clear effect of strain rate on the material rheology, no clear effect is observed for the occurrence of fracture.

Therefore, the DM corresponds to a transition from a mechanics dominated by fluid flow (at lower  $g_s$ ) to a mechanics dominated by solid deformation. At that point, neither deformation mechanism is efficient and ductility is very low.

Another transition is observed in Fig. 8.2(c). Indeed, these tests were done just below the eutectic temperature, but a fragile behaviour is still observed. For the test done at the lower strain rate ( $10^{-3} \text{ s}^{-1}$ ), temperature has more time to evolve (see Fig. 8.4) and the transition from a fragile to a ductile behaviour can be observed.

The measured fracture stress and strain for the AU2 alloy in the mushy zone are reported on Fig. 8.3. The classical U-shape of the ductility curve is retrieved together with the sharp increase of stress at fracture above the DM (see Sec. 2.3.4). These two quantities appear to be independent of strain rate. The error bars correspond to the evolution of solid fraction during the test due to its non-isothermal nature. Naturally this evolution is more important at low solid fraction and for low strain rate.

The point reported at  $g_s = 0.99$  corresponds to the stress-strain curves shown on Fig. 8.2(c). The tests are done at  $540^\circ\text{C}$  but solid fraction would be 0.99 if eutectic solidification is not considered, *e.g.*, because of an undercooling. The tests with a ductile behaviour are reported with a filled square whereas the brittle behaviour at this value of  $g_s$  is reported with an open square. For these tests, the strain at the viscoplastic plateau is reported as the strain at fracture is difficult to evaluate and would be far out of the graph range. Similarly, the stress reported is the stress at the beginning of the viscoplastic plateau as the apparent strain hardening is mainly due to temperature evolution.

The behaviour of the Al-4wt%Cu (AU4) in the mushy zone is fairly close to the AU2 behaviour. Yet, the transition from a fragile to a ductile behaviour occurs at a significantly lower temperature. Indeed, stress at fracture as a function of temperature is reported on Fig. 8.4 for both AU2 and AU4. Fragile behaviour is reported with open

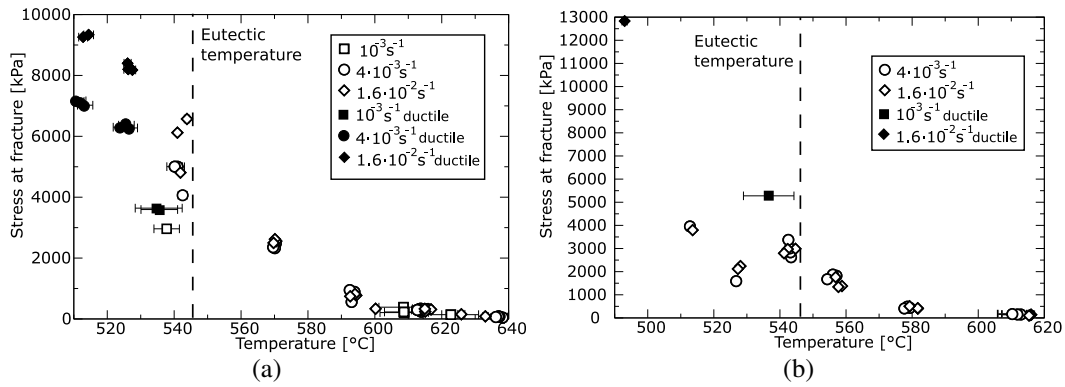


**Figure 8.4:** Stress at fracture as a function of temperature (a) AU2 (b) AU4.

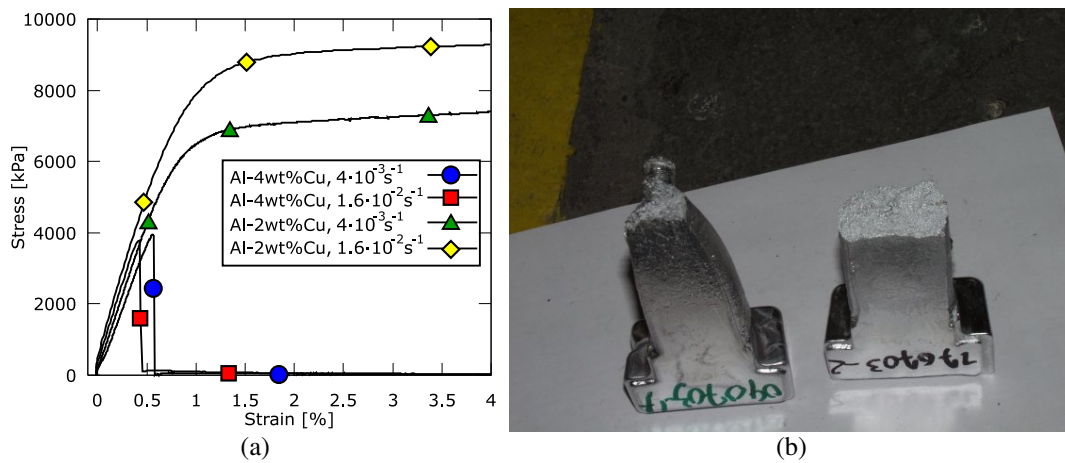


**Figure 8.5:** Comparison between the behaviour of AU2 and AU4 at 510°C. (a) Stress-strain curves. (b) Test specimens after deformation.

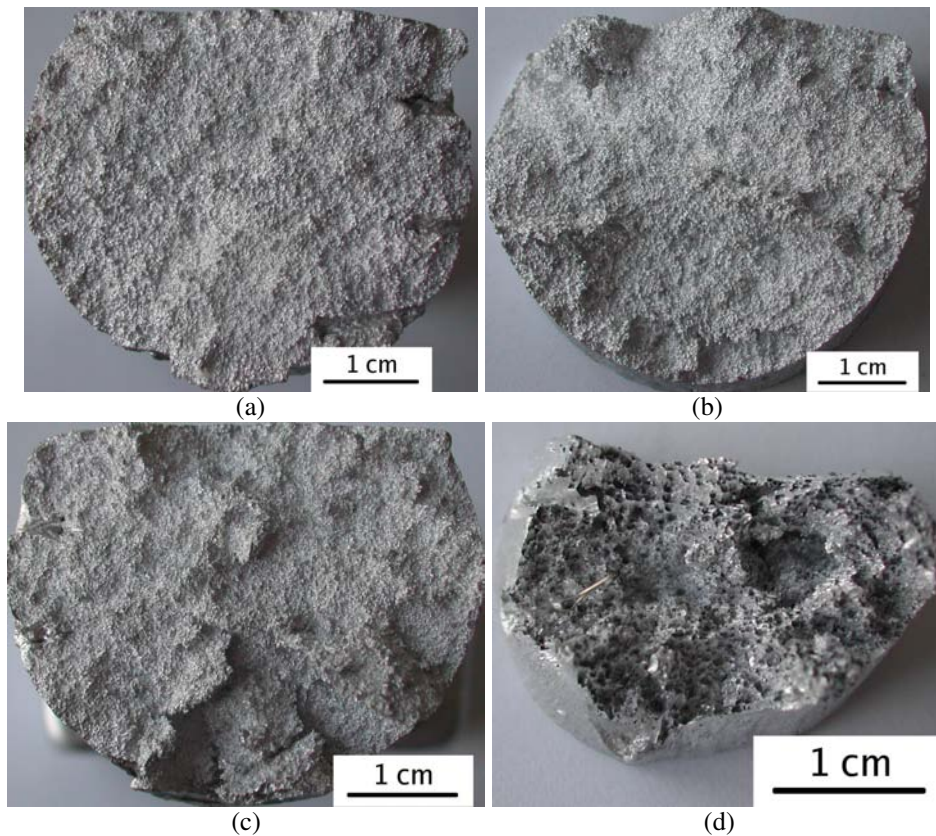
symbols whereas ductile behaviour is reported with filled symbols. For the AU2 alloy, the fragile-ductile transition occurs around  $T = 530^{\circ}C$ , *i.e.*,  $15^{\circ}C$  below the eutectic temperature. For the AU4 alloy, only two samples exhibit a ductile behaviour, one at  $540^{\circ}C$  and a strain rate of  $10^{-3} s^{-1}$ , the other at  $490^{\circ}C$  and  $1.6 \times 10^{-2} s^{-1}$ .

Figure 8.5(a) shows the stress-strain curves for AU2 and AU4 samples tested at  $510^{\circ}C$ , *i.e.*,  $25^{\circ}C$  below the eutectic temperature. At low strain, the two alloys have about the same behaviour. Brittle fracture occurs rapidly for the AU4 alloy whereas the AU2 samples have a viscoplastic deformation. Figure 8.5(b) shows the test specimens after rupture, the AU2 sample has encountered a significant deformation and striction, whereas the AU4 sample is almost not deformed.

The experiments done with the 5182 alloy give qualitatively the same results as with the Al-Cu alloys but as only a few experiments have been carried on we do not present them here (see [38]).

### 8.1.2 Observations of fracture profiles

As observed with the naked eye, the fracture surfaces of the samples present original profiles and seem very different from classical fracture surfaces (Fig. 8.6). Note that



**Figure 8.6:** Fracture profiles as observed with the naked eye. (a) Brittle failure, low  $g_s$  ductility (AU2 T=615°C  $g_s=0.92$ ) (b) Brittle failure at the DM (AU2 T=595°C  $g_s=0.95$ ) (c) Brittle failure, high  $g_s$  ductility (AU4 T= 540°C) (d) Ductile failure (AU2 T=525°C ).

it is difficult to really reproduce the 3D nature of the surface on a 2D photograph. In particular, the surfaces appear much smoother than what they really are.

Samples fractured at a solid fraction below the DM (Fig. 8.6(a)) present a shiny aspect (which is not well reproduced on the picture), an important rugosity is observed up to a few millimetres but at a larger scale the profile is relatively flat. At the DM (Fig. 8.6(b)), the height variations become important at any visible scale. Some chips of metal detach from the surface and remain fixed by one side. These chips are present at any visible scale (from small ones of a fraction of millimetre to large ones of several centimetres). The shiny aspect is reduced. For higher solid fractions, the rugosity increases together with the density of chips (Fig. 8.6(c)). The profile for the ductile failure is very different (Fig. 8.6(d)), an important striction is observed together with the presence of spikes and cupules characteristic of ductile rupture.

Metallographic observations of a section normal to the fracture surface are presented on Fig. 8.7. In all the samples, important porosity is observed. Indeed, liquid metal is brought to the sample by a small channel (see Fig. 5.1) and therefore liquid feeding is not sufficient to ensure a perfectly sound metal. Moreover, the compositions studied naturally tend to form porosity [30]. At low  $g_s$  (Fig. 8.7(a)), fracture does not penetrate deep in the material. With increasing solid fraction, damage is observed deeper in the material (Figs. 8.7(b), 8.7(c)). This phenomenon recalls the formation of chips on the



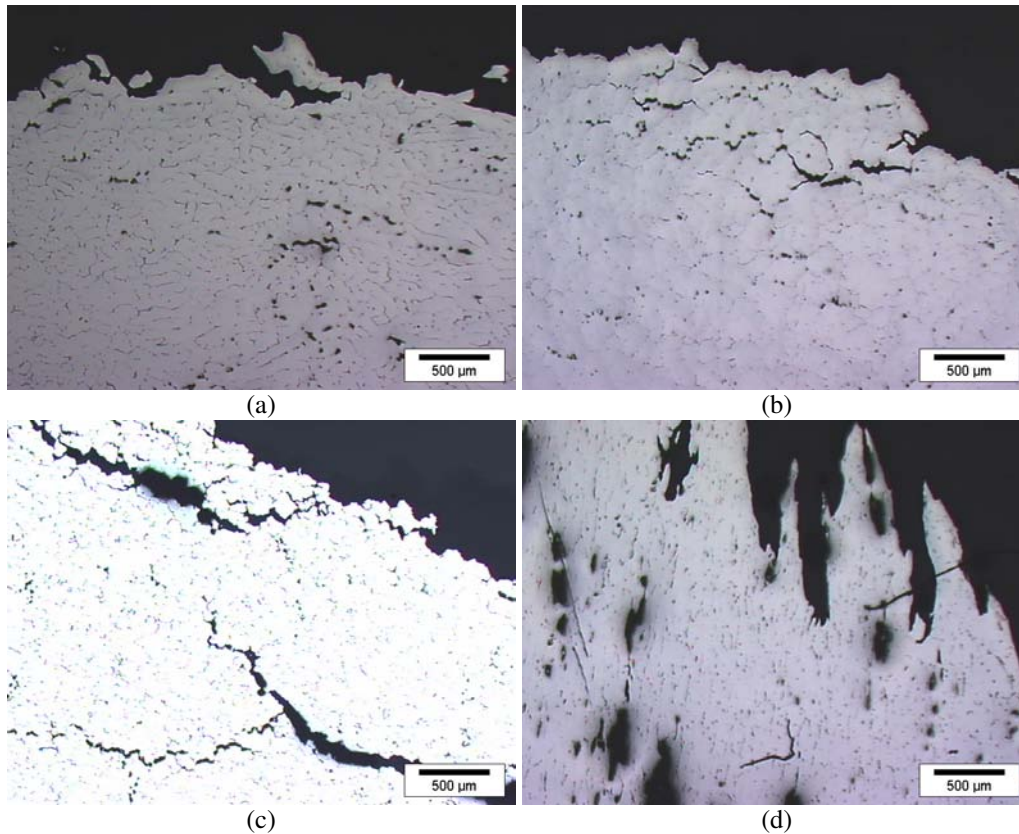


**Figure 8.7:** Metallographies of the fracture profile. (a) Brittle failure, low  $g_s$  ductility (AU2 T=636°C  $g_s=0.8$ ) (b) Brittle failure at the DM (AU2 T=595°C  $g_s=0.95$ ) (c) Brittle failure, high  $g_s$  ductility (AU4 T=525°C) (d) Ductile failure (AU2 T=525°C).

fractured surfaces. Moreover, this phenomenon can also be understood considering that as  $g_s$  increases, solid grains start to coalesce and form grain clusters (see Sec. 2.3.6). As grain clusters become bigger, fracture should follow longer paths to go around them.

On ductile failure profiles, spikes and cupules are visible (Fig. 8.7(d)). Moreover, an important damage is observed in the material even far from the fracture surface (Fig. 8.8(b)). This damage appears as elongated pores and has probably developed from the as-cast porosity. Indeed, in the AU4 alloy with a ductile fracture, deformation at rupture is less important and damage appears as nearly spherical cavities (Fig. 8.8(a)).

Electron microscope observations of the samples presented in Fig. 8.7 are shown on Fig. 8.9. A back scattered electron detector is used (atomic mass contrast) and therefore the copper rich zones appear in light grey.

At the lower solid fraction (Fig. 8.9(a)), the smooth contour of the globular grains is visible. There are copper-rich zones around the grains. This is due to the liquid films that have been pumped between the grains by capillarity after fracture.

At the DM (Fig. 8.9(b)), the grains appear more polygonal as solidification is more advanced. Moreover, local coalescence between the grains can be observed, *i.e.*, the presence of grain clusters. Gaps are locally present between the clusters, which, once again, illustrates the localization of deformation. In those gaps, copper rich bridges can be observed. They probably result from liquid menisci which did not break down during fracture (see Sec. 2.2.1).



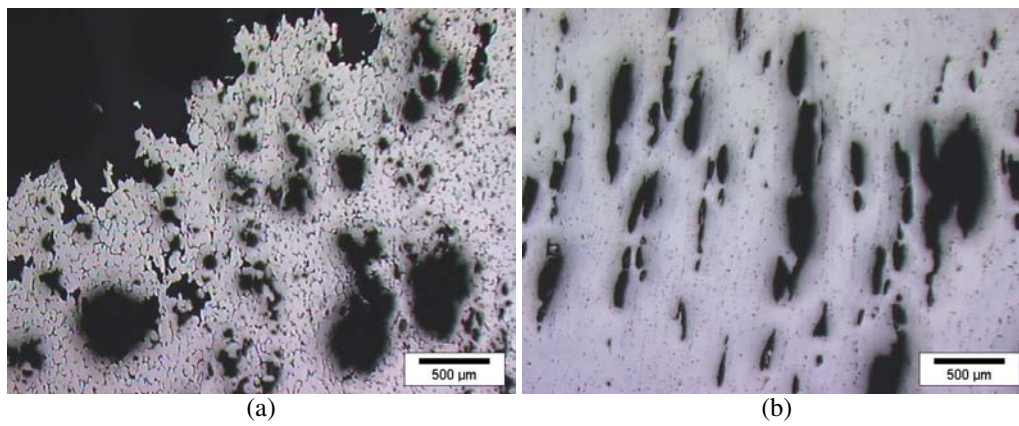


**Figure 8.8:** Observation of damage in ductile failures. (a) AU4  $T=490^{\circ}\text{C}$ . (b) AU2  $T=525^{\circ}\text{C}$ , far from the fracture surface.

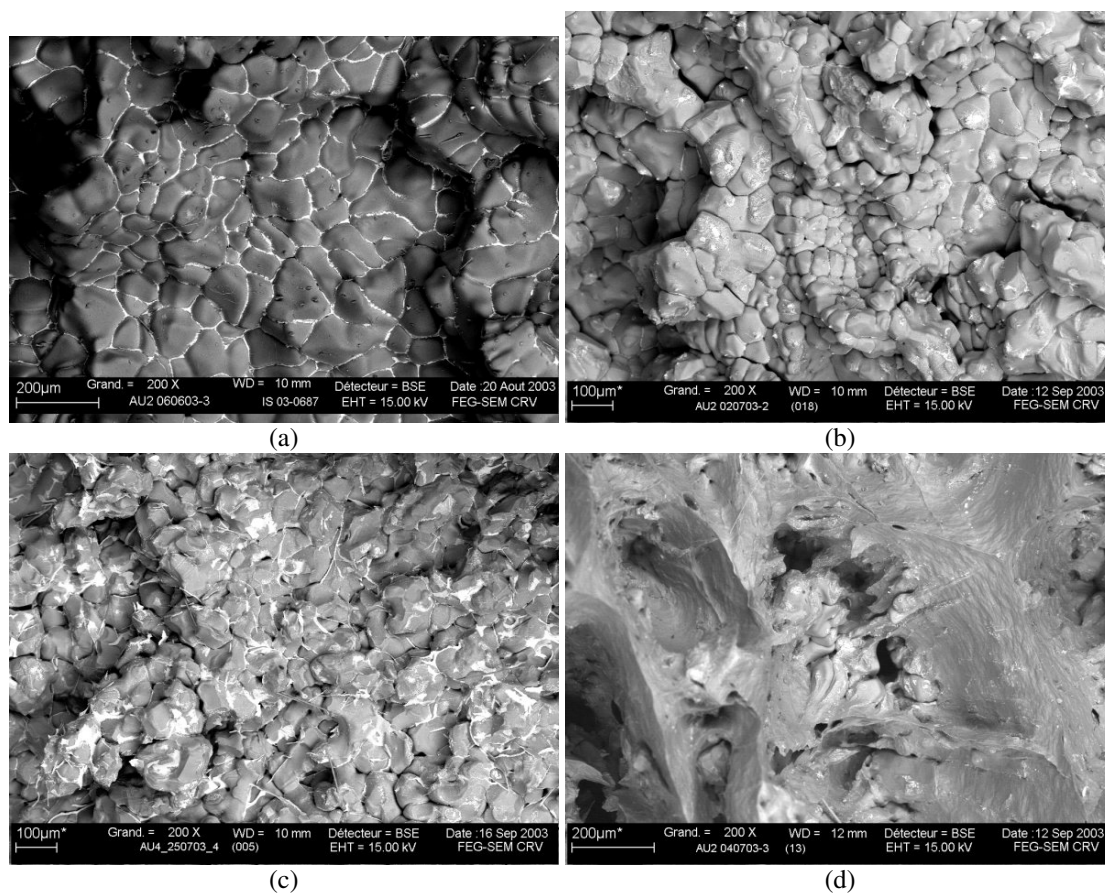


**Figure 8.9:** Back Scattered Electron microographies of fracture surfaces (atomic mass contrast). (a) Brittle failure, low  $g_s$  ductility(AU2  $T= 636^{\circ}\text{C}$   $g_s= 0.8$ ) (b) Brittle failure at the DM (AU2  $T= 595^{\circ}\text{C}$   $g_s = 0.95$ ) (c) Brittle failure, high  $g_s$  ductility (AU4  $T= 525^{\circ}\text{C}$ ) (d) Ductile failure (AU2  $T= 525^{\circ}\text{C}$ ).

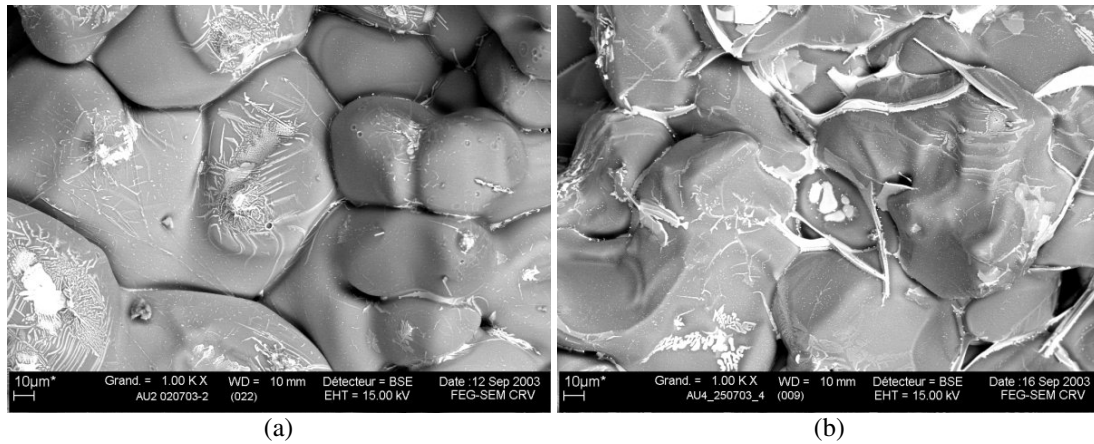


**Figure 8.10:** Detailed view of fracture surfaces (atomic mass contrast). (a) Brittle failure above eutectic temperature (AU2  $T = 595^{\circ}\text{C}$   $g_s = 0.95$ ) (b) Brittle failure well below eutectic temperature (AU4  $T = 525^{\circ}\text{C}$ ).

In Fig. 8.9(c), the presence of grain clusters and the localization of deformation is also visible. Yet, sharp copper rich zones are observed (see below).

Finally, on the ductile fracture profile (Fig. 8.9(d)), an important plastic deformation is visible. Moreover, locally, in the cupules, the smooth contour of some non-deformed solid grains can be observed. This clearly indicates that damage has grown from as-cast porosity.

A more detailed view of the fracture surfaces is given on Fig. 8.10. On Fig. 8.10(a), some copper rich spikes are observed: they are frequently reported on hot tear surfaces as already mentioned in Sec. 2.2.1 [34, 35]. Some more extended copper rich zones can also be observed, they might result from the breakdown of liquid menisci (before they solidify). Moreover, the coalescence between the grains is even clearer at that scale.

On Fig. 8.10(b), the shape of copper rich zones is clearly different. Indeed, the sample has fractured well below the eutectic temperature ( $525^{\circ}\text{C}$ ). Therefore, the copper rich zones represent secondary phases already solidified before fracture. This points out the importance of coalescence not only for the primary phase but also between secondary and primary phases.

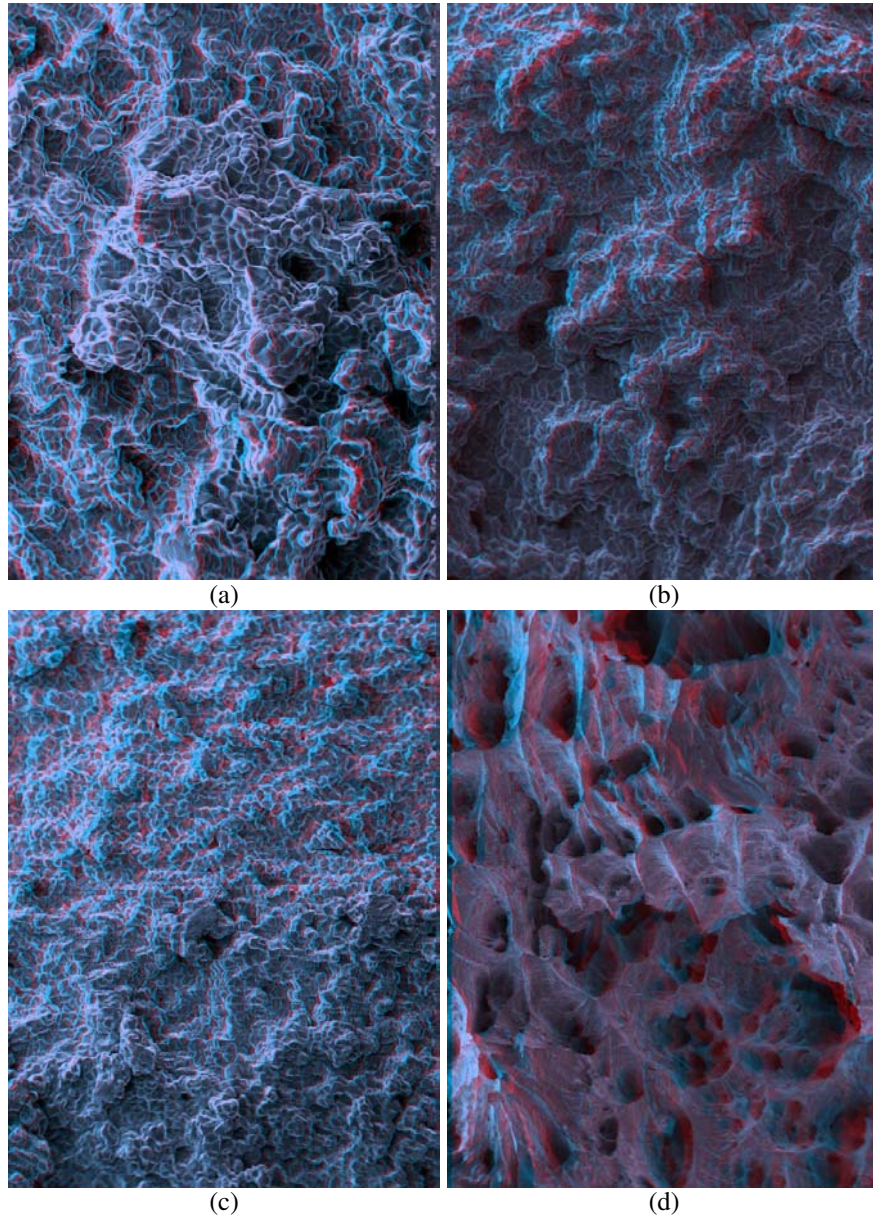
### 8.1.3 Scaling analysis of fracture surfaces

The scaling analysis of the fracture surfaces has been done by T. Meredith during her student project at the LSMX [122]. The fracture surfaces have been reconstructed by a stereo pair of SEM images as described in Sec. 5.1.3. From these profiles, the height-height correlation function (Hurst Transformation) has been computed by a small c program developed during the project (Eq. 4.13).

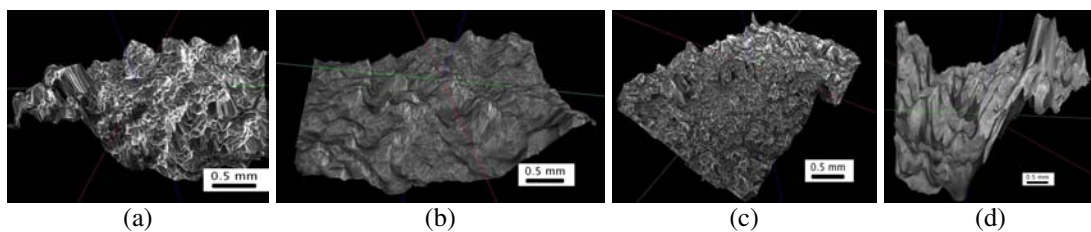
The idea of this analysis, together with the introduction to the field, was given by L. Ponson from the Fracture Group of the CEA, Saclay France [117]. He also performed further analysis on the recorded fracture profiles.

Figure 8.11 shows the stereo pair of SEM images as taken for four different samples, these images should be viewed with blue-red glasses. We used a commercial software, MeX [123], to reconstruct a meshing of the surfaces from the interpolation of the stereographic images. Figure 8.12 shows the SEM images as projected on this mesh.





**Figure 8.11:** Stereographic SEM images of fracture surfaces (a) Brittle failure, low  $g_s$  ductility (AU2 T= 636°C  $g_s$ = 0.8) (b) Brittle failure at the DM (AU2 T= 595°C  $g_s$  = 0.95). (c) Brittle failure, high  $g_s$  ductility (AU4 T= 525°C) (d) Ductile failure (AU2 T= 525°C). (to be viewed with blue-red glasses)



**Figure 8.12:** Same fracture surfaces as reconstructed by the MeX software [123].

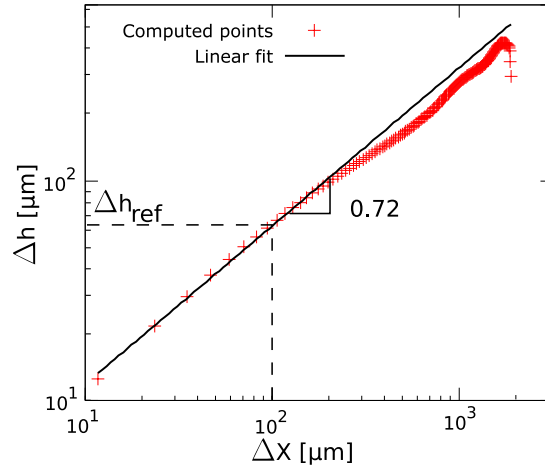


**Figure 8.13:** Hurst transformation in the  $x$  direction (AU2  $T = 595^\circ\text{C}$   $g_s = 0.95$ ). (T. Meredith)

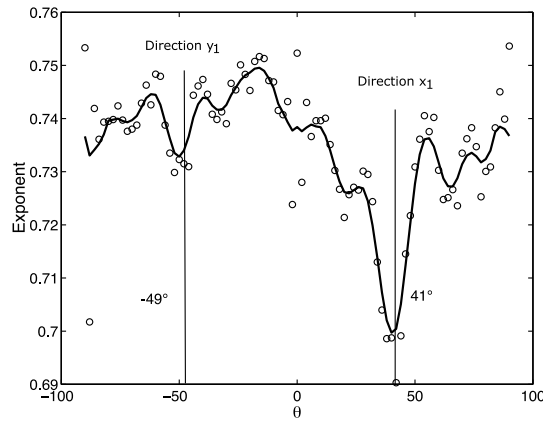
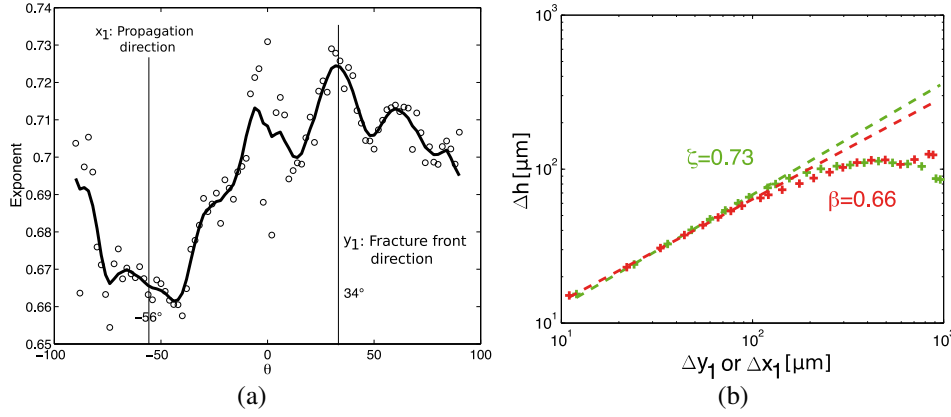


**Figure 8.14:** Hurst exponent as a function of the angle  $\theta$  (AU2  $T = 636^\circ\text{C}$   $g_s = 0.8$ ). (L. Ponson)

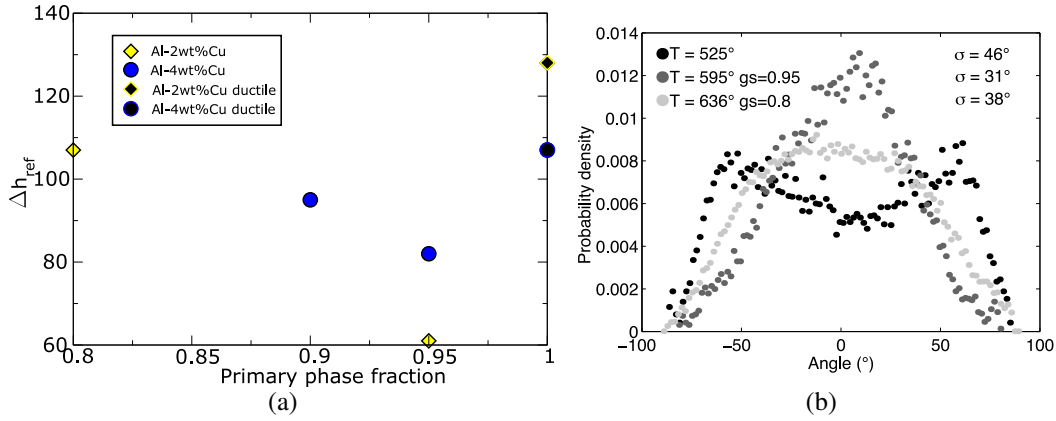
Let us note  $x$  the vertical direction on Fig. 8.11 and  $y$  the horizontal direction. Figure 8.13 shows the Hurst transformation in the  $x$  direction as computed for an AU2 alloy at the DM, *i.e.*, the average of Eq. 4.11 is done for all pair of points with  $\Delta y = 0$  and a given  $\Delta x$ . A power law fit is used to find the Hurst exponent in this direction. Note that the quality of data is necessarily lower when  $\Delta x$  reaches the size of the image as the number of points on which the average can be done is limited. Then, the frame  $x, y$  is rotated by an angle  $\theta$  and the analysis is done in the new  $x$  direction.

Figure 8.14 shows the Hurst exponent as a function of the angle  $\theta$  as computed for an AU2 alloy broken at  $636^\circ\text{C}$ . The value found is consistent with the "universal" value measured in most materials (Sec. 4.2.2)[113]. Yet, the anisotropy of this Hurst exponent is very low and is not sufficient to define clearly a propagation direction of the fracture. On a sample of AU2 alloy broken at  $525^\circ\text{C}$  (ductile failure), a weak anisotropy of the Hurst exponent was also observed.

On Fig. 8.15(a) the same calculation is represented for a AU2 alloy broken at the ductility minimum. This time, the anisotropy of the Hurst exponent is pronounced and allows to define a new frame  $(x_1, y_1)$  where  $x_1$  corresponds to the propagation direction



**Figure 8.15:** Sample AU2  $T = 595^\circ\text{C}$   $g_s = 0.95$  (a) Hurst exponent as a function of the angle  $\theta$  (b) Hurst transformation in the two principal directions,  $x_1$  and  $y_1$ . (L. Ponson)



**Figure 8.16:** (a)  $\Delta h_{ref}$  as a function of primary phase fraction (T. Meredith) (b) Distribution of the local slopes in the rugosity profile for three AU2 samples. (L. Ponson)

of the crack. This propagation direction corresponds to a diagonal from the left down corner to the right top corner of Fig. 8.11(b). Figure 8.15(b) shows the Hurst transformation in direction  $x_1$  and  $y_1$  with the determination of the exponent in these directions, respectively  $\beta$  and  $\zeta$ . These two exponents are consistent with the values measured on most materials [114].

Therefore, hot tears appear at first sight as "classical" fractures with a Hurst exponent around 0.75. The absence of anisotropy at low- $g_s$  fracture is maybe due to the fracture mechanism in which no clear fracture propagation direction can be defined. Indeed, we have seen on Fig. 8.1(a) that fracture is very smooth at low  $g_s$ . Note also that the anisotropy behaviour of fracture is observed in experiments where a propagation direction is clearly imposed to the system, *e.g.*, a single-edge notched beam [114], which is not the case in a uniaxial traction of a cylinder. Similarly, the progressive coalescence of damage in the ductile failure may not allow to define a propagation direction.

Further information on the fracture mechanism can be obtained with the Hurst transformation. We choose a characteristic length of  $100\ \mu\text{m}$ , *i.e.*, the average grain size, and

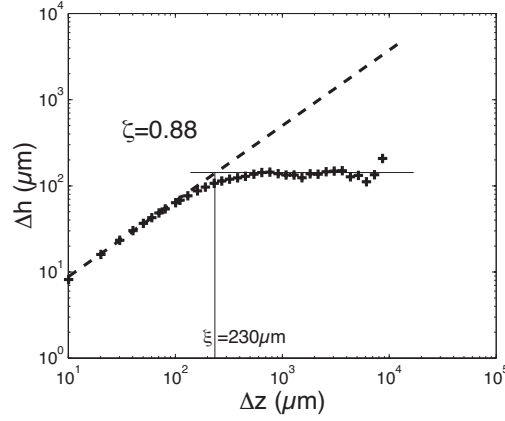


**Figure 8.17:** Hurst transformation on a profile measured with a mechanical profilometer (AU2 T= 636°C  $g_s = 0.8$ ). (L. Ponson)

report the value of  $\Delta h(\Delta x = 100)$  (noted  $\Delta h_{ref}$  see Fig. 8.13). This measure allows to characterize the amplitude of rugosity at the scale of the grain. This function is reported on Fig. 8.16(a) as a function of the solid fraction at fracture<sup>1</sup>. It appears that the local amplitude of rugosity is less important for brittle failures at the DM ( $g_s = 0.95$ ). This measure is clearly confirmed by the observation of the stereographic fractographies (Fig. 8.11). Moreover, Fig. 8.16(b) shows the distribution of local slopes in the rugosity profile for three AU2 samples. The predominance of sharp slopes is visible at T=636°C and T=525°C but not at the DM (T=595°C).

Another quantity that can be extracted is the length scale  $\xi$  above which the self-affine behaviour is not visible anymore. Yet, the SEM images are too local to do correctly such measurement. L. Ponson has measured the profile of a AU2 broken at 636°C with a mechanical profilometer that allows to do measurement at much scale larger scale (Fig. 8.17). On this measurement,  $\xi$  is clearly visible. Its value is 230  $\mu\text{m}$ , *i.e.*, only a few grains. Therefore, the fracture at low  $g_s$  has a rugosity at the scale of the grain  $\Delta h_{ref}$  on the order of the grain size itself, but it remains confined in a layer of a few grains ( $\xi$ ). This is confirmed by the observations of Figs. 8.11(a) and 8.6(a). The measure of  $\xi$  should be interesting for other temperatures but we did not have enough time to do it. It is probable that  $\xi$  becomes much larger at the DM, as clued by the naked eye observations (Fig. 8.6(b)).

Yet, it is important to note that the notion of self affinity supposes that the height of the surface  $z$  can be expressed as a function of the two other direction ( $x, y$ ), *i.e.*, there are no overhang in the surface (which is the case in most fracture surfaces). We have observed in brittle failures at high  $g_s$  the presence of layers which tend to detach from the surface (Figs. 8.6(b), 8.6(c) and 8.7(c)). In that case, the height of the surface is not uniquely defined for a given ( $x, y$ ). Naturally, the SEM images only record the highest points of the surface, but a complete analysis of the fracture surface should include the presence of these overhangs. A possible method would be to vapour-deposit nickel on the fracture surface and examine different sections of the sample with a Backscattered Electron Detector [105]. Such a method would allow us to check whether the apparent

<sup>1</sup> The AU4 rupture below the eutectic temperature (525°C) with a fragile profile is reported at  $g_s = 0.95$ , which correspond to the fraction of primary phase at the eutectic temperature.

self-affine behaviour of the highest points in the interface results from a self-similar nature of the whole interface [151].

### 8.1.4 Summary

We have experimentally characterized two transitions in the behaviour of the mushy zone.

The ductility minimum (DM) is observed at  $g_s = 0.95$  which is in good agreement with the value reported in the literature for heavily inoculated alloys (see Sec. 2.3.6). We have seen in this work that this point corresponds to the transition from a deformation mechanism dominated by fluid flow to a deformation mechanism dominated by solid deformation. Moreover, at the DM, coalescence between grains begins and grain clusters are observed on fracture surfaces.

A transition from a fragile fracture to a ductile fracture is observed below the eutectic temperature. This points out the importance of the coalescence undercooling on the formation of a fully coherent solid. The experiments on the AU4 alloy also outlined the importance of coalescence undercooling between grains of primary phase and the secondary phase.

An important question remains: at which solid fraction and under which conditions a "natural" hot crack occurs? Indeed, the in-situ measurement of a hot crack formation in a casting is difficult. The study of post-mortem fracture profiles might allow to define more precisely these conditions, in particular with the use of the tools presented in Sec. 8.1.3. Yet, these tools still require further developments.

## 8.2 Laser remelting experiments

These laser remelting experiments have been done by L. Germond during his student project at the LSMX [10]. The experimental protocol is presented in Sec. 5.2.

### 8.2.1 Crack statistics

Figure 8.18 shows optical micrographs of the laser traces after polishing (Sec. 5.2). The traces have been obtained for a laser beam velocity  $v_b$  of 20 mm/s and for the four alloys considered, respectively non grain refined (NGR), grain refined (GR), NGR + barium, GR + barium (see Sec. 5.2). The laser spot is displaced from the right to the left of the pictures. Several cracks can be observed, most of them start from the edges of the laser trace and seem to propagate along the temperature gradient. Some cracks at the centreline can be observed [152]. Note also that the underlying grain structure can be observed, in particular the difference between NGR and GR microstructures is visible.

Using these micrographs, the number of cracks and their length has been measured. Table 8.1 shows the statistics of the crack repartition for each laser trace. An increase in crack density is clearly observed with an increase of the spot velocity, the refining of the microstructure and the addition of barium. This last point corroborates the work of G. Chichignoud *et al.* which has shown a decrease of the solid-liquid surface energy with the addition of barium (see Sec. 2.3.5)[125]. Indeed, a reduction of the solid-liquid surface energy increases the coalescence undercooling and thus should increase the hot cracking sensitivity [33] (see Sec. 2.3.5).



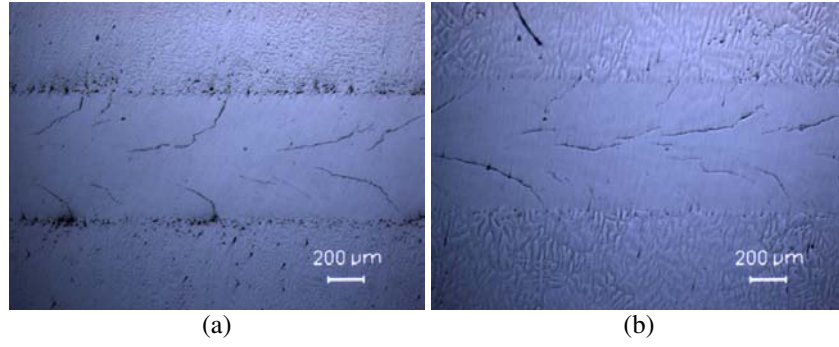


**Figure 8.18:** Metallographies of the laser traces for a spot velocity  $v_b$  of 20 mm/s (a) NGR + Ba (b) GR + Ba.

Alloy	NGR			GR			NGR + Ba			GR + Ba		
Laser spot velocity [mm/s]	10	20	30	10	20	30	10	20	30	10	20	30
Number of cracks [-]	1	56	72	19	84	82	33	84	92	29	65	102
Average length [ $\mu\text{m}$ ]	303	133	136	96	141	160	94	147	126	142	210	188
Minimum lenght [ $\mu\text{m}$ ]	303	26	26	28	10	28	20	28	15	41	5	22
<b>Maximun lenght [<math>\mu\text{m}</math>]</b>	<b>303</b>	<b>387</b>	<b>476</b>	<b>237</b>	<b>462</b>	<b>840</b>	<b>291</b>	<b>534</b>	<b>411</b>	<b>373</b>	<b>696</b>	<b>1062</b>
Mean deviation [ $\mu\text{m}$ ]		87	89	55	88	157	59	108	91	75	141	148
Total crack length [ $\mu\text{m}$ ]	303	7432	9776	1823	11875	13104	3090	12385	11635	4115	13629	19178
<b>Cracks density [<math>\text{mm}^{-1}</math>]</b>	<b>0.05</b>	<b>1.43</b>	<b>2.11</b>	<b>0.31</b>	<b>2.28</b>	<b>2.82</b>	<b>0.53</b>	<b>2.38</b>	<b>2.51</b>	<b>0.71</b>	<b>2.61</b>	<b>4.13</b>
Average density [ $\text{mm}^{-1}$ ]	1.12			1.71			1.73			2.36		

**Table 8.1:** Statistics of cracks length and number in each sample.

## 8.2.2 Grain orientation relations

In order to study in more details the effect of coalescence undercooling on the formation of hot cracks, an estimation of the grain boundary energy is essential.

Figure 8.19 shows maps of grain orientation as recorded by an EBSD detector (see Sec. 5.2). These maps cover the whole laser trace and are reconstructed from several images. The grain structure of the unmodified metal is visible together with the structure of the remelted grains. The software provided with the EBSD system can then look for the zones with a strong variation of orientation and identify them as grain boundaries. Figure 8.20 shows the same laser traces as represented on Fig. 8.19 but with a representation of the grain boundaries. A colour code is used to represent the scalar estimation of the boundary misorientation  $\theta$  (see Sec. 5.2). Note that very low misorientation boundaries cannot be detected as they are considered as belonging to the same grain.

The last step is to identify the position of fractures on this EBSD map. Yet, the pictures directly taken with the secondary electron detector of the microscope could not be superimposed directly with the EBSD maps. Indeed, these maps are taken with a  $70^\circ$  tilt angle which results in an appreciable deformation of the picture. Hopefully, the EBSD detector also provides a map of the signal intensity, called the band contrast field. As the signal in fractures is very low, this information allowed us to localize their position.



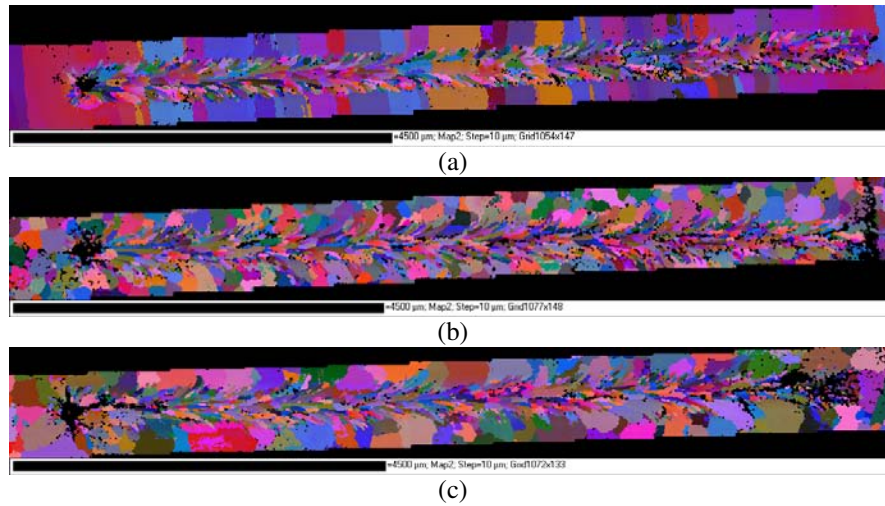


**Figure 8.19:** Map of the whole laser trace as analysed by EBSD, each colour corresponds to a grain orientation ( $v_b=20$  mm/s). (a) NGR (b) GR (c) GR + Ba.

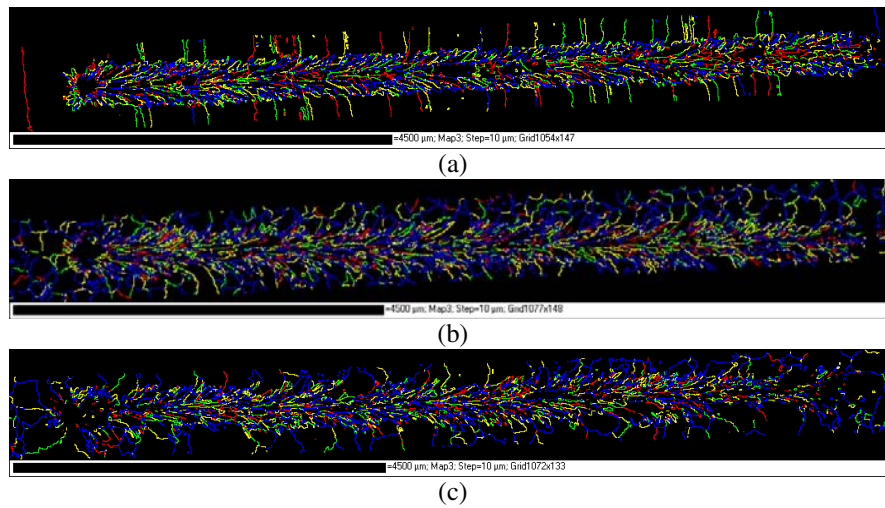


**Figure 8.20:** Same laser traces, the colours indicates the misorientation  $\theta$  at grain boundaries. red:  $5^\circ < \theta \leq 20^\circ$ , green:  $20^\circ < \theta \leq 30^\circ$ , yellow:  $30^\circ < \theta \leq 40^\circ$ , blue:  $40^\circ < \theta \leq 45^\circ$ .

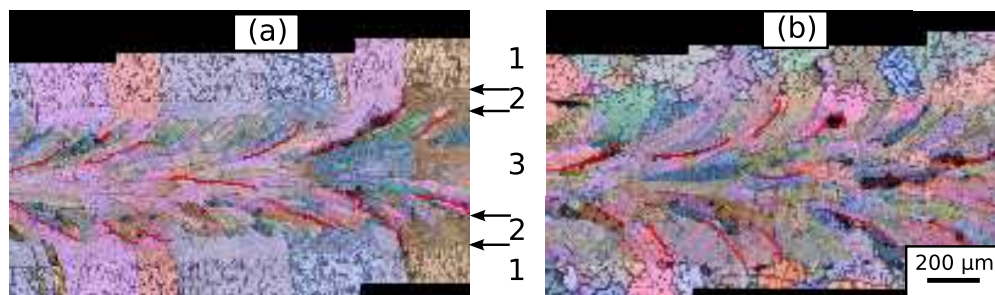


**Figure 8.21:** Superposition of the Euler angle indexation and of the band contrast information. The cracks are outlined in red. (a) NGR (b) GR ( $v_b=20$  mm/s)

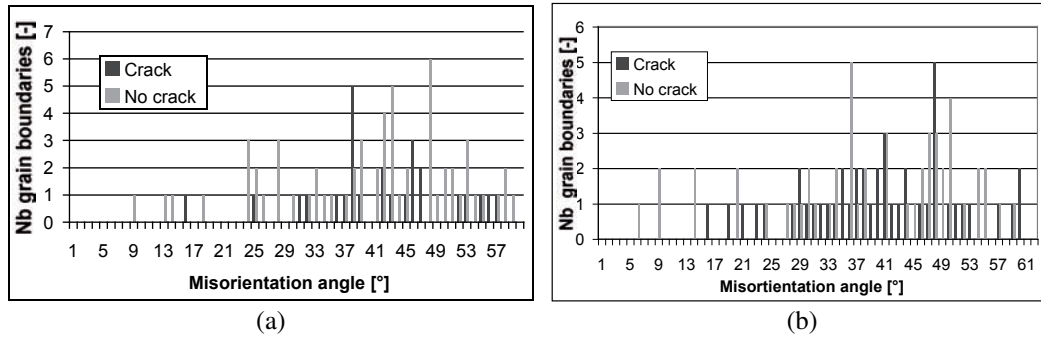


**Figure 8.22:** Statistics of the number of lateral crack as a function of the scalar estimate of grain boundary misorientation  $\theta$ . (a) GR (b) GR + Ba ( $v_b=30\text{mm/s}$ )

The superimposition of the orientation map together with the band contrast map is shown on Fig. 8.21. The cracks have been outlined in red. This superimposition also reveals the microstructure of the unmodified metal and therefore allows to distinguish three zones. Zone 1, the metal is unmodified. Zone 2, the metal has been remelted but has grown epitaxially from the grains located at the weld trace periphery. Zone 3, new grains have nucleated and grown in the direction of the temperature gradient. This last morphology is due to the strong convection in the liquid melt, induced by the Marangoni effect [153].

As expected, the cracks are always observed at the grain boundaries and therefore their shape is imposed by solidification mechanisms. It is interesting to note that on the NGR alloy, no cracks are observed in the epitaxial zone, whereas they are present in the GR alloy. Indeed, the columnar microstructure in the NGR alloy results from a growth selection. All the grains have one crystallographic axis approximately oriented in the same direction (the direction of the thermal gradient during the solidification of the columnar grains). Therefore, the average misorientation between two columnar grains is lower than between two equiaxed grains. As a consequence, in the NGR alloy the misorientation between two epitaxial grains is relatively low and no crack forms. This mechanism explains the influence of the refining on the crack statistics (Table 8.1).

Finally, the repartition of grain boundary misorientation is reported on Fig. 8.22 for two laser traces on a GR alloy, without and with Ba. Cracked grain boundaries are reported with a red bar whereas grain boundaries without cracks are reported with a yellow bar. No cracks are observed at very low misorientations. For the alloy without Ba only one crack is observed for  $\theta < 25^\circ$  whereas several cracks are observed for the alloy with Ba.

These results tend to corroborate two important points (Sec. 2.3.5).

- The coalescence of grains can be decisive for the formation of hot cracking.
- Addition of a surfactant such as Ba increases the coalescence undercooling and therefore increases hot cracking sensitivity.

## Chapter 9

# Transitions of the mushy zone

In this chapter, we present results obtained with the KPL model. This relatively simple model already allows to study transitions which occur during solidification (Sec. 2.3.6).

## 9.1 Grain structure evolution

### 9.1.1 Formation of grain clusters

The solidification model presented in Chap. 6 allows to compute the solidification of large mushy zones. Figure 9.1 shows the type of result that can be obtained under steady conditions for the directional solidification of an Al-1wt%Cu alloy [136]. The thermal conditions of this Bridgman-type solidification are a vertical thermal gradient of 60 K/cm and a velocity of  $1.6 \times 10^{-2}$  cm/s (*i.e.*, cooling rate of -1 K/s). The average grain density was fixed to  $10^8 \text{ m}^{-2}$ , *i.e.*, average grain size of  $100 \mu\text{m}$  (14 000 grains in the present simulation).

The temperature profile is shown on the right of Fig. 9.1 together with the average solid fraction profile,  $g_s$ , computed in horizontal sections of the grain structure shown at the center. The liquid is shown in black and the grains with various grey shades. As the grains are much smaller than the extent of the mushy zone ( $100 \mu\text{m}$  compared to more than 1 cm), 4 enlargements of the grain structure are shown on the left with the corresponding scale for typical regions of the mushy zone that are further discussed hereafter. The location of these zones in the grain structure is indicated with rectangles.

In this low-concentration alloy,  $g_s$  rapidly increases just below the liquidus and accordingly the liquid channels are already fairly narrow in the first enlargement (Fig. 9.1(a)). Their width is mainly a function of the distance between the associated nucleation centers: the closer the nuclei, the thinner the width of the liquid channel. As solidification proceeds, smaller channels get closed while larger ones remain open. Note that the coalescence undercooling at the final stage of solidification (Sec. 6.1.2) is not accounted for in this picture in order to emphasise the mechanical contact between the grains. Indeed, nanometric liquid channels already provide a important mechanical resistance (see Sec. 7.2). This phenomenon leads to the formation of *grain clusters*, *i.e.*, a cluster being defined as a group of connected solid grains. Such clusters are observed on hot tear fractographies (Sec. 8.1.2). In Fig. 9.1, the grains belonging to the same cluster are shaded with the same grey level.

The 4 zooms in Fig. 9.1 characterize well the evolution of the cluster morphology

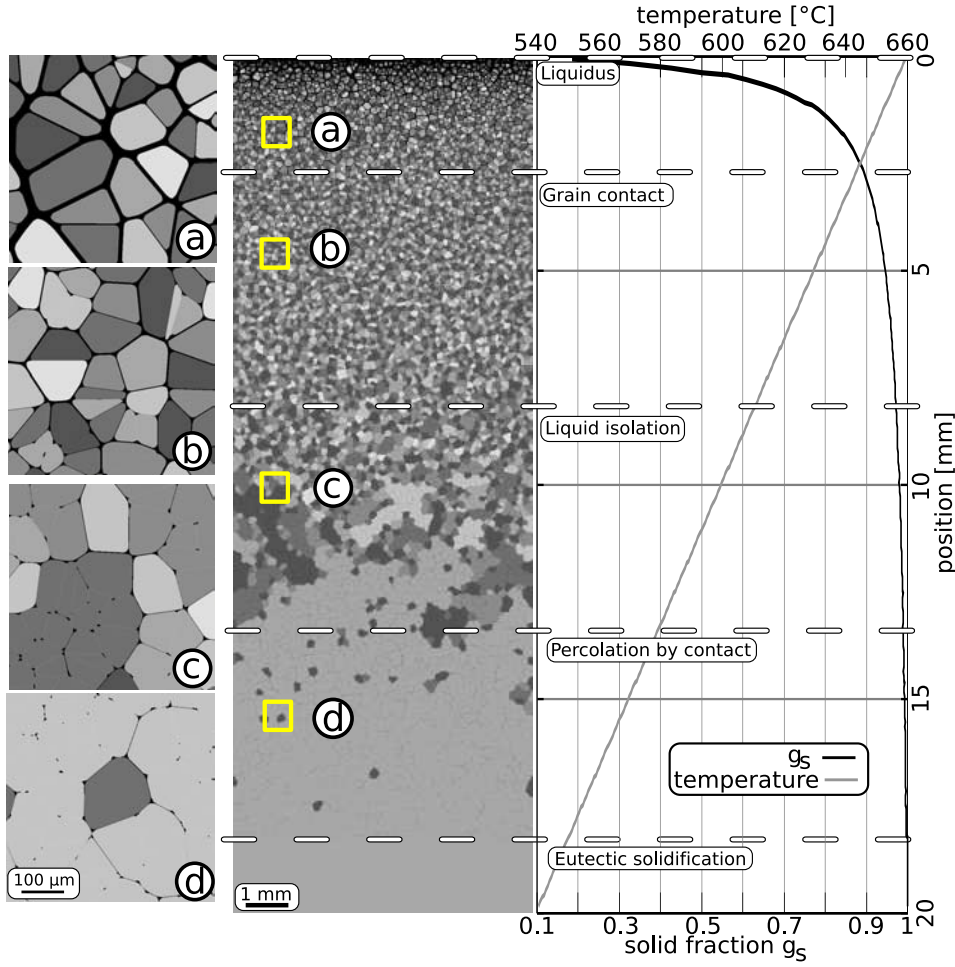


**Figure 9.1:** Calculated mushy zone for an Al-1wt%Cu alloy cooled down at -1 K/s in a gradient of 6000 K/m. In order to emphasize the formation of grain clusters, grains in mechanical contact are shaded with the same grey level.

in the mushy zone: in (a) (typically for  $0 < g_s < 0.89$ ), most of the grains are isolated; in (b) ( $0.89 < g_s < 0.97$ ), clusters of a few grains are formed; in (c) ( $0.97 < g_s < 0.99$ ), larger clusters are visible, with a few isolated liquid films remaining inside; in (d) ( $0.99 < g_s < 1$ ), the solid network is continuous and continuous liquid films in the mush no longer exist. These different stages are further analysed in this section. But note already that cluster formation is directly induced by the stochastic nature of the nucleation centre location, a feature that has not been considered in past simulation works related to hot tearing.

In order to quantify the clustering or aggregation of grains, it is interesting to compute the specific solid-liquid surface (in 2D length),  $S_v$ , *i.e.*, the surface of the solid-liquid interface,  $S_{s/l}$ , divided by the volume (surface in 2D) of the domain,  $\Omega$  (see also Sec. 3.2.1). This quantity can be normalised by the characteristic length scale of the microstructure  $d$ , in the present case the grain radius:

$$S_v^\circ = \frac{S_{s/l}d}{\Omega} \quad (9.1)$$

Figure 9.2 shows the computed normalised specific surface,  $S_v^\circ$ , as a function of  $g_s$ ,

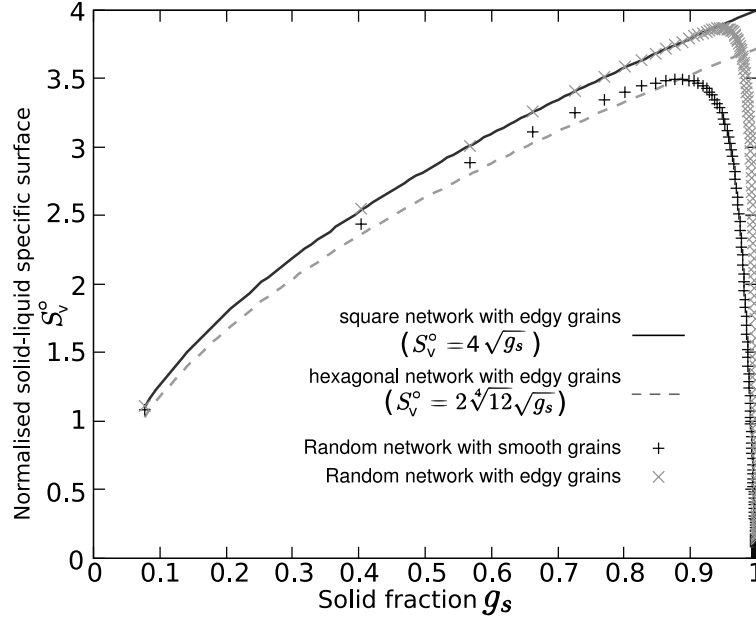


**Figure 9.2:** Normalised specific solid-liquid interfacial area,  $S_v^o$ , as a function of the volume fraction of solid. The theoretical curves calculated for the hexagonal and square networks are also shown.

for a small isothermal volume of an Al-1wt%Cu alloy cooled down at -1 K/s. The + and the × correspond to the random network of smooth and edgy grains, respectively. These two curves are compared with the regular square and hexagonal arrangements of edgy grains, the lowest normalised specific surface occurring for the hexagonal network, at least for  $g_s < 0.8$  (analytical expressions given in Fig. 9.2). As can be seen,  $S_v^o$  for these regular arrangements raises monotonically with the solid fraction until  $g_s = 1$  where it falls abruptly to 0. For the random numerical models,  $S_v^o$  has a maximum and smoothly falls to 0, even for the edgy grains. This maximum is reached when the natural increase of solid-liquid interface with grain size is compensated by the progressive closure of liquid channels, *i.e.*, this maximum reveals the formation of an increasing number of clusters. As the grains are slightly rounded in the smooth grain model, they come into contact earlier ( $g_s = 0.89$ ) as compared with the edgy grain model ( $g_s = 0.92$ ). The value of  $g_s$  corresponding to the maximum of  $S_v^o$  will be denoted  $g_{s,maxS}$ , and corresponds to a number of contacts between grains that is sufficient to overcome the increase of the solid-liquid surface during solidification. It has been marked with a dashed white line in Fig. 9.1 and is referred to as *grain contact*.

### 9.1.2 Localization of feeding

In order to study the permeability of the mushy zone, an isothermal volume element of the mushy zone is considered at various instants (or values of  $g_s$ ). Neglecting solidification shrinkage and imposing a pressure difference between the left and right vertical sides of the domain while the top and bottom boundaries are closed, the Poiseuille flow is computed for a volume element containing typically  $50 \times 50$  grains (size  $5 \times 5 \text{ mm}^2$ ). This numerical experiment allows to view the mush as a homogeneous porous medium and to compute its global permeability.

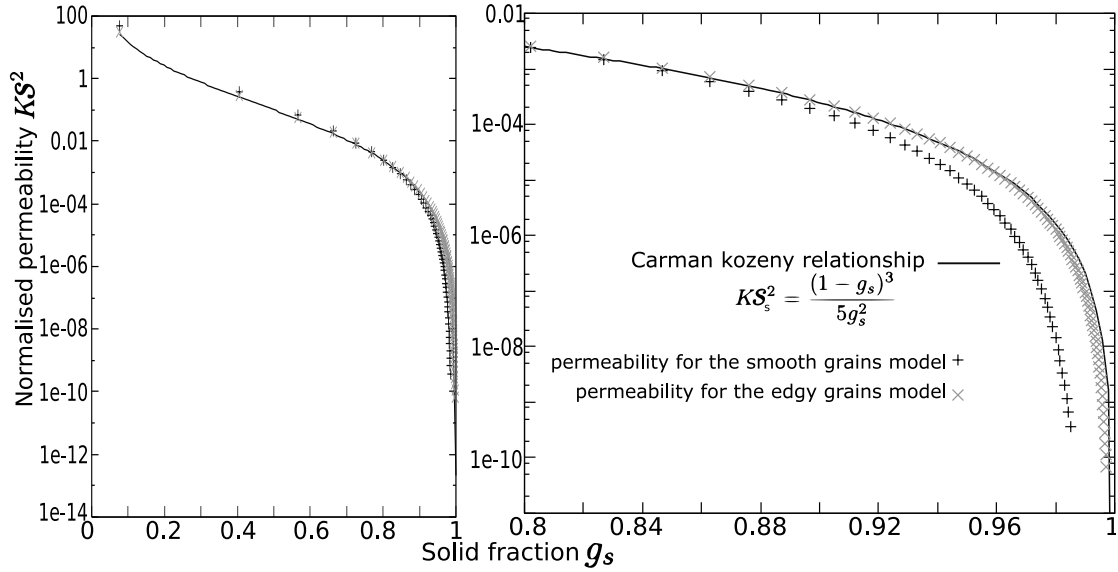


**Figure 9.3:** Permeability,  $\kappa$ , normalised with the square of the intrinsic specific solid-liquid interface,  $S_s$ , as calculated for a random network of grains with the KPL model, assuming edgy or smooth grains. The Kozeny-Carman (KC) relationship is also represented for comparison.

Figure 9.3 shows the computed permeability  $\kappa$  normalised by the square of the intrinsic specific surface  $S_s$ , which is the specific surface (length in 2D) of the solid-liquid interfaces per unit volume of solid  $V_s$ , *i.e.*,  $S_s = \frac{S_v}{g_s}$ . The Kozeny-Carman (KC) relationship which relates the normalised permeability of a packed bed to the solid fraction is also displayed. As presented in Sec. 3.2.3, the general form of this equation is derived from a theoretical network of pipes, while the factor 5 is empirical but shows good agreement with most grain arrangement [69]. Note that this form of the KC equation is presented as it is widely used in hot cracking literature and allows a direct comparison with experimental work [90], the form of Eq. 3.31 naturally gives the same results. As can be seen, the permeability calculated with the KPL model, for both smooth and edgy grains (but without losses!), follows the KC relationship fairly accurately up to very high solid fraction. But for  $g_s > 0.92$  ( $0.98$ ) with the smooth (edgy) grain model, the calculated permeability becomes significantly lower than the prediction of KC. Whereas, for a regular hexagonal network of grains, it was found that the calculated permeability follows the KC relationship until the very end of solidification [128]. This can be explained by two factors:

- First of all, at high  $g_s$ , a few liquid channels are still present but no longer participate to feeding, whereas in a regular arrangement of grains, all the channels remain connected and liquid until  $g_s = 1$ . In this respect, the smooth grain model leaves isolated liquid pockets at triple junctions and thus induces a departure from KC earlier as compared with the edgy grain model. This situation is actually closer to observations on organic or metallic alloys, which reveal liquid droplets in between grains or dendrites (see, *e.g.*, Sec. 2.2.1 Fig. 2.7)[35]. Despite the

<sup>1</sup>In Ref. [136] the notations for  $S_s$  and  $S_v$  are inverted for a coherency with the work of Nielsen *et al.* [90]. In this manuscript we use the present notations which are more widely accepted.

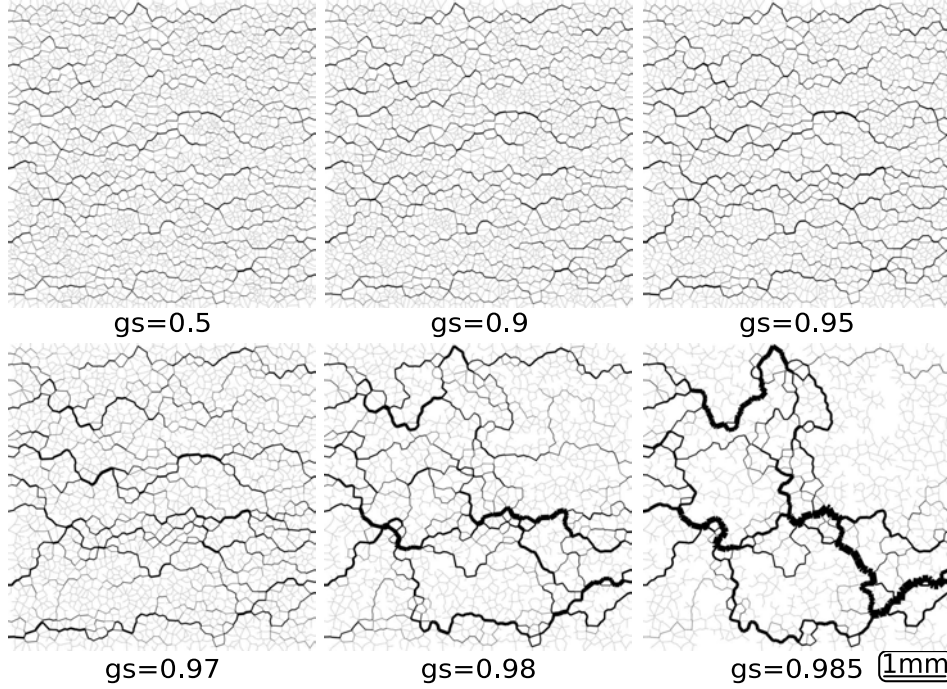


**Figure 9.4:** Fluid flow through an isothermal mushy zone volume element ( $5 \times 5 \text{ mm}^2$ ), the width of each channel being proportional to the local flow normalized by the overall flow.

fact that these liquid droplets have a positive curvature, the effect of which is not taken into account with the solidification model (Sec. 6.2), the smooth grain model is nevertheless a much better approximation. Therefore this model will be exclusively used hereafter, unless otherwise stated.

- The second reason of departure from the KC relationship can be found in Fig. 9.4. In this figure, the intergranular flow calculated with the KPL smooth grain model is represented with a line, the thickness of which is proportional to the local flow and normalized by the overall flow (*i.e.*, relative flow intensity). At low  $g_s$ , the intergranular flow is fairly well distributed among the different channels. When  $g_s > 0.97$ , the flow tends to be localized along preferential paths. For  $g_s = 0.98$ , the flow only goes through a few preferential paths while most open liquid channels, despite the fact they are still connected to the continuous channel network, carry a negligible part of the flux (thin grey channels).

As pointed out by A. Hoadley, this localization of flux at high solid fraction should have an influence on the tortuosity  $r$  of the flow, *i.e.*, the ratio of the actual path length of the flow to the length of the porous media (Sec. 3.2.3) [154]. In the present numerical calculation, tortuosity is estimated by the following formula:

$$r = \frac{1}{L_{tot}\Phi_{tot}} \sum_i L_i \Phi_i \quad (9.2)$$

where  $L_{tot}$  is the length of the sample,  $\Phi_{tot}$  is the overall liquid flow in the mush,  $L_i$  is the length of channel  $i$  and  $\Phi_i$  is the liquid flow through this channel<sup>2</sup>, the sum being done on

<sup>2</sup>As no losses are considered here, fluid flow is constant within a channel.



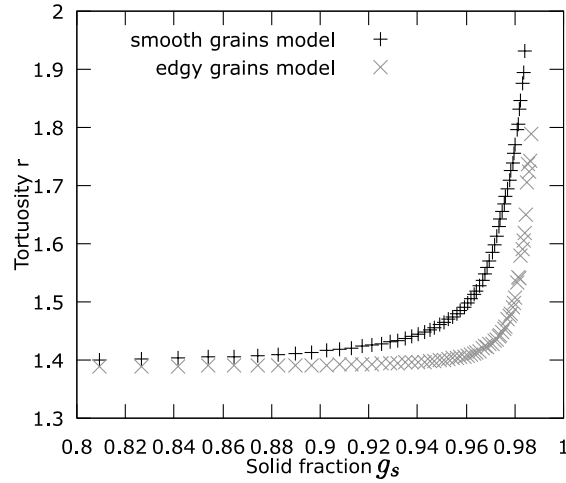


**Figure 9.5:** Evolution of tortuosity  $r$  as a function of solid fraction.

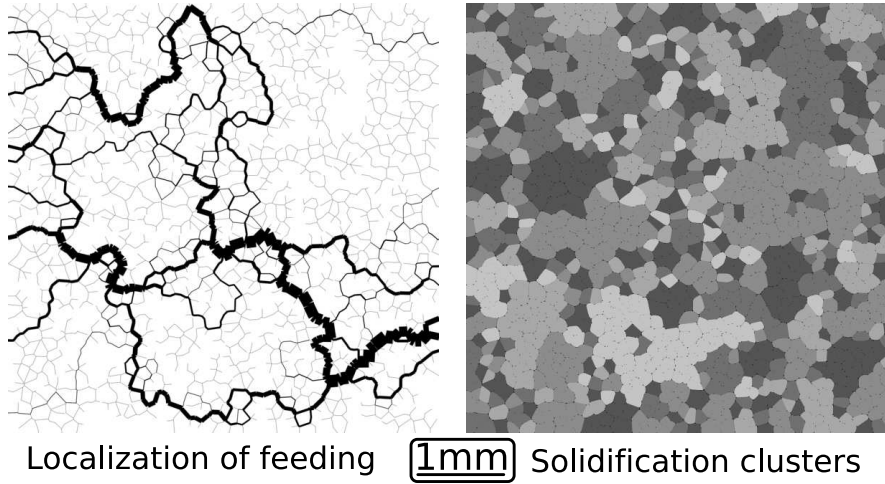


**Figure 9.6:** Comparison between flow localisation and grain clusters structure for an isothermal mushy zone at  $g_s=0.985$ .

every channel in the mush. This quantity is the ratio of the average path length weighted by the local flux to the sample length. Therefore, it corresponds to the definition of tortuosity.

Figure 9.5 shows tortuosity  $r$  measured as a function of solid fraction for both the edgy and smooth grains model. Up to very high solid fraction,  $r$  is constant around 1.4 which is, once again, in good agreement with the KC law (Eq. 3.32). Around  $g_s = 0.92$  the tortuosity of the mush increases and diverges as the solid fraction increases. Note that the increase of the tortuosity precisely corresponds to the divergence between the KC law and the calculated permeability. However, the sole introduction of the tortuosity divergence in the KC law is not sufficient to reproduce the strong divergence of permeability as calculated.

Figure 9.6 shows the localization of feeding and the cluster structure of the same isothermal mushy zone with a solid fraction  $g_s=0.985$ . The characteristic length scale of feeding (typically 2 mm at this solid fraction) is substantially larger than the charac-



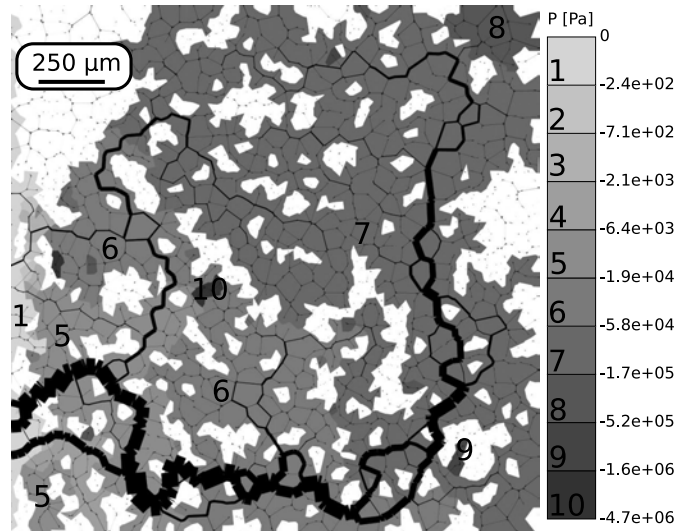


**Figure 9.7:** Pressure profile and fluid flow induced by solidification shrinkage for a  $2 \times 2 \text{ mm}^2$  mushy zone element. In this sample  $T = 590^\circ\text{C}$  and  $g_s = 0.984$ . The width of each channel is magnified proportionally to the local flow and its local pressure is indicated with a grey scale (drawn also within the adjacent grains).

teristic size of the clusters (typically 1 mm). Indeed, a single channel with a very low permeability can block a whole feeding path. Such finding illustrates well the predictions of the continuum percolation theory as presented in Sec. 4.1.2 [17, 101].

Figure 9.7 is another illustration of feeding localisation at high volume fraction of solid. It shows a mushy zone of an Al-1wt%Cu alloy with  $g_s = 0.98$ , the liquid flow in this case being associated with solidification shrinkage. The flow is imposed nil on the right side of the domain, while a nil pressure is imposed on the left side (the top and bottom edges are again closed). The grey scale in this case represents the pressure in the liquid phase. Although the pressure is defined only in the liquid channels, the grey scale is also represented within the grains for visibility. White areas correspond to liquid channels which are no longer connected to the main liquid pocket on the left and in which the pressure calculation is no longer performed. The width of the liquid channels has been magnified again proportionally to the local flow.

It appears that there is mainly one path that feeds the entire mush. As a result, a large pressure drop occurs along the main feeding path, typically from 0 kPa at the entrance to -170 kPa near region 7. It is clear that, in real cases, such large pressure drops should be released by the formation of pores/hot cracks. A few channels (white areas) are no longer fed while huge negative pressures (MPa) can be observed in some liquid channels (regions 9 or 10). Such high depression, associated with the hypothesis of fixed and rigid grains, will clearly compete with the solid grain deformation/displacement when mechanical aspects are considered (Sec. 10.1).

The feeding ability of a mush can be divided into two steps. At low volume fraction of solid, the mush is well described with a KC law with the grain size as a typical length scale. At higher value of  $g_s$ , it is described by the percolation theory, *i.e.*, with a characteristic length scale which increases with the solid fraction. At this stage, the treatment of the mush as a continuum is not straightforward as feeding is extremely localised. The transition between these two regimes is linked with the appearance of

isolated liquid channels, *i.e.*, open liquid channels that are not connected to the feeding network anymore. This *interdendritic separation*, a term widely used in the literature to describe this occurrence (Sec. 2.3.6)[66, 56], is of course ideal for the initiation of hot tears (Sec. 3.1.1)[23, 68]. In the present contribution, we also argue that liquid feeding is fairly localised at this stage.

From these simulations, the volume fraction of solid,  $g_{s,1\%ilc}$ , at which 1% of the liquid channels become isolated from the feeding network is computed and called *liquid isolation*. For an Al-1wt%Cu cooled down at -1 K/s,  $g_{s,1\%ilc} = 0.97$  (see the corresponding white dashed line drawn in Fig. 9.1). Note that the divergence of the tortuosity can be equally used as an indicator of this transition.

It should still be kept in mind that this model overestimates the volume fraction of solid at which flow becomes localized, as it is still 2D and neglects any liquid encapsulated within the grains due to a destabilisation of the interfaces, *i.e.*, globular-dendritic grains.

### 9.1.3 Percolation of solid grains

By definition, a cluster is fully surrounded by a liquid film. As solidification proceeds, the size of the clusters increases until a unique cluster spreads over the whole domain. Note that, in 2D, only one phase can be continuous, either the solid or the liquid<sup>3</sup>, whereas both can be continuous in 3D. In a volume element of uniform temperature such as that shown in Fig. 9.6, the continuity of the liquid path from the left to the right side can be tested. When there is no longer a liquid path, the solid phase has percolated. In the present case, two criteria can be selected to detect this percolation: 1) the grains can be in "mechanical contact" but still separated by nanometric liquid films; 2) the grains are coalesced and the interfaces are dry. These two percolation criteria are called *percolation by contact* and *percolation by coalescence* or *percolation by bridging*, respectively. The corresponding values of  $g_s$  are labelled  $g_{s,pct}$  and  $g_{s,pbr}$ , respectively. In the first case, a continuous liquid film still exists but does not allow feeding anymore. It could induce brittle fracture along a still wet path. In the second case, the mechanical behaviour of the mush should be very close to that of the fully (ductile) solid material as only a few discontinuous liquid channels remain. In our model, for an Al-1wt%Cu cooled down at -1 K/s,  $g_{s,pct} = 0.985$ , a value which is in good agreement with that introduced in the literature [23, 68]. It is also drawn with a dashed white line in Fig. 9.1 and corresponds visually to the formation of a continuous cluster. Note that the line of percolation by coalescence is not reported in this figure as it occurs fairly below the eutectic solidification.

Figure 9.8 shows the structure of the clusters for the same mushy zone according to the two percolation criteria. It is clear that clusters formed of truly coalesced grains are always much smaller than clusters of grains which are simply in mechanical contact (with still a nanometric liquid layer). On the second column of Fig. 9.8, a single cluster spawns in the mush according to the mechanical contact criterion, while a relatively fine cluster structure remains according to the bridged interface criterion.

Such a situation illustrates the experimental observation of a transition from brittle to ductile failure below the eutectic temperature (Sec. 8.1.1). Moreover, it raises, once

<sup>3</sup>Note that in our case the situation is different from site percolation as liquid channels and solid bounds are along different networks (dual one from each other) [131].

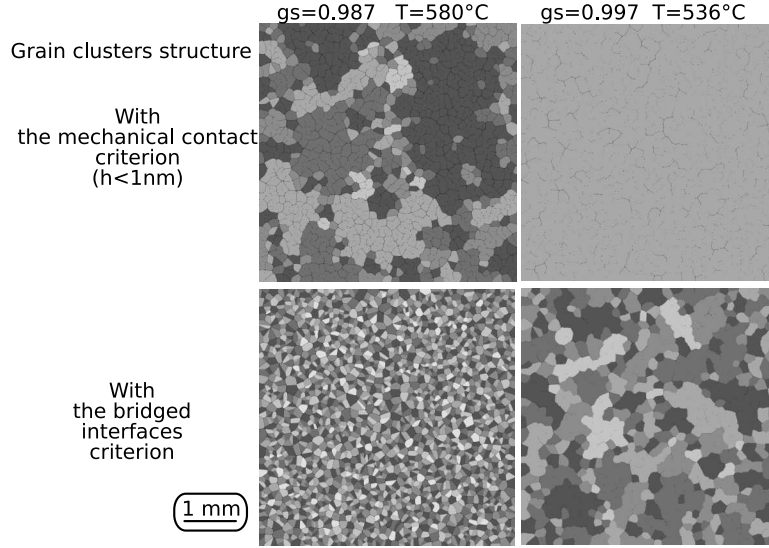


**Figure 9.8:** Grain clusters structure for two different criteria, *mechanical contact* and *coalesced/bridged interfaces*. The alloy considered is an Al-1wt%Cu cooled at -1K/s.

again, the question of the influence of eutectic solidification on the definitive bridging of the solid.

## 9.2 Morphological maps for the mushy zone

### 9.2.1 Definition of the transition points

Four transitions have been identified in the previous section: 1)  $g_{s,maxS}$  (grain contact), when the grain contacts overcome the increase of the solid-liquid interface; 2)  $g_{s,1\%ilc}$  when 1% of the liquid channels are isolated from the feeding network; 3)  $g_{s,pct}$  when percolation of the solid grains is achieved by simple contact between them (with the possibility of having nanometric liquid films in between); and 4)  $g_{s,pbr}$  when the solid grains are percolated via truly coalesced/bridged boundaries.

The first two characteristic values of  $g_s$  do not correspond to percolation transitions, just to some states of the mushy zone, but the two last ones are. At  $g_{s,pct}$  or  $g_{s,pbr}$ , the morphology of the mushy zone switches from a continuous liquid path to a continuous cluster. As described in Sec. 4.1.3, the standard error for the percolation threshold (*i.e.*, apparition of a continuous cluster) varies according to a power law of the domain (sample) size  $D$  [17] :

$$\sqrt{\langle (g_{s,c} - \langle g_{s,c} \rangle_D)^2 \rangle_D} >_D \sim D^{-\frac{1}{\nu}} \quad (9.3)$$

The average labelled  $\langle \cdot \rangle_D$  is performed over a large number of simulations done for a given domain of size,  $D$ , with various random nuclei configurations. Each of these simulations will give a slightly different value of  $g_{s,c}$ , the threshold value at which percolation occurs (in our case, formation of one big cluster by contact or by bridging).  $\langle g_{s,c} \rangle_D$  is the average percolation threshold for a domain size  $D$ . Thus, the left hand term of Eq. 9.3 is the mean deviation of the threshold values. The coefficient  $\nu$  is the correlation length exponent, equal to 4/3 in 2D (Sec. 4.1.1) [17].

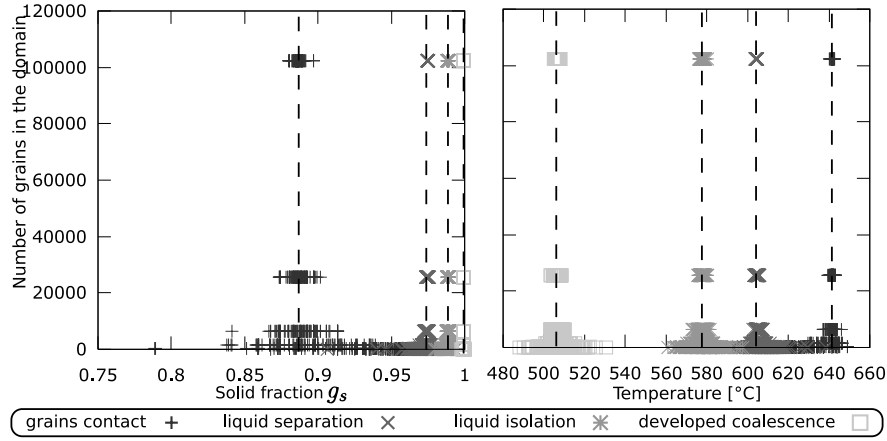


**Figure 9.9:** Different transitions of the mushy zone (horizontal axis) as a function of the domain size (vertical axis) according to the following criteria: grain contact (+),  $g_{s,maxS}$ , liquid isolation ( $\times$ ),  $g_{s,1\%ilc}$ , percolation by contact ( $*$ ),  $g_{s,pct}$ , and by bridging ( $\square$ ),  $g_{s,pbr}$ . For each domain size, 100 calculations were carried out with various repartitions of the nuclei.

In order to check this tendency, simulations have been carried out for an isothermal square domain containing from 100 to 102400 grains. For each domain size, 100 simulations were performed with different repartitions of the nuclei. The computations were done for an Al-1wt%Cu alloy cooled down at -1 K/s. Figure 9.9 shows the computed solid fraction and temperature at which the 4 transitions are observed as a function of the domain size. Each symbol corresponds to one computation. As can be seen, small domains give a wide spread of the percolation thresholds, while for large domains, the results of the computations are almost superimposed. Nevertheless, the scattered values for small domains are well centred around the mean value. For the two percolation criteria, the domain dependence (Eq. 9.3) is well verified: the exponent  $1/\nu$  is found to be  $0.71 \pm 0.015$  for the percolation by contact and of  $0.73 \pm 0.04$  for the percolation by bridging.

Although the grain contact and liquid isolation values,  $g_{s,maxS}$  and  $g_{s,1\%ilc}$ , do not correspond to percolation phenomena, they have also been reported in Fig. 9.9. They converge to well defined values when the size  $D$  of the domain increases. For grain contact, a coefficient close to the correlation length exponent is found ( $1/\nu = 0.704 \pm 0.001$ ) whereas for liquid isolation, this coefficient is closer to unity ( $1/\nu = 1.11 \pm 0.04$ ). For this last exponent, the discrepancy with the percolation exponent value might be due to the influence of the domain boundary on the liquid isolation criterion (*i.e.*, a liquid film channel touching the border becomes isolated as soon as the two neighbouring channels are closed, whereas, for a liquid film channel within the domain, with four first neighbours in average, there are many more possible paths that can keep it connected to the main liquid network).

Although limited to 2D, this study brings already two valuable informations: First, it enables to determine a critical threshold value of  $g_s$  according to a given criterion for an infinite system; Second, for a finite volume of a real mushy zone, *e.g.*, in a thermal gradient, it allows to assess the dispersion of this critical threshold value due to the specific configuration. Such dispersion is especially important for the occurrence of hot tears, which presents an intrinsic random nature (see, *e.g.*, Sec. 8.1.1 Fig. 8.2(c)).

### 9.2.2 Parameters sensitivity

The 4 calculated transitions are reported in the Al-Cu phase diagram as a function of two parameters: the cooling rate,  $\dot{T}$ , and the solid-liquid interfacial energy,  $\gamma_{sl}$  (Fig. 9.10). For a fixed density of grains, the first parameter controls essentially microsegregation and thus the temperature at which the first grain contacts are established. More precisely, microsegregation is controlled via the Fourier number,  $Fo$ :

$$Fo = \frac{D_s \Delta T_0}{d^2 |\dot{T}|} \quad (9.4)$$

where  $d$  is the average grain radius,  $\Delta T_0$  the equilibrium solidification interval and  $D_s$  is the diffusion coefficient in the solid. Although the Fourier number influences the actual solid fractions at which the various transitions occur<sup>4</sup>, its main influence is through the  $T(g_s)$  relationship itself: for a fixed value of  $g_s$  characterising a given transition of the mushy zone, a fast cooling rate (low  $Fo$ ) tends to give a relationship  $g_s(T)$  close to Scheil-Gulliver (*i.e.*, lower value of  $T(g_s)$ ), whereas a slow cooling rate (high  $Fo$ ) makes it closer to lever rule. Moreover, the cooling rate influences a second dimensionless number:

$$C = \frac{1}{d} \left( \frac{D_l \Gamma_{sl}}{|\dot{T}|} \right)^{1/3} \quad (9.5)$$

which corresponds to the ratio of the average radius of curvature at grain corners over the average grain size  $d$  (see Eq. 6.15). A fast cooling rate (small  $C$  number) lead to edgy grains, with a low amount of residual liquid, *i.e.*, contact between grains occurs at higher solid fraction.

The second parameter  $\gamma_{sl}$  is influencing the final stage of coalescence [33]: as repulsive grain boundaries, *i.e.*, boundaries which are characterised by a large coalescence undercooling, are given by  $\gamma_{gb} > 2\gamma_{sl}$ , lowering the value of  $\gamma_{sl}$  tends to increase the number of repulsive grain boundaries, *i.e.*, to delay the formation of percolation by bridging.

At the same time, decreasing the solid-liquid interfacial energy has a tendency to make the grains more edgy via its influence on the  $C$  number, and thus to increase the volume fraction of solid at which the transitions occur.

These trends are shown in Fig. 9.10 where the 4 transitions calculated with the granular model have been reported for various concentrations of Cu, keeping the same conditions as those of Fig 9.1. Note that the solidus has not been reported on the maps as it is meaningless, mainly due to microsegregation. As described above, an increased cooling rate makes the transition lines steeper. A decrease of the interface energy significantly shifts down the transition line associated with percolation by bridging and slightly shifts down the other transitions lines.

As expected, for very low solute content, a fully coalesced solid appears quickly, before eutectic solidification. Moreover, for a large nominal concentration in Cu (more than 8 wt% Cu), eutectic solidification occurs before contact between the grains. In the concentration range where the hot tearing sensitivity increases (0.5-3 wt% Cu), most of the solidification time is spent between liquid isolation and percolation by contact, where localisation phenomena are intense. For nominal concentrations where the

<sup>4</sup>In particular, no geometrical length arises at the two limits of Scheil-Gulliver ( $Fo = 0$ ) and of lever rule ( $Fo = \infty$ ), *i.e.*, all the liquid channels become closed at the same time when  $g_s = 1$ , and thus no gradual transition occurs within the mushy zone.

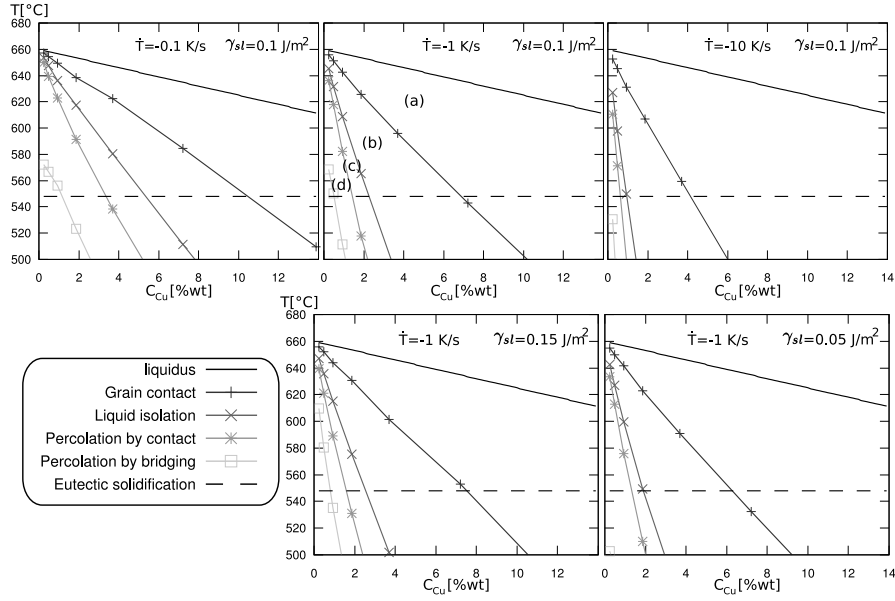


**Figure 9.10:** Morphological maps of the mushy zone for different values of the cooling rate,  $\dot{T}$ , and of the solid liquid surface energy,  $\gamma_{sl}$ . The domains labelled with the letters a-d correspond to the four grain structures in Fig. 9.1.

hot cracking sensitivity decreases ( $> 3$  wt% Cu), solidification time is spent between grain contact and liquid isolation. Note that, in a way, this finding is similar to the Clyne-Davis hot tearing criterion (Sec. 3.1.1)[23], but in the present model no a priori parameters are required.

These transitions might help in understanding the main deformation mechanism of the material at high temperature, in relation with hot tearing. Between the liquidus and the point of grain contact (*i.e.*,  $0 < g_s < g_{s,maxS}$ ), grains moves freely in the mush and liquid feeding is easy (figure 9.1 (a)). Between grain contact and liquid isolation (*i.e.*,  $g_{s,maxS} < g_s < g_{s,1\%ilc}$ ), the permeability of the mush decreases drastically and the formation of clusters starts to localise deformation (figure 9.1 (b)). Between liquid isolation and percolation by contact (*i.e.*,  $g_{s,1\%ilc} < g_s < g_{s,pct}$ ), feeding is almost impossible and very localised. Moreover, large clusters are present; this localises deformation induced by thermal contraction and solidification shrinkage at the cluster boundaries (figure 9.1 (c)). This region of the mushy zone is therefore very brittle. Between percolation by contact and percolation by coalescence (*i.e.*,  $g_{s,pct} < g_s < g_{s,pbr}$ ), the mechanical properties of the mush are very close to the fully solid material. Deformation of the mushy zone will be more ductile, but at some remaining liquid films, opening is still possible, with probably plastic deformation of the already established solid bridged (figure 9.1 (d)). Once the material has reached the line of percolation by coalescence, its mechanical properties are very close to the fully solid material.

# Chapter 10

## Mushy zone mechanics

### 10.1 Traction tests

#### 10.1.1 Redistribution of fluid

In order to investigate the mechanical properties of the mushy zone under a tensile load, two numerical experiments are used.

Their boundary conditions (BC) are presented on Fig. 10.1. On the left side, the fluid flux is imposed nil together with the solid velocity in the  $x$  direction (horizontal). The solid velocity in the  $y$  direction is free. Therefore, this BC corresponds to a symmetry plane of the problem. A similar BC is applied in the  $y$  direction, on the bottom side of the sample. On the right side, the solid velocity in the  $x$  direction is imposed to  $\dot{\epsilon}L$  where  $L$  is the size of the sample and  $\dot{\epsilon}$  the imposed strain rate. Moreover, the fluid velocity is imposed nil on this boundary<sup>1</sup>.

The two cases differ from the BC applied on the top boundary. In the first case (Fig. 10.1(a)), the pressure on the solid and on the liquid is imposed to  $P_0$ , which, therefore, corresponds to the average hydrostatic pressure on the system. Note that the fluid flux is not imposed and a fluid flow is possible via this boundary. Thus, this

<sup>1</sup>Note that for BC, the liquid flux is considered in the frame of the solid grains. With a Eulerian point of view, a fluid flux is observed due to the advection of the solid

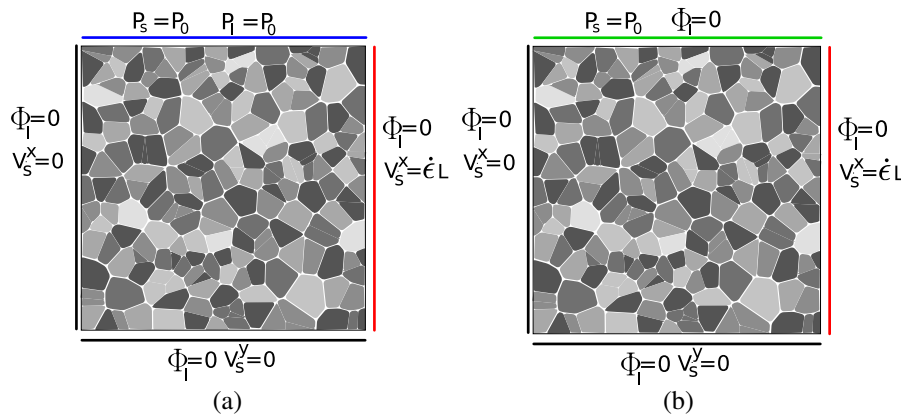


**Figure 10.1:** Boundaries conditions for two traction tests along the  $x$  axis. (a) With ideal feeding. (b) Without feeding.

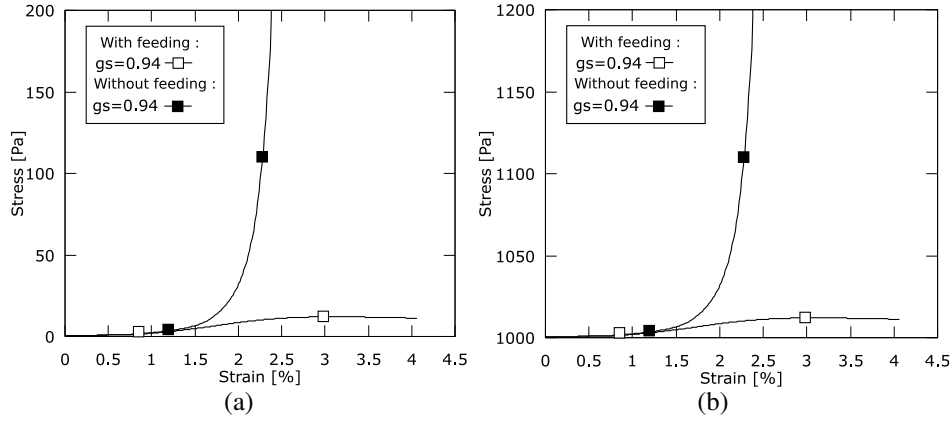


**Figure 10.2:** Stress strain curves for a sample at  $g_s = 0.94$  and with a strain rate  $\dot{\epsilon} = 4 \times 10^{-3} \text{ s}^{-1}$ . (a)  $P_0 = 0$  (b)  $P_0 = -1 \text{ kPa}$ .

situation corresponds to a sample in contact with a liquid pocket at pressure  $P_0$  and will be called "ideal feeding".

In the second case, the fluid flow is imposed nil on the top boundary. This corresponds to a situation where feeding is impossible. Note that these BC are similar to those in the model derived by Lahaie and Bouchard for a regular arrangement of hexagonal grains (see Sec. 3.1.3)[75].

Naturally, a real situation would be in between those two extremes, depending on the design of the casting. A pressure  $P_0$  is imposed on the solid. In both cases, the solid velocity on the top boundary is free, *i.e.*,  $V_s^x$  and  $V_s^y$  are not imposed.

In these numerical experiments, the solidification of the system is calculated first and then the mechanics of the mushy zone is computed without further solidification.

Figure 10.2 shows the stress-strain curves for a sample at  $g_s = 0.94$  cooled down at  $-1 \text{ K s}^{-1}$  before traction (this value will be exclusively used hereafter). The strain rate is  $\dot{\epsilon} = 4 \times 10^{-3} \text{ s}^{-1}$ .

The curves in Fig. 10.2(b) have been calculated for the same situation shown in Fig. 10.2(a) but with a pressure  $P_0$  1 kPa lower. The resulting curves can be perfectly superimposed, the stresses in Fig. 10.2(b) being simply shifted up by 1 kPa. Indeed,  $P_0$  corresponds to the external hydrostatic pressure imposed to the system, and as described by the Terzaghi effective stress, the behaviour of the mush only depends on the difference between the applied stress and the hydrostatic pressure (see Sec. 3.2.4)<sup>2</sup>. This remark is important as it allows to simply extent the following results to any value of the hydrostatic pressure.

At low strain, the two tests in Fig. 10.2(a) follow a similar line. At 1.5% strain, stress increases abruptly in the test without feeding, whereas it remains low in the test with perfect feeding.

This phenomenon can be understood by looking at the local deformation mechanisms. Figure 10.3 shows an isothermal mushy zone with a solid fraction of 0.92. This mushy zone is submitted to a traction with a strain rate of  $\dot{\epsilon} = 4 \times 10^{-3}$  but is represented

<sup>2</sup>From the numerical point of view, it is clear that a situation with no grain displacement and a uniform pressure is a solution of the problem matrix. Therefore, by linearity of the equations, any solution of the problem can be shifted up by a uniform value of the pressure without affecting the displacement of the grains.



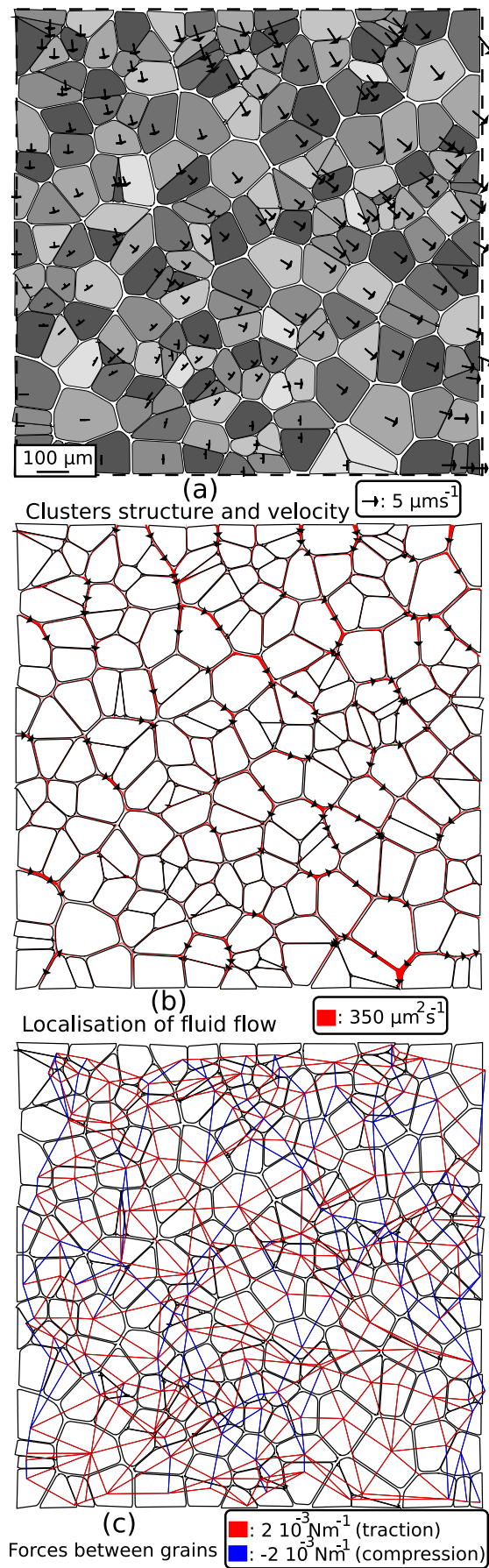


**Figure 10.3:** Mushy zone at zero strain for an isothermal mushy zone with  $g_s = 0.92$  and  $\dot{\epsilon} = 4 \times 10^{-3} \text{ s}^{-1}$ .

at nil strain. The cluster structure together with the grain velocity field is represented on the upper part of the figure.

On Fig. 10.3(b), the fluid flow has been represented with lines whose width is proportional to the fluid flow, the direction of the flow being represented by a black triangle. If two grains get closer, they squeeze out liquid from the channel and the width of the line increases (maybe more visible on Fig. 10.4). On the contrary, if they move away from each other, liquid is pumped in the channel. As can be seen on Fig. 10.3, deformation of the mush is achieved by fluid flow but these flows are small and remain extremely local. Therefore, a long-range feeding of the mush is not necessary. Both tests (with and without feeding) give the same behaviour of the mush. Stresses in the sample are very low.

Indeed, in Fig. 10.3(c) the forces between the grains are represented by a line whose width is proportional to the absolute value of the force. A blue (dark grey) line represents a compression force whereas a red (light grey) line represents a traction force. In this sample the forces are very low and the lines representing the forces are almost not visible.

Figure 10.4 shows the same mushy zone after 4% strain and with the possibility of feeding. On Fig. 10.4(a) the initial shape of the sample is represented by a dashed square. It is important to note that deformation is essentially localized in a few channels, roughly oriented normally to the traction direction. Therefore, to accommodate deformation, the fluid tends to flow from channels oriented in the direction of the stress to channels oriented normally to the stress. This is also confirmed by the representation of forces on Fig. 10.4(c) that shows traction in the  $x$  direction and compression in the  $y$  direction.

It is also interesting to note that fluid flow is much more important on Fig. 10.4(b) as compared with Fig. 10.3(b). However, the imposed strain rate is the same in both cases. This shows that redistribution of fluid occurs on more important distances with the accumulation of deformation. Fluid flow from the upper border is clearly visible (Fig. 10.4(b)) and allows to relax stresses in the upper part of the sample (Fig. 10.4(c)).

On Fig. 10.5, a similar mushy zone with the same deformation is represented in the case where no feeding is allowed. An important fluid flow can also be observed. Yet, as no feeding from the top is possible, fluid has to follow more difficult paths and therefore stresses in the samples are more important.

In summary, at low strain, deformation is accommodated by local redistribution of the liquid. As deformation gets more important, more channels get closed and fluid redistribution occurs at a larger scale. At that point, the feeding ability of the mush becomes important.

### 10.1.2 Transition in the feeding mechanism

Figure 10.6 shows stress-strain curves for various solid fractions. On Fig. 10.6(a) the same behaviour as described previously can be observed. Naturally, the deformation at which feeding becomes important decreases with the solid fraction.

For  $g_s > 0.97$  this behaviour is not observed anymore. The curves for the test with and without feeding do not follow the same line even at nil strain.

Once again, the local observation of the mushy zone brings some information. Figure 10.7 shows a mushy zone with 0.975 solid fraction. Even though the deformation of the mush is nil, an important redistribution of the fluid can be observed. Moreover,

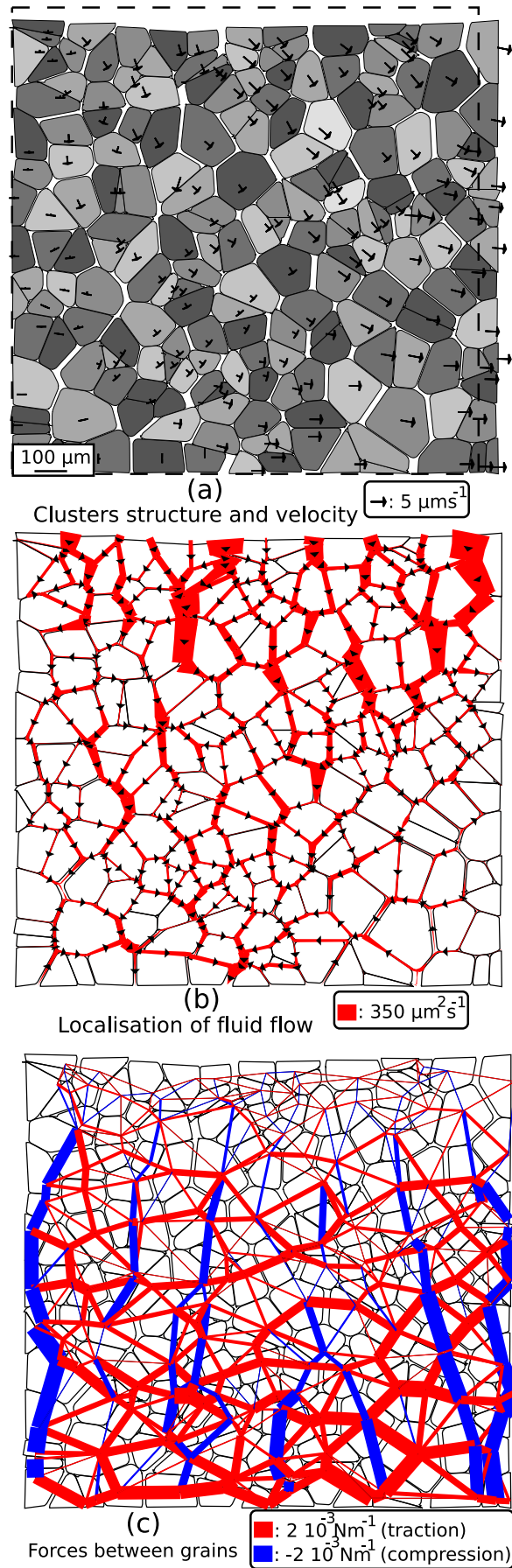


**Figure 10.4:** Mushy zone at 4% strain for an isothermal mushy zone with  $g_s = 0.92$  and  $\dot{\epsilon} = 4 \times 10^{-3} \text{ s}^{-1}$ . Feeding from the upper face is possible.

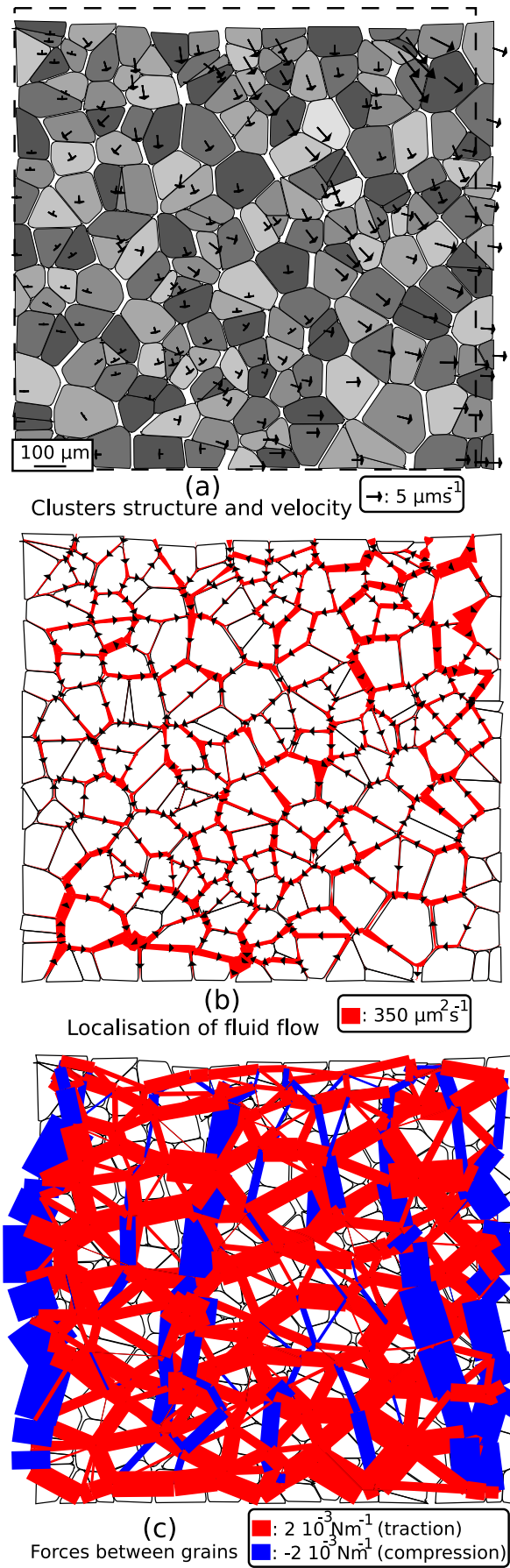


**Figure 10.5:** Mushy zone at 4% strain for an isothermal mushy zone with  $g_s = 0.92$  and  $\dot{\epsilon} = 4 \times 10^{-3} \text{s}^{-1}$ . Feeding is impossible.

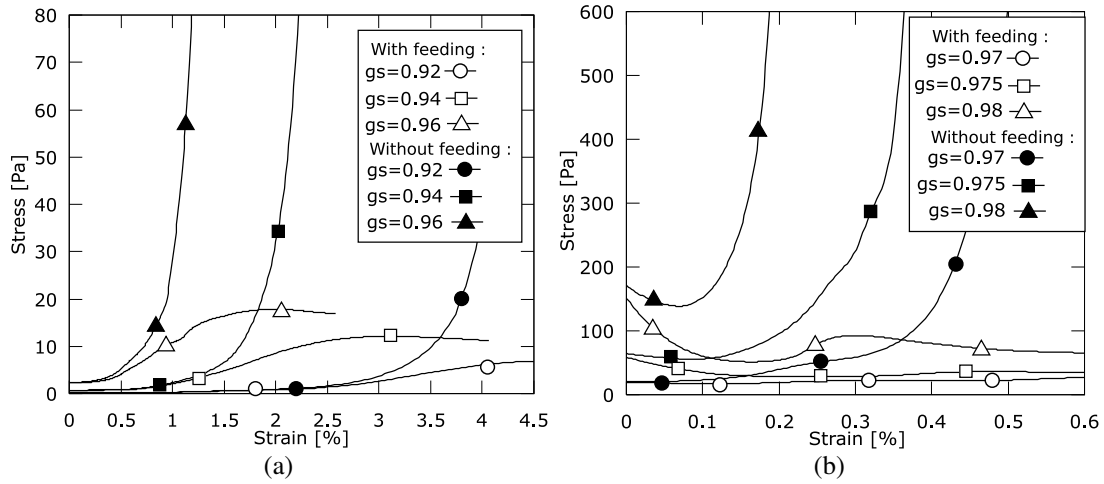


**Figure 10.6:** Stress as a function of strain with  $\dot{\epsilon} = 4 \times 10^{-3} \text{ s}^{-1}$ . (a)  $g_s < g_{s,1\%lc}$  (liquid isolation see Sec. 9.1.2) (b)  $g_s > g_{s,1\%lc}$ .

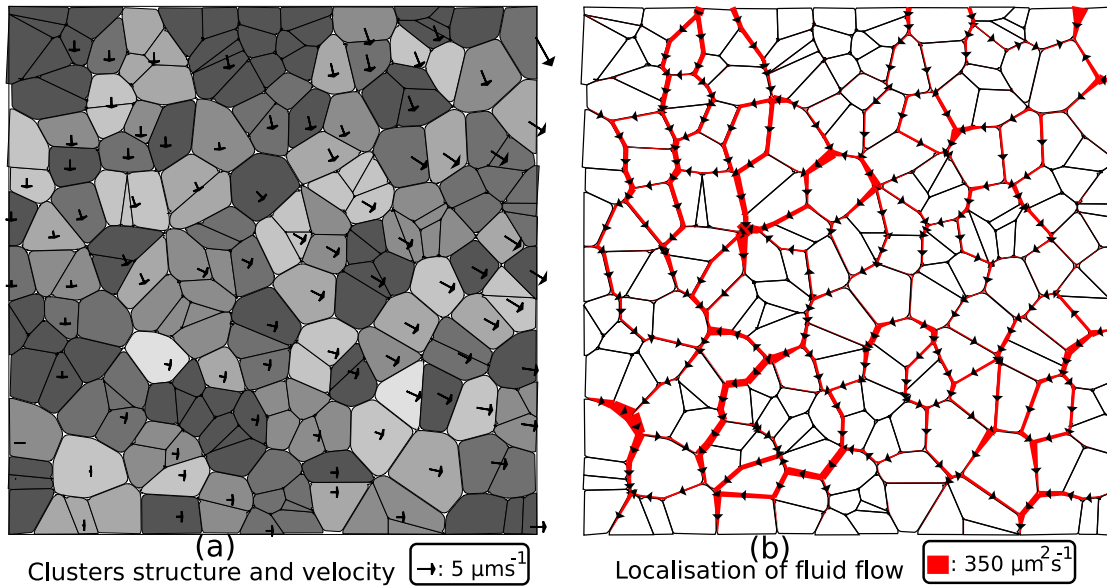


**Figure 10.7:** Mushy zone at zero strain for an isothermal mushy zone with  $g_s = 0.975$  and  $\dot{\epsilon} = 4 \times 10^{-3} \text{ s}^{-1}$ . Feeding from the upper face is allowed.

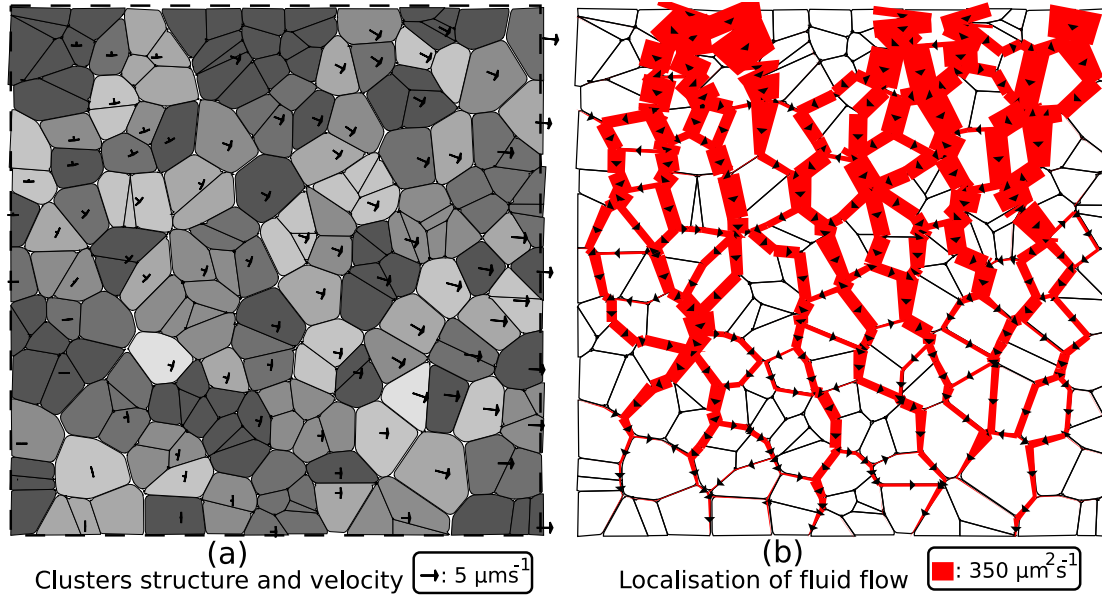


**Figure 10.8:** Mushy zone at 0.05% strain for an isothermal mushy zone with  $g_s = 0.975$  and  $\dot{\epsilon} = 4 \times 10^{-3} \text{ s}^{-1}$ . Feeding from the upper face is allowed.

fluid coming from the upper boundary is clearly redistributed in the channels. The same mushy zone is represented for 0.05 % strain. Most of the fluid which accommodates deformation is brought from the upper boundary.

Therefore, above  $g_s = 0.97$  the deformation mechanism due to local fluid redistribution is not possible anymore due to the presence of relatively large clusters. Note that this point has already been identified as the *liquid isolation* transition  $g_{s,1\%ilc}$ , i.e., the point at which the permeability of the mush deviates from the Kozeny-Carman relationship (see Sec. 9.1.2).

Now, we see that this solid fraction also corresponds to the point where accommodation of deformation by fluid flow becomes extremely difficult. Therefore, it can be identified with the ductility minimum point experimentally observed (see Sec. 8.3), also called coalescence solid fraction by some authors (see Sec. 2.3.6). Yet, we find this point for  $g_s = 0.97$  and experiments shows that it occurs for  $g_s = 0.95$ . As already mentioned, this might be due to the 2D nature of the model which under-estimates the size of the last liquid films (cylindrical instead of spherical)

Moreover, if we compare the points at which feeding becomes important on Fig. 10.6(a) and the experimental ductility reported in Fig. 8.3, we see a good agreement if 0.02 is subtracted to the solid fraction given by the numerical model.

Yet, the experimental stress-strain curves are clearly different from the curves reported on Fig. 10.6(a). This is maybe because we have considered a material without any strain at the beginning of the traction which is clearly not the case for a real casting. In particular, the fluid flow through the mush due to feeding does impose strains in the mushy zone [45].

Moreover, a good description of these curves would imply the modelling of solid deformation, in particular for  $g_s > g_{s,1\%ilc}$ .

Unfortunately, due to a lack of time once the model was developed and tested, it was not possible to exploit its full potential. Nevertheless, these first results are very



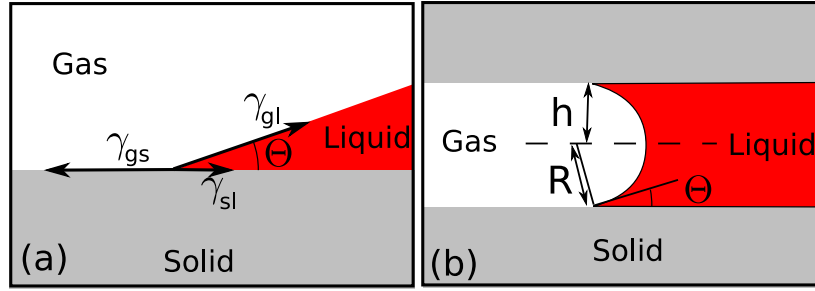


**Figure 10.9:** (a) Equilibrium of forces at triple junction. (b) Shape of the meniscus between two grains.

encouraging. They show the localization of feeding and strains in the network of discrete grains.

## 10.2 Toward a criterion for hot tearing

### 10.2.1 A simple model for hot tear nucleation

Following the work on porosity [31, 98], a criterion for hot crack nucleation can be written:

$$p_l < p_c = p_H - \Delta p_\gamma \quad (10.1)$$

where  $p_l$  is the local pressure in the liquid,  $p_H$  is the equilibrium pressure of dissolved gases associated with the maximum solubility and  $\Delta p_\gamma$  the over-pressure in the gas bubble due to surface tension.  $p_c$  represents the cavitation pressure at which a pore forms. In porosity models, this value is expressed as a function of dissolved gaseous elements concentration, but here we will simply consider it equal to 0.

As the liquid channels are small compared with the capillarity length, the liquid-gas interface is an arc of a circle of radius  $R$ . The equilibrium at triple junctions (Fig. 10.9 (a)) imposes

$$\gamma_{lg} \cos \Theta = \gamma_{sg} - \gamma_{sl} \quad (10.2)$$

and thus

$$R = \frac{h}{\cos \Theta} \quad (10.3)$$

where  $h$  is the half width of the liquid channel (Fig. 10.9 (b)) and  $\Theta$  de dihedral angle. Therefore

$$\Delta p_\gamma = \frac{\gamma_{lg}}{R} = \frac{\cos \Theta \gamma_{lg}}{h} = \frac{\gamma_{sg} - \gamma_{sl}}{h} = \frac{I}{h} \quad (10.4)$$

Where  $I$  is called the impregnation factor, its value being around  $1 \text{ Jm}^{-2}$  for Al and  $h$  is the local half width of the channel. It is interesting to note that if we consider an elementary displacement of the liquid-gas interface toward the liquid (pore growth), an extra work should be furnished to the sytem due to interfacial forces  $\Delta W_\gamma$

$$dW_\gamma = 2h\Delta p_\gamma dx = 2(\gamma_{sg} - \gamma_{sl})dx \quad (10.5)$$

which precisely corresponds to the energy necessary to replace two solid-liquid interfaces by 2 solid gas interfaces.

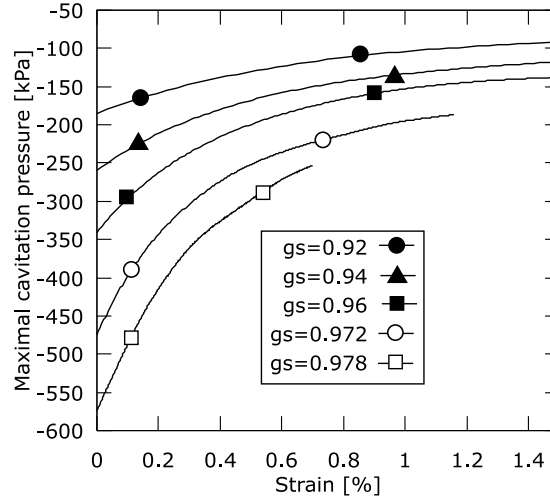


**Figure 10.10:** Maximum value of the cavitation pressure in the mushy zone as a function of strain for an impregnation factor  $I$  of  $1 \text{ Jm}^{-2}$ .

The important point here is that  $p_c$  is strongly dependent on  $h$ , indeed

$$\frac{\partial p_c}{\partial h} = \frac{I}{h^2} \sim 4 \times 10^4 \text{ Pa } \mu\text{m}^{-1} \quad (10.6)$$

where a characteristic half channel width of  $5 \mu\text{m}$  is considered. Moreover, in the previous section we have seen that deformation is localized on a few channels. This remark is also important for the propagation of the hot crack as a variation of a few percents in the channel width breaks down the liquid menisci (see Ref. [155] for a description of menisci dynamics).

The maximum cavitation pressure is plotted on Fig. 10.10 as a function of deformation for isothermal mushy zone with various solid fraction, deformed with a strain rate of  $\dot{\varepsilon} = 4 \times 10^{-3} \text{ s}^{-1}$ . This pressure corresponds to the pressure necessary for cavitation of a pore in the largest channel of the mush,  $h_{\max}$ . This channel width decreases with increasing  $g_s$  and considerably increases with strain, in particular for high solid fraction samples. Note that this evolution is largely independent of the other parameters.

The variations of  $p_c$  due to strain are therefore more important than the variation of pressure drop due to strain rate. This phenomenon can explain the apparent insensitivity of hot cracking to strain rate.

This idea is further illustrated on Fig. 10.11 where a mushy zone is represented at various strain levels. In this test  $\dot{\varepsilon} = 4 \times 10^{-3} \text{ s}^{-1}$ ,  $g_s = 0.92$  and feeding from the upper surface is not allowed. Moreover, the localization of the fluid flow and the grain velocity are represented on the same picture. Channels in which feeding is not represented (white channels), correspond to those in which a pore has nucleated. In order to reach depressions able of producing cavitation of a pore, the pressure at the upper boundary was fixed to  $P_0 = -120000 \text{ Pa}$ . Moreover, the impregnation factor  $I$  was fixed to  $1 \text{ Jm}^{-2}$ .

Figure 10.11 clearly shows the nucleation of pores in the largest channels in which deformation has been localized. Note that this approach allows estimating the appearance of damage in the mushy zone, but cannot model fracture as it would require to model explicitly the deformation of the solid grains.



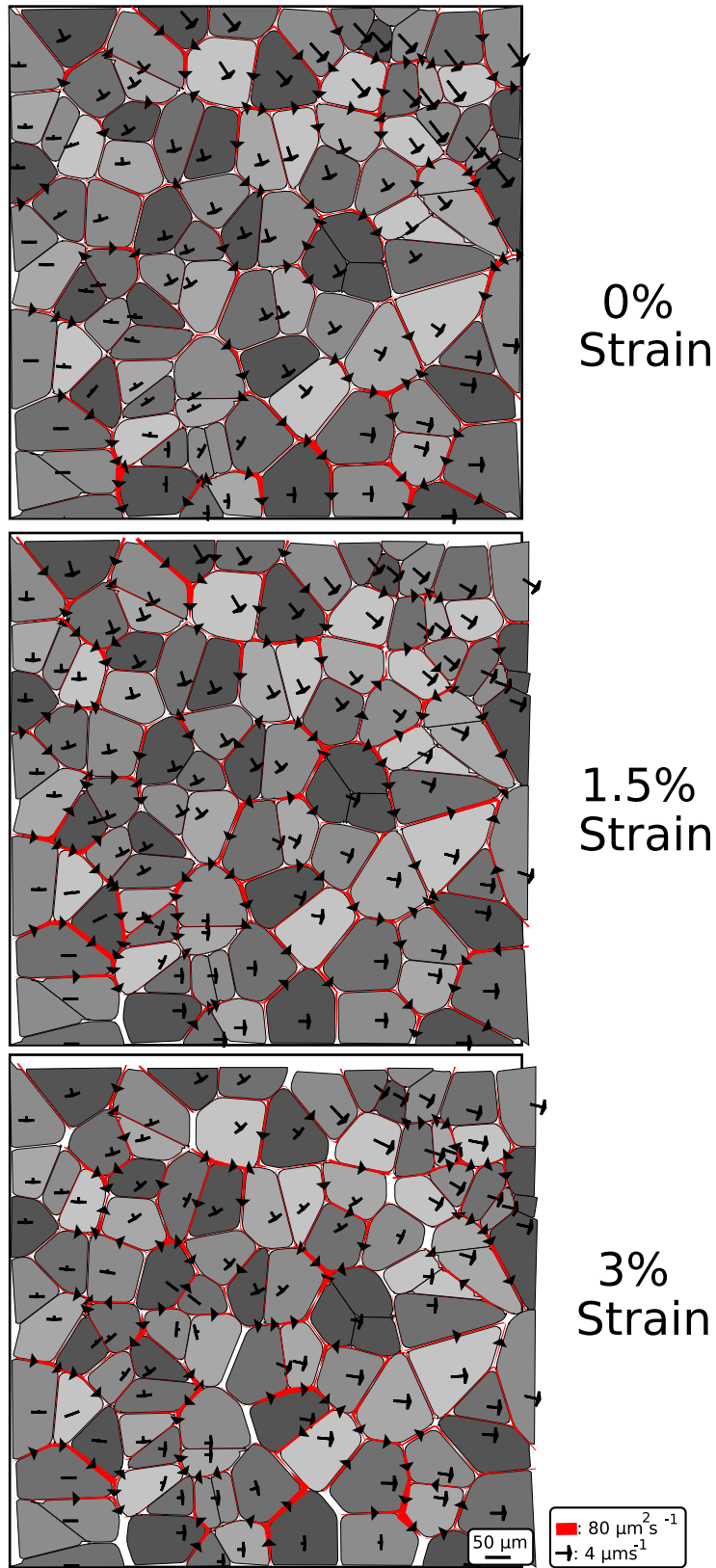


**Figure 10.11:** Mushy zone at various strain levels with  $g_s = 0.92$  and  $\dot{\epsilon} = 4 \times 10^{-3} \text{ s}^{-1}$ . Grain velocity (black arrows) and fluid flow (grey lines) are represented on the same picture. The channels on which feeding is not represented (white channels) correspond to those where a pore has nucleated. Feeding from the upper surface is not allowed



# Chapter 11

## Conclusion

As widely described in the literature, three transitions can be observed in the tensile behaviour of a mushy zone. At the traction coherency ( $g_s^{tc} = 0.6$  for a globular microstructure), the material starts to transmit measurable stresses and ductility is relatively important. Ductility decreases with increasing solid fraction and reaches a minimum for a given solid fraction called the ductility minimum or coalescence transition ( $g_s^{coal} = 0.95$  for a globular microstructure). Above this solid fraction, the stress at rupture and the ductility increase strongly with solid fraction. In the fully solid region, a transition from inter to intra-granular rupture is finally observed.

Mushy zones are extremely sensitive to hot cracking for solid fractions around the ductility minimum. The traction tests done at Alcan CRV illustrate that this point corresponds to a transition from a deformation mechanism dominated by fluid flow to a mechanism dominated by solid viscoplasticity. At the minimum of ductility, none of these two deformation mechanisms is efficient and the material is extremely brittle.

The numerical models developed during this work give a deeper insight into the transitions of the mushy zone. The Voronoi solidification model shows the progressive formation of a continuous solid phase by the formation of increasingly larger grain clusters. Two transitions are observed : grain contact, which denotes the formation of grains clusters, and solid percolation, *i.e.*, the formation of a continuous solid phase.

Moreover, the KPL model shows a strong localization of feeding for solid fraction above  $g_{s,1\%ilc} = 0.97$ . This localization induces a permeability of the mush much lower than the predictions of the Kozeny-Carman law. The mechanical model also outlines that above this point the deformation mechanism based on fluid flow is not efficient anymore. Therefore, this point corresponds to the ductility minimum. The difference between the computed solid fraction  $g_{s,1\%ilc} = 0.97$  and the experimental one  $g_s^{coal} = 0.95$  is probably due to the two-dimensional nature of the model, which underestimates the size of the last liquid films.

The mechanical model shows the strong localization of deformation due to the discrete nature of the grains. This deformation is localized in channels normal to the stress direction which therefore becomes ideal sites for the nucleation and the propagation of a hot crack. Moreover, the localization of thermal shrinkage at the edges of the grain clusters should reinforce the concentration of deformation. However, due to a lack of time, the full exploitation of the mechanical model could not be carried on.

Finally, it is interesting to note that the results of this work are essentially due to the consideration of two physical phenomena that are classically hidden by the averaging procedure of continuum approaches:

- The first phenomenon is the random nature of nucleation, which induces a progressive formation of a continuous solid phase during solidification (Chap. 9). This includes the formation of grain clusters and the localization of feeding at high solid fraction.
- The second phenomenon is precisely the granular nature of the mushy zone (Chap. 10). This granular nature induces a further localization of deformation (beside the localization due to grain clusters). Recently, Gourlay and Dahle have experimentally outlined the importance of this granular nature of solidifying alloys [156, 157].

Therefore, this model constitutes an ideal basis for a more precise formulation of continuum constitutive equations (Sec. 3.2) which would be able to account for these two points. Moreover, considering the very low computation time of the model, its extension to three dimensions is clearly feasible.

It is also important to point out the limits of the model. The most important one is maybe the non-consideration of grain rotations. This hypothesis is necessary to have a tractable model as the detection of contacts between randomly oriented polygonal grains is extremely computation intensive [140]. However, this hypothesis reduces the degrees of freedom of the grain but maybe more important, forbid to model locally the deformation of the solid grains.

Therefore, a complementary approach to the present one would be to start the mechanical calculation from the fully solid part, including the clusters attached or next to this zone. Knowing the deformation and thus the velocity of the points located in this region, the fluid flow induced by shrinkage and these deformations could be computed with the KPL model. This new approach could benefit from the results of the present model for the fluid part, but would be more accurate at very high solid fraction. It is expected that their domain of validity would precisely cross at the minimum of ductility.

# Appendix A

## List of symbols

### Roman letters

Symbol	Description	Units
$\overleftrightarrow{A}$	Antisymmetric part of the elementary matrix	—
$\overrightarrow{b}$	Second member of a matricial problem	—
$c_p$	Heat capacity	$\text{JK}^{-1}\text{kg}^{-1}$
$c$	Solute concentration	mass%
$C$	Coherency	—
$C$	Dimensionless number relative to grain corner	—
$C$	Point on the interface (middle of the channel)	—
$d_f$	Fractal dimension	—
$d_a^N$	Distance from the cluster centre to the interface	m
$D$	Solute diffusion coefficient	$\text{m}^2\text{s}^{-1}$
$\overleftrightarrow{E}$	Elementary matrix	—
$F$	Force	N
$Fo$	Fourier Number	—
$g_\alpha$	Volumetric fraction of phase $\alpha$	—
$\overrightarrow{g}$	Gravity acceleration	$\text{ms}^{-2}$
$h$	Half width of a channel	m
$H$	Hurst exponent	—
$\overleftrightarrow{I}$	Unit tensor	—
$k$	Partition coefficient	—
$K$	Viscoplastic coefficient	—
$l$	Topothesy	m
$L$	Latent heat of solidification	$\text{Jkg}^{-1}$
$L$	Channel length	m
$L_c$	Matching channel length	m
$m$	Liquidus slope	$\text{Kat}\%^{-1}$
$m$	Strain rate sensitivity coefficient	—
$M_\alpha$	Interfacial momentum transfer	$\text{Nm}^{-3}\text{s}^{-1}$
$M$	Point on the interface	—
$\overrightarrow{n}$	Outward normal to a domain	—
$Norm$	Normalization factor due to solidification	—
$O$	Cluster centre	—
$p$	Pressure (continuum fields)	$\text{Pa}(\text{Nm}^{-2})$

$p$	Occupation probability	—
$P$	Pressure (discrete points)	Pa
$T$	Temperature	°C, K
$\overleftrightarrow{S}$	Symmetric part of the elementary matrix	—
$S_f$	Volumetric entropy of fusion	$\text{JK}^{-1}\text{m}^{-3}$
$S$	Surface	$\text{m}^2$
$S_v$	Interface specific surface	$\text{m}^{-1}$
$S_s$	Interface specific surface per unit solid	$\text{m}^{-1}$
$t$	Time	s
$\overrightarrow{t}$	Force density	Pa
$\overleftrightarrow{U}$	Unknown vector	—
$v$	Velocity (continuum fields)	$\text{ms}^{-1}$
$v_b$	Laser spot velocity	$\text{ms}^{-1}$
$V$	Velocity (discrete points)	$\text{ms}^{-1}$
$w$	Interface velocity	$\text{ms}^{-1}$
$\dot{W}$	Power dissipation	$\text{Js}^{-1}$

### Greek letters

Symbol	Description	Units
$\alpha$	Dilatation rate	$\text{s}^{-1}$
$\alpha$	Angle at grain corner	°
$\beta$	Hurst exponent in the propagation direction	—
$\beta$	Solidification shrinkage coefficient	—
$\beta_T$	Thermal expansion coefficient	$\text{K}^{-1}$
$\beta_c$	Solutal expansion coefficient	$\text{mass}\%^{-1}$
$\gamma$	Interfacial energy	$\text{Jm}^{-2}$
$\gamma$	Cluster mass exponent	—
$\Gamma_\alpha$	Interfacial mass transfer	$\text{kgm}^{-3}\text{s}^{-1}$
$\Gamma_{sl}$	Gibbs-Thomson coefficient	Km
$\delta$	Thickness of the diffuse solid-liquid interface	m
$\overleftrightarrow{\varepsilon}$	Strain rate tensor	$\text{s}^{-1}$
$\dot{\varepsilon}$	Scalar strain rate	$\text{s}^{-1}$
$\dot{\varepsilon}_{eq}$	Equivalent viscoplastic shear rate	$\text{s}^{-1}$
$\zeta$	Hurst exponent normal to the propagation direction	—
$\eta$	Coordinate in the Landau transformation	—
$\theta$	Misorientation angle	°
$\Theta$	Dihedral angle	°
$\kappa$	Permeability	$\text{m}^2$
$\mu$	Viscosity	Pas
$\mu$	Permeability exponent	—
$\nu$	Correlation length exponent	—
$\xi$	Correlation length	m
$\rho$	Density	$\text{kgm}^{-3}$
$\overleftrightarrow{\sigma}$	Stress tensor	Pa
$\overleftrightarrow{\sigma}_s^e$	Terzaghi effective stress	Pa
$\sigma_s^{eq}$	Von Mises stress	Pa

$\overleftrightarrow{\tau}$	Deviatoric part of the stress tensor	Pa (Nm <sup>-2</sup> )
$\Phi$	Fluid flow	m <sup>2</sup> s <sup>-1</sup>
$\psi$	FEM test function	—
$\omega$	Viscoplastic potential	J s <sup>-1</sup>
$\Omega$	Volume of the REV	m <sup>2</sup> (2D), m <sup>3</sup> (3D)
$\Omega_{i_p}$	Liquid volume entrapped in the grain envelope	m <sup>2</sup> (2D)
$\Omega_{i_l}$	Liquid volume in the idealized liquid channel	m <sup>2</sup> (2D)

## Subscripts and superscripts

Symbol	Description
$\alpha$	Given phase
$a, b, c$	solid grains
$c$	Critical (percolation threshold)
$coal$	Coalescence
$e$	Effective
$el$	Elastic
$gb$	Grain boundary
$i, j, k$	Integration points in the liquid
$i \rightarrow j$	from $i$ to $j$
$l$	Liquid
$lg$	Liquid-gaz
$maxS$	Grain contact transition ( $S_v$ maximum)
$N$	Normal
$p$	Plastic
$p$	Pore
$pcb$	Percolation by bridging
$pct$	Percolation by contact
$pk$	Maximum packing
$R$	Rounded interface
$s$	Solid
$sc$	Shear coherency
$sp$	Solid percolation
$sl$	Solid-liquid
$s, k, l$	Liquid channels
$tc$	Traction coherency
$tot$	Total
$T$	Tangential
$1\%ilc$	Isolation of liquid channels
$*$	Interface
$\infty$	Flat interface
$\circ$	Dimensionless

## Operators

Symbol	Description
$d$	Differential
$\partial$	Partial differential
$\Delta$	Variation
$\chi_\alpha$	Function whose value is 1 in phase $\alpha$ , 0 elsewhere
$\langle . \rangle$	Average
$\int$	Integral
$\Sigma$	Sum
$\cdot$	Scalar product
$\nabla$	Gradient
$\nabla \cdot$	Divergence
$:$	Contracted product
$\cdot^t$	Transposition
$\int$	Integral along the interface



## Appendix B

### Solute balance at a grain corner

In this appendix we derive in more details the solute balance at the grain corner used for the solidification model with smooth grain interfaces (Sec. 6.2).

Considering a section of the flat interface far from the corner (see Fig. 6.3), the speed of the interface can be estimated from the following flux balance.

$$h \frac{\partial c_l^\infty}{\partial t} = c_l^\infty (1 - k) v^\infty - j_{bd}^\infty \quad (\text{B.1})$$

The left hand term represents the variation of solute in the liquid, where  $h$  is the thickness of the liquid film. The first right hand term corresponds to the solute rejected in the liquid due to the advance of the interface and  $j_{bd}^\infty$  is the flux pumped in the solid by back-diffusion. Similarly, a solute balance on the liquid part surrounding the corner (see Fig. 6.3) can be derived. If  $\Omega$  denotes this domain, one has.

$$\int_{\Omega} \frac{\partial c_l}{\partial t} ds = c_l^R (1 - k) R \sin \alpha v^R - \alpha R j_{bd}^R + \Phi \quad (\text{B.2})$$

Please note that this balance accounts for the flux  $\Phi$  exchanged between the flat and curved portions of the interface.

The variation of solute concentration at the interface is imposed by the cooling rate and  $\partial_t c_l^\infty = \partial_t c_l^R = \dot{T}/m$ . As a consequence, whatever is the precise repartition of solute around the grain corner, the variation of solute around the grain corner can be estimated by:

$$\int_{\Omega} \frac{\partial c_l}{\partial t} ds = S_{\Omega} \frac{\dot{T}}{m} \quad (\text{B.3})$$

where  $S_{\Omega}$  is the area of the domain surrounding the round corner. As  $v^r = v^\infty / \cos \alpha$  (see main section), Eqs B.1, B.2 and B.3 give:

$$S_{\Omega} \frac{\dot{T}}{m} = \frac{c_l^R}{c_l^\infty} R \tan \alpha (h \frac{\dot{T}}{m} + j_{bd}^\infty) - \alpha R j_{bd}^R + \Phi \quad (\text{B.4})$$

Considering that  $c_l^R/c_l^\infty \sim 1$  and neglecting the differences of back diffusion along the flat and curved parts of the interface, one gets:

$$(S + Rh \tan \alpha) \frac{\dot{T}}{m} = Rh \tan \alpha \frac{\dot{T}}{m} + \Phi \quad (\text{B.5})$$

where the surface  $S_{\Omega}$  have been separated into the surface delimited by the extension of the flat interface ( $Rh \tan \alpha$ ) and an extra surface  $S$  represented in grey in Fig. 6.3. As

stated in the main part, one retrieves the fact that the solute rejected by the flat interface moving at velocity  $v^\infty$  is equivalent to that rejected by the curved interface moving at a velocity  $v' = v^\infty / \cos \alpha$ . Removing this term on the left and right hand sides finally gives:

$$S \frac{\dot{T}}{m} = \Phi \quad (\text{B.6})$$

This represents the solute balance between the solute flux induced by the Gibbs-Thomson effect and the geometrical advantage of a corner for diffusion.

## Appendix C

# Detailed integration of the constitutive equations

In this appendix, we give more details on the integration of the constitutive equations for the mechanical model (Chap. 7).

### C.1 Stress tensor

In Sec. 7.2.2 the fluid flow in the  $y$  direction has been neglected (by dimensional analysis). The integration of the constitutive equation for a fluid flow in the  $x$  direction (see Fig. 7.2) gives the fluid velocity in the  $x$  direction together with the pressure  $p$  in the channel.

$$p(x) = \frac{3\mu V^N}{4h^3} \left( x^2 - \left( \frac{L_c}{2} \right)^2 \right) + \frac{P_j - P_i}{L_c} x + \frac{P_i + P_j}{2} \quad (\text{C.1})$$

$$v_x(x, y) = \left( \frac{3V^N}{4h^3} x + \frac{P_j - P_i}{2\mu L_c} \right) (y^2 - h^2) + \frac{V_b^T - V_a^T}{2h} y + \frac{V_b^T + V_a^T}{2} \quad (\text{C.2})$$

Yet, the integration of the fluid flow in the  $y$  direction allows to compute the full stress tensor in the liquid.

We have for an incompressible fluid

$$\nabla \cdot \vec{v} = 0 \quad (\text{C.3})$$

As the speed profile along the  $x$  axis is already defined (Eq. C.2), we get:

$$\frac{\partial v_y}{\partial y} = -\frac{\partial v_x}{\partial x} = -\frac{3V^N}{4h^3} (y^2 - h^2) \quad (\text{C.4})$$

with

$$V^N = V_b^N - V_a^N \quad (\text{C.5})$$

thus

$$v_y = -\frac{V^N}{4h^3} y^3 + \frac{3V^N}{4h} y + \frac{V_b^N + V_a^N}{2} \quad (\text{C.6})$$

where the constant of integration satisfies both boundaries conditions  $v_y(y = -h) = V_a^N$  and  $v_y(y = h) = V_b^N$ . Thus, taking the dimensional form of Eq. 7.36

$$\frac{\partial p}{\partial y} = \mu \frac{\partial^2 v_y}{\partial y^2} \quad (\text{C.7})$$

We get the variation of pressure along the  $y$  direction

$$p = -\frac{3V^N}{4h^3}y^2 + f(x) \quad (\text{C.8})$$

where  $f(x)$  is the pressure in the channel for the line  $y = 0$  which we take equal to the pressure profile of Eq. C.1. Finally the pressure profile is:

$$p(x, y) = \frac{3\mu V^N}{4h^3} \left( x^2 - \left( \frac{L_c}{2} \right)^2 - y^2 \right) + \frac{P_j - P_i}{L_c} x + \frac{P_i + P_j}{2} \quad (\text{C.9})$$

As stated in the dimensional analysis, the pressure loss in the  $y$  direction is negligible in front of the pressure variation in the  $x$  direction. Note that we found here the relationship  $\Delta P_y / \Delta P_x \sim h^2 / L_c^2$  whereas the dimensional analysis gives a relationship  $\Delta P_y / \Delta P_x \sim h / L_c$  (Eq. 7.38).

The stress tensor in the liquid can be derived from :

$$\overleftrightarrow{\sigma}(x, y) = \begin{pmatrix} -p + 2\mu \frac{\partial v_x}{\partial x} & \mu \left( \frac{\partial v_x}{\partial y} + \frac{\partial v_y}{\partial x} \right) \\ \mu \left( \frac{\partial v_x}{\partial y} + \frac{\partial v_y}{\partial x} \right) & -p + 2\mu \frac{\partial v_y}{\partial y} \end{pmatrix} \quad (\text{C.10})$$

and thus

$$\overleftrightarrow{\sigma}(x, y) = \begin{pmatrix} -p + \frac{3\mu V^N}{2h^3}(y^2 - h^2) & \left( \frac{3\mu V^N}{2h^3}x + \frac{P_j - P_i}{L_c} \right)y + \mu \frac{V_b^T - V_a^T}{2h} \\ \text{''} & -p - \frac{3\mu V^N}{2h^3}(y^2 - h^2) \end{pmatrix} \quad (\text{C.11})$$

where  $p$  is given by Eq. C.9. Note that the  $\partial_x v_y$  term is nil. This stress field is coherent as we can check that :

$$\nabla \cdot \overleftrightarrow{\sigma}(x, y) = \vec{0} \quad (\text{C.12})$$

For the simplicity of the equations, we choose to neglect the variation of pressure in the  $y$  direction (Eq. C.1). Thus, we should also neglect the  $y^2$  terms in the diagonal of the stress tensor as they are exactly of the same order.

$$\overleftrightarrow{\sigma}(x, y) = \begin{pmatrix} -p & \left( \frac{3\mu V^N}{2h^3}x + \frac{P_j - P_i}{L_c} \right)y + \mu \frac{V_b^T - V_a^T}{2h} \\ \text{''} & -p \end{pmatrix} \quad (\text{C.13})$$

Note that the divergence of this tensor is not nil anymore. However, considering this stress tensor, the sum of forces and of rotational momentum on the boundaries of a channel are nil [158], which is the condition for the coherency of the numerical scheme.

## C.2 Mass balance

Even if the mass balance equations are relatively simple, their integration should be done carefully. In particular, we have a Lagrangian point of view on the solid and an Eulerian point of view on the liquid.

We derive the mass balance around a vertex  $i$  connected to the vertices  $j, k, l$  by the channels  $s, t, u$  and surrounded by the grains  $a, b, c$ , respectively (see Fig. C.1). We consider a control volume  $\Omega$  which goes through the middle of each channel and each centroid of the solid grains. This control volume is an Eulerian control volume, *i.e.*, it does not move with the solid grains. If we draw such a volume around each vertex, we

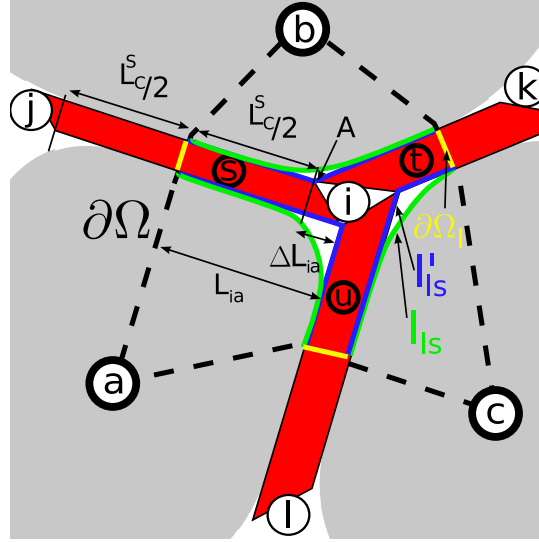


Figure C.1: flux balance around one vertice

define a tessellation of the system, and thus this control volume is suitable for a mass balance of the system.

The simplest way to obtain the fluid mass balance inside the domain  $\Omega$  is to consider only the part of  $\Omega$  where we have the fluid,  $\Omega_l$ . As the fluid is incompressible we have:

$$\int_{\Omega_l} (\nabla \cdot \vec{v}_l) d\Omega = 0 \quad (\text{C.14})$$

and thus

$$\int_{\partial\Omega_l} (\vec{v}_l \cdot \vec{n}) ds + \int_{I_{ls}} (\vec{v}_l \cdot \vec{n}) ds = 0 \quad (\text{C.15})$$

where  $I_{sl}$  corresponds to the solid liquid interface inside the domain  $\Omega$ ,  $\partial\Omega_l$  is the part of  $\partial\Omega$  that is liquid and  $\vec{n}$  is the normal pointing outward the domain.

Let us consider the idealized solid liquid interfaces  $I'_{ls}$  which corresponds to the idealized channel geometry used for the estimation of pressure drop (see Fig. C.1).

Around each grain, the interfaces  $I'_{ls}$  and  $I_{ls}$  form a closed loop. Therefore, the nil divergence of the fluid flow gives :

$$\int_{I_{ls}} (\vec{v}_l \cdot \vec{n}) ds = \int_{I'_{ls}} (\vec{v}_l \cdot \vec{n}) ds \quad (\text{C.16})$$

which can be written with the notation of Sec. 7.2 :

$$\int_{I_{ls}} (\vec{v}_l \cdot \vec{n}) ds = \sum_s (L_{ib} V_b^N - L_{ia} V_a^N) \quad (\text{C.17})$$

where the sum over  $s$  is the sum on the channels connected to vertex  $i$ , the indices  $a$  and  $b$  being changed into grains having similar role when the channel is changed.

The fluid flow through  $\partial\Omega_l$  is given by Eq. 7.44

$$\int_{\partial\Omega_l} (\vec{v}_l \cdot \vec{n}) ds = \sum_s \Phi_{i \rightarrow j}^s(x=0) \quad (\text{C.18})$$

with

$$\Phi_{i \rightarrow j}^s(x=0) = \frac{2h^{s3}}{3\mu L_c^s}(P_i - P_j) + 2h^s \frac{V_b^T + V_a^T}{2} \quad (\text{C.19})$$

and where the superscript  $^s$  denotes the channel  $s$ .

Finally, Eqs. C.17 and C.18 gives :

$$\sum_s \frac{2h^{s3}}{3\mu L_c^s}(P_i - P_j) + 2h^s \frac{V_b^T + V_a^T}{2} + L_{ib}V_b^N - L_{ia}V_a^N = 0 \quad (\text{C.20})$$

which can be written

$$\sum_s \Phi_i^s = 0 \quad (\text{C.21})$$

with

$$\Phi_i^s = \frac{2h^{s3}}{3\mu L_c^s}(P_i - P_j) + 2h^s \frac{V_b^T + V_a^T}{2} + L_{ib}V_b^N - L_{ia}V_a^N \quad (\text{C.22})$$

This equation can be viewed as a mass balance over the small white triangle surrounding vertex  $i$  on Fig. C.1, where the  $\Phi_i^s$  are the flux flowing out of each face of the triangle.

Similarly, if the flux is computed for a vertex  $j$ , *i.e.*, on the other side of the channel with respect to the tangential vector  $\vec{T}$ , we have

$$\Phi_j^s = \frac{2h^{s3}}{3\mu L_c^s}(P_j - P_i) - 2h^s \frac{V_b^T + V_a^T}{2} + L_{ib}V_b^N - L_{ia}V_a^N \quad (\text{C.23})$$

The superscript  $^s$  is omitted when non-necessary.

# Bibliography

- [1] D. Cardon. *Le monde des teintures naturelles*. Belin, 2003.
- [2] Ch. Singer. *Earliest Chemical Industry*. The Folio Society, London, 1948.
- [3] Pline. *Histoire naturelle*. J.J. Dubrochet, 1848.
- [4] C. Boucher. *L'aluminium et ses alliages: soudabilité, métallurgie du soudage*. Publications du Soudage et de ses Applications, 2000.
- [5] L. Backerud, E. Krol, and J. Tamminen. *Solidification characteristics of aluminium alloys*. Skanuminium, 1986.
- [6] International aluminium institute. <http://www.world-aluminium.org/>, 2006.
- [7] P.D. Grasso. *Coalescence and mechanical behaviour of semi-solid aluminium alloys in relation to hot tearing*. PhD thesis, EPFL, no 3037, 2004.
- [8] W. Roth. Deutsches Patent Nr. 974 203, 1936.
- [9] E.F. Emley. Continuous casting of aluminium. *Int. Metals Rev.*, page 75, June 1976.
- [10] L. Germond. Etude de la sensibilité à la fissuration à chaud par refusion laser d'un alliage d'aluminium. Student project LSMX EPFL, 2004.
- [11] C. Dumur. Sculptures raku. <http://www.claudine-dumur.com/>.
- [12] T. Ivie and W. Noffsinger. Blue fox gallery. [www.bluefoxgallery.com/](http://www.bluefoxgallery.com/).
- [13] W. Kurz and D. Fischer. *Fundamental of solidification*. (Trans. Tech. Publ.), 1998.
- [14] V. Mathier, J.-M. Drezet, and M. Rappaz. Two-phase modeling of hot tearing in aluminium alloys using a semi-coupled method. In C-A Gandin and M. Bellet, editors, *Modeling of casting, Welding, And Advanced Solidification Processes XI*, page 643, 2006.
- [15] A. Jacot and M. Rappaz. A pseudo-front tracking technique for the modelling of solidification microstructures in multi-component alloys. *Acta Mater.*, 50:1909–26, 2002.
- [16] J.J. Hoyt, M. Asta, and A. Karma. Atomistic simulation methods for computing the kinetic coefficient in solid-liquid systems. *Interf. Scie.*, 10:181–189, 2002.
- [17] D. Stauffer and A. Aharony. *Introduction to percolation theory*. Taylor and Francis, 1994.
- [18] V. Mathier. PhD thesis, EPFL, 2007.
- [19] B. Commet and A. Larouche. An integrated approach to control hot tearing in sheet ingot casting. In *Light Metals*. TMS, 2006.

- [20] J.-M. Drezet, M. Rappaz, G.-U. Grun, and M. Gremaud. Determination of thermophysical properties and boundary conditions of direct chill-cast aluminum alloys using inverse methods. *Met. Mater. Trans. A*, 31(6):1627–34, 2000.
- [21] D. Warrington and G. J. McCartney. Hot cracking in aluminium alloys 7050 and 7010. a comparative study. *Cast Metals*, 3:202, 1991.
- [22] M. Braccini. *Optimisation des pièces moulées : Étude des phénomènes de fissuration à chaud dans les alliages Al-Cu*. PhD thesis, INPG, 2000.
- [23] T.W. Clyne and G.J. Davies. The influence of composition on solidification cracking susceptibility in binary alloy systems. *J. Brit. Foundry*, 74:65–73, 1981.
- [24] S. Instone, D. StJohn, and J. Grandfield. New apparatus for characterising tensile strength development and hot cracking in the mushy zone. *Int. Jour. Cast Met. Res.*, 16:441, 2006.
- [25] J. Spittle and A. Cushway. Influences of super heat and grain structure on hot tearing susceptibilities of al-cu alloy castings. *Met. Tech.*, 10:6, 1983.
- [26] U. Feurer. Mathematisches modell der warmrissneigung von binaren aluminiumlegierungen. *Giesserei Forsch*, 28:75–80, 1976.
- [27] W.I. Pumphrey and D.C. Moore. *J Inst. Met.*, 425:439, 1947.
- [28] B. Commet, P. Delaire, J. Rabenberg, and J. Storm. Measurement of the onset of hot cracking in dc cast billets. In P. N. Crepeau, editor, *Light Metals*, page 711. TMS, 2003.
- [29] M. Easton, J. Grandfield, D. StJohn, and B. Rinderer. The effect of grain refinement and cooling rate on the hot tearing of wrought aluminium alloys. *Mat. Scien. Forum*, 519-521:1675, 2006.
- [30] J. Campbell. *Castings*. Butterworth Heineman, 1991.
- [31] Ch. Pequet, M. Gremaud, and M. Rappaz. Modeling of microporosity, macroporosity, and pipe-shrinkage formation during the solidification of alloys using a mushy-zone refinement method: Applications to aluminum alloys. *Met. Trans. A*, 33A:2095, 2002.
- [32] P.J. Wray. The geometry of two-phase aggregates in which the shape of the second phase is determined by its dihedral angle. *Acta Met.*, 24:125, 1975.
- [33] M. Rappaz, A. Jacot, and W. Boettinger. Last stage solidification of alloys : Theoretical model of dendrite arm and grain coalescence. *Met. Mater. Trans.*, 34A:467–479, 2003.
- [34] J.F. Grandfield, J.A. Taylor, and C.J. Davidson. Tensile coherency in semi-solid AZ91 alloy. In H. Kaplan, editor, *Magtech*. TMS, 2002.
- [35] I. Farup, J.M. Drezet, and M. Rappaz. In situ observation of hot tearing formation in succinonitrile-acetone. *Acta Mater.*, 49:1261–69, 2001.
- [36] J.-M Drezet, O. Ludwig, and M. Rappaz. Un nouveau critère de fissuration à chaud. In *Mecamat*, page 30. ENS Cachan, 1999.
- [37] O. Ludwig. *Etude expérimentale et modélisation du comportement rhéologique d'alliages Al-Cu en cours de solidification dans le cadre de la fissuration à chaud en coulée continue*. PhD thesis, INPG, 2004.
- [38] S. Vernède. Traction à l'état pâteux : Etude des propriétés mécaniques d'alliages d'aluminium à l'état semi-solide. Master's thesis, ECP, 2003.



- [39] B. Commet. private communication, ALCAN CRV, 2003.
- [40] A.B. Phillion, S.L. Cockcroft, and P.D. Lee. X-ray micro-tomographic observations of hot tear damage in an Al-Mg commercial alloy. *Scripta Mat.*, 55:489–92, 2006.
- [41] C. Davidson, D. Viano, L. Lu, and D. H. Stjohn. Observation of crack initiation during hot tearing. *Int. Jour. Cast Met. Res.*, 19:59, 2006.
- [42] C. Pequet. *Modelling of microporosity, macroporosity and pipe shrinkage formation during the solidification of aluminium alloys, using a mushy zone refinement method*. PhD thesis, EPFL, 2002.
- [43] M. Braccini, C.L. Martin, A. Tourabi, Y. Bréchet, and M. Suéry AND. Low shear rate behavior at high solid fractions of partially solidified al8 wt.% cu alloys. *Mat. Scien. Eng. A*, A337:1–11, 2002.
- [44] A.H. Dahle and L. Arnberg. Development of strength in solidifying aluminium alloys. *Acta Mater.*, 45(2):547–59, 1997.
- [45] O. Ludwig, J.M. Drezet, Ch. Martin, and M. Suéry. Rheological behavior of Al-Cu alloys during solidification. *Met. Mater. Trans.*, 36A:1525–35, 2005.
- [46] T. Sumitomo, D.H. StJohn, and T. Steinberg. The shear behaviour of partially solidified Al-Si-Cu alloys. *Mat. Scie. Eng. A*, A289:18–29, 2000.
- [47] S. M. Nabulsi. *The behavior of Semi Solid Aluminium-Silicon alloys in a directed shear cell*. PhD thesis, University of Queensland, 1998.
- [48] S.A. Metz and M.C. Flemings. *AFS Trans.*, page 329, 1969.
- [49] A.H. Dahle and D.H. StJohn. Rheological behavior of the mushy zone and its effect on the formation of casting defects during solidification. *Acta Mater.*, 47(1):31–41, 1999.
- [50] T.G. Nguyen, D. Favier, and M. Suery. Theoretical and experimental study of the isothermal mechanical behaviour of alloys in the semi-solid state. *Int. J. Plas.*, 10:2663, 1994.
- [51] J.-M. Drezet, O. Ludwig, M. M’Hamdi, H.-G. Fjaer, and C.L. Martin. FEM modeling of the compressibility of partially solidified al-cu alloys: Comparison with a drained compression test. In Alton T. Tabereaux, editor, *Light Metals*. TMS, 2004.
- [52] J.A. Spittle, S. Brown, J.D. James, and R.W. Evans. Mechanical properties of partially molten aluminium alloys. In *Proc 7th Intern Symp on Physical Simulation of Casting, Hot Rolling and Welding*, page 81. Tsukuba: National Research Institute for Metals, 1997.
- [53] M. Suéry, Ch. Martin M. Braccini, and Y. Bréchet. Determination of the rheological behavior of partially solidified alloys for the prediction of casting defects. *Adv. Eng. Mat.*, 3:589, 2001.
- [54] B. Magnin, L. Maenner, L. Katgerman, and S. Engler. Ductility and rheology of an Al4.5% Cu alloy from room temperature to coherency temperature. *Mate. Scien. Forum*, 217-222:1209–1214, 1996.
- [55] T. Nakagawa, P. Suvanchai, T. Okane, and Umeda. Deformation behavior during solidification of steels and aluminium alloys. *Mat. Scien. For.*, 215-216:377, 1996.
- [56] D.G. Eskin, Suyitno, and L. Katgerman. Mechanical properties in the semi-solid state and hot tearing of aluminium alloys. *Prog. Mat. Scie.*, 49:629–711, 2004.

- [57] I.I. Novikov. Goryachelomkost tsvetnykh metallov i splavov (hot shortness of non-ferrous metals and alloys). *Moscow: Nauka*, page 299, 1966.
- [58] F. Matsuda, H. Nakagawa, and S. Kazuhiko. Dynamic observation of solidification and solidification cracking during welding with optical microscope (i) - solidification front and behavior of cracking. *Trans. Jap. Weld. Ins.*, 11:67–77, 1982.
- [59] W.T. Read and W. Shockley. Dislocation models of crystal grain boundaries. *Phys. Rev.*, 78(3):275–289, May 1950.
- [60] V. Mathier, A. Jacot, and M. Rappaz. Coalescence of equiaxed grains during solidification. *Mod. Sim. Mat. Sci. Eng.*, 12:479–490, 2004.
- [61] D. Porter and K. Easterling. *Phase transformations in metals and alloys*. (Chapman and Hall), Oxford, second edition, 1992.
- [62] A. Fallet, G. Chichignoud, Ch. Martin, M. Suéry, and Ph. Jarry. Influence of barium addition on the microstructure and the rheological behaviour of partially solidified Al-Cu alloys. *Mat. Scie. Eng. A*, 426:187, 2006.
- [63] G.C. Gullo, K. Steinhoff, and P.J. Uggowitzer. In M. Rosso G.L. Chiarmetta, editor, *Proceedings of the 6th International Conference on Semi-Solid Processing of Alloys and Composites*, pages 367–372, 2000.
- [64] N. Wang, S. Mokadem, M. Rappaz, and W. Kurz. Solidification cracking of superalloy single- and bi-crystals. *Acta Mat.*, 52:3173, 2004.
- [65] H. Fredrikson and B. Lethinen. Continuous observation of hot crack formation during the deformation and heating in SEM. In *Solidification and casting of metals*, pages 260–267, 1973.
- [66] J.C. Borland. Generalised theory of super-solidus cracking in welds. *Brit. Weld. J.*, 7:508, 1960.
- [67] E. Niyama, T. Uchida, M. Morikawa, and S. Saito. *AFS Int. Cast. Met. J.*, sept.:53–63, 1982.
- [68] M. Rappaz, J. Drezet, and M. Gremaud. A new hot-tearing criterion. *Met. Mater. Trans.*, 30A:449–55, 1999.
- [69] P.C. Carman. Fluid flow through granular beds. *Trans. Inst. Chem.*, 15:150, 1935.
- [70] J.-M. Drezet and M. Rappaz. Prediction of hot tears in DC-cast aluminum billets. In *Light Metals*, 2001.
- [71] M. Braccini, M. Suéry, C. Laguerre, and M. Stucky. Influence de l'affinage sur la fissuration à chaud des alliages d'aluminium-cuivre utilisés en fonderie. *La Revue de Métallurgie*, fev:157, 2003.
- [72] J. Grandfield, C. Davidson, and J. Taylor. Application of a new hot tearing analysis to horizontal direct chill cast magnesium alloy AZ91. In *Light Metals*. TMS, 2001.
- [73] J. Grandfield, L. Lu, M. Easton, C. Davidson, D. StJohn, and B. Rinderer. The effect of grain refinement on hot tearing of AlMgSi alloy 6060. In *Light Metals*. TMS, 2005.
- [74] C.H. Dickhaus, L. Ohm, and S. Engler. *Trans. AFS*, 118:677, 1993.

- [75] D.J. Lahaie and M. Bouchard. Physical modeling of the deformation mechanism of semisolid bodies and a mechanical criterion for hot tearing. *Met. Mater. Trans. B*, 32B:697–705, 2001.
- [76] D.C. Drucker. In *Berkley Int. Mat. Conf.*, pages 795–833. Willey, 1964.
- [77] M. M’Hamdi, Asbjorn Mo, and H.G. Fjaer. Tearsim: A two-phase model addressing hot tearing formation during aluminum direct chill casting. *Met. Trans. A*, 37A:3069, 2006.
- [78] M. Rappaz, M. Bellet, and M. Deville. *Modélisation numérique en science et genie des matériaux*. PPUR, 1998.
- [79] J. Ni and C. Beckermann. A volume-average two phase model for transport phenomena during solidification. *Met. Trans. B*, 22B:349, 1991.
- [80] R. de Boer. Contemporary progress in porous media theory. *Appl Mech Rev*, 53:323, 2000.
- [81] G. Laschet and S. Benkey. Thermomechanical two-phase modelling of the mushy zone during solidification in casting processes. In *COUPLED PROBLEMS*, 2005.
- [82] I. Farup and A. Mo. Two-phase modeling of mushy zone parameters associated with hot tearing. *Met. Trans. A*, 31A:1461, 2000.
- [83] M. M’Hamdi, A. Mo, and Ch. Martin. Two-phase modeling directed toward hot tearing formation in aluminium direct chill casting. *Met. Mater. Trans.*, 33A:2081–93, 2002.
- [84] X. Doré, H. Combeau, and M. Rappaz. Modelling of microsegregation in ternary alloys: Application to the solidification of Al-Mg-Si. *Acta Mater.*, 48:3951–3962, 2000.
- [85] H. Combeau, J.M. Drezet, A. Mo, and M. Rappaz. Modeling of microsegregation in macrosegregation computations. *Met. Mater. Trans.*, 30A(27A):2314–2327, 1996.
- [86] K. Terzaghi. *Theoretical soil mechanics*. Willey : New York, 1943.
- [87] H. P. G. D’Arcy. *Les fontaines publiques de la ville de Dijon*. Victor Valmon Paris, 1856.
- [88] O.N. Scholes, S.A. Clayton, A.F.A. Hoadley, and C. Tiu. Permeability anisotropy due to consolidation of compressible porous media. *Transp. Por. Med.*, pages Published online, in press, 2006.
- [89] J. Kozeny. Uber kapillare leitung des wassers im boden: sitzunsber. *Akad. Wiss Wien.*, 136:271–306, 1927.
- [90] O. Nielsen, L. Arnberg, A. Mo, and H. Thevik. Experimental determination of mushy zone permeability in aluminum-copper alloys with equiaxed microstructures. *Met. Mater. Trans. A*, 30A:2455–62, 1999.
- [91] D. Bernard, O. Nielsen, L. Salvo, and P. Cloetens. Permeability assessment by 3D interdendritic flow simulations on microtomography mappings of Al-Cu alloys. *Mat. Scie. Eng. A*, 392:112–120, 2005.
- [92] J.-M. Drezet and G. Eggler. High apparent creep activation energies in mushy zone microstructures. *Scripta Met.*, 31:757, 1994.
- [93] V. Laxmanan and M.C. Flemings. Deformation of semi-solid Sn-15%Pb alloy. *Met. Trans. A*, 11A:1927, 1980.

- [94] C.L. Martin, D. Favier, and M. Suéry. Viscoplastic behaviour of porous metallic materials saturated with liquid. part i : Constitutive equations. *Int. J. Plasticity*, 13-3:215, 1997.
- [95] C.L. Martin, D. Favier, and M. Suéry. Fracture behaviour in tension of viscoplastic porous metallic materials saturated with liquid. *Int. J. Plasticity*, 15:981, 1999.
- [96] J. Lemaitre and J.L. Chaboche. *Mécanique des matériaux solides*. Dunod, Paris, 1988.
- [97] J.C. Michel and P. Suquet. The constitutive law of nonlinear viscous and porous materials. *J. Mech. Phys. Solids*, 40:783, 1992.
- [98] G. Couturier, J-L. Desbiolles, and M. Rappaz. A porosity model for multi-gas systems in multicomponent alloys. In *Modeling of Casting Welding and Advanced Solidification Processes*. (TMS Publ., Warrendale, PA, USA), 2006.
- [99] M. Lagnès and A. Lesne. *Invariances d'échelle*. Belin, 2003.
- [100] S. Smirnov and W. Werner. Critical exponents for two-dimensional percolation. *Math. Res. Lett.*, 8:729, 2001.
- [101] B.I. Halperin, S. Feng, and P.N. Sen. Differences between lattice and continuum percolation transport exponents. *Phys. Rev. Lett.*, 54(22):2391–94, 1985.
- [102] E.T. Gawlinski and H.E. Stanley. Continuum percolation in two dimensions: Monte carlo tests of scaling and universality for non-interacting discs. *J. Phys. A*, 14:L291–L299., 1981.
- [103] A.R. Kerstein. Equivalence of the void percolation problem for overlapping spheres and a network problem. *J. Phys. A*, 16:3071–3075, 1983.
- [104] S. Feng, B.I. Halperin, and P.N. Sen. Transport properties of continuum systems near the percolation threshold. *Phys. Rev. B*, 35:197, 1987.
- [105] E. Bouchaud. Scaling properties of cracks. *J. Phys: Condens. Matter*, 9:4319–4344, 1997.
- [106] G. Cantor. Über unendliche, lineare punktlannigfaltigkeiten. *Math. Annalen*, 21:545, 1883.
- [107] B. Mandelbrot. *The fractal geometry of nature*. Freeman, San Fransisco, 1982.
- [108] W. Sierpinski. Sur une courbe cantorienne dont tout point est un point de ramification. *C. R. Acad. Sci. Paris*, 160:302, 1915.
- [109] B. Mandelbrot. How long is the coast of Britain ? statistical similarity and fractional dimension. *Science*, 155:636, 1967.
- [110] A. Bunde and S. Havlin. *Fractals in science*, chapter A brief introduction to fractal geometry, page 1. Springer-Verlag, 1994.
- [111] J. Kertész and T. Vicsek. *Fractals in science*, chapter Self-affine interfaces, page 89. Springer-Verlag, 1994.
- [112] J.C. Russ. *Fractal surfaces*. Plenum Press, 1994.
- [113] E. Bouchaud, G. Lapasset, and J. Planès. Fractal dimension of fractured surfaces: A universal value? *Europhys. Lett.*, 13, 1990.

- [114] L. Ponson, D. Bonamy, H. Auradou, G. Mourot, E. Bouchaud S. More and, C. Guillot, and J.P. Hulin. Anisotropic self-affine properties of experimental fracture surfaces. *Int. J. Fracture*, 140:27–36, 2006.
- [115] J.M. Boffa, C. Allain, and J.P. Hulin. Experimental analysis of fracture rugosity in granular and compact rocks. *Eur. Phys. J. Appl. Phys.*, 2:281, 1998.
- [116] L. Ponson, H. Auradou, P. Viè, and J.P. Hulin. Low self-affine exponents of fractured glass ceramics surfaces. *Phys. Rev. Lett.*, 97:125501, 2006.
- [117] L. Ponson. *Crack propagation in disordered materials*. PhD thesis, Ecole Polytechnique, 2006.
- [118] F. Family and T. Vicsek. *Dynamics of Fractal Surfaces*. World Scientific, Singapore, 1991.
- [119] L. Ohm and S. Engler. Festigkeigenschaften erstarrender randschalen aus aluminium-legierungen - teil 1. *Geisereiforschung*, 42, 1990.
- [120] L. Maenner. Propriétés mécaniques d’un alliage AU5 en cours de solidification. Technical report, Pechiney Crv.
- [121] C. Sigli, L. Maenner, C. Sztur, and R. Shahani. Phase diagram, solidification and heat treatment of aluminium alloys. In *International Conference on Aluminum Alloys*, pages 87–98. Jap. Inst. Light Met., 1998.
- [122] T. Meredith. Etude d’alliages d’aluminium en cours de solidification. Master’s thesis, LSMX EPFL, 2006.
- [123] Alicona Imaging. <http://www.alicon.com/>.
- [124] M. Rheme. Dendrite growth directions in AlZn alloys. Master’s thesis, EFPL, 2007.
- [125] G. Chichignoud. Etude de la distribution des films eutectiques en fin de solidification d’un alliage d’aluminium. Master’s thesis, INPG, 2003.
- [126] A.J. Schwartz, M. Kumar, and B.L. Adams. *Electron Backscatter Diffraction in Materials Science*. KLUMER, 2000.
- [127] V. Mathier. Experimental study and numerical modeling of coalescence in heavily inoculated aluminium alloys. Master’s thesis, EPFL, 2003.
- [128] S. Vernède and M. Rappaz. Transition of the mushy zone from continuous liquid films to a coherent solid. *Phil. Mag.*, 86(23):3779–94, 2006.
- [129] S. Vernède and M. Rappaz. A simple and efficient model for mesoscale solidification simulation of globular grain structures. *Acta Mater.*, 55(5):1703, 2007.
- [130] Ch. Charbon and M. Rappaz. Shape of grain boundaries during phase transformations. *Acta Mater.*, 44:2663–68, 1996.
- [131] A. Okabe, B. Boot, K. Sugihara, and S.N. Chiu. *Spatial tessellations*. (Wiley), second edition, 1999.
- [132] C.B. Barber, D.P. Dobkin, and H.T. Huhdanpaa. The quickhull algorithm for convex hulls. *ACM Trans. of Mathematical Software*, 22:469–83, 1996.
- [133] V.R. Voller and S. Sundarraaj. *Mater. Sci. Tech.*, 9:474–481, 1993.

- [134] I. Ohnaka. Mathematical analysis of solute redistribution during solidification with diffusion in solid phase. *Trans. ISIJ*, 26:1045, 1986.
- [135] D.B. Kothe, W.J. Rider, S.J. Mosso, and J.S. Brock. Technical report, Los Alamos Research Laboratories, 1996.
- [136] S. Vernède, Ph. Jarry, and M. Rappaz. A granular model of equiaxed mushy zones: Formation of a coherent solid and localization of feeding. *Acta Mater.*, 54:4023–34, 2006.
- [137] R. Folch and M. Plapp. Quantitative phase-field modeling of two-phase solidification. *Phys. Rev. E*, 72(1):011602, 2005.
- [138] H. J. Diepers and A. Karma. Globular-dendritic transition in equiaxed alloy solidification. In *Solidification Processes and Microstructures*. M. Rappaz, Ch.Beckermann, R. Trivedi, (TMS Publ., Warrendale, PA, USA), 2004.
- [139] T.E. Quested and A.L. Greer. Athermal heterogeneous nucleation of solidification. *Acta Mater.*, 53:2683–2692, 2005.
- [140] J.-A. Ferrez. *Dynamic triangulations for efficient 3D simulation of granular materials*. PhD thesis, EPFL, no 2432, 2001.
- [141] L. Pournin, M. Weber, M. Tsukahara, J.-A. Ferrez, M. Ramaioli, and Th.M. Liebling. Three-dimensional distinct element simulation of spherocylinder crystallization. *Granular Matter*, 7:119–126, 2005.
- [142] Ch. Martin, D. Bouvard, and G. Delette. Discrete element simulations of the compaction of aggregated ceramic powders. *J. Amer. Cera. Soc.*, 89:3379, 2006.
- [143] K.H. Huebner and E.A. Thornton. *The finite element method for engineers*. Willey Interscience, 1982.
- [144] G. Remenieras. *L'hydrologie de l'ingénieur*. Collection EDF, 1986.
- [145] Israelachvili. *J. Colloid and Interf. Scie.*, 110:263, 1986.
- [146] P. Tabeling. *Introduction à la microfluidique*. Belin, 2003.
- [147] P. G. De Gennes. *Langmuir*, 18:3413, 2002.
- [148] H.B. Casimir. On Onsager's principle of microscopic reversibility. *Rev. Mod. Phys.*, 17:343, 1945.
- [149] R.F. Sekerka and W. W. Mullins. Proof of the symmetry of the transport matrix for diffusion and heat flow in fluid system. *J. Chem. Phys.*, 73:1413, 1980.
- [150] H. Weiland, B.L. Adams, and A.D. Rollett, editors. *Grain Growth in Polycrystalline Materials*, volume 3. TMS, 1998.
- [151] C.S. Nolle, B. Koiller, N. Martys, and M.O. Robbins. Morphology and dynamics of interfaces in random two-dimensional media. *Phys. Rev. Lett.*, 71:2075, 1993.
- [152] O. Hunziker, D. Dye, and R.C. Reed. On the formation of a centreline grain boundary during fusion welding,. *Acta. Mat.*, 48:4191, 2000.
- [153] A. Auert. Etude numerique de la compétition de croissance lors de traitement laser de superalliages monocristallins. Master's thesis, LMPH, EPFL, 2003.

- 
- [154] A. Hoadley. Private communication, 2006.
  - [155] P.-G. de Gennes, F. Brochard-Wyart, and D. Quéré. *Gouttes, bulles, perles et ondes*. Belin, 2002.
  - [156] C.M. Gourlay and Dahle. Dilatant shear bands in solidifying metals. *nature*, 445:70, 2007.
  - [157] C.L. Martin. Alloys go with the grain. *nature*, 445:34, 2007.
  - [158] S. Vernède and M. Rappaz. A few equations for a granular mechanical model. Technical report, EPFL LSMX/ ALCAN CRV, 2006.





# Curriculum Vitae

Stéphane VERNÈDE  
[stephane.vernede@gmail.com](mailto:stephane.vernede@gmail.com)

08 October 1980  
 married  
 French nationality

## Education

2002-2003	Master of science, Material science	Paris 6 University
2000-2003	Master of engineering, Applied Physics	Ecole Centrale Paris
1998-2000	Preparation Classes, Physics Chemistry	Orsay, France
1998	Baccalauréat, Science	Antony, France

## Work Experience

2003-2006	Voreppe Research Center (CRV), ALCAN, France / Computational Materials Laboratory (LSMX), EPFL	Doctorate thesis
	• Study of hot cracking in aluminum alloys.	
2003, 6 months	CRV, ALCAN, France	Internship
	• Experimental study of hot cracking.	
2001-2002	Ecole Centrale Paris, France / Research Laboratories of France Museums, Louvre	Student project
	• Study of ancient ceramics glazing processes.	
2001, 2 months	Valinox, titanium tube factory, Changzhou, China	Internship

## Languages

French	Mother tongue
English	Fluent
Chinese Mandarin	Intermediate (~1200 characters)

## Computer skills

Operating systems	Unix-Linux, Windows, MacOSX
Languages	C-C++, BASH, Perl

## Hobbies

Martial Arts, clay modelling, Computer Science.



# List of publications

## Articles

- S. Vernède and M. Rappaz. A simple and efficient model for mesoscale solidification simulation of globular grain structures. *Acta Mater.*, 55(5):1703, 2007.
- S. Vernède, Ph. Jarry, and M. Rappaz. A granular model of equiaxed mushy zones: Formation of a coherent solid and localization of feeding. *Acta Mater.*, 54:4023–34, 2006.
- M. Rappaz, J.M. Drezet, V. Mathier, and S. Vernède. Towards a micro-macro model for hot tearing. *Mat. Sci. Forum*, 519-521:1665–1673, 2006.
- S. Vernède and M. Rappaz. Transition of the mushy zone from continuous liquid films to a coherent solid. *Phil. Mag.*, 86(23):3779–94, 2006.

## Conferences

- M. Rappaz, J.M. Drezet, V. Mathier, and S. Vernède. Towards a micro-macro model of hot tearing. In *Aluminium Alloys*. ICAA, 2006.
- S. Vernède, Ph. Jarry, and M. Rappaz. A granular model for mushy zones: Application to hot tearing. In *Modeling of Casting, Welding and Advanced Solidification Processes - XI*, pages 635–642, 2006.
  - **Award for best oral communication.**
- S. Vernède and M. Rappaz. A granular model of hot tearing and interdendritic feeding. *Euromat*, 2005.
- M. Rappaz and S. Vernède. Transition of the mushy zone from continuous liquid films to a coherent solid. In *Frontiers in solidification science*. TMS, 2005.